Technische Universität München
Fakultät für Physik

Preparations for the Proton-Radius Measurement at AMBER
and
Operation of Silicon-Microstrip Detectors at COMPASS

Christian Dreisbach

Vollständiger Abdruck der von der Fakultät für Physik der Technischen Universität München zur Erlangung des akademischen Grades eines

Doktors der Naturwissenschaften (Dr. rer. nat.)

genehmigten Dissertation.

Vorsitz: apl. Prof. Dr. Norbert Kaiser

Prüfer*innen der Dissertation:

1. Prof. Dr. Stephan Paul
2. apl. Prof. Dr. Hubert Kroha

Die Dissertation wurde am 17.08.2022 bei der Technischen Universität München eingereicht und durch die Fakultät für Physik am 31.08.2022 angenommen.

For my parents,
family and friends

Abstract

The charge radius of the proton can be determined by measuring the slope of the electric form factor G_{E} at small squared four-momentum transfer Q^2. Numerous elastic scattering and laser spectroscopy measurements of the proton radius have been performed with contradicting results —the so-called *proton radius puzzle*. Within this thesis, substantial contributions have been worked out for the proposal to measure the proton radius in high-energy elastic muon-proton scattering at the M2 beam line of CERN's Super Proton Synchrotron going back to Prof. S. Paul. Originally being part of an addendum to the program of the COmmon Muon Proton Apparatus for Structure and Spectroscopy (Compass) collaboration written in the year 2018, it has now been taken over in the new Apparatus for Meson and Baryon Experimental Research (Amber) collaboration. The high-precision measurement at low Q^2 is realized with a high-pressure hydrogen Time Projection Chamber (TPC), a technology developed and contributed by the Petersburg Nuclear Physics Institute (PNPI) and being envisaged also for a sister experiment at Mainzer Mikrotron (MAMI). This allows a new view on the systematics compared to electron scattering. The core setup consists out of silicon and scintillating fiber tracking detectors up- and downstream of the TPC and a novel streaming Data Acquisition (DAQ) to combine the drift time of the TPC with fast tracking detectors. A beam test of a new unified tracking station utilizing scintillating fibers and monolithic pixel-silicon detectors and commissioning of the novel DAQ system are foreseen during 2022 as preparation for an envisaged physics run starting mid of 2023.

Simulations and analysis of the final setup are performed within this thesis. Evaluation of the redundant measurement of the scattering kinematics at a comparable precision show the capability of extracting the radius with an absolute precision < 1 %. Optimizations of the geometry and material budget for the Unified Tracking Station (UTS) and TPC construction are achieved to reach this level of precision.

Within this thesis, the organization of a feasibility test measurement in the year 2018 and results of the ongoing analysis are presented. After a thorough selection of scattered muon events, a timestamp-based matching between tracking and TPC data is used to extract kinematic relations, i.e., the kinetic energy of the recoil proton and muon scattering angle. This timestamp approach is used as predecessor of the novel DAQ system to verify the capability of the combined data taking of tracking and TPC. Based on these results, fundamental insights to the Letter of Intent (LoI) and the subsequent proposal for the proton radius measurement within the novel Amber collaboration are contributed. Muon-electron scattering as intended calibration channel for momentum reconstruction is evaluated as being part of the obtained data set.

As part of this work, a pilot run in 2021 as requirement for an anticipated physics run was organized. It is described together with initial goals set in close communication with CERN's Super Proton Synchrotron Committee (SPSC). With a similar approach as the feasibility test in 2018 a close-to-final setup geometry was constructed. Silicon-microstrip tracking detectors and a down-scaled version of the final TPC is used with the timestamp-based approach to extract correlated events for ongoing studies of the TPC energy resolution in the muon beam.

As a second part of this thesis, the author was responsible for the setting up and operating the existing silicon-microstrip detectors during the Compass data takings in 2016 to 2022 and their employment for the proton-radius-related beam tests for Amber in 2018 and 2021. Besides upgrades of the used cooling system, required time calibrations have been created and improved and the performance of the detectors is evaluated during those years.

Zusammenfassung

Der Ladungsradius des Protons kann durch Messung der Steigung des elektrischen Formfaktors G_{E} bei kleinem quadrierten Viermomententransfer Q^2 bestimmt werden. Zahlreiche Messungen des Protonenradius durch elastische Streuung und Laserspektroskopie wurden mit widersprüchlichen Ergebnissen durchgeführt - das sogenannte *Protonenradius-Puzzel*. Im Rahmen dieser Arbeit wurden wesentliche Beiträge für den auf Prof. S. Paul zurückgehenden Vorschlag zur Messung des Protonenradius in der hochenergetischen elastischen Myonen-Protonen-Streuung an der M2-Strahllinie des Super-Protonen-Synchrotrons des CERN erarbeitet. Ursprünglich Teil eines Addendums zum Programm der Compass Kollaboration aus dem Jahr 2018, wurde es nun in die neue Amber Kollaboration übernommen. Die hochpräzise Messung bei niedrigem Q^2 wird mit einer Hochdruck-Wasserstoff TPC realisiert. Einer Technologie, die vom PNPI entwickelt und beigesteuert wurde und auch für ein Schwestern-Experiment bei MAMI vorgesehen ist. Dies ermöglicht einen neuen Blick auf die Systematik im Vergleich zur Elektronenstreuung. Der Kernaufbau besteht aus Silizium- und Faser-Spurdetektoren, die vor- und hinter der TPC positioniert sind. Ein Strahltest einer neuen, vereinheitlichten Spurrekonstruktions-Station (UTS) mit szintillierenden Fasern und monolithischen Pixel-Silizium-Detektoren sowie die Inbetriebnahme des neuartigen Streaming-DAQ-Systems sind für das Jahr 2022 als Vorbereitung für einen geplanten Datennahme ab Mitte 2023 vorgesehen.

Simulationen und Analysen des endgültigen Aufbaus werden im Rahmen dieser Arbeit durchgeführt. Die Auswertung der redundanten Messung der Streukinematik bei vergleichbarer Genauigkeit zeigt die Fähigkeit, den Radius mit einer absoluten Genauigkeit von < 1 ‰ zu extrahieren. Optimierungen der Geometrie und des Materialbudgets für die UTS- und TPC-Konstruktion wurden durchgeführt, um diese Genauigkeit zu erreichen.

In dieser Arbeit werden die Durchführung einer Machbarkeits-Testmessung im Jahr 2018 und die Ergebnisse der laufenden Analyse vorgestellt. Nach einer sorgfältigen Auswahl von gestreuten Myonenereignissen wird ein zeitstempelbasierter Abgleich zwischen Spurrekonstruktion- und TPC-Daten verwendet, um kinematische Beziehungen zu extrahieren. Die Verwendung dieses Zeitstempel-Ansatzes als Vorläufer des neuartigen DAQ-Systems wird genutzt, um die Fähigkeit der kombinierten Datenaufnahme von Spurrekonstruktion und TPC zu verifizieren. Basierend auf diesen Ergebnissen werden grundlegende Erkenntnisse zum LoI und dem anschließenden Vorschlag für die Protonenradiusmessung innerhalb der neuartigen Amber-Kollaboration beigetragen. Die Myon-Elektron-Streuung als beabsichtigter Kalibrierungskanal für die Impulsrekonstruktion wird als Teil des erhaltenen Datensatzes evaluiert.

Im Rahmen dieser Arbeit wurde ein Pilotlauf im Jahr 2021 als Voraussetzung für einen zu erwartenden Datennahme organisiert. Dieser wird zusammen mit den ersten Zielen beschrieben, die in enger Kommunikation mit dem SPSC des CERN festgelegt wurden. Mit einem ähnlichen Ansatz wie beim Machbarkeitstest im Jahr 2018 wurde eine nahezu finalen Aufbaugeometrie erstellt. Silizium-Mikrostreifen-Spurrekonstruktionsdetektoren und eine verkleinerte Version der finalen TPC werden mit dem zeitstempelbasierten Ansatz verwendet, um korrelierte Ereignisse für laufende Studien zur Energieauflösung des TPC im Myonenstrahl zu extrahieren.

Als zweiter Teil dieser Arbeit war der Autor für den Aufbau und den Betrieb der bestehenden Silizium-Mikrostreifen-Detektoren während der COMPASS-Datennahmen in den Jahren 2016 bis 2022 und deren Einsatz für die protonenradiusbezogenen Strahltests für AMBER in den Jahren 2018 und 2021 verantwortlich. Neben Verbesserungen des verwendeten Kühlsystems wurden die erforderlichen Zeitkalibrierungen erstellt und verbessert, sowie die Auflösung und Effizienz der Detektoren in diesen Jahren bewertet.

Contents

Part I

Proton Charge-Radius Measurement

CHAPTER 1

The Proton Charge-Radius in High-Energy Elastic Muon-Proton Scattering

Atoms are the building blocks of all visible matter in the universe. Their arrangement and interactions are part of everyday life. Studying their fundamental properties has always been a quest for science. The proton and its neutral partner, the neutron, which together built up the nucleus in atoms, obtains a special role in defining the quantities of elements. Despite the proton's fundamental character, basic quantities like its size are not yet measured with consistent results. Its extent is given by its internal charge distribution. This charge radius of the proton is encoded in its electric form factor, and it can be determined by measuring the slope of this form factor at small four-momentum transfer obtained from elastic scattering processes of point-like probes like electrons or muons. Besides numerous scattering measurements, also the different approach of hydrogen spectroscopy to obtain the proton radius have been performed with partly contradicting results, often referred to as the *proton radius puzzle*. A measurement of the proton charge radius using high-energy elastic muon-proton scattering at the M2 beam line at the Super Proton Synchrotron (SPS) located in the north area at Conseil Européen pour la Recherche Nucléaire (CERN) was proposed by the new AMBER collaboration to take place starting mid of 2023 [1, 2]. This high-precision Proton-Radius Measurement (PRM) at low Q^2, performed with a high-pressure hydrogen-filled TPC, can contribute to a solution of the puzzle, especially due to the different systematic effects of this approach compared to those of elastic electron-proton scattering. In this chapter, the current situation of the proton radius puzzle is described and the novel approach of using an active-target TPC in elastic muon-proton scattering is put into perspective with existing and upcoming experiments. The requirements of the proposed setup are elaborated together with the ongoing studies in layout and detector geometry. Furthermore, the resulting acceptance and resolutions are discussed with the view of an envisaged physics measurement at CERN in 2023/2024.

1.1 Proton Radius Puzzle

Since the 1950s attempts are ongoing to extract the proton charge radius [3]. Elastic electron-proton scattering measurements were performed to probe the spatial distribution of the charge inside the proton. In Fig. 1.1 a time-sorted compilation of measurements on the proton-radius puzzle is shown. A clear discrepancy between two favored values — the lower 0.84 fm and larger 0.88 fm, is visible without a clear tendency and results in this puzzle. The proposed measurement is placed here arbitrarily at 0.86 fm with the expected uncertainty as described in more detail in Sec. 1.2.9.

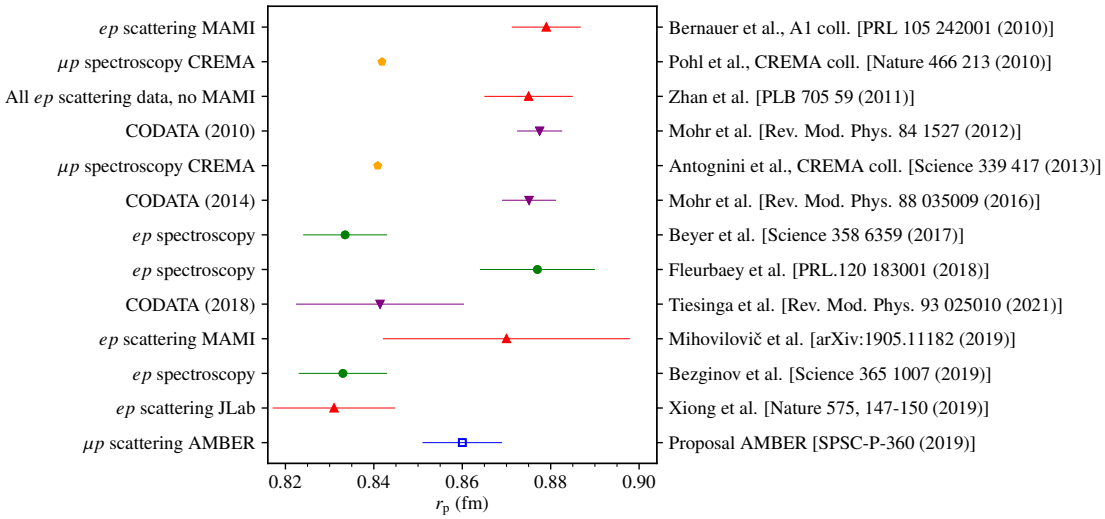

Figure 1.1: Compilation of results on the proton-radius puzzle, sorted by time. Electron-proton scattering and spectroscopy (red/green), muon-proton spectroscopy (orange) and summary data (purple) is shown with the value of this proposed measurement (blue) arbitrarily placed at 0.86 fm, with the projected uncertainty. Error bars represent statistical and systematic uncertainties added in quadrature. Composed together with [4, 5].

With one of the most recent results in experimental extraction of the proton charge-radius preformed by Proton Radius (PRAD) collaboration [6] an additional lower value for the proton radius has been published. Nevertheless, comparing the underlying cross-section data between the previous A1 data [7] and the recent PRAD data as given in Fig. 1.2, shows a tension between both data sets, which has not yet been fully understood. With the PRAD data (blue) and their respective fit to extract the proton radius, a clear discrepancy between the earlier cross-section data obtained by the A1 collaboration in Mainz (red) is present, especially for $Q^2 > 0.01$ GeV$^2/c^2$. Forced parametrizations to extract the radius value obtained by the PRAD collaboration based on the A1 data cannot describe the respective cross-section results. The difference of the two data sets requires further investigation.

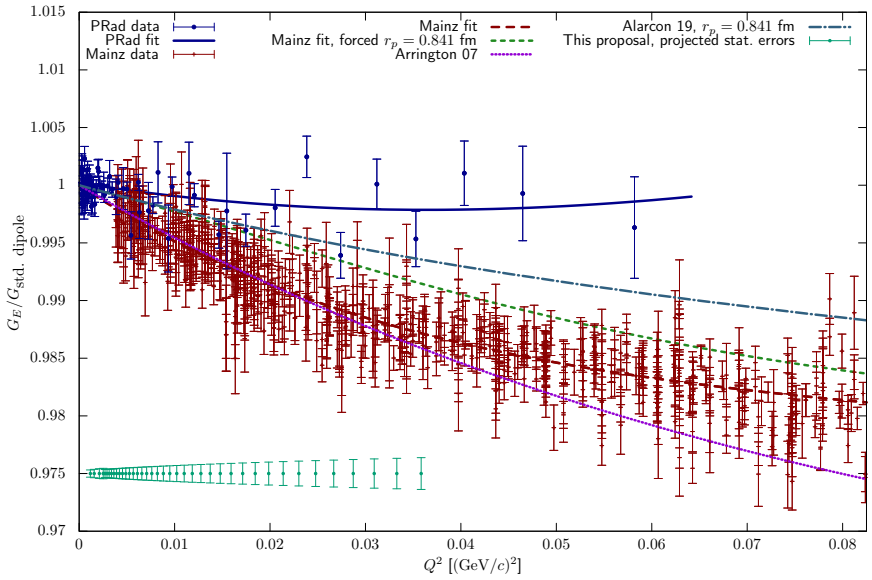

Figure 1.2: Comparison of the cross-section data of the PRad and Mainz A1 collaboration. Different parametrizations to extract the proton charge-radius based on the different data sets are shown. The anticipated Q^2-range with the respective uncertainty for the Amber collaboration are indicated. Figure taken from [8] (modified).

To contribute to the solution of the puzzle, the Amber collaboration proposes a measurement of the proton charge-radius in high-energy elastic muon-electron scattering. The anticipated range of Q^2 is $10^{-3} \leq Q^2/(\text{GeV}^2/c^2) \leq 4 \cdot 10^{-2}$ and is shown in Fig. 1.2 with the respective expected uncertainties. The unique location of the M2 beam line at CERN is used providing different muon momenta between 60 and 190 GeV at rates up to $4 \cdot 10^7$ Hz. The planned beam momenta will be 100 GeV for the measurement and a possible lower 60 GeV momentum for systematic studies at a beam rate of $2 \cdot 10^6$ Hz is foreseen (cf. Sec. 1.2.2). The Amber spectrometer provides tracking, momentum reconstruction, muon identification and calorimetry. This allows a precise measurement of the muon trajectory and in addition the study of radiative effects contributing to the measured momentum transfer by using the information obtained by photons measured in the calorimeter. This spectrometer is the continuation of the existing Compass spectrometer and will be transferred from the Compass to the Amber collaboration towards 2023.

Furthermore, a redundant measurement of the scattering process will be performed by utilizing an active-target pressurized-hydrogen TPC at up to 20 bar besides the tracking of the scattered muon. This allows to measure the kinetic energy of the recoiling proton in combination with the measurement of the muon. The resulting data set will contribute due to its different systematics compared to elastic electron-proton scattering and the novel measurement principle to a solution of the puzzle of the proton-charge radius. In addition, if the extracted values from electron and muon scattering differ, the basic concept of lepton-flavor universality would be violated. Possible hints of such a violation have already been seen in the decay of B-mesons [9].

According to [10–13] theory provides a determination of the proton radius in the scope of dispersion theory. Nevertheless, additional measurements are welcomed to further increase the precision on this basic quantity. As a different approach, measuring the Lamb shift [14] as the difference between the first and second excited energy levels in hydrogen provides information about the size of the proton. Using a laser to determine the required energy to excite the electron from the first to the second energy level away from the influence of the proton reveals the size of it. This approach is performed in regular hydrogen [15] and also muonic-hydrogen spectroscopy, where the electron is replaced by a muon. Due to its 200x larger mass of the muon, it is closer to the proton and therefore even more sensible to the size of it. Recent results of the Charge Radius Experiment with Muonic Atoms (CREMA) collaboration [16] further increase the discrepancy between the two results significantly due to the high precision of the measurement. In electron-proton scattering, the most recent PRAD result is consistent with the lower value and also with results stemming from the hydrogen spectroscopy [6]. Nevertheless, a persistent discrepancy on the cross-section level is present and requires additional data [8]. New insights are expected from the Muon proton Scattering Experiment (MUSE) collaboration utilizing different beam particle types (μ, e) and an upgraded version of the PRAD experiment. Further experiments are planned covering different kinematic ranges. In Tab. 1.1 a list of those planned experiments is given contributing to further knowledge on the proton radius topic.

Table 1.1: Upcoming lepton-proton scattering experiments within the next years. Their respective beam properties and kinematic ranges are given.

	beam	Q^2 (10^{-3} GeV$^2/c^2$)	E_{beam} (GeV)
MAGIX/MESA [17]	e	0.01 – 20	0.02 – 0.1
MUSE/PSI [18]	e/μ	2 – 80	0.1 – 0.2
PRad-II/JLAB [6]	e	0.02 – 60	0.7 – 2
PRES/MAMI [19]	e	1 – 20	0.72
Prorad/Orsay [20]	e	0.01 – 0.3	0.03 – 0.14
ULQ2/Tohoku [21]	e	0.3 – 8	0.06
AMBER/CERN [2]	μ	1 – 40	100

1.1.1 From Form Factor to Charge Radius

The electromagnetic form factors G_E and G_M of the proton encodes its response to outer electric and magnetic fields and is correlated with its extent. In a dipole approximation motivated by the proton's substructure, both factors depend on the squared four-momentum transfer in elastic-scattering events, typically denoted as Q^2.

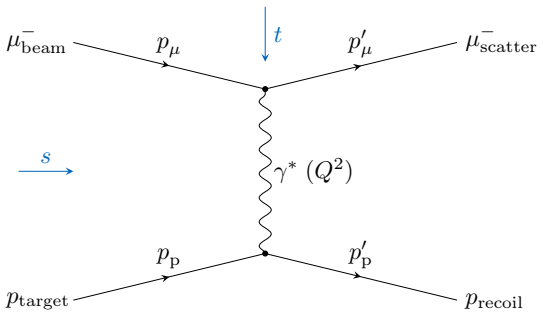

Figure 1.3: First order Feynman diagram of elastic muon-proton scattering with the momentum transfer $Q^2 = -t$ carried by the virtual photon between the scattered muon off a resting target proton and the recoiling proton. The s- and t-channel directions are indicated.

In Fig. 1.3 the first-order Feynman diagram of the elastic-scattering process of muon and proton is shown. For the proposed measurement at AMBER, a hydrogen (proton) target is foreseen. The incoming beam muons are scattered off the protons at rest, resulting in a deflected muon and a recoiling proton. The momentum transfer between both is carried by the connecting virtual photon. The charge distribution of the proton encoded in the electric form-factor G_E can be probed by measuring this momentum transfer. The slope of the electric form factor at zero momentum transfer defines the mean square charge-radius as

$$\langle r_\mathrm{p}^2 \rangle = -6\hbar^2 \frac{\mathrm{d}G_\mathrm{E}\left(Q^2\right)}{\mathrm{d}Q^2}\bigg|_{Q^2=0} . \tag{1.1}$$

With the form factor given as Taylor expansion as

$$G_\mathrm{E}\left(Q^2\right) = 1 - \frac{1}{6}\frac{Q^2\langle r_\mathrm{p}^2\rangle}{\hbar^2} + \cdots . \tag{1.2}$$

To obtain the mean squared charge-radius the form factor needs to be measured at very small values of Q^2. The resulting slope is directly proportional to the charge radius via $\langle r_\mathrm{p}^2\rangle$. In the dipole approximation (cf. Fig. 1.4), the electric and magnetic form factor can be expressed as

$$G_{\mathrm{E}}(Q^2) = \frac{G_{\mathrm{M}}(Q^2)}{\mu_{\mathrm{p}}} = \frac{1}{\left(1 + \frac{Q^2}{a^2}\right)^2} \equiv G_{\mathrm{D}}(Q^2). \tag{1.3}$$

Here, the constant $a^2 \approx 0.71\,\mathrm{GeV}^2/c^2$ is obtained from the general behavior of electron scattering especially at $Q^2 > 0.1$ GeV and $\mu_p = 2.79$ as the magnetic moment of the proton. The proton radius, defined as the root mean square of its charge distribution, is then given by

$$\langle r_{\mathrm{p}}^2 \rangle = -6\hbar^2 \frac{\mathrm{d}G_{\mathrm{E}}\left(Q^2\right)}{\mathrm{d}Q^2}\bigg|_{Q^2 \to 0} \overset{\text{dipole}}{=} \frac{12}{a^2} \approx (0.81\ \mathrm{fm})^2 \quad \Rightarrow \quad r_{\mathrm{p}}^{\mathrm{rms}} \approx 0.8\ \mathrm{fm}. \tag{1.4}$$

With the radius in this approximation given by

$$r_{\mathrm{p}} = \hbar\sqrt{\frac{12}{a^2}}. \tag{1.5}$$

1.1.2 Elastic Muon-Proton Scattering Cross-Section

With the Feynman diagram shown in Fig. 1.3 for the elastic scattering of a muon off a proton the transferred squared four-momentum is defined as

$$q^2 = \left(p_\mu - p_{\mathrm{p}}\right)^2. \tag{1.6}$$

It can be expressed in terms of the incoming and outgoing lepton energy E_μ and E'_μ and momenta $\vec{p}_\mu$ and $\vec{p}'_\mu$ and the muon scattering angle θ as

$$\begin{aligned} -q^2 = Q^2 &= -(p_\mu - p'_\mu)^2 \\ &= -2m_\mu^2 + 2E_\mu E'_\mu - 2\left|\vec{p}_\mu\right|\left|\vec{p}'_\mu\right|\cos(\theta). \end{aligned} \tag{1.7}$$

In the high-energy approximation ($E \gg m$), Eq. (1.7) is commonly approximated as

$$Q^2 \approx 4E_\mu E'_\mu \sin^2(\theta/2). \tag{1.8}$$

The absolute momenta of the incoming and outgoing muon can be expressed by

$$\left|\vec{p}_\mu\right| = \sqrt{E_\mu^2 - m_\mu^2} \quad \text{and} \quad \left|\vec{p}'_\mu\right| = \sqrt{E_\mu'^2 - m_\mu^2}. \tag{1.9}$$

The elastic cross-section can be written as given in [1]

$$\frac{\mathrm{d}\sigma^{\mu\mathrm{p}\to\mu\mathrm{p}}}{\mathrm{d}Q^2} = \frac{\pi\alpha^2}{Q^4 m_\mathrm{p}^2 \vec{p}_\mu^{\,2}} \left[\left(G_\mathrm{E}^2 + \tau G_\mathrm{M}^2 \right) \frac{4E_\mu^2 m_\mathrm{p}^2 - Q^2(s - m_\mu^2)}{1+\tau} - G_\mathrm{M}^2 \frac{2m_\mu^2 Q^2 - Q^4}{2} \right], \tag{1.10}$$

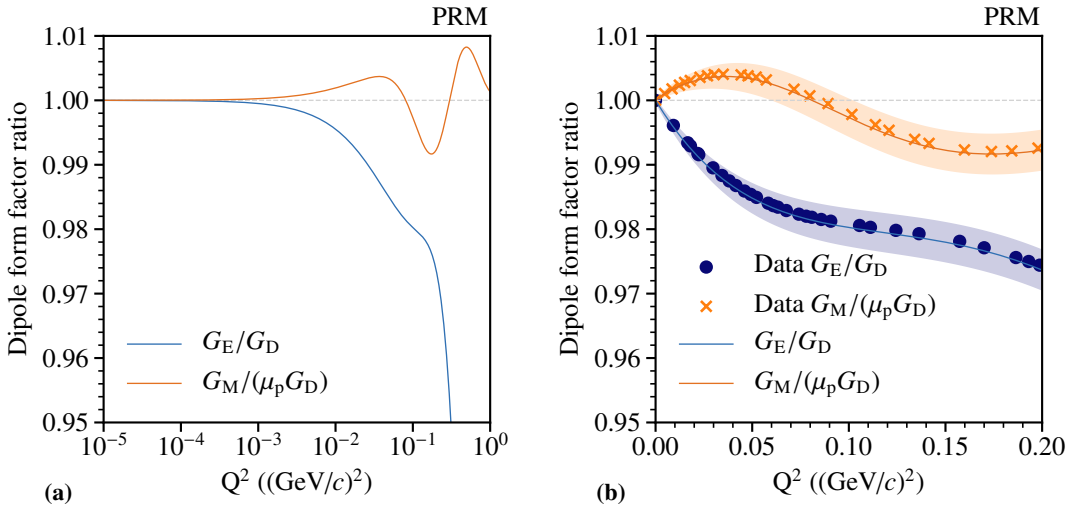

Figure 1.4: In (a) the electric and magnetic form factor G_E and G_M normalized to the dipole form factor G_D are shown based on the parametrizations of measured data shown in (b) with uncertainty bands. Parameterizations and data taken from [7].

where $\tau = Q^2/4m_\mathrm{p}^2$ and the squared center-of-mass momentum energy s, defined within the laboratory frame where the target proton is at rest by

$$\begin{aligned} s &= (p_\mu + p_\mathrm{p})^2 \\ &= 2E_\mu m_\mathrm{p} + m_\mathrm{p}^2 + m_\mu^2. \end{aligned} \tag{1.11}$$

The elastic cross-section is commonly written in the so-called Rosenbluth separation [22]. Electric and magnetic form factor are split into single terms according to [23] as

$$\frac{\mathrm{d}\sigma^{\mu\mathrm{p}\to\mu\mathrm{p}}}{\mathrm{d}Q^2} = \frac{4\pi\alpha^2}{Q^4} R \left(\epsilon G_\mathrm{E}^2 + \tau G_\mathrm{M}^2 \right) \tag{1.12}$$

with the recoil and longitudinal-polarization variables

$$R = \frac{\vec{p}_\mu^{\,2} - \tau\left(s - 2m_\mathrm{p}^2\,(1+\tau)\right)}{\vec{p}_\mu^{\,2}\,(1+\tau)} \qquad \text{and} \qquad \epsilon = \frac{E_\mu^2 - \tau\left(s - m_\mu^2\right)}{\vec{p}_\mu^{\,2} - \tau\left(s + 2m_\mathrm{p}^2\right)(1+\tau)}. \tag{1.13}$$

The cross-section is shown in Fig. 1.33. In Fig. 1.4(a), the ratio between G_E and G_M to the dipole form factor G_D is shown. Deviations from the dipole approximations are visible with increasing Q^2 in the order of 2 % around 10^{-1} GeV$^2/c^2$ for G_E.

1.1.3 Calculation of Q^2

Using the common approximation for Q^2 for the scattered lepton as given in Eq. (1.8) one neglects the mass of the lepton. For the electron case this is valid, but for the 200x heavier muon the mass plays an important role. Based on the conservation four-momentum transfer

$$p_\mu + p_\mathrm{p} - p'_\mu = p'_\mathrm{p} \qquad \text{and} \tag{1.14}$$

$$(p_\mu + p_\mathrm{p} - p'_\mu)^2 = p'^2_\mathrm{p}, \tag{1.15}$$

Eq. (1.15) results in

$$m_\mu^2 + E_\mu m_\mathrm{p} - E_\mu E'_\mu + \left|\vec{p}_\mu\right|\left|\vec{p}'_\mu\right|\cos(\theta) - E'_\mu m_\mathrm{p} = 0. \tag{1.16}$$

Using Eq. (1.9) to express $\left|\vec{p}'_\mu\right|$ in terms of E'_μ and reordering the equation in E'_μ one obtains

$$\left|\vec{p}_\mu\right|\sqrt{E'^2_\mu - m_\mu^2}\cos(\theta) = E'_\mu\left(m_\mathrm{p} + E_\mu\right) - m_\mu^2 - E_\mu m_\mathrm{p}. \tag{1.17}$$

A quadratic solution for E'_μ can be obtained by using the following substitutions:

$$A = \left|\vec{p}_\mu\right|\cos(\theta), \quad B = m_\mathrm{p} + E_\mu, \quad C = -m_\mu^2 - E_\mu m_\mathrm{p}, \tag{1.18}$$

results to

$$A\sqrt{E'^2_\mu - m_\mu^2} = E'_\mu B + C. \tag{1.19}$$

Solving Eq. (1.19) for E'_μ gives the quadratic solution, which reads as

$$E'_{\mu,1,2} = \frac{BC}{A^2 - B^2} \pm \frac{A}{A^2 - B^2}\sqrt{m_\mu^2\left(A^2 - B^2\right) + C^2}. \tag{1.20}$$

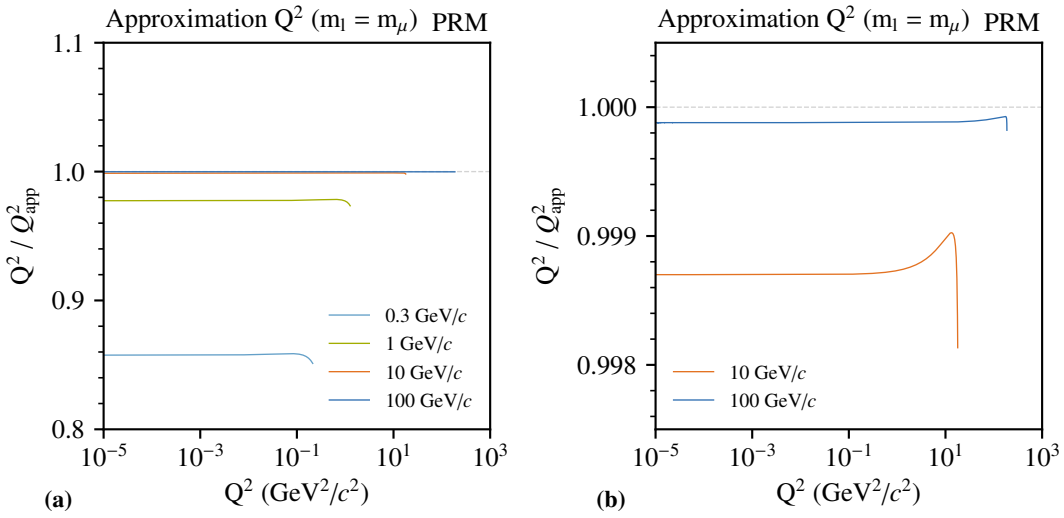

Figure 1.5: Impact of the Q^2 approximation (Q^2_{app}) in the high-energy case in lepton-proton scattering by neglecting the respective lepton mass for different beam momenta compared to the exact calculation. In (a) the muon case is shown for different beam momenta. A close-up is shown in (b).

The two solutions of Eq. (1.20) need to satisfy the relation in Eq. (1.19). In most cases, the negative solution result is valid. The exact Q^2 dependency between the beam energy E_μ and the scattering angle θ from Eq. (1.7) can be calculated. The effect of the approximation, as given in Eq. (1.8) used to calculate Q^2 for the muon case, is shown in Fig. 1.5. Whereas the effect for electrons can be neglected due to their small mass, the effect for muons is contributing at lower momenta, i.e., for beam momenta of $O(300\ \text{MeV})$ the effect is about 15 %. With increasing beam momenta it becomes smaller and for the anticipated momentum of 100 GeV it is around 0.1 %. For larger Q^2 values, the deviation from the constant value is visible towards the maximal Q^2, which can be expressed as

$$Q^2_{\text{max}} = \frac{4 \cdot m_{\text{p}}^2 \cdot \left|\vec{p}_\mu\right|}{s}, \tag{1.21}$$

with the center-of-mass energy s given in Eq. (1.11). The Q^2 value can also be calculated by measuring the kinetic energy of the recoil proton as it is used in the combined measurement with the TPC. Based on the given definition of Q^2, one obtains

$$t = -Q^2 = (p'_{\text{p}} - p_{\text{p}})^2 \Leftrightarrow \tag{1.22}$$

$$E'_p = \frac{Q^2}{2m_{\text{p}}} + m_{\text{p}} = E_{\text{p,kin}} + m_{\text{p}} \tag{1.23}$$

$$\Rightarrow E_{\text{p,kin}} = \frac{Q^2}{2m_{\text{p}}}. \tag{1.24}$$

1.2 Proton Charge-Radius Measurement at AMBER

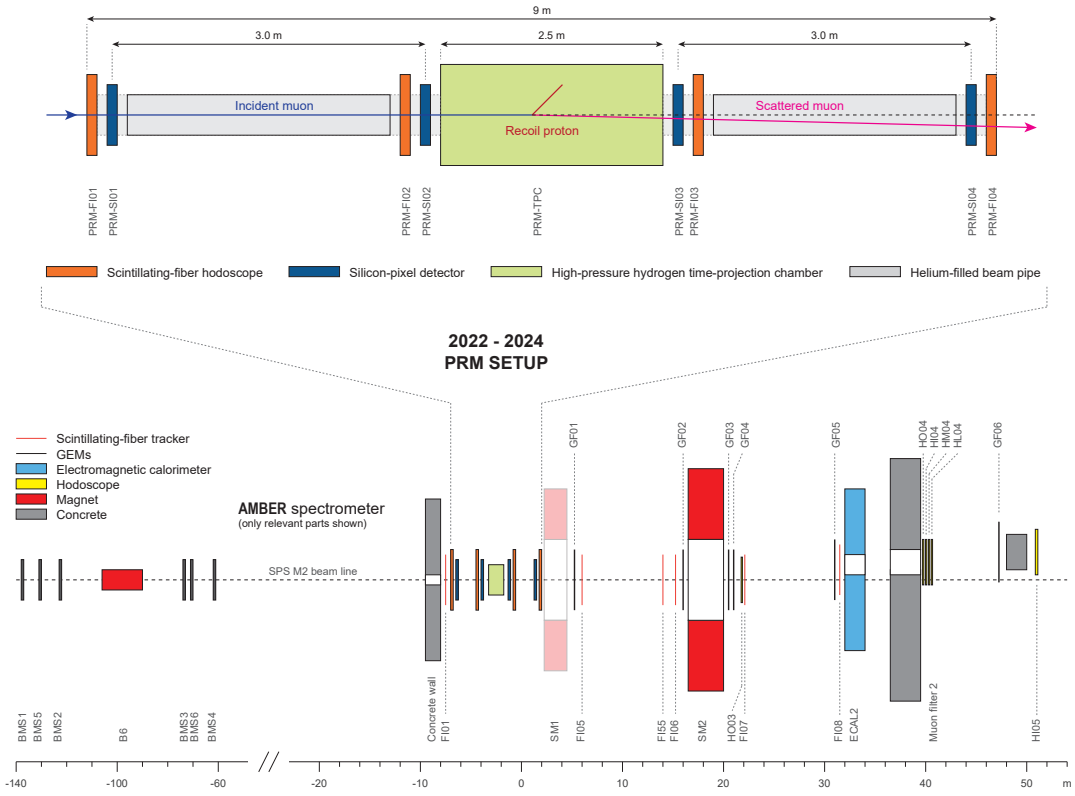

Figure 1.6: Schematic layout of the setup for a proton charge-radius measurement using the AMBER spectrometer. The core setup shown in the top for the measurement consisting of TPC, silicon tracking detectors, helium tubes and fiber trackers is located in the target area of the spectrometer. Tracking detectors are indicated along the spectrometer as well as dipole magnets for momentum measurement. Only relevant parts are shown. Figure taken from [2].

Based on the current situation of the proton charge-radius measurement and its ongoing puzzle as discussed in Sec. 1.1, the proposed muon-proton elastic-scattering at high energies [1] puts the PRM campaign at AMBER and CERN's M2 beam line in a unique position. Measuring at low-Q^2 values suppresses the contribution of the magnetic form factor G_M according to Eq. (1.12) since $\tau \to 0$. In the case of high-energetic muons with energies $E_\mu > 10\,\mathrm{GeV}/c$, the recoil and longitudinal-polarization variables $\epsilon \to 1$ and $R \to 1$. The elastic cross-section measurement in this kinematic region is directly proportional to the electric form factor G_E . Furthermore, the radiative corrections are much smaller compared to electron-proton scattering and are below 1 % according to [24] for the anticipated kinematic region. The PRM program plans to measure at muon beam momenta between 60 GeV and 100 GeV covering a Q^2 range of $10^{-3} \leq Q^2/(\mathrm{GeV}^2/c^2) \leq 4 \cdot 10^{-2}$. Whereas the measurement is planned to use a momentum of 100 GeV, systematic studies correlated with angular acceptance and multiple scattering can be performed using the lower 60 GeV momentum. The resulting angular range of the scattered

muon is 0.3–2 mrad for 100 GeV beam momentum and increases for a momentum of 60 GeV to 0.5–3 mrad. The precise measurement of these small scattering angles requires a low material budget of the setup. Due to the active target and the introduced ionization noise, a maximal beam rate of $2 \cdot 10^6$ Hz is anticipated to obtain the required energy resolution (cf. Sec. 1.2.2). Besides measuring the scattered muon trajectory, the kinetic energy of the recoil proton inside a pressurized hydrogen active-target TPC at up to 20 bar will be utilized to have a redundant measuring principle of the scattering process. In addition, a full-scale magnetic spectrometer is foreseen. It provides momentum reconstruction, muon identification and calorimetry. The goal is to provide data, which allow an extraction of the proton charge radius with an absolute precision < 1 % in the novel elastic muon-proton scattering approach compared to the traditional electron case.

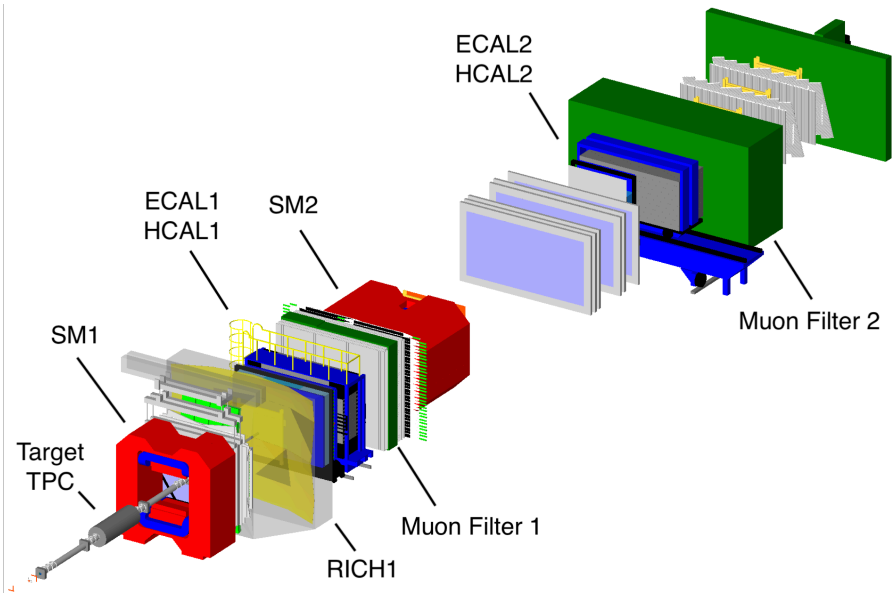

Figure 1.7: The spectrometer as GEANT4 simulation. The beam enters the setup from the lower left corner. The core setup is visible in the target area (Target TPC) with the respective parts of the spectrometer are labeled.

The layout of the planned setup is shown in Fig. 1.6 as a schematic drawing. The core setup placed in the target area of the spectrometer is shown at the top with its 2.5 m long high-pressure hydrogen TPC as a target in the center with the beam entering from the lower left side. The beam axis is defined as the z-direction and x and y are oriented along the horizontal and vertical direction, respectively. The TPC is equipped with dedicated 0.5 mm thick beam windows with a diameter of 70 mm allowing the beam particles to enter and leave the active volume without passing larger material budgets. Silicon and scintillating-fiber tracking detectors are used with an active area of $90 \times 90\,\mathrm{mm}^2$ and $96 \times 96\,\mathrm{mm}^2$, respectively. They are placed up- and downstream of the TPC along the 3 m long lever arm. This so-called baseline improves the angular- and vertex z-resolution. Helium filled beam pipes along the lever arms are used to decrease multiple scattering in air.

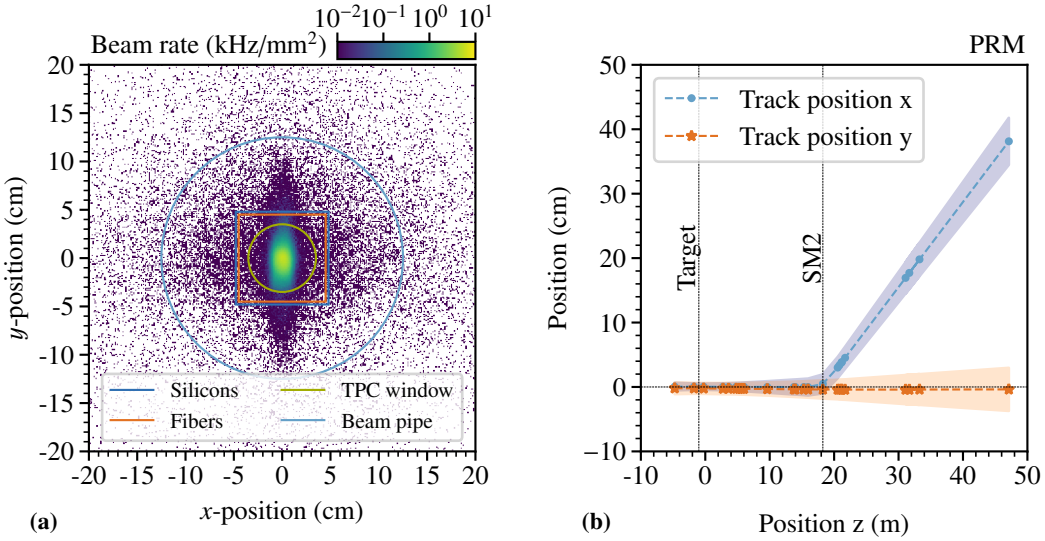

Figure 1.8: Simulated beam properties for the PRM layout. In (a) the beam flux in the target position is shown with the size of the core components indicated. In (b) the simulated track position in x- and y-projection along the spectrometer for the single magnet operation at a beam momentum of 100 GeV is shown. Single detector planes are indicated as dots. Simulation of the beam profile is provided by [25].

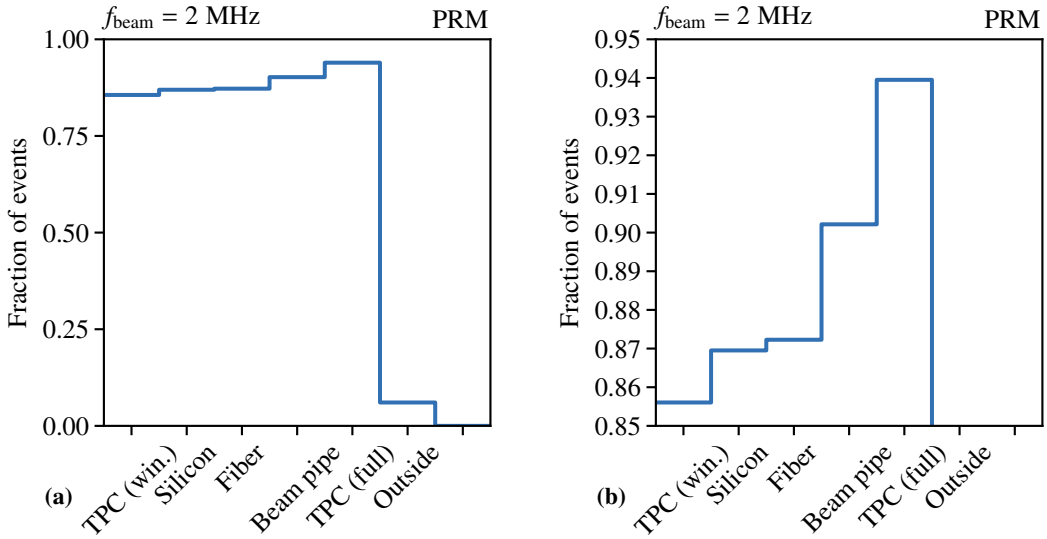

Figure 1.9: Estimated fraction of beam particles passing through the individual detector area parts. In (a) the full scale is shown. A close-up view is shown (b).

The foreseen beam profile at the position of the core detector elements is shown in Fig. 1.8(a). The active areas as well as the TPC beam windows enclose the central part of the beam and only a minor fraction is outside. Due to the beam optics, the extent along the y-axis is more pronounced.

The beam is well covered by the tracking detectors and passes through the beam windows of the TPC. Sufficient surface overlap between the detector elements guarantees overlap between the tracking detectors especially during the positioning. The beam pipes are designed in the way that they cover the particularly extended y-direction of the beam. The expected fraction of beam coverage for the individual detectors is shown in Fig. 1.9. About 85 % of the incoming particles passes through the TPC beam windows and the tracking detectors. More than 90 % passes through the inner part of the beam pipes and the additional 5 % of the beam pass through the outer structure of the TPC. The small beam fraction passing outside of the active areas is expected to have only minor contributions on the event reconstruction.

The usage of the spectrometer offers momentum reconstruction using the magnet Spectrometer Magnet 2 (SM2) combined with tracking detectors. Mainly scintillating fiber detectors (FI) and novel GEM Free-Running (GF) detectors are used to cover the required small-angle part (cf. Fig. 1.6). To fit the 10 m long PRM core setup into the target area of the spectrometer, the first dipole magnet (SM1) will not be used to avoid influence by the fringe field on the small angle tracking in the target area. This change in magnet configuration especially downstream of Spectrometer Magnet 1 (SM1) requires repositioning of the detectors for the data taking along the spectrometer with respect to the default configuration used in previous measurements. The simulated beam position along the spectrometer is shown in Fig. 1.8(b). Furthermore, muon identification is provided using the Muon Filter 2 (MF2). It uses absorber layers to stop incoming hadrons [26] allowing only muons to pass through. Together with tracking and hodoscopes at the most downstream positions of the spectrometer muon tracks can be identified. To measure the radiative effects or identify electrons, electromagnetic calorimetry is provided by the Electromagnetic Calorimeter 2 (ECAL2), particular for small angles. Additional larger tracking detectors (Multi-Wire Proportional Chamber (MWPC)) and hodoscopes are foreseen to cover the central horizontal part of ECAL2 along the bending direction of the SM2 to allow a distinction between charged and non-charged tracks.

The momentum of the incoming beam particle is measured by the so-called Beam Momentum Station (BMS). Six stations are positioned in the M2 beam line close to the target area. Three stations are placed upstream and three downstream of the Bend 6 (B6) dipole magnet (cf. Fig. 1.10). With the operation of a TPC combined with tracking detectors covering time windows from $\mathcal{O}(300\ \text{ps})$ to $\mathcal{O}(100\ \mu\text{s})$ a novel continuously running DAQ is required and will replace the existing triggered DAQ system. This so-called Free-Running Trigger-less Data Acquisition System (FriDAQ) will continuously read out all detectors and will use a software-based high-level trigger to select events.

The full setup is included in the GEANT4-based simulation framework "Total Geometry And Tracking (TGEANT)" allowing detailed studies of the overall layout. A screenshot of the visualization is shown in Fig. 1.7. In the following, studies are based on this implementation and a realistic beam profile to evaluate the performance of the spectrometer and its single components.

1.2.1 The M2 Beam Line

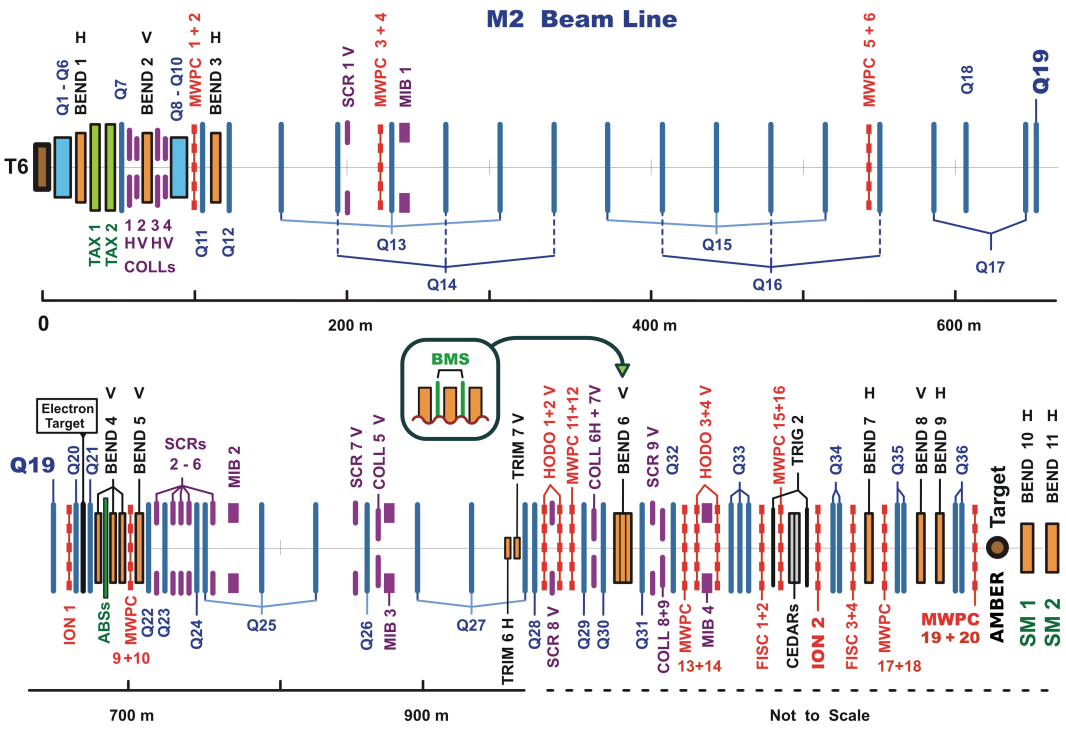

Figure 1.10: The M2 beam line guiding secondary and tertiary particle beams with momenta up to 225 GeV to the experimental area where the AMBER spectrometer and is located. From the T6 production target quadrupols (Q) and bending magnets (BEND) are used for beam steering. Collimators (COLLs) and scrapers (SCR) are used for beam cleaning. Different ionization chambers (ION) and MWPCs are used for the beam position measurement. The BMS stations for momentum measurement are indicated. Figure taken from [26], modified.

The AMBER experiment is located in the North Area of CERN at the SPS, which provides a primary proton beam with momenta of up to 225 GeV to the M2 beam line supplying the AMBER spectrometer. Different particles, including secondary hadron beams and tertiary muon or electron beams can be produced using a beryllium production target [26, 27] and are guided through the M2 beam line towards the spectrometer. Beryllium production targets of different thickness are used to regulate the beam intensity. Particles are delivered in so-called spills. A spill is a 4.8 s long continuous extraction of primary protons from the SPS towards the production target. This results in a continuous stream of the selected particle type using the beam line. Spills are grouped in so-called super-cycles with a duration of 28 s or larger. Per each super cycle, one or more spills can be delivered. For beam particle identification, two Cherenkov Detectors with Achromatic Ring focus (CEDAR) can be installed, if required, in the beam line upstream of the spectrometer.

For muon beams, the primary hadrons of the production target are guided though a 600 m long decay tunnel. After additional absorbers and beam scrapers, the resulting beam is guided along an additional 400 m long cleaning section towards the surface and the spectrometer. A schematic drawing of the beam line is shown in Fig. 1.11. Muon momenta between 60 and 160 GeV can be delivered at rates of up to $4 \cdot 10^7$ Hz [25].

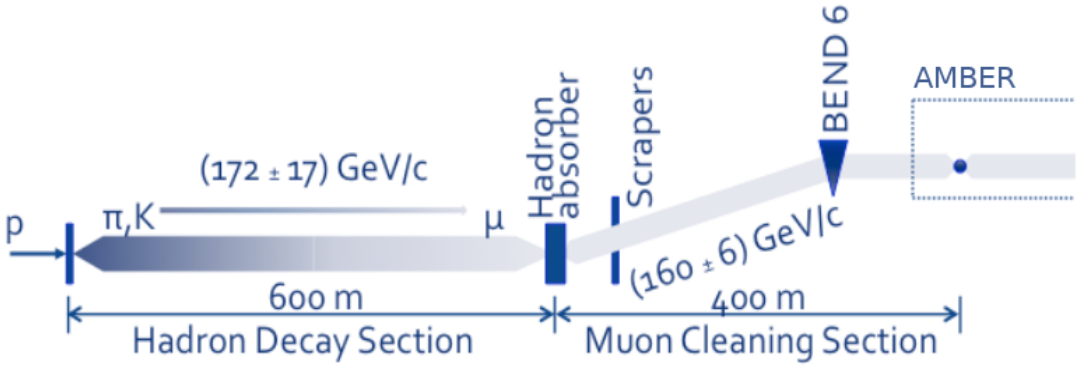

Figure 1.11: Muon setting of the M2 beam line for the nominal 160 GeV momentum including hadron decay section, absorbers and scrapers. Figure taken from [28], modified.

1.2.2 The Time-Projection Chamber for Recoil-Proton Measurement

For the direct measurement of the kinetic energy of the recoil proton to determine the four-momentum transfer Q^2 (cf. Eq. (1.24)) and the angle of the proton trajectory, an active-target hydrogen-pressure Time Projection Chamber is foreseen. A novel TPC is planned to be constructed and will be based on the experience of the existing Ionization Chamber for Hadronic Reactions (IKAR) TPC, which has already been operated in the 1970s at the WA9 and NA8 experiment at CERN in several elastic-scattering experiments [29–31]. The new TPC is developed and contributed by PNPI and being envisaged also for a sister experiment at MAMI for the Proton Radius in Electron Scattering (PRES) experiment, which has the goal of measuring the proton radius in elastic electron-proton scattering [19]. The common usage will provide calibration for the drift time and energy resolution using the precise electron beam.

A schematic drawing of the TPC is shown in Fig. 1.12. Four drift cells, each with a length of 400 mm, are placed inside the pressurized-hydrogen volume. The main data taking will be performed at 20 bar pressure to cover the large Q^2-range and resulting proton ranges in hydrogen of up to 285 mm (cf Fig. 1.14). For the operation of the TPC, a so-called gas circulation system is required. The hydrogen gas needs to be purified from water, oxygen and other contamination to not affect the drift time or energy resolution due to attachments on molecules. The beam will pass through beam windows on the up- and downstream side, each with a diameter of 70 mm. The windows are produced out of 0.5 mm thick beryllium to minimize the material budget for the traversing muons. Studies are ongoing to use a carbon-fiber-based solution to replace the beryllium-based windows due to safety reasons. A segmented anode structure is used as readout plane. A schematic of this pad plane is shown in Fig. A.1. An electric field is applied between

the anode structure and the cathode. A so-called Frisch grid [32] is installed 10 mm in front of the readout planes to avoid induction signals from drifting ions. Drift times of about 100 µs are expected. The TPC will be operated in the so-called ionization-mode, e.g., no gas-amplification to directly measure the kinetic energy of the recoil proton by collecting the resulting ionization along the proton's path. All anode pads will be read at once to provide the full event information. Besides the recoil energy, the corresponding proton track inclination can be measured by using the time difference between the signals arriving at the single readout pads. The angle determination depends on the proton track length and is affected by straggling along the path and is expected to be in the order of about 10 mrad. An azimuthal angular resolution of up to 170 mrad can be obtained depending on the track length, i.e., number of crossed pads [33]. In addition, the vertex z-position can be determined by combining the time information from tracking and the drift time. With the expected time resolution of 40 ns the vertex z-position can be determined with a precision of 0.4 mm. Details on the single components are summarized in Tab. A.1. [19]

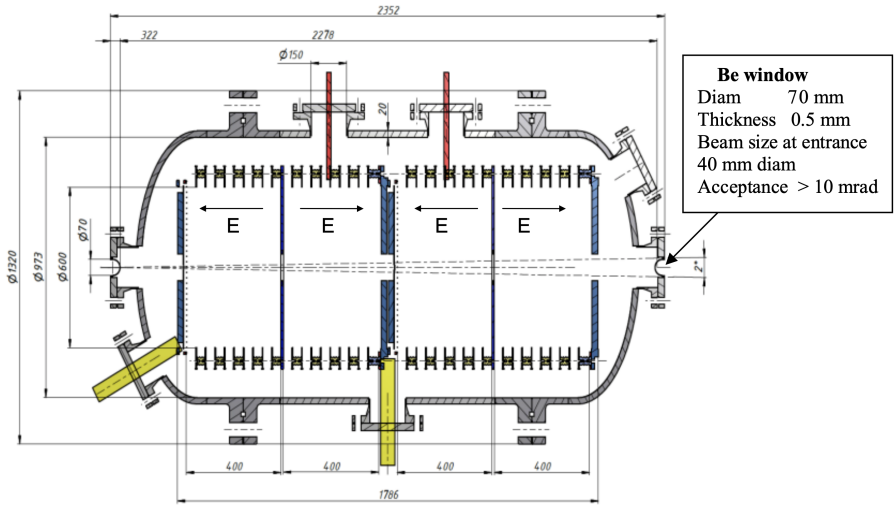

Figure 1.12: Technical drawing of the main TPC. Dimensions and drift fields are indicated as well as the properties of the beam windows. Figure taken from [2], modified.

Studies have been performed to optimize the geometry of the segmented anode structure [33]. The presented one is the most favorable one at this point in terms of energy, angular and spatial resolution. Simulated signals and a noise evaluation using ANalysis SYStem (ANSIS) [34] and GARFIELD++ [35] is used to model a so-called pad-response function and to mimic the response in the simulation similar to the real data taking. The anode structure will be segmented as shown in Fig. 1.13(a) together with the expected beam profile and has an optimized energy and spatial resolution of the recoil proton track as well as electronic noise [36]. The inner pad has a diameter of 10 mm and the following rings add 40 mm each, with a 0.1 mm gap between the single pads. The outer ring will have a radius of 24 mm and serves as an indicator ring for protons leaving the active TPC volume. In total, the anode plane will have a radial size of 309 mm, including the 24 mm outer indicator ring.

Beam muons traversing through the hydrogen gas produce ionization along their path. This so-called beam-induced noise has been studied in test beam data and adds up to about 70 keV at the proposed beam rate of $2 \cdot 10^6$ Hz in the central region at 20 bar pressure and includes also 20 keV pure electronic noise due to capacitance [37]. This beam-induced noise is the limiting factor of the beam rate for the measurement in order to obtain the necessary energy resolution in the TPC [2]. The largest beam-induced noise is expected in the center and the first ring, with an increase along the y-direction due to the beam profile. An average beam flux of about 20 kHz/mm^2 is expected in the central pad and a comparable rate in the pads of the first ring, as shown in Fig. 1.13(c), with an increase for the pads along the y-direction. The noise results in a relative Q^2-resolution of about 13 % for the lowest proposed $Q^2 = 0.001$ GeV$^2/c^2$($T_\mathrm{p} = 530$ keV) on one pad, which results in an 6 % uncertainty in the measured differential cross-section [2]. Since the kinetic recoil energy is determined by the sum of deposited energy on each crossed pad, the corresponding pad noise is summed up quadratically [38]. The inner pad and the first ring are affected by the beam noise. This results into a total resolution of

$$\Delta T_{\mathrm{p,max}} = \sqrt{n_{\mathrm{pads}} \cdot \sigma^2_{\mathrm{pad}}} = \sqrt{2 \cdot 70^2 \text{ keV} + 7 \cdot 20^2 \text{ keV}} = 110 \text{ keV}. \tag{1.25}$$

With a kinetic energy of $T_\mathrm{p} = 10.66$ MeV for a recoil proton at the maximum $Q^2 = 0.02$ GeV$^2/c^2$, which is fully stopped inside the active volume, the relative energy resolution is expected to be $\Delta T_{\mathrm{p,max}}/T_\mathrm{p} = 10$ %. To adapt for the resolution at lower Q^2 values at the nominal 20 bar pressure, a dedicated measurement at a lower pressure of 4 bar is foreseen. At this lower pressure, the beam-induced noise is reduced by a factor of five and the obtained data will be used to correct the low Q^2 values recorded in the nominal pressure setting [38].

In Fig. 1.14(a), ranges are shown for different pressure settings for hydrogen gas. The values are data from the National Institute for Standards and Technology (NIST). The projected range reassembles the average trajectory length, which the proton will pass until it stops and takes into account multiple scattering along its path [39]. They serve as validation of the simulation and as estimate for the proton ranges in pressurized hydrogen. To measure the full deposited kinetic energy of the recoil proton, it needs to be stopped inside the active volume of the TPC and the resulting ionization charge along its path needs to be fully collected by the anode plane. In Fig. 1.14(b), simulated proton ranges for the IKAR TPC and the new TPC are shown. The IKAR TPC provides an active radial size of 229 mm for the anode plane. As indicator for protons leaving the active volume the most outer ring information is used and therefore the effective radius of the anode plane is smaller. By this, it can measure the full kinetic energy of protons up to $Q^2 = 0.008$ GeV$^2/c^2$ at its nominal 8 bar pressure. The new TPC will be equipped with a larger anode plane of 309 mm radial size. Same holds here for the most outer ring, reducing the effective size to 285 mm to ensure stopped protons. With its maximal pressure of up to 20 bar, protons carrying a $Q^2 = 0.02$ GeV$^2/c^2$ can be fully stopped inside the active volume. This restriction of the Q^2 range can be further extended by using energy-loss measurements along the proton path. This method can be used to determine the initial kinetic energy of the proton. Studies are ongoing to evaluate the resulting precision, but first results show that a resolution of about 4 % at $Q^2 = 0.08$ GeV$^2/c^2$can be achieved [2].

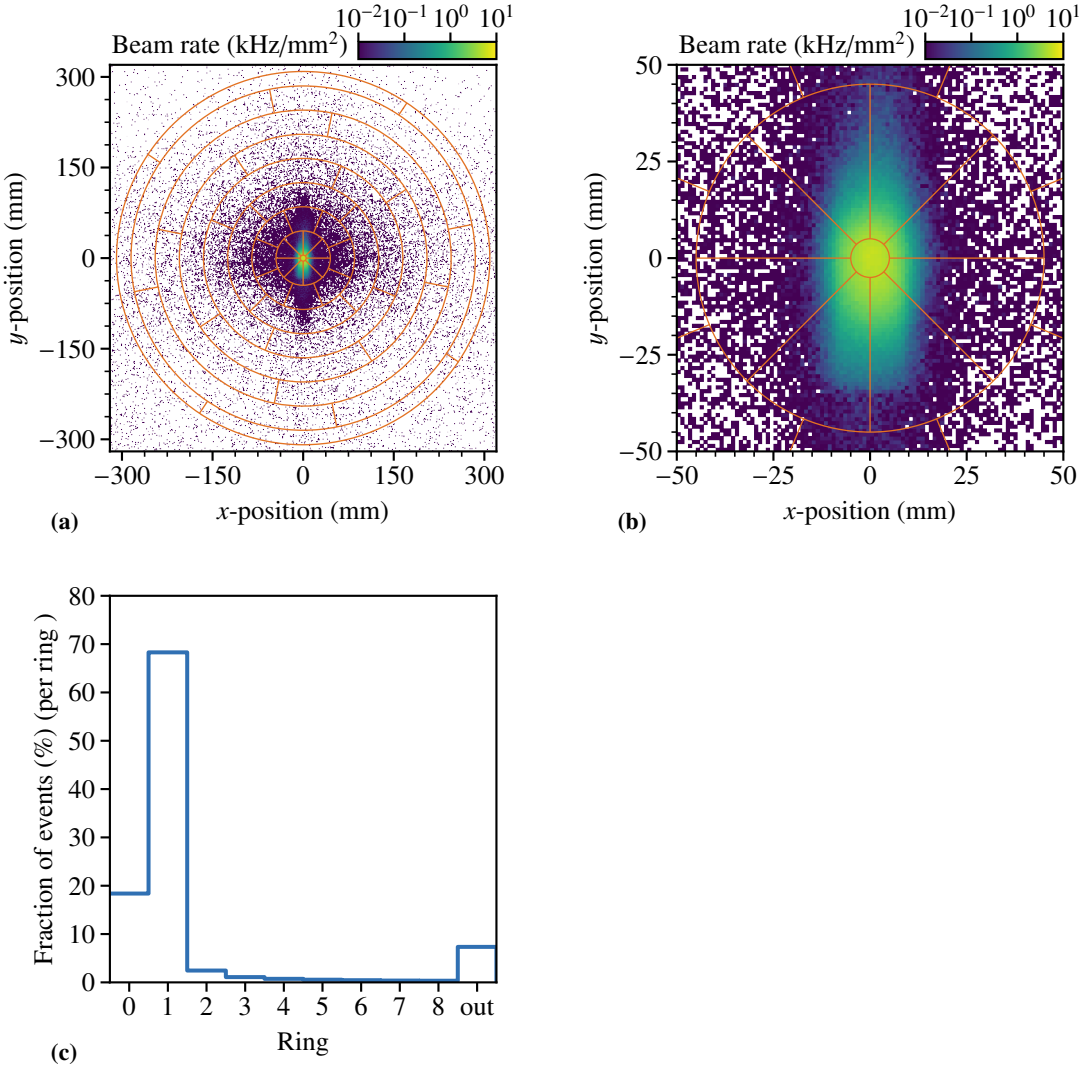

Figure 1.13: Estimated beam flux and resulting fraction on the segmented anode plane. In (a) the anode structure and the expected beam flux is shown, with a close-up of the central region shown in (b). The distribution of events for the central pad and the single rings is shown in (c).

In Fig. 1.15(a), the energy deposit E_{TPC} in the TPC depending on Q^2 is shown. After reaching its maximum range inside the active volume, only a fraction of the proton energy is deposited inside the TPC. With increasing Q^2 the deposited energy reduces. Depending on Q^2, the proton track is further inclined and with increasing Q^2 deviating from the perpendicular orientation of up to $\theta_{\mathrm{p}} = 1.49$ rad at $Q^2 = 0.02$ GeV$^2/c^2$. Especially, close to the cathode or anode structures, this effect needs to be taken into account to exclude material effects. The respective angles for protons and muons are shown in Fig. A.2 based on the kinematic calculations. As shown in Fig. 1.15(b), up to 3 cm displacement of the proton track along the z-axis is present for $Q^2 = 0.02$ GeV$^2/c^2$.

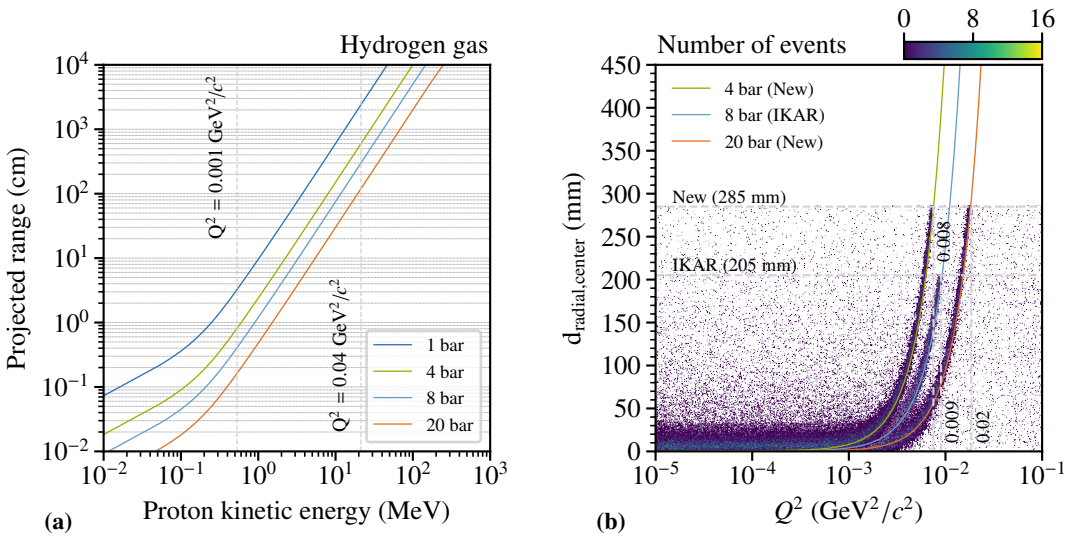

Figure 1.14: Proton projected ranges in hydrogen at different pressures are shown in (a). Values are taken from [39]. The proposed Q^2-range is indicated. A comparison of the IKAR TPC and the planned TPC in terms of proton ranges is shown in (b).

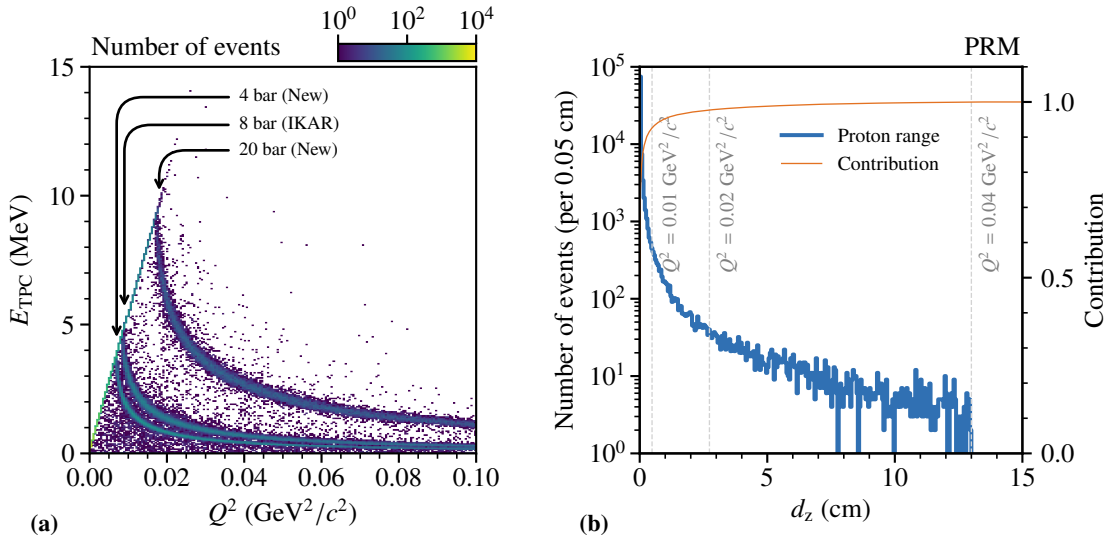

Figure 1.15: The simulated energy loss inside the different TPCs is shown in (a). The resulting z-component of the traveled proton distance is shown in (b) with different Q^2 indicated and the resulting contribution to the data set based on the cross-section.

1.2.3 Unified Tracking Station

The muon trajectory will be measured by the so-called target-tracking system. The system consists of four Unified Tracking Station (UTS). Two stations each are placed in a 3 m distance with respect to each other along the lever arms up- and downstream of the TPC. To obtain the spatial resolution required to measure small scattering angles of $O(100\ \mu\text{rad})$, the Silicon-Pixel detector (SPD) together with the Scintillating-Fiber Hodoscope (SFH) are operated. Both will be placed together in the UTS. A schematic drawing of one UTS is shown in Fig. 1.16. The SPD is based on the ALICE Pixel Detector (ALPIDE) Monolithic Active Pixel Sensor (MAPS) developed for the upgrade of the Inner Tracking System (ITS) of A Large Ion Collider Experiment (ALICE) [40]. The SPD will cover an active area of $90 \times 90\,\text{mm}^2$, with the SFH slightly larger providing an active area of $96 \times 96\,\text{mm}^2$ to ensure a full coverage of the SPD. Three layers of the SPD and four layers of the SFH will be installed.

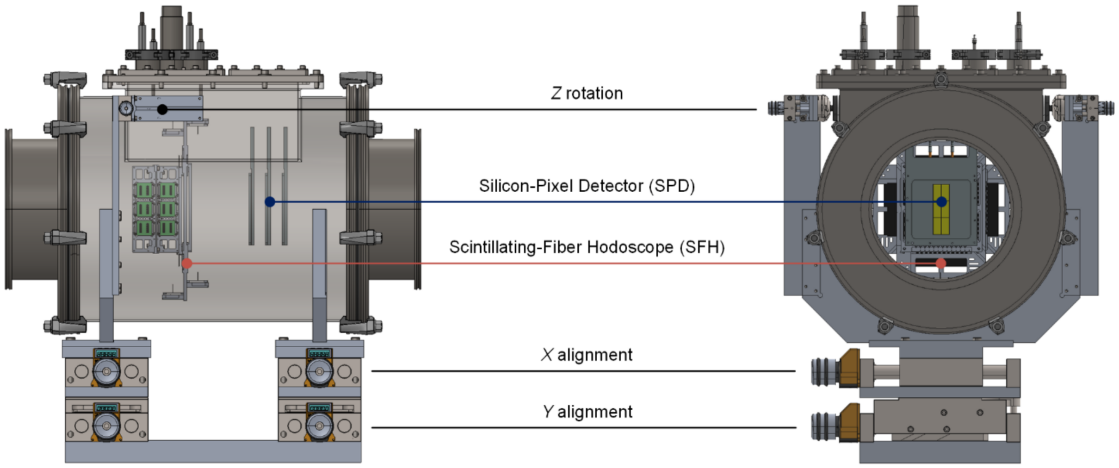

Figure 1.16: Technical drawing of the UTS. The SPD and SFH detector planes are indicated as well as the positioning system for the alignment. Figure taken from [41].

Development and tests of the UTS are ongoing. During the pilot run in 2021, first beam tests with single ALPIDE chips have been performed. In addition, lab tests of the SFH are being performed to evaluate the performance of the fiber readout system based on Silicon Photomultipliers (SiPMs) as well as the resulting signal and light output. A first prototype with 8 fibers have been tested in a parasitic manner at a test beam location downstream of the COMPASS spectrometer[1] in 2022 and the obtained results with a 160 GeV muon beam are currently being analyzed [42]. A beam test of a partially equipped UTS in the target location of the current COMPASS spectrometer is scheduled for end of 2022. The station will be placed in the focused muon beam close to its final location to evaluate the resolution and efficiency at the anticipated rate and the new FriDAQ-based readout (cf. Sec. 1.2.4) under realistic conditions. In the following more details on the SPD and SFH are given.

[1] Same location as the feasibility test in 2018 (cf. Chap. 2).

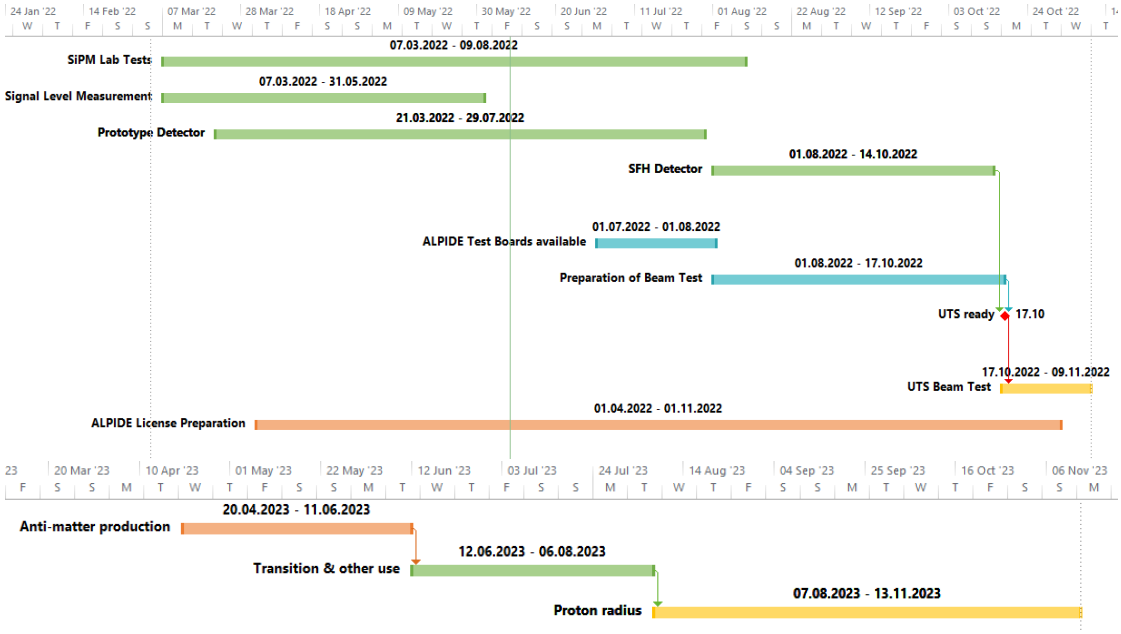

Figure 1.17: Timelines for the UTS projects (SFH and SPD) including foreseen beam tests in 2022 (top). Anticipated time lines for a possible PRM beam time in 2023 (bottom). Figure taken from [41].

Silicon-Pixel Detector

The ALPIDE is a $15 \times 30\,\mathrm{mm}^2$ large sensors with $512 \times 1\,024$ pixels, each with a size of $28 \times 28\,\mu\mathrm{m}^2$, providing a spatial resolution of about 8 µm. The pixels provide hit/no-hit information only. The expected cluster size is large enough to further improved the precision using the single pixel position to obtain sub-pixel resolution [40]. The sensor has a thickness of 50 µm and an integration time of about 5 µs. To distinguish single hits at the 2 MHz beam rate and to provide single-hit time information, the SFH information is required to disentangle the expected 10 pile-up hits per time window. The in-pixel readout supports the foreseen free-running DAQ system presented in Sec. 1.2.4. A total of three planes per UTS station are planned with a spacing of 50 mm between them along the beam direction. A sketch of a single plane is shown in Fig. 1.18(a). Each plane will consist out of a matrix of 6×3 sensors, resulting in an active area of $90 \times 90\,\mathrm{mm}^2$. They are mounted on a carbon fiber plate, which provides mechanical support and heat dissipation. The carbon plate is attached to a holding frame, which includes cooling pipes. The central sensors will be mounted on the backside of the support plate to minimize dead zones by overlapping the inactive parts. A so-called FlexPCB is glued onto the sensors for electrical connections consisting of a stack of aluminum coated conductor layers.

The design of the FlexPCB is optimized in this work towards a low material budget and studies have been performed to obtain the current choice of the so-called FDI-A-24-Flex [43] design. The single layers are listed in Tab. 1.2 with a schematic drawing shown in Fig. 1.19(b). The main contributions to the material budget are the carbon cooling plate (38 %) and the silicon material of the sensor (23 %). Other investigated designs are based on copper instead of aluminum as

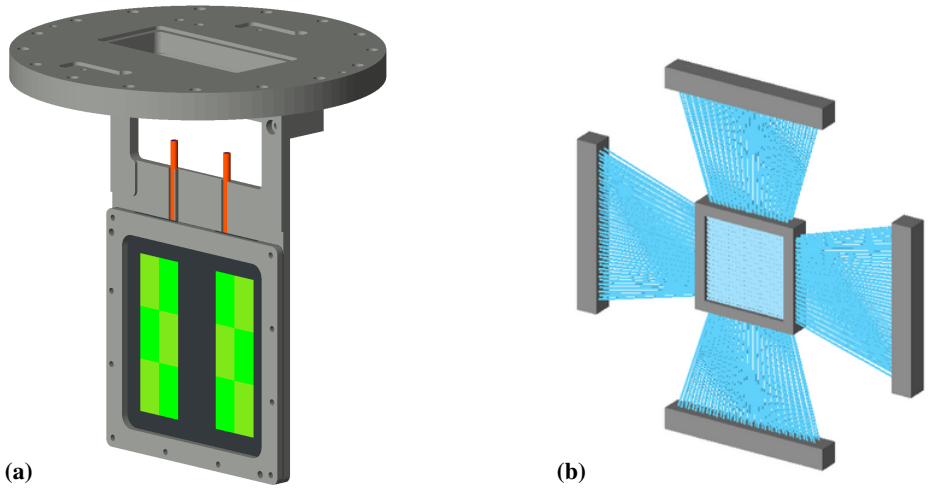

Figure 1.18: GEANT4 implementation of the a SPD (a) and SFH (b). The carbon plate (black) as mounting for the ALPIDE chips (green) is visible as well as the cooling copper pipe (orange). Each fiber (blue) of the SFH is mounted on a holding frame (grey) is connected to a single SiPM on the outside.

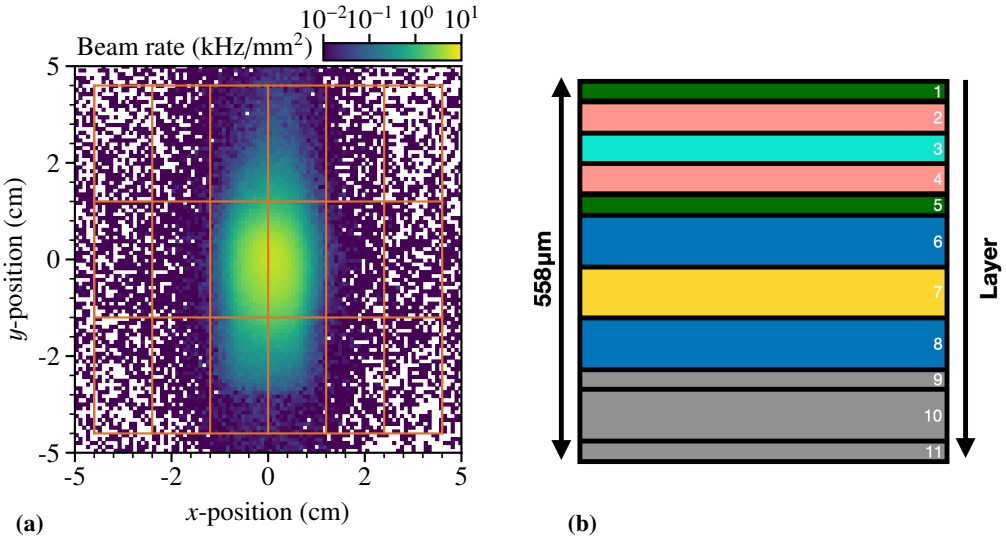

Figure 1.19: Estimated beam flux on an ALPIDE plane is shown in (a). The detector areas are indicated (cf. Fig. 1.18(a)). In (b) the FlexPCB of the ALPIDE sensor is shown with its different layers indicated [43]. Material details listed in Tab. 1.2.

conductor layers, resulting in an increased material budget. A thinner carbon cooling plate with half the thickness was evaluated, but according to simulations, the resulting heat-dissipation is not sufficient [43]. With this design, a total material budget of $X/X_0 = 0.231$ % for a total thickness of 558 µm is obtained per plane. As comparison, those results are lower than the requirements foreseen for the original usage in the ALICE ITS. They require on average a value of 0.3 % [44], whereas the current design also has a more homogeneous material distribution by moving cooling elements outside the acceptance.

Table 1.2: Material budget for the FDI-A-24 Flex-based stack with aluminum conductors. [43]

layer	item	A	Z (u)	d (cm)	density $\left(\mathrm{g/cm^3}\right)$	X_0 $\left(\mathrm{g/cm^2}\right)$	X/X_0 (%)	contrib. (%)
1	solder mask (epoxy)			0.0030	1.250	34.99	0.011	4.64
2	aluminum layer (Al)	26.982	13	0.0014	2.699	24.01	0.016	6.82
3	Kapton			0.0010	1.420	40.58	0.003	1.516
4	aluminum layer (Al)	26.982	13	0.0014	2.699	24.01	0.016	6.82
5	solder mask (epoxy)			0.0030	1.250	34.99	0.011	4.64
6	glue flex (C)	12.011	6	0.0050	0.958	43.01	0.011	4.82
7	ALPIDE (Si)	28.085	14	0.0050	2.329	21.82	0.053	23.12
8	glue to plate (C)	12.011	6	0.0080	0.958	43.01	0.018	7.72
9	carbon fleece (C)	12.011	6	0.0020	0.400	43.01	0.002	0.81
10	cold plate (C)	12.011	6	0.0240	1.583	43.01	0.088	38.28
11	carbon fleece (C)	12.011	6	0.0020	0.400	43.01	0.002	0.81
	Total:			0.0558			0.231	100.00

Scintillating-Fiber Hodoscope

The Scintillating-Fiber Hodoscope (SFH) is based on 500 µm thick squared fibers. Each fiber is coupled to a single SiPM on both sides for readout. The intrinsic thermally induced noise of the SiPMs, the so-called dark-count rate, is reduced by the usage of a coincidence signal between both sides. This reduces and stabilizes the dark-count rate from initially 100 kHz per fiber down to 100 Hz [2]. A dedicated cooling system is foreseen to keep the SiPM at a constant low temperature to further reduce the dark-count rate. The SFH will provide timing information with a resolution of about 300 ps required mainly for the SPD to distinguish pile-up hits. A full SFH will consist of four layers with 192 fibers each in two layers oriented in x- and y-direction with an overlapping central area of $96 \times 96\,\mathrm{mm}^2$. A schematic drawing is shown in Fig. 1.18(b). With a shift between layers by 250 µm along their projection, an effective spatial resolution of 250 µm is achieved. The fibers are placed in bunches of eight in two layers two minimize the position uncertainty due to manufacturing [45]. The fibers have a total length of about 40 cm and are completely active between the SiPMs. [2]

A possible influence of the beam component passing outside the central area could add additional unwanted hit rate in the fibers. To estimate this influence outside the central tracking area the hit position in the simulation is used. The ratio between the hits in the central area and hits recorded in the outer areas is given by

$$R_{\mathrm{hit,halo}} = \frac{n_{\mathrm{hit,\,in}}}{n_{\mathrm{hit,\,out}}}. \tag{1.26}$$

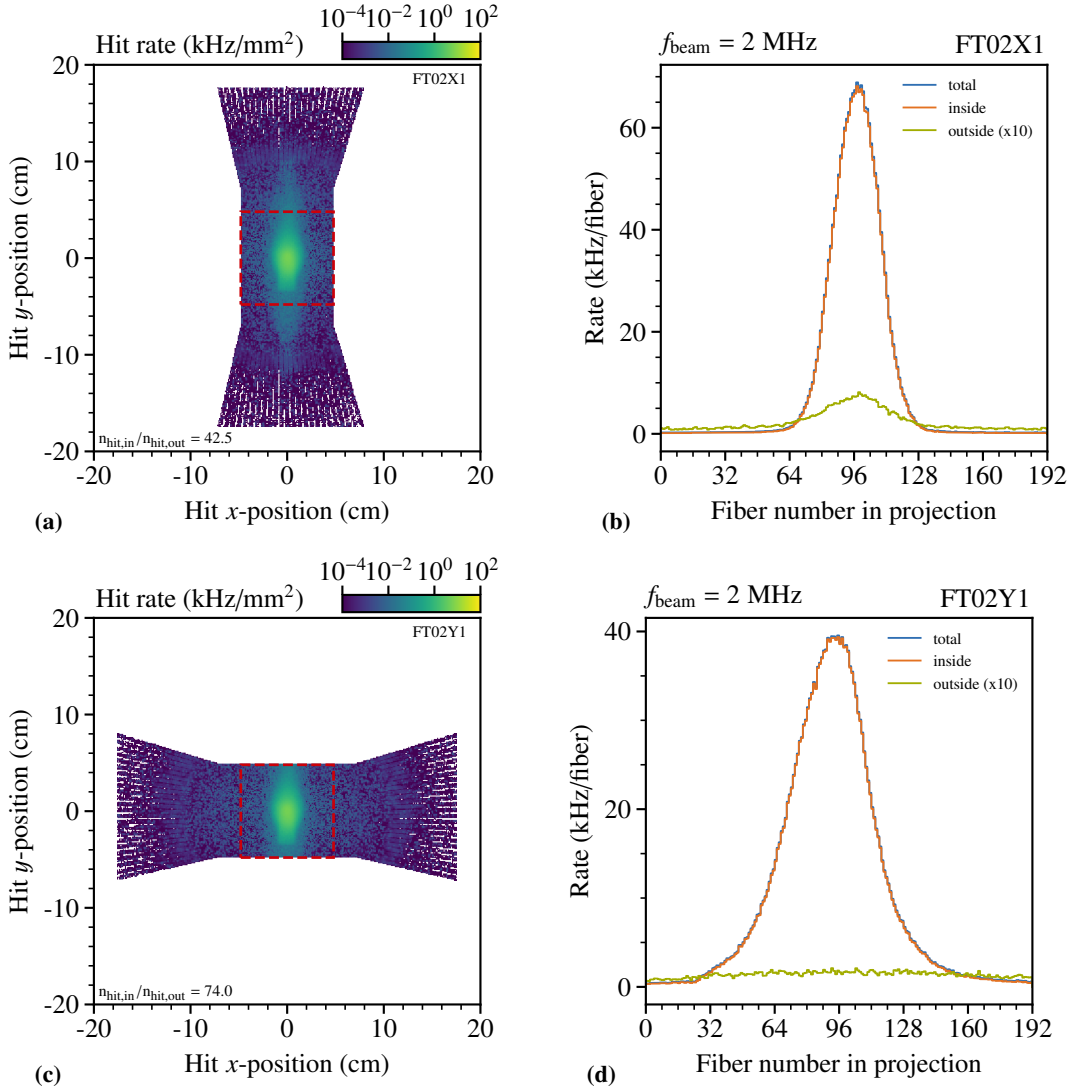

Figure 1.20: Fiber hit positions and rate for the x- and y-projection of the FT02 station. In (a) and (b) the respective position with the central $96 \times 96\,\mathrm{mm}^2$ area marked in red. The overall ratio between inner and outer hits is given in the figure. In (c) and (d) the corresponding rates per fiber are shown. The different contributions between the inner and outer part. The other projections can be found in App. A.8.

The results are shown in Fig. 1.20 for FT02 as being closest to the target and the beam focus point. Overall the ratio $R_{\mathrm{hit,halo}}$ between central and outer hits depend on the projection. Whereas the x-planes show a ratio of about $R_{\mathrm{hit,halo}} = 42$, the y-planes have an about two times higher ratio of $R_{\mathrm{hit,halo}} = 74$ due to the larger beam extend along the y-direction. The expected rate is around 70 kHz per fiber, which is in the same order as the dark-count rate of a single SiPM without additional suppression. The estimated background rate by hits outside the inner tracking area is below 1 kHz per channel. Due to the beam profile, the rates are slightly lower in the y-projection.

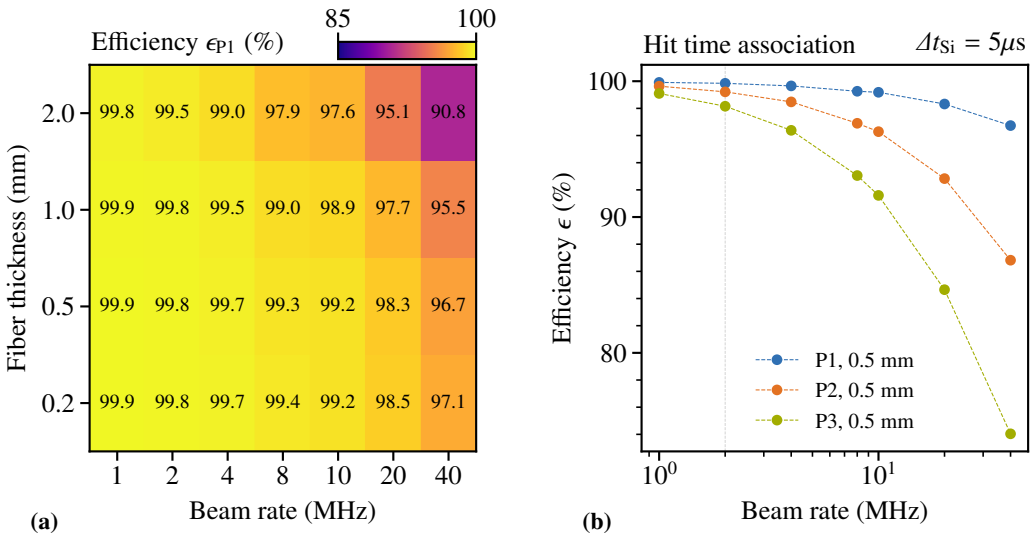

Figure 1.21: SFH tracklet to hit association with the SPD for different rates and fiber thicknesses are shown in (a). A spacing of 20 cm between the three consecutive SPD planes (P1 to P3) is used. Association efficiency with single hits on the three SPD planes is shown in (b).

At the anticipated 2 MHz beam rate, about 10 pile-up hits are expected within the integration time of the SPD. Using the hit- and time information of the SFH allows to disentangle those. Tracklets in the SFH upstream of each SPD are extrapolated on the respective SPD planes to evaluate, if by this simple approach using the closest hit would result into a sufficient result. The results are shown in Fig. 1.21 for beam rates up to 40 MHz and different fiber thicknesses to study the influence of the SFH resolution. In this study, the SPD planes have been placed with a spacing of 20 cm towards the SFH and with respect to each other, whereas the current design uses the 20 cm as a maximal distance between the SFH and the last SPD plane. At 2 MHz, a hit-time association efficiency of 99.8 % can be achieved for the foreseen 500 µm thick fibers on the first ALPIDE plane. With increasing distance to the SFH, the hit association drops to about 98 %. In the future, a more sophisticated method of hit association between the SFH and SPD is foreseen to be included in the hit and track reconstruction, but the preliminary results show already a sufficient efficiency.

The initial idea for the SFH was to use 250 µm thick fibers. Due to the smaller light output and the more challenging mechanical handling, the 500 µm thick fibers are chosen in the end. They show a sufficient spatial resolution for the hit-time measurement. A study has been performed, whether the scattering angle of the muon could be determined by using only the SFH for the reconstruction. The results are shown in Fig. 1.24. At a low $Q^2 = 0.001$ GeV$^2/c^2$ the vertex z-resolution increases by a factor four and scattering angle, and Q^2 resolution by more than 60 % compared to a combined usage of SPD and SFH, although the material budget is reduced by excluding the SPD. Therefore, the combined operation of the SFH and SPD is required. Using only the SFH does not provide a sufficient spatial resolution, as shown in Fig. 1.24.

1.2.4 Free-Running Data Acquisition

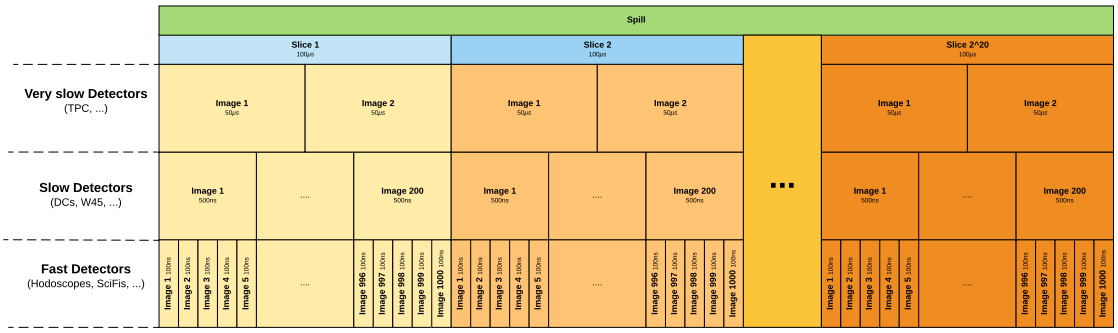

Figure 1.22: Time slicing for the new free-running DAQ. Figure taken from [46].

Starting with the PRM campaign at AMBER, the current existing trigger-based DAQ system will be changed towards a novel, so-called free-running DAQ. This FriDAQ will continuously stream the detector data. The data stream will use a coarse reconstruction and will be analyzed online by a software-based trigger. This so-called High-Level Trigger (HLT) tags events, if they fulfill a defined trigger condition. This continuous data stream is required to allow the combination of information from detectors with different integration times. Using a hardware-based trigger would require to store data in the front-end electronics for the time until the trigger decision arrives, which is not feasible at this time.

In the PRM case, the planned TPC has an integration time (drift time) of about 100 µs. On the other hand, detectors like the SFH have an integration time of 300 ps. These integration times of the different detectors are used as so-called time images. The time length of the time images is individual for each detector. They are tagged with timestamps and merged together in the way that multiple time images are combined in so-called time slices as shown in Fig. 1.22 [46]. This time-slice building will be performed online by Field Programmable Gate Array (FPGA) cards. The merged data is then evaluated by the HLT. For the PRM setup, this HLT trigger condition will include proton-like signals in the TPC and/or a deflected muon track.

Dedicated DAQ test and first simulation-based HLT studies have been performed in 2021 and confirmed the required performance of DAQ and its bandwidth. This new data and event format compared to the previous hardware-trigger-based event structure requires adaption of the current data handling. Adaptions are ongoing in the scope of developing a new so-called DAQ decoding library to handle the new streaming data format. Further development of the HLT framework is ongoing as well as the resulting event building process. The event reconstruction needs to be adapted in order to handle this new data format to take into account the overlap of real events across the different time images.

1.2.5 Helium Beam Pipes

To measure scattering angles with high precision, the overall material budget of the setup needs to be reduced to minimize the effect of multiple scattering. Therefore, dedicated helium-filled beam pipes are foreseen to be placed along the lever arms to reduce the multiple scattering in air. The distance between the two UTS defined as baseline along each up- and downstream lever arm influences the maximal measurable scattering angles and the resolution. This geometrical acceptance and the vertex z-resolution for the scattered muon have been studied with a beam momentum of 100 GeV to evaluate this effect and to optimize the required distance. It is found that a 3 m long baseline results in an optimal choice in terms of resolution and acceptance and is suitable for the available space.

The x-y-size of the single detector modules in the UTS predicts the acceptance for the scattered muon. Hits within the SPD of each UTS are required to reconstruct the scattering angle. In Fig. 1.23(a) the result for the acceptance with different baseline lengths is shown. Due to the steep fall of the cross-section with increasing Q^2 as shown in Fig. 1.33, the data has been simulated with a flat Q^2-distribution to obtain sufficient statistics across a large Q^2-range. With increasing baseline, the acceptance of events with large Q^2 and therefore large muon scattering angle drops. Whereas a shorter baseline of 0.5 m can cover scattering events with Q^2 up to 10 GeV^2/c^2. A baseline of 5 m is limited to about $Q^2 \approx 1\ \mathrm{GeV}^2/c^2$. The anticipated Q^2-range $10^{-3} \leq Q^2/(\mathrm{GeV}^2/c^2) \leq 4 \cdot 10^{-2}$ is well covered by all studied configurations. The influence of multiple scattering is visible for events with $Q^2 < 10^{-3}\ \mathrm{GeV}^2/c^2$. Those events are systematically shifted to larger Q^2 values of about $10^{-3}\ \mathrm{GeV}^2/c^2$. More details on the effect of multiple scattering are discussed in Sec. 1.2.7.

The baseline length dictates the vertex z and angular resolution. With increasing length d, improved resolutions are expected. According to [47], the pure geometrical angular resolution $\Delta\theta_{\mathrm{geom}}$ can be expressed in the small-angle approximation by the detector hit position x and its uncertainty Δx for the baseline length d as

$$\theta_{\mathrm{geom}} = \frac{x}{d} \qquad \text{and} \qquad \Delta\theta_{\mathrm{geom}} = \frac{\Delta x}{d}. \tag{1.27}$$

The respective resolutions are obtained by using a Gaussian distribution within single slices in Q^2. The results for the angular resolution with different baseline lengths are shown in Fig. 1.23(b). The resolution is independent of the Q^2 in the given range. This results in a linear behavior of the resolution due to the main contribution given by multiple scattering as constant offset by the material budget. With the anticipated 3 m long baseline, a resolution of about $\Delta\theta = 25$ µrad is expected, which is dominated by the multiple scattering (cf. Sec. 1.2.7). The results for the related relative Q^2-resolutions are shown in Fig. 1.23(d). Baseline lengths larger than 3 m result only in minor improvements. At $Q^2 = 10^{-3}\ \mathrm{GeV}^2/c^2$ a relative resolution of about 15 % can be achieved. Further details are discussed in [47].

The vertex z-resolution is related to the scattering angle. It improves with longer baseline, as shown in Fig. 1.23(c). Baselines with a length larger than 3 m do not show a further improvement. A resolution of around $\Delta z = 9$ cm at $Q^2 = 0.001$ GeV$^2/c^2$can be achieved. In the final measurement the tracking information will be combined with the TPC measurement. Using the time difference between the measured muon and the proton track together with the drift time of the TPC, resolutions of $\Delta z = 0.4$ mm can be reached (cf. Sec. 1.2.2).

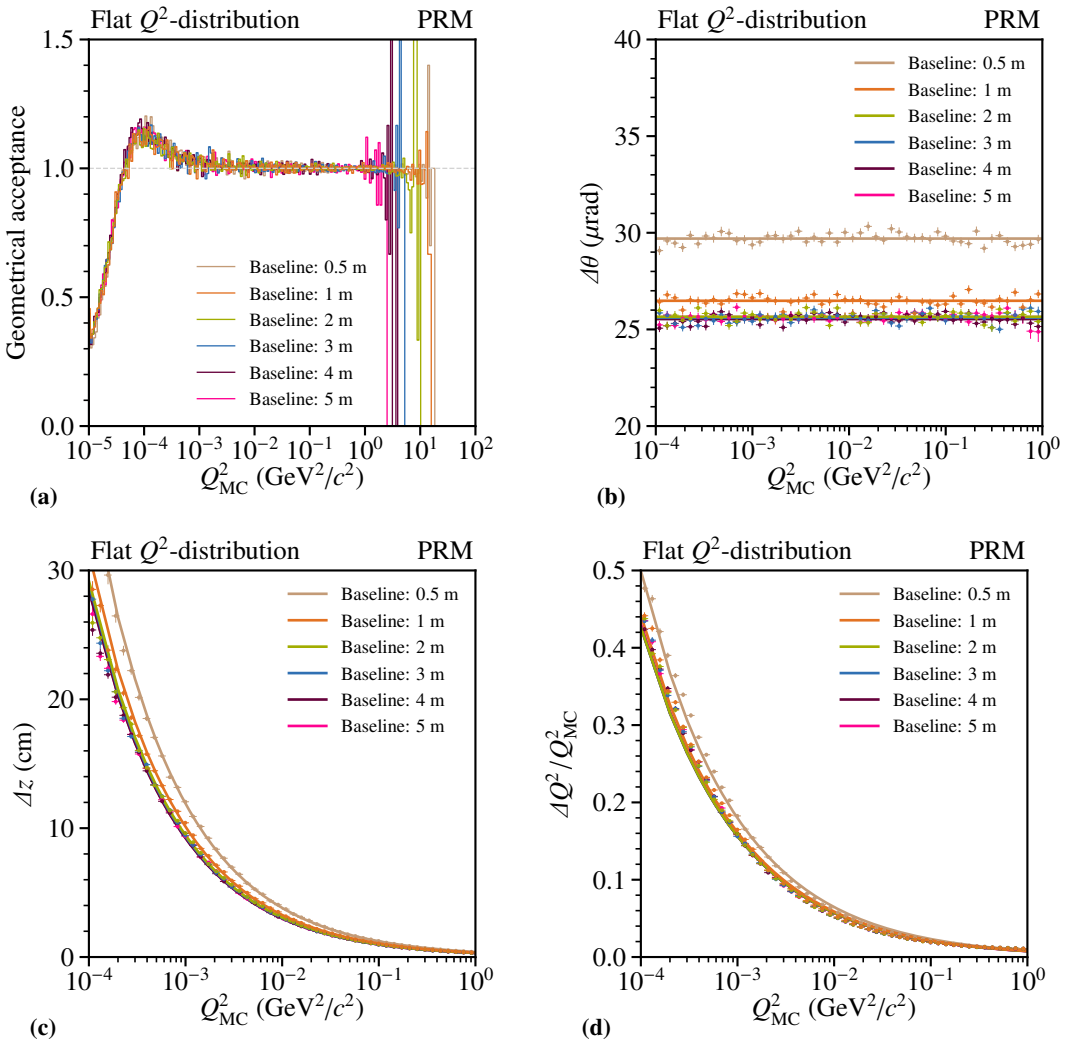

Figure 1.23: Baseline length studies for a beam momentum of 100 GeV. The geometrical acceptance is shown in (a). In (b) the angular resolution is shown. The vertex z-resolution is shown in (c) and the relative Q^2 resolution is shown in (d). A flat Q^2-distribution is used to cover the kinematic range. Details on the used parametrization are given in App. A.4.

The effect of multiple scattering along the air-filled lever arms becomes visible, especially for the angular resolution. A comparison between the usage of an air- or helium-filled 3 m long beam pipe is shown in Fig. 1.24. An improvement of the angular resolution shown in Fig. 1.24(b) of about 8 % is achieved. The effect on the vertex z-resolution is similar, as shown in Fig. 1.24(c). Furthermore, a comparison by using only the SFH (cf. Sec. 1.2.3) is shown. Here the overall resolutions drastically worsen due to the lower resolution compared to the SPD and the reduction of the material budget does not compensate this effect.

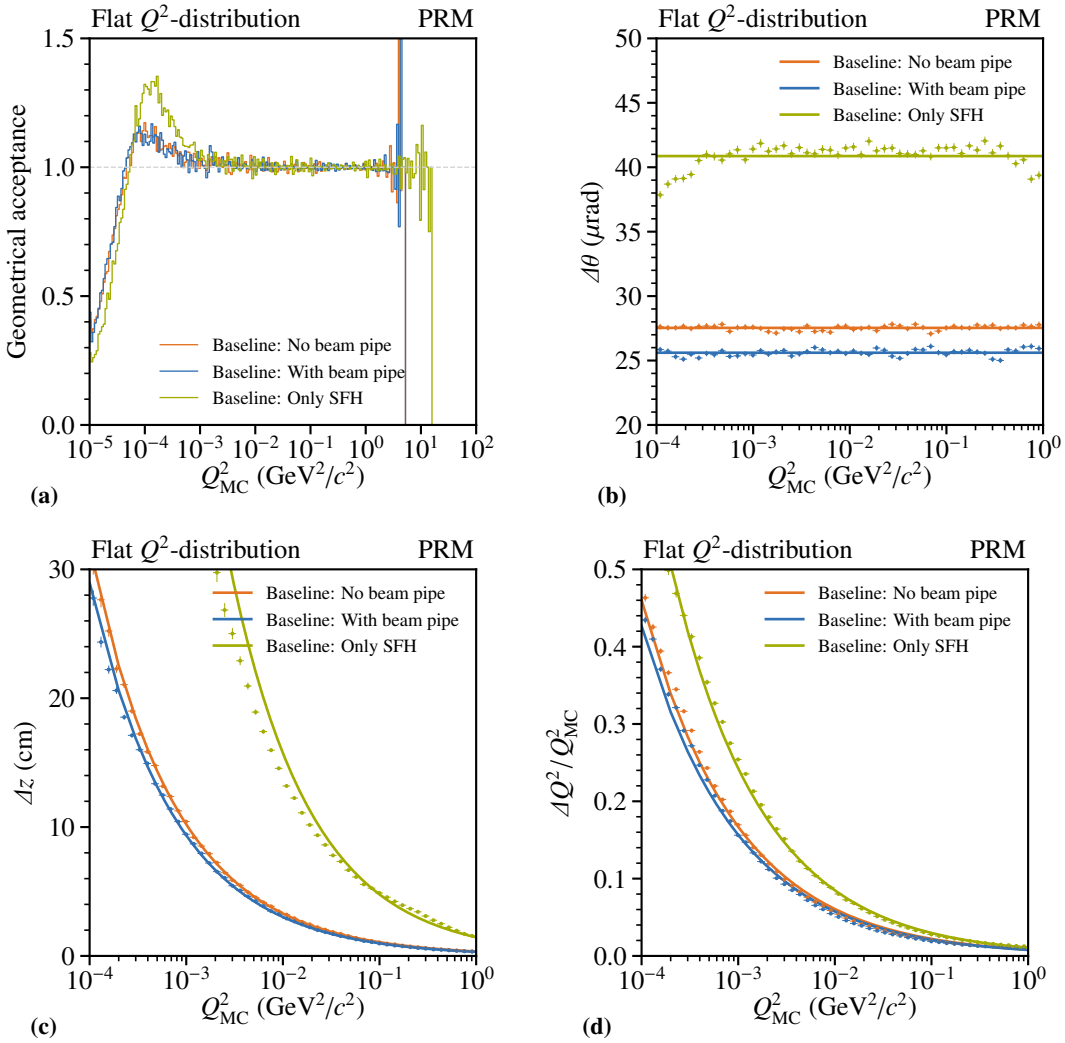

Figure 1.24: Comparison between the air- and helium filled beam pipes for the geometrical acceptance (a), angular resolution (b), vertex z-resolution (c) and resulting Q^2-resolution (d). A study is included showing the result of using only the SFH detectors.

Due to the non-negligible size of the beam profile in x- and y-direction, the diameter of the beam pipe may affect the surrounding detectors by adding additional material too close to the beam axis. This can result in muon trajectories creating secondary tracks along the material hitting the detectors and creating additional background. Results of two possible options with outer diameters of 150 mm (DN150) and 250 mm (DN250) are presented in Fig. 1.25. The vertex position of secondary tracks stemming from the beam muon, mainly electrons created along the beam pipes, is shown in Figs. 1.25(a) and 1.25(c) for the different diameter options. Especially the larger extent of the beam along the y-direction increases the number of secondaries in the beam pipe along this projection. As illustration, the effect of the secondaries on the active target TPC is shown in Figs. 1.25(b) and 1.25(d). Single simulated secondary tracks originating from the beam pipe are clearly visible, and their position depends on the respective radius. Although the overall contributions by those secondary tracks reaching the inside of the TPC is around 0.03 %, the resulting energy deposition is around 1 MeV as shown in Fig. 1.26(a) and in the energy region of the recoil proton. It is expected that the event signature can be distinguished in terms of signal shape, since it is induced by mostly electrons, but further studies are required to evaluate the effect especially for hadronic events. For the SPD and SFH, additional secondary tracks contribute as background on the 10^{-4} to 10^{-5} level, respectively.

An overview of the contribution of secondary tracks originating from the different diameter options is shown in Fig. 1.26(a). Whereas a total of about 15 % are expected to be created within the inner 50 mm radius along the beam pipe, the contribution from the structure itself is smaller. An overall contribution of about 0.22 % is expected of tracks created along the beam pipes with the DN250 property.

In conclusion, a DN250 helium-filled beam pipe is foreseen with 3 m long baseline between the detectors. This will provide a sufficient resolution for the measurement. Contributions by secondary tracks inside the active-target and the tracking detectors are considered to be small, but have to be studied further. The beam pipes will be directly connected to the UTS and the TPC. No additional beam windows are required between the UTS and the beam pipes, except on the up- and downstream side of the core setup to ensure a close helium volume and the beam windows of the TPC.

1.2.6 Beam Properties

Using an active target comes with requirements on the beam properties due to the direct response to the beam itself. For a clean selection of elastic scattering events inside the TPC volume, it is favorable to have a well-focused beam in the center of the TPC along the about 10 m long core setup. In addition, the beam particles should enter and leave the TPC through its up- and downstream beryllium windows to avoid additional material effects. This requires a sufficiently focused and parallel beam. Dedicated beam studies have been performed to match these requirements. Currently, the main data taking is foreseen to use a muon beam with a momentum of 100 GeV and an intensity of 2 MHz limited by the TPC due to the induced beam ionization noise (c.f. Sec. 1.2.2). This well-focused beam is required in order to have it well centered inside the TPC pad plane.

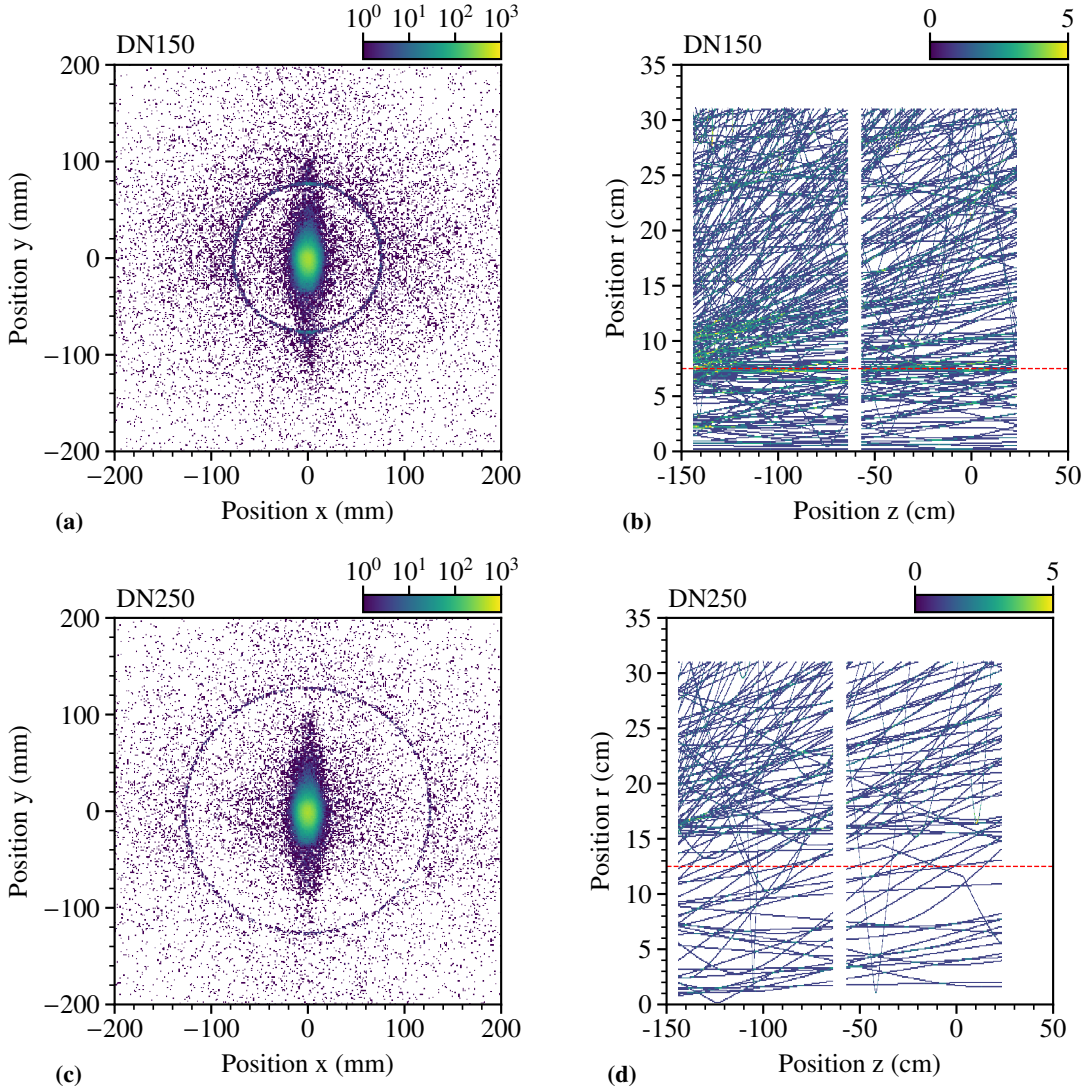

Figure 1.25: Simulated secondary track positions originating from the incoming muon beam for the beam pipe diameters DN150 and DN250 are shown. The integrated vertex distribution along the beam direction for the different diameters is shown in (a) and (c). An example of resulting trajectories in the TPC volume of secondary tracks originating from the beam pipe are shown in (b) and (d) with the respective diameter indicated.

Studies have been performed within the scope of new experiments at the M2 beam line [28] as the PRM campaign of AMBER and simulated beam profiles are provided. The beam properties are simulated in the so-called beam-line coordinate system and need to be translated into the spectrometer coordinate system. Details can be found in App. A.5. For the simulation of the setup, the simulated beam profile is used and as realistic as possible. The beam simulation is based on the M2 beam-line optics, provided by [25] and is generated at $z = 1\,130\,\mathrm{m}$ in beam-line

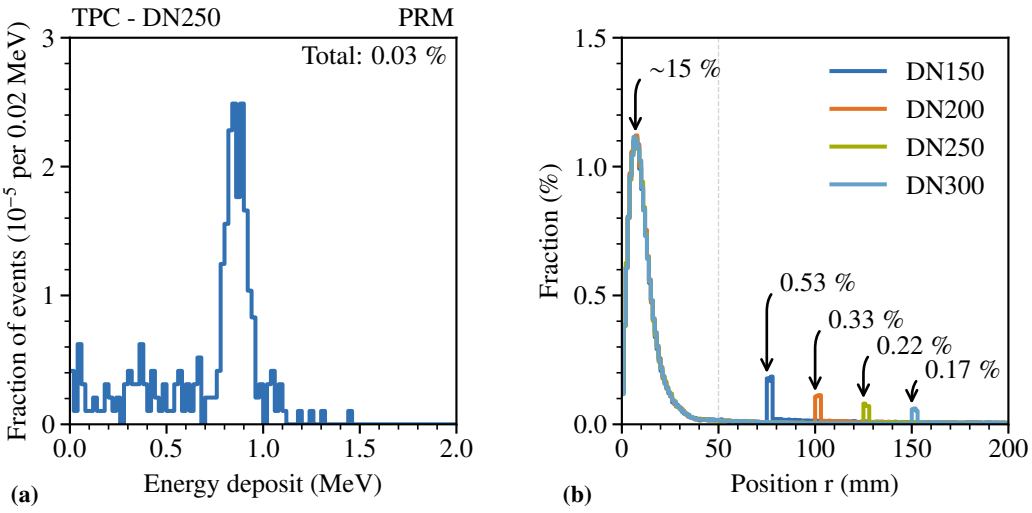

Figure 1.26: In (a) the energy deposit in the TPC of secondary tracks caused by beam pipe material interaction (mostly electrons) is shown. The integrated fraction of secondary tracks created by the beam muon originating from beam pipe interaction for different diameters is shown in (b).

coordinates. This corresponds to $z = 0.3$ m in spectrometer coordinate system. The profile in x-y-direction and its divergence with respect to the beam axis $\mathrm{d}x/\mathrm{d}z$ and $\mathrm{d}y/\mathrm{d}z$ are shown in Figs. 1.27(a) and 1.27(b), respectively. The beam size along the x- and y-direction is shown in Fig. 1.27(a) for the target position. Although the profile shows an enlargement in y the central point of the beam is well-focused with around $\sigma_{xy} \approx 10$ mm. The gradients along the beam axes are shown in Fig. 1.27(b).

The momentum distribution is shown in Fig. 1.27(c). The beam is expected to be well centered around the expected momentum of 100 GeV with a spread of about $\sigma_p = 5$ GeV/c. A so-called halo component is indicated, which is expected to accompany the beam particles. This halo component consists of particles that pass through material along the beam line[2]. Especially the low-momentum tail is dominated by halo particles. During the measurement, the incoming beam as well as the momenta for the muon before and after the scattering will be measured.

The muon beam has in general a large halo component, as it can be seed in Fig. 1.27(d) shown for ranges of ±30 m along the x- and y-direction. The overall flux in this region is expected to be $< 15\%$ outside the central part, as also evaluated in Fig. 1.9(b). The halo component is simulated up to ±30 m around the beam axis and enables further studies of larger components like trigger and veto.

[2] In the simulation these particles can be distinguished and studied individually. Under realistic conditions this is not possible.

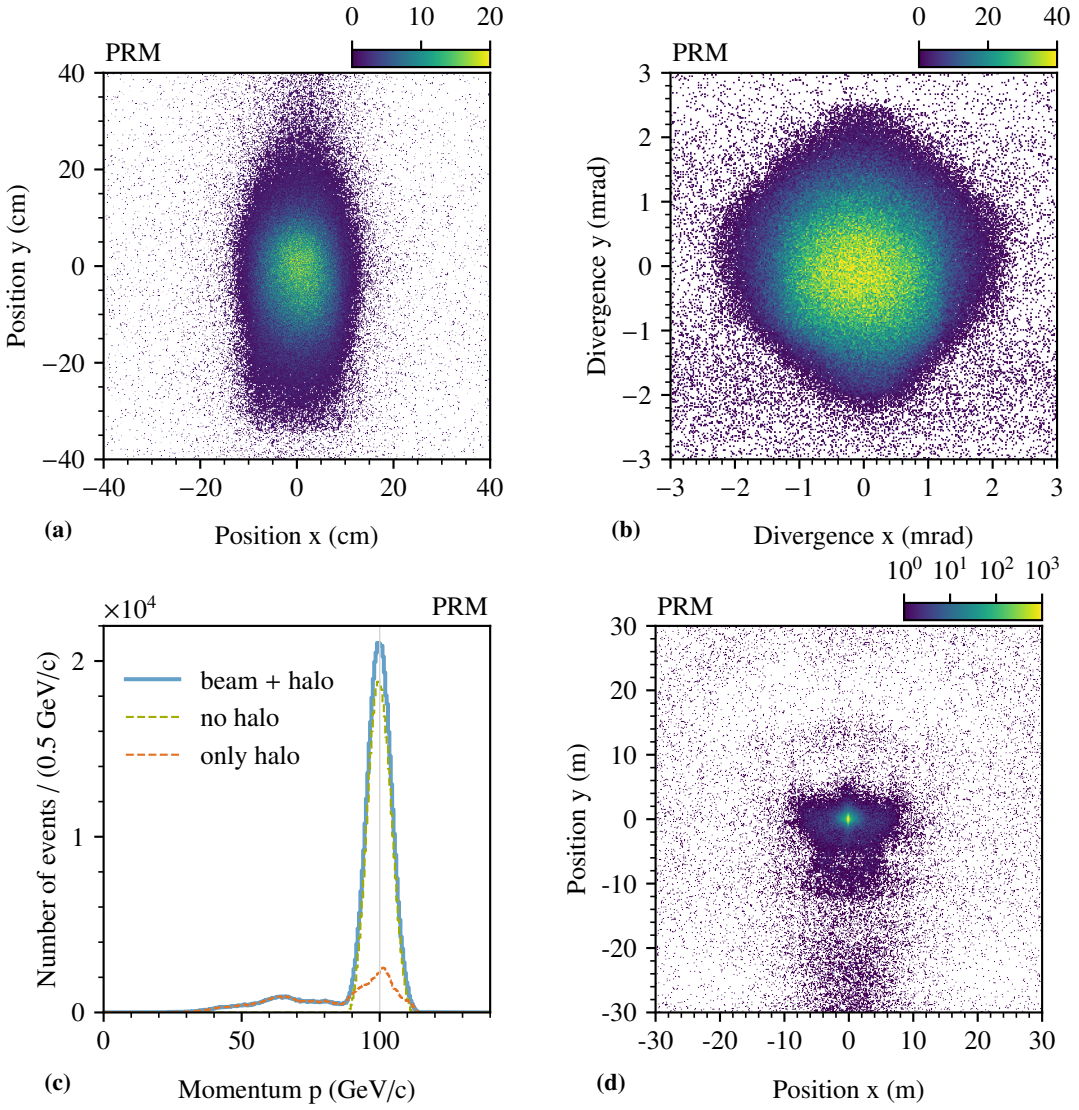

Figure 1.27: The central beam profile in x-y-position is shown in (a) and divergence dx/dy is shown in (b). The simulated beam momentum is shown in (c) with the halo component indicated. In (d) the full beam halo along x- and y-position up to 30 m is shown. The input is used for the simulation. The simulated beam profile is provided by [25] and is based on the simulation of the M2 beam line for a muon beam with a momentum of 100 GeV at $z = 0.3$ cm.

1.2.7 Estimate of Multiple Scattering

If a charged particle passes through material, it is deflected by multiple small-angle changes. This effect is dominated by Coulomb scattering from nuclei and is well described for small angles within a Gaussian approximation as given in [48] by

$$\Delta\theta = \frac{13.6\ \text{MeV}}{\beta c p} z \sqrt{\frac{X}{X_0}} \left[1 + 0.038 \ln\left(\frac{X z^2}{X_0 \beta^2} \right) \right], \tag{1.28}$$

with p, βc, and z as the momentum, velocity and charge number of the projectile. The thickness of the scattering medium is given by X/X_0 in units of radiation length. For several layers or mixtures of materials, the deflection due to multiple scattering is obtained via the sum of X and X_0 for the total traversed material. For the total contribution to the measured scattering angle, the resolution of the respective detector needs to be taken into account. The uncertainties are added quadratically as

$$\Delta\theta_{\text{tot}} = \sqrt{(\Delta\theta)^2 + \left(\Delta\theta_{\text{det}}\right)^2}. \tag{1.29}$$

The effect of multiple scattering is considered to be the dominant source for the angular uncertainty. The resulting combined uncertainty of multiple scattering induced by the materials is obtained according to [48] via the summation of the single radiative lengths as

$$\left(\frac{X}{X_0}\right)_{\text{total}} = \sum_{\left(\frac{X}{X_0}\right)_i \in \text{ materials}} \left(\frac{X}{X_0}\right)_i. \tag{1.30}$$

The angular uncertainty results into an uncertainty on the measured Q^2 and with uncertainty propagation using Eq. (1.8) it is given by

$$\Delta Q^2 \approx \sqrt{(\Delta\theta)^2 \left[\frac{\delta Q^2}{\delta\theta} \right]^2} \tag{1.31}$$

$$= \sqrt{(\Delta\theta)^2 \left[4 E_\mu E'_\mu \sin\left(\frac{\theta}{2}\right) \cos\left(\frac{\theta}{2}\right) \right]^2}. \tag{1.32}$$

The material budget is estimated from the implementation in the simulation and the effect of multiple scattering is evaluated. In Fig. 1.29(a), the material budget for a single UTS along the beam direction is given. It contains the Polymethylmethacrylate (PMMA)-coated polystyrene fibers of the SFH (cf. Sec. 1.2.3) and the ALPIDE material with the FlexPCB stack of the SPD (cf. Sec. 1.2.3). Each UTS contributes with a material budget of $X/X_0 = 1.28$ %. For the overall

multiple scattering budget, only the inner part between the first and last measured trajectory point contributes to the effect of angular uncertainty due to multiple scattering. Therefore, the inner two UTS will contribute to the total material budget. The TPC material budget along the beam direction is shown in Fig. 1.29(b). With the two main contributions of the target pressurized-hydrogen gas and the beryllium beam windows, a total radiation length of $X/X_0 = 1.44$ % is obtained. Possible non-uniform contributions of the copper-based Frisch grid at the anode position (cf. Sec. 1.2.2) need to be studied in future. A total material budget of $X/X_0 = 4.07$ %, as shown in Fig. 1.29(c), is obtained with two UTS, the TPC and taking into account the material budget along the helium-filled beam pipes.

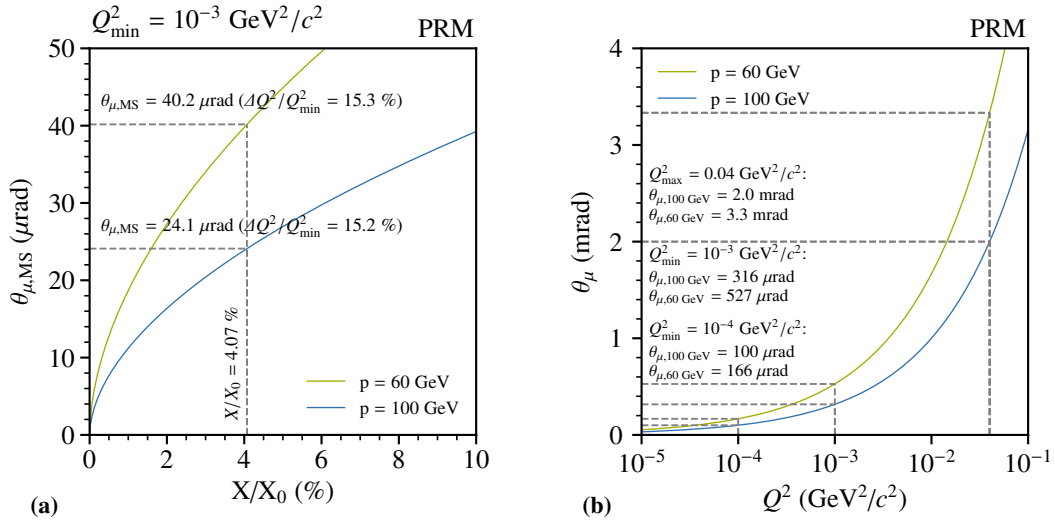

Figure 1.28: In (a) the calculated effect of multiple scattering as a function of the material budget is shown. Resulting muon scattering angle as a function of Q^2 is shown in (b) for two different beam momenta.

A 2-d view of the material distribution based on the simulation is shown in Fig. 1.29(d) with the single structures of the tracking detectors and the TPC vessel visible. The radiation length is given along the beam axis. The central area provides the presented material budget. In Fig. 1.28(a) the calculated Q^2-resolution is shown according to Eq. (1.32) for two different beam momenta. As comparison the $Q^2 = 10^{-4}$ GeV$^2/c^2$ value is given. At a beam momentum of 100 GeV a total uncertainty on the scattering angle due to multiple scattering of about 24 μrad is obtained and a resulting relative Q^2-resolution of about 15 %. These values are consistent with the values obtained from the simulation as presented in Fig. 1.24. For completeness, the expected muon scattering angles and the limits of the anticipated Q^2-range are given in Fig. 1.28(b). The multiple scattering effect is in the same order of magnitude at Q^2 values below 10^{-4} GeV$^2/c^2$ which corresponds to 100 μrad. The obtained resolution in Q^2 is compatible with the TPC measurement (cf. Sec. 1.2.2) and allows the foreseen combined measurement of the muon and proton track.

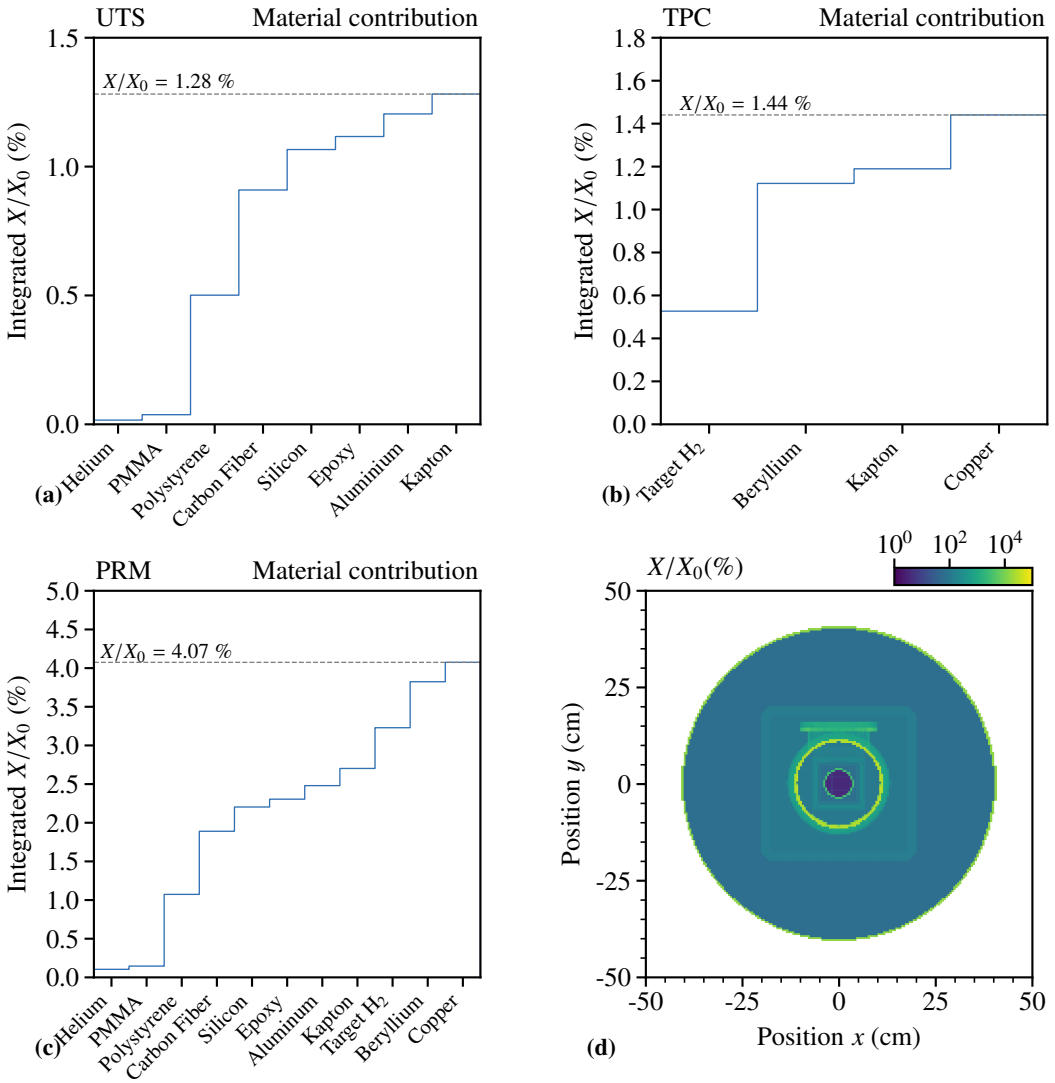

Figure 1.29: Material budget of the PRM core setup. In (a) the integrated material budget of one UTS is shown and in (b) for the TPC. The total material budget containing everything inside the up- and downstream UTS is shown in (c). A 2-d integrated view along the beam axis is shown in (d).

1.2.8 Radiative Effects

Charged leptons are accompanied by radiative effects. This emission of photons influences the differential cross-section for the elastic lepton-proton scattering (cf. Eq. (1.12)). Although this effect is reduced in muon-proton scattering compared to the electron-proton scattering due to the higher mass of the muon, it remains still a non-negligible effect. In Fig. 1.30 the first-order contributions of the radiative effects are shown. The emission of bremsstrahlung photons from lepton and proton directly affects the scattering angle and therefore alters the measured scattering process. In addition, internal virtual-photon processes can occur, which cannot be measured experimentally, but also influence the measured momentum transfer. These effects need to be taken into account for the determination of the elastic scattering cross-section.

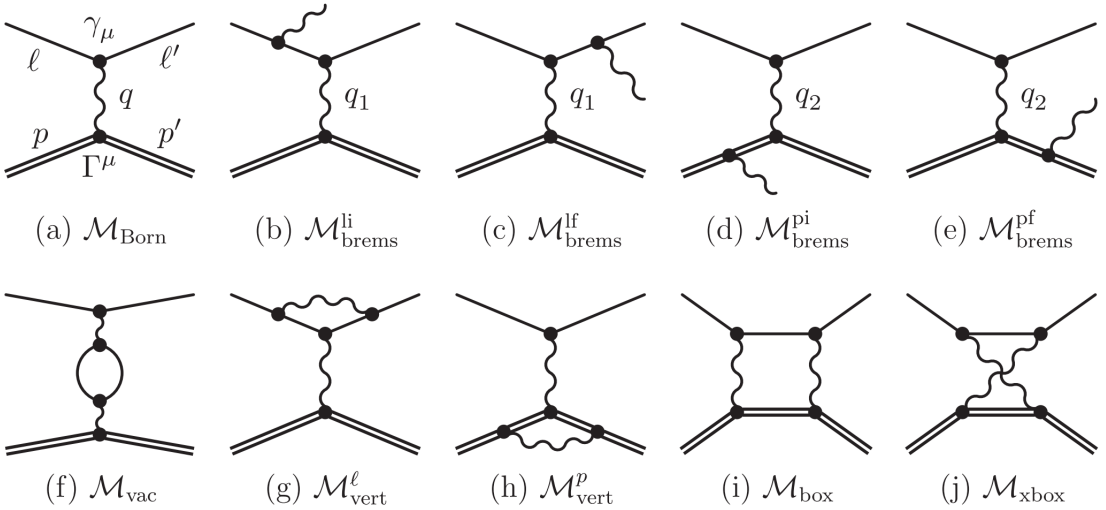

Figure 1.30: Leading and next-to-leading order Feynman diagrams for the elastic scattering of charged leptons off protons. In (a) the underlying first-order reaction is shown and (b) to (e) show the respective first-order bremsstrahlung processes from lepton and proton. The exchange of virtual photons is shown in (f) to (j). Here, the vacuum polarization, the vertex corrections for lepton and proton and the two-photon corrections are shown. Figure taken from [49].

The expected contributions for the elastic muon-proton scattering are summarized in Fig. 1.31. The single contributions by the vacuum polarization, the virtual photon-loops and the soft bremsstrahlung are shown and add up to about 1 % in the anticipated region for the Q^2-range of $10^{-3} \leq Q^2/(\mathrm{GeV}^2/c^2) \leq 4 \cdot 10^{-2}$. As example, the event generator Elastic Scattering of Electrons and Positrons on Protons (ESEPP) [49] provides simulation of elastic lepton scattering, including radiative effects. Studies are foreseen to evaluate the Electromagnetic Calorimeter (ECAL) performance of the spectrometer in radiative events based on this or similar event generators. The envisaged setup including the spectrometer has the advantage of being able to measure the bremsstrahlung photons and evaluate the results with respect to the expected values from theory. Although the overall corrections in the muon case are small, studies are ongoing to apply those required corrections to the data, as they cannot be neglected. According to [50] the proposed measurement approach has the advantage of single radiative corrections cancel each other.

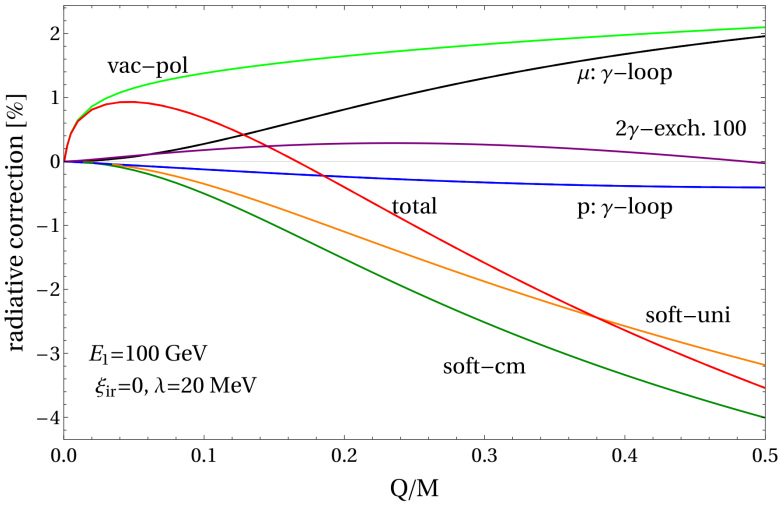

Figure 1.31: Radiative corrections for the anticipated beam momentum of 100 GeV in elastic muon-proton scattering. The individual radiative corrections from vacuum polarization, the virtual photon-loops and soft bremsstrahlung are shown together with their sum. Figure taken from [24].

1.2.9 Required Number of Events and Expected Event Rate

For the extraction of the proton charge radius from the electric form factor different parametrizations are available. The expected precision on the radius depends on the available number of scattering events. In Fig. 1.32 an estimate for the number of events required to obtain a certain precision on the extracted radius using different parametrizations is shown. Using polynomial functions and the dipole approximation as possible parametrizations for the electric form factor, which are besides other, further described in [47], results in different precision on the extracted radius. For example, a third-order polynomial function would require about 70 million events in the foreseen Q^2-range of $10^{-3} \leq Q^2/(\mathrm{GeV}^2/c^2) \leq 4 \cdot 10^{-2}$ to reach the envisaged precision on the radius of < 1 % [2]. This parametrization was used in the initial proposal for the measurement. Studies have shown that this required number of events cannot be reached and therefore a fall-back solution compared to this conservative scenario is performed in the following. The statistical uncertainty on the proton radius for a polynomial parametrization with fixed third-order term ($<r^6>$), as similar performed also in multiple analyses [51, 52], requires less number of events to reach the aimed precision.

The TPC as an active target is influenced by the beam-induced ionization noise. This plays a dominant role especially at small recoil proton energies as they are present in the low Q^2-region as described in Sec. 1.2.2. To obtain a calibration data set for this region, a dedicated low-pressure measurement is required. Therefore, the measured elastic scattering cross-section in the planned Q^2-range has to be collected in two dedicated measurements. One with a low hydrogen-pressure in the TPC as calibration and another one with the nominal pressure. For the low-pressure data set the TPC is operated at 4 bar and allows measuring at reduced ionization noise, which is lowered by a factor of five due to the lower pressure. This results in an increased resolution of the

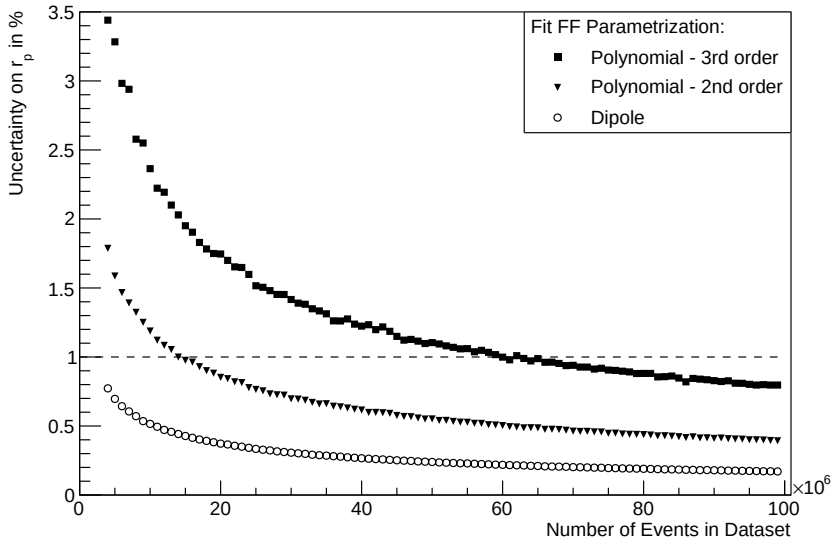

Figure 1.32: Estimated precision on the proton charge radius based on the number of events for different form factor parametrizations for the anticipated Q^2-range. Figure taken from [47].

Table 1.3: Planned measurements with respective number of events and settings as visualized in Fig. 1.33. The values are from the initial proposal [2] and the planned new splitting are indicated.

type	pressure (bar)	Q^2-range (GeV$^2/c^2$)	int. cross-section (mb)	events ($\times 10^6$)	fraction (%)	comment
full	20	0.0010 – 0.0400	0.2507	70	100	prop.
low-Q^2	4	0.0010 – 0.0080	0.2261			
low-Q^2	4	0.0010 – 0.0025	0.1555	6	8	new
high-Q^2	20	0.0025 – 0.0400	0.0952	27	38	new
overlap	4/20	0.0025 – 0.0080	0.0706			

measured proton energy. The required relative resolution for the kinetic energy of 6 % is fulfilled as discussed in Sec. 1.2.2. The measurement is split as given in Tab. 1.3. The upper limit is given by the maximal range of a proton that can be fully stopped within the active TPC volume at the given pressure setting.

As an estimate on the required beam time, the gross features of the measurement are sketched in the following. As starting point, the elastic muon-electron cross-section is used as given in Eq. (1.10) according to the dipole approximation shown in Fig. 1.33 with the Q^2-range indicated. Due to the $1/Q^4$-dependence of the cross-section, the contribution with increasing Q^2-values is strongly suppressed. The evaluated integral for the planned Q^2-range of the differential cross-section results to

$$\sigma_{\mathrm{D}}^{\mu p\to\mu p} = \int_{0.001\,\mathrm{GeV}^2/c^2}^{0.04\,\mathrm{GeV}^2/c^2} \frac{d\sigma_{\mathrm{D}}^{\mu p\to\mu p}}{dQ^2} dQ^2 = 0.2507\ \mathrm{mb}. \tag{1.33}$$

This takes into account the extension of the Q^2 range up to $Q^2 = 0.04\ \mathrm{GeV}^2/c^2$ by using the energy loss starting from $Q^2 = 0.02\ \mathrm{GeV}^2/c^2$, where the proton is not fully stopped in the active TPC volume. The cross-section is covered by the 4 and 20 bar measurement. The resulting overlap region used for normalization between the two measurements contains about 28 % of the events and can later be used to study systematic effects.

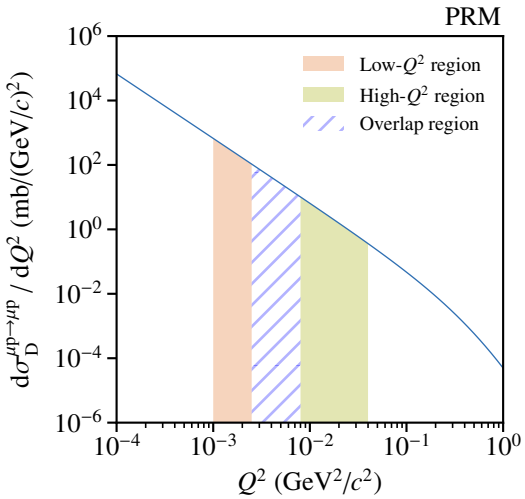

Figure 1.33: Elastic muon-proton dipole cross-section with the kinematic region indicated as low and high-Q^2 part together with the overlapping region for normalization. The respective integrals are listed in Tab. 1.3.

As example, first the estimate to obtain the initially planned 70 million scattering events [2] and the resulting event rate is presented. The luminosity L can be defined as

$$L = \Phi_{\mathrm{beam}} \cdot n_{\mathrm{target}} \cdot l_{\mathrm{target}} \qquad \text{with} \qquad n_{\mathrm{target}} = 2 \cdot \frac{\rho_{\mathrm{H_2}}}{M_{\mathrm{H_2}}}, \tag{1.34}$$

with the target length $l_{\mathrm{target}} = 4 \cdot 40$ cm of the four target cells and the n_{target} as the number of protons in the hydrogen gas. To obtain the number of target protons, the following values for the hydrogen density $\rho_{H_2,\mathrm{NTP}}$ at Normal Temperature and Pressure (NTP), molecule mass $M_{\mathrm{H_2}}$ are used, resulting to

$$\rho_{\mathrm{H_2,NTP}} = 0.084 \frac{\mathrm{kg}}{\mathrm{m}^3} \qquad \text{and} \qquad M_{\mathrm{H_2}} = 2 \cdot 1.008\ \mathrm{u} = 3.348 \cdot 10^{-27}\ \mathrm{kg} \tag{1.35}$$

and the operation pressures of the TPC of 4 bar for the low-Q^2 calibration region and the nominal 20 bar. The resulting number of target protons can be calculated for the different pressure scenarios as

$$n_{\text{target, NTP}} = 2 \cdot \frac{\rho_{\text{H}_2,\text{NTP}}}{M_{H_2}} = 2 \cdot \frac{0.084 \frac{\text{kg}}{\text{m}^3}}{3.348 \cdot 10^{-27}\ \text{kg}} = 5.018 \cdot 10^{25} \text{m}^{-3}, \tag{1.36}$$

$$n_{\text{target, 4 bar}} = \frac{4\ \text{bar}}{1.013\ \text{bar}} \cdot 5.018 \cdot 10^{25} \text{m}^{-3} = 1.982 \cdot 10^{26}\ \text{m}^{-3}, \quad \text{and} \tag{1.37}$$

$$n_{\text{target, 20 bar}} = \frac{20\ \text{bar}}{1.013\ \text{bar}} \cdot 5.018 \cdot 10^{25} \text{m}^{-3} = 9.908 \cdot 10^{26}\ \text{m}^{-3}. \tag{1.38}$$

The luminosity for the different pressure scenarios based on the expected beam flux of $\Phi_{\text{beam}} = 2 \cdot 10^6$ muons per second is then given as follows

$$\begin{aligned} L_{4\ \text{bar}} &= \Phi_{\text{beam}} \cdot n_{\text{target, 4 bar}} \cdot l_{\text{target}} && (1.39)\\ &= 2 \cdot 10^6\ \text{Hz} \cdot 1.982 \cdot 10^{26}\ \text{m}^{-3} \cdot 1.6\ \text{m} && (1.40)\\ &= 6.342 \cdot 10^{32} \frac{\text{Hz}}{\text{m}^2} = 6.342 \cdot 10^4 \frac{\text{Hz}}{\text{b}}, \quad \text{and} && (1.41)\\ L_{20\ \text{bar}} &= \Phi_{\text{beam}} \cdot n_{\text{target, 20 bar}} \cdot l_{\text{target}} && (1.42)\\ &= 2 \cdot 10^6\ \text{Hz} \cdot 9.908 \cdot 10^{26}\ \text{m}^{-3} \cdot 1.6\ \text{m} && (1.43)\\ &= 3.171 \cdot 10^{33} \frac{\text{Hz}}{\text{m}^2} = 3.171 \cdot 10^5 \frac{\text{Hz}}{\text{b}}. && (1.44) \end{aligned}$$

The resulting rates are obtained with

$$\begin{aligned} f &= \sigma_{\mu\text{p}} \cdot L, \qquad \text{yielding} && (1.45)\\ f_{4\ \text{bar, low}-Q^2} &= 0.1555\ \text{mb} \cdot 6.342 \cdot 10^4 \frac{\text{Hz}}{\text{b}} = 9.862\ \text{Hz}, && (1.46)\\ f_{20\ \text{bar, high}-Q^2} &= 0.0952\ \text{mb} \cdot 3.171 \cdot 10^5 \frac{\text{Hz}}{\text{b}} = 30.188\ \text{Hz}, \quad \text{and} && (1.47)\\ f_{20\ \text{bar, full}} &= 0.2507\ \text{mb} \cdot 3.171 \cdot 10^5 \frac{\text{Hz}}{\text{b}} = 79.497\ \text{Hz}. && (1.48) \end{aligned}$$

During the nominal data taking, the 20 bar pressure setting is used to cover the full Q^2-range, but requires the calibration for the low-Q^2 events. About 1.9 spills per minute are expected from the SPS (cf. Sec. 1.2.1). This results in a mean duty cycle of about 14 %. An overall efficiency for the spill delivery is assumed to be about 80 %. A conservative reconstruction efficiency of about

Table 1.4: List of parameters for the data taking beam parameters. Number for spill average based on COMPASS 2018 data: 504738 recorded spills from SPS to COMPASS within 186 days of data taking. Values taken from [2].

type	value
SPS spill length	4.8 s
SPS spills per minute	1.88
SPS mean duty cycle	14.0 %
SPS efficiency	80.0 %
Tracking efficiency	85.0 %

85 % is taken into account. A list of the respective beam line operation parameters is given in Tab. 1.4. According to the cross-section, the initial 70 million events need to be split into about 43 million events at the low-pressure setting and 27 million at the nominal 20 bar setting. The required number of events for the two different pressure settings results to

$$N_{\text{days, low}-Q^2} = \frac{27 \cdot 10^6 \text{events}}{9.862 \ \frac{\text{events}}{s}} \cdot \frac{1}{60 \cdot 60 \cdot 24} \cdot \frac{1}{0.14 \cdot 0.80 \cdot 0.85} = 333 \text{ days} \quad \text{and} \tag{1.49}$$

$$N_{\text{days, high}-Q^2} = \frac{43 \cdot 10^6 \text{events}}{30.188 \ \frac{\text{events}}{s}} \cdot \frac{1}{60 \cdot 60 \cdot 24} \cdot \frac{1}{0.14 \cdot 0.80 \cdot 0.85} = 173 \text{ days.} \tag{1.50}$$

With the idea of a full measurement within one year with an available beam times of to 150 to 180 days, those splitting of the measurements is not feasible. Due to the small rate, especially for the 4 bar measurement of < 10 Hz, the required number of events would be unreasonable and large in this conservative scenario. Therefore, as discussed before, a smaller number of events is anticipated based on the uncertainty assumption of a fixed $<r^6>$ term in the polynomial parametrization of the form factor as fall-back solution. This scenario results in a comparable precision as listed in Tab. 1.5. A total number of 33 million elastic scattering events in the full Q^2-range is required. The measurement will be split into a 4 bar measurement with 6 million events and a 20 bar measurement with 27 million events. The required beam time results to

$$N_{\text{days, low}-Q^2} = \frac{6 \cdot 10^6 \text{events}}{9.862 \ \frac{\text{events}}{s}} \cdot \frac{1}{60 \cdot 60 \cdot 24} \cdot \frac{1}{0.14 \cdot 0.80 \cdot 0.85} = 74 \text{ days} \quad \text{and} \tag{1.51}$$

$$N_{\text{days, high}-Q^2} = \frac{27 \cdot 10^6 \text{events}}{30.188 \ \frac{\text{events}}{s}} \cdot \frac{1}{60 \cdot 60 \cdot 24} \cdot \frac{1}{0.14 \cdot 0.80 \cdot 0.85} = 109 \text{ days.} \tag{1.52}$$

Table 1.5: Possible splitting of the data taking for different Q^2-ranges and systematic studies at different pressure settings to achieve the proposed precision of the proton radius given a order-three polynomial form-factor parametrization in Q^2. Values based on [51, 53].

stat. prec. (%)	fixed $<r^6>$ (%)	Q^2 (GeV$^2/c^2$)	statistics (x10^6)	pressure (bar)	time (days)
1.2	0.6	0.0025 - 0.04	37	20	150
1.6	0.7	0.0010 - 0.04	6 + 27	4 + 20	74 + 109

syst. study	beam	momentum (GeV)	pressure (bar)	time (days)	comment
charge dep.	μ^+	100 GeV	20	25–50	under study
energy dep.	μ^-	60 GeV	20	25–50	under study

Using only the high-Q^2 region in the nominal 20 bar pressure setting would result into a precision of 0.6 % on the extracted radius with fixed third-order term ($<r^6>$) based on events recorded within 150 days as conservative assumption. To take into account the contribution of low-Q^2 events and to be able to compare the obtained data along a sufficient large Q^2-range it is important to measure also at Q^2 values < 0.0025 GeV$^2/c^2$. The proposed new required number of events based on the fixed third-order term, would be feasible within about 180 days and would result in a precision of 0.7 %. Furthermore, the foreseen overlap between the two data sets allow systematic studies. In addition, possible systematic studies can be performed. A study at a different lepton charge would allow a validation of the reconstruction since the magnet settings and reconstruction need to be adapted accordingly. At a lower momentum of 60 GeV mainly the scattering angle of the muon is increased and allows studies of the acceptance and in addition the influence by multiple scattering.

1.2.10 Planning

A main data-taking period is envisaged during the beam time in 2024. A preceding commissioning phase could start mid of 2023 due to the transition phase between the prior anti-proton cross-section measurement at AMBER, which requires a different target-region geometry with respect to the PRM layout. Preparations for the data taking will be performed along 2021 to mid 2023 as sketched in Tab. 1.6. The different phases are shortly described in the following.

Table 1.6: Tentative beam time schedule for the PRM in the upcoming two years with the respective phases. [2]

Phase	Year	Task	Time (days)	Particle	p (GeV)	Rate (μ/s)	Comment
Ia	2021	Preparation	–	μ^+/μ^-	160	10^5-10^7	Parasitic testing
Ib	2021	Pilot run	20	μ^+/μ^-	100	$2\cdot10^6$	M2 test-beam, prototype setup
IIa	2022	UTS test	20	μ^+/μ^-	100	$\geq 2\cdot10^6$	Target area, partially equipped
IIb	2023	Comm.	90	μ^+/μ^-	100	$2\cdot10^6$	Target area, full setup
IIIa	2024	Data taking	74	μ^+/μ^-	100	$2\cdot10^6$	Q^2: $1.0\cdot10^{-3}$ – $8\cdot10^{-3}$ GeV$^2/c^2$
IIIb	2024	Data taking	109	μ^+/μ^-	100	$2\cdot10^6$	Q^2: $2.5\cdot10^{-3}$ – $4\cdot10^{-2}$ GeV$^2/c^2$

Phase Ia: Parasitic Tests

Single detector components can be tested under realistic beam conditions in the downstream test location of COMPASS. The same location was used for the 2018 test measurement (cf. Chap. 2). At this location, parasitic beam tests during the COMPASS data taking can be performed. The beam has a large spacial extent and the momentum distribution is broader compared to the beam at the target location due to the traversed material along the spectrometer. General beam-related tests were foreseen for the SFH and SPD. Efficiency and hit-time association studies (cf. Sec. 1.2.3) between the SFH and SPD were planned to be performed together with tests of the new DAQ system and related software also in the scope of the preparation for the anticipated pilot run end of 2021 (cf. Chap. 3). Due to time constraints of the production for the SFH and SPD, those planned parasitic tests could not be performed.

Phase Ib: M2 test-beam location

A prior pilot run was foreseen as preparation for the main data taking to validate the TPC performance in the muon beam and to further study the properties of the planned setup. The pilot run took place in the M2 test-beam location in October 2021. At this location, an area of about 13 m length upstream of the COMPASS target position was available. This allowed a close-to-final layout of the pilot run setup. The beam conditions are comparable to those at the COMPASS target location. Studies of the TPC energy resolution have been performed in combination with tracking of the scattered muon. Results are presented in Chap. 3.

Phase IIa: UTS test

To evaluate the detector performance under final beam conditions, a partially equipped UTS as prototype is planned to be placed close to the target location of COMPASS similar to its final position in the PRM setup in October 2022. It will be placed on a dedicated holding structure directly in the muon beam and will be operated parasitically during the ongoing COMPASS data taking. Dedicated beam tests with a 100 GeV muon beam at an anticipated beam rate of $2 \cdot 10^6$ Hz will be performed in close communication with the COMPASS collaboration. Those beam tests will allow rate and DAQ tests of the SFH and SPD. Studies of the efficiency and the hit-time association between the SPD and SFH are foreseen. First results are expected end of this year.

Phase IIb: Commissioning

In the first half of 2023, the AMBER anti-proton production cross-section measurement is planned. For this measurement the liquid-helium target of COMPASS will be reused (cf. [2]). After this measurement campaign a transition phase is foreseen to restructure the target area of the spectrometer and to install the PRM setup. The remaining beam time can be used as commissioning phase of the TPC as well as the UTS, the new DAQ system (cf. Sec. 1.2.4) and the spectrometer. The following winter break can be utilized for further improvements prior the following data taking in 2024.

Phase III: Data Taking

A possible start of the data taking is foreseen in spring 2024. As discussed in Sec. 1.2.9 the data taking will be split into two parts and cover the planned Q^2-range. No additional transition phase is required between the two measurements. About 180 days of beam time would be required to reach the expected statistics. To take into account systematic effects, both beam charges can be used.

1.3 Summary and Outlook

The measurement of the proton charge radius in high-energy elastic muon-proton scattering using an active-target pressurized-hydrogen TPC combined with the AMBER spectrometer will provide a unique data set to contribute to a solution of the proton radius puzzle. For this, the novel measurement principle based on the redundant measurement of recoil protons and muon tracking is applied together with the usage of a magnetic spectrometer providing momentum reconstruction, muon identification and calorimetry.

The expected relative energy resolution of the TPC, which is influenced by beam-ionization noise, is expected to be on the required 6 % level for this measurement. The chosen readout plane structure of the TPC matches the requirements in terms of spatial and energy resolution to extract recoil proton energies and allows a correlation of proton and muon tracks. Additional methods are further under study to extend the anticipated Q^2-range of $10^{-3} \leq Q^2/(\mathrm{GeV}^2/c^2) \leq 4 \cdot 10^{-2}$ to larger values. First energy-loss reconstruction studies have shown that a precision of 4 % can be achieved for Q^2 values up to $Q^2 = 0.08\ \mathrm{GeV}^2/c^2$.

The foreseen 10 m long core setup requires operating the spectrometer in the new single-magnet mode in order to not influence the tracking by a possible fringe field. This adaption of the spectrometer with respect to its nominal usage requires changes in layout and track reconstruction. As beam momentum calibration, the elastic muon-electron scattering is foreseen. The angular correlation between muon and electron can be used to correct the momentum measurement of the BMS in the beam line.

Novel ALPIDE-based silicon-pixel detectors are foreseen to be used as tracking detectors for the muons and determine the scattering angle with high precision. They will be combined in the UTS with scintillating fibers in order to disentangle pile-up events in the ALPIDE. The overall time planning foresees a first parasitic test of this UTS in October 2022 with intensive tests beforehand. Optimization of the material budget of the single detector components has been performed, especially for the interface structures of the ALPIDE. This so-called FlexPCB has been evaluated and a suitable geometry including a cooling solution has been found, which is currently in production.

The scintillating fibers of the SFH are fully active between the central area and their readout. Studies have shown that the influence of the beam passing through the outer parts does not contribute significantly to a false hit rate. With the combination of those fibers and the ALPIDE modules, a high efficiency in the required hit-time association can be achieved, which sustains rates of up to a factor of five higher than the anticipated one. Using only the SFH to reconstruct the scattered muon does not provide a sufficient resolution and requires the additional SPD.

To further minimize the multiple scattering effect, studies of the geometry especially in terms of additional helium-filled beam pipes have been performed. Using a 3 m long lever arm combined with the usage of beam pipes results in a sufficient geometrical acceptance and resolution in the full Q^2-range. The influence of the additional beam pipe material along the beam axis is expected to be small. Based on these optimizations, a total material budget of around $X/X_0 = 4$ % for the setup is achieved, which results in sufficient resolution to determine the muon scattering

angle in this multiple-scattering-dominated measurement. Calculations for possible radiative effects have been performed and show low contribution in muon scattering compared to electron scattering. Nevertheless, further studies especially in terms of simulations on these processes are foreseen.

In total, two data sets for the foreseen Q^2-range are required to extract the proton radius with the anticipated precision. A dedicated low-pressure data set is used to evaluate the beam-induced noise at low proton energies for the TPC. The obtained calibrations can then be used to correct the low-energy protons in the full Q^2-range data set measured at the nominal pressure. About 33 million scattering events are required, which can be obtained during 180 days of beam time. This is sufficient to extract the proton radius at an anticipated precision of below 1 % depending on the chosen parametrization of the radius. With the ongoing developments and performed beam tests, such as the feasibility test measurement in 2018 (cf. Chap. 2) and the pilot run end of October 2021 (cf. Chap. 3), experience has been obtained with this type of measurement. Dedicated tests of the UTS are foreseen end of 2022 and a possible commissioning phase of the setup could take place in the second half of 2023 with a following first physics run starting in 2024.

CHAPTER 2

Feasibility Test Measurement at COMPASS

As preparation for the proposed measurement of the proton charge radius at AMBER [1] a first feasibility test was performed in the year 2018[1]. The main goals were to verify that a measurement of recoil protons in an active-target pressurized-hydrogen TPC are possible with a sufficient energy resolution and can be combined with tracks determined by a separate tracking system. Furthermore, the behavior of the TPC within the high-rate muon beam and its influence by the beam-ionization noise (cf. Sec. 1.2.2) is of interest as it is influencing the energy resolution.

For this, a test setup consisting out of a prototype TPC, the so-called ACTAF2 (cf. Sec. 2.1.3), and four silicon-microstrip tracking detectors (cf. Sec. 2.1.4) was constructed at the downstream test-beam location of the COMPASS spectrometer. This prototype TPC was designed for measurements at a pencil-like electron beam. Therefore, the concept of measuring recoiling protons with a radial segmented readout plane and the behavior within the broad muon beam with an extent of up to a few centimeters, needs to be evaluated, especially in terms of the energy resolution due to the induced beam ionization noise. The TPC and tracking events are recorded with dedicated DAQ systems, since the drift time of the TPC is too large to allow a common hardware-based trigger for both systems. This concept serves as predecessor of the streaming DAQ system (cf. Sec. 1.2.4), which is not available at this time. To allow a combined measurement of the proton and muon of one event, a timestamp-based correlation is used.

The measurement took place in a parasitic mode in parallel to the data taking of COMPASS during the pion-induced Drell-Yan program. This program utilizes a pion beam with a momentum of 190 GeV/c together with a polarized ammonia proton target [54]. To avoid a high rate of secondary particles from the interactions along the target in the downstream tracking detectors a dedicated hadron absorber was installed downstream of the target. It consists out of a mixture of aluminum and tungsten to ensure a passage of only muons. In this configuration, only muons are passing through the spectrometer and, especially at the test beam location, about 50 m downstream of the target region and the spectrometer at the test-beam location. The momentum of the resulting muon-pairs of the Drell-Yan process at this location is washed out due to the production process

[1] The test run took place from 19.03.2018 until 15.05.2018.

and the passed materials. In addition, the beam axis at the downstream test location is deflected due to the two spectrometer magnets SM1 and SM2 (cf. Fig. 1.6) located upstream of the test setup, which needs to be taken into account for positioning of the setup.

To reach the main goals of the feasibility test, a precise beam optics is not required. Various studies and tests were performed to evaluate the performance and characteristics of the setup and especially the TPC. To evaluate the TPC also the performance of the used silicon detectors is subject of interest. This feasibility test provides important knowledge and experience for the final measurement and served as foundation for its proposal (cf. [2]). In the following, the setup is described and results of the analysis are presented.

2.1 Setup of the Test Measurement

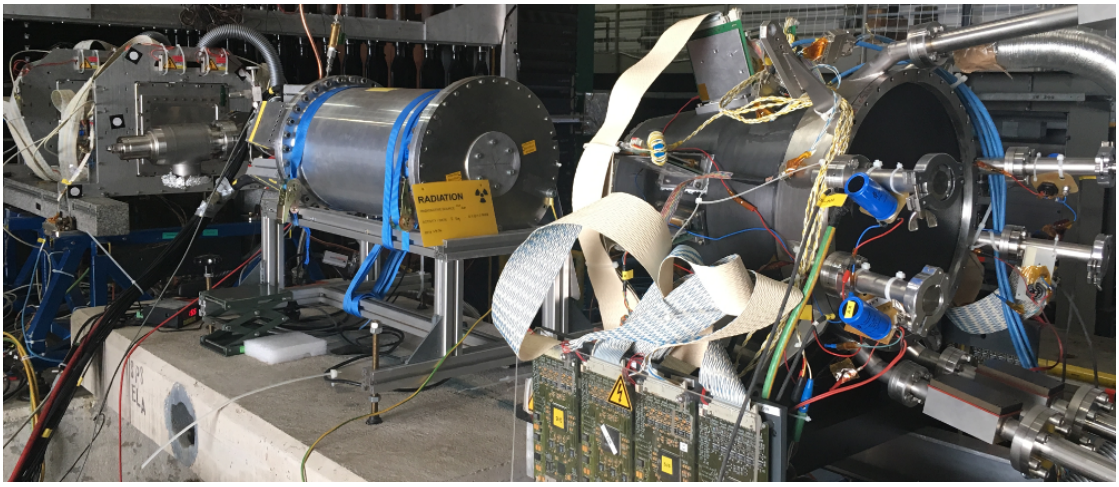

Figure 2.1: Setup of the feasibility test at COMPASS. The TPC is visible in the center surrounded by silicon-microstrip tracking detector up- and downstream.

The setup consists out of the Active Target For FAIR 2 (ACTAF2) TPC (cf. Sec. 2.1.3) surrounded by four silicon-microstrip tracking detectors (cf. Sec. 2.1.4), two placed upstream and two downstream of the TPC. In Fig. 2.1 a picture of the test setup with the TPC in the center and the four silicon detectors is shown. The TPC operates as active target using pressurized hydrogen gas at a maximum of 8 bar as proton target and measures the energy deposition of recoil protons originating from elastic muon-proton scattering process. In addition, beam noise (cf. Sec. 1.2.2) is induced due to ionization along the trajectory of the traversing muons, which accumulates in the chamber and disturbs the energy resolution of the measured charge produced by the recoil proton and therefore the overall determined kinetic energy of it.

The incoming muon trajectory is measured by two silicon detectors upstream of the TPC. Two additional silicon detectors downstream of the TPC allow reconstruction of scattered muon with a vertex and corresponding scattering angle. The overall setup has a length of about 460 cm. To select incoming muons, a beam trigger system (cf. Sec. 2.1.2) is used. It consists out of two

separate trigger elements. A segmented trigger element Beam Trigger 1B (BT1B) is used to withstand the high beam-rate and to obtain rough information about the beam position during commissioning. In addition, a monolithic element Beam Trigger 1A (BT1A) of the same size is installed, which allows generating a coincidence signal with the segmented one to minimize false triggers.

A schematic drawing is shown in Fig. 2.2. The initial positions of the detectors are obtained based on a dedicated survey [55] of the respective outer structures. Since the test setup is independent of the COMPASS environment, a separate coordinate system is introduced. As origin of the coordinate system, the upstream position of the TPC volume is used.

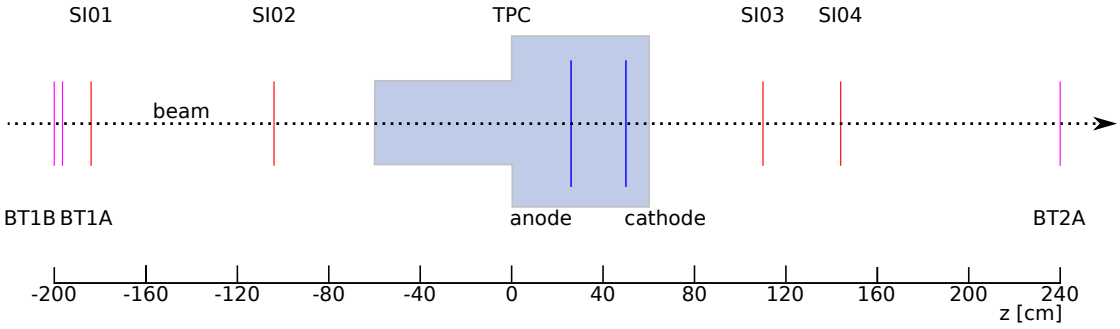

Figure 2.2: Schematic drawing of the feasibility test setup with the beam entering from the left side. Beam trigger elements (purple) are placed on the upstream side. The four silicon trackers (red) surround the TPC. Anode and cathode (blue) defining the active volume of the TPC with the readout located on the anode. Precise positions of the single elements can be found in Tab. B.2.

2.1.1 DAQ Systems

The TPC detector has a maximal expected drift time between anode and cathode of about 64 µs depending on the point of interaction inside this volume. This delay between the interaction and the measured signal is too large for the used front-end electronics of the tracking systems if used with a common hardware trigger. The used Analog Pipeline [Voltage Mode] in 0.25 μm silicon CMOS technology (APV25) chip (cf. Sec. 5.1) for the readout of the silicon detectors can only delay the respective trigger signal up to 4 µs based on a so-called ring buffer [56]. Although the TPC can generate its own trigger signal, the possible buffer of the APV25 chip is not sufficient to keep the data of the same event. Therefore, the TPC uses its own trigger and the tracking system relies on a dedicated beam trigger.

To allow a common event recording, two dedicated DAQ systems are introduced for the TPC and the tracking system. To correlate events, a common timestamp based on the so-called speaking time [57, 58] (cf. Sec. 2.2) is generated and broadcast by the TPC DAQ and recorded by the tracking DAQ. This speaking time provides event time information for the TPC and can be used to translate the tracking event time into the same time system of the TPC and vice versa. A Time-to-Digital Converter (TDC) in the tracking DAQ records the broadcast time information and allows correlating events based on this common time information. The approach of two dedicated

DAQ systems and a later event correlation is used as predecessor of the future streaming DAQ (cf. Sec. 1.2.4), which continuously reads the data from the front-end electronics and records so-called time-slices of each detector. Those time slices are then combined on a later stage. This concept is approached with the timestamp-based matching of events.

For the tracking DAQ, a scaled-down version of the COMPASS DAQ is used. This DAQ system is normally used for testing purpose of COMPASS front-end electronics. It consists out of a single so-called readout engine, which operates the DAQ control and initial storage of the incoming data. For the combined data taking the existing COMPASS DAQ system is extended in the way that a common start and stop of both DAQs is possible. Also, the corresponding data recording run number is forwarded from the tracking DAQ to the one of the TPC. The data is stored on the respective DAQ systems and later copied to the common storage on the CERN Tape Archive (CTA) (cf. App. B.3).

2.1.2 Trigger System

During the data taking, two different types of triggers are used to select physics events. For the selection of incoming beam muons, a beam trigger system is used for the tracking detectors. In addition, the TPC generates its own trigger signal based on a given threshold for energy deposition inside the chamber. This self-generated trigger signal is also recorded by the tracking DAQ for later calibration purposes. To ensure the recording of each TPC trigger, it vetos each attempt of other triggers reaching the tracking DAQ and is not affected by any manual reduction of the trigger rate, so-called prescaling. The maximal trigger rate of the TPC is around 200 Hz [37], whereas the tracking DAQ can record up to 40 kHz.

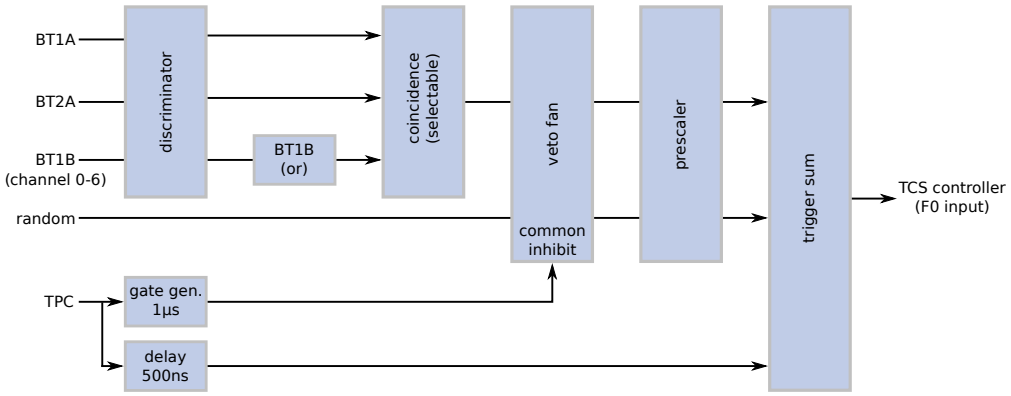

Figure 2.3: Trigger logic scheme of the coincidence trigger logic for the silicon-microstrip tracking detectors in combination with the TPC self-generated trigger. The TPC trigger generates a gate and vetos other triggers during that time. A delay is used between single TPC triggers. After applying a prescaling the beam trigger signals are combined with the TPC trigger and sent to the Trigger Control System (TCS) controller. Information provided by [59].

For the tracking system two scintillator trigger elements BT1A and BT1B read out by Photomultipier Tubes (PMTs) shown in Fig. 2.4, each with a total size comparable to the active area of $70 \times 50\,\mathrm{mm}^2$ of the silicon detectors, are used. One of the two trigger elements is segmented into seven slabs, which provide a rough estimate on the beam position due to the measured rate in the single slab and is used for beam tuning at the beginning of the data taking without using the more complex silicon detectors. A coincidence signal between the two scintillator elements are required to generate a trigger on an incoming muon. The APV25 chip of the silicon detectors limits the maximal trigger rate to a theoretical rate of 40 kHz [56]. A so-called spill buffer card stores the incoming data of the detectors before it is written to disk. Due to a limited bandwidth of the used older version of the spill buffer card, the overall trigger rate needs to be reduced to about 25 kHz, which guarantees that the buffer of the spill buffer card can be emptied on time before new data arrives.

Depending on the beam rate used during the COMPASS data taking, manual adaptions of the prescaling were required. Although the beam size is much wider, lowering the rate on the detectors at the downstream location of the setup, prescalers between 1 and 16, which can be set in steps of 2^n, are needed to adapt the incoming rate. The chosen prescaler value depends on the delivered protons from the SPS to the production target (cf. Sec. 1.2.1), its selected size and whether pion or muon beam is used. Chosen values during the data taking are listed for the respective conditions in Tab. B.1.

The beam trigger and self-generated trigger signal of the TPC need to be merged to generate the final trigger signal for the tracking DAQ. For this, a trigger logic is implemented. The scheme of the trigger logic is shown in Fig. 2.3. The signals of the monolithic beam trigger elements BT1A and Beam Trigger 2A (BT2A) as well as the single channel signals of the segmented trigger element are fed into a discriminator to select only those signals above a certain threshold of the PMTs. A coincidence signal is generated from the single beam-trigger elements. For the test run, a coincidence signal between one of the single channels of the segmented trigger element (as OR) and the upstream monolithic element is generated. Prescalers are applied before the resulting triggers are fed to the overall trigger sum.

Besides the beam trigger, the TPC generates a trigger signal in its self-triggering mode. Each trigger signal of the TPC creates a 1 µs gate, vetoing all other trigger attempts. In addition, the trigger signal of the TPC is delayed by 500 ns and added to the trigger sum. By this, each TPC trigger is ensured to be recorded. Furthermore, random triggers are installed for calibrations and testings of the detectors. The combined trigger sum is then fed into the TCS controller, which handles the trigger distribution, to finally generate the trigger signal for tracking DAQ. For each triggered event, the trigger type is recorded using an Intelligent FPGA-based Time-to-Digital-Converter (iFTDC). [59]

Beam Trigger Elements

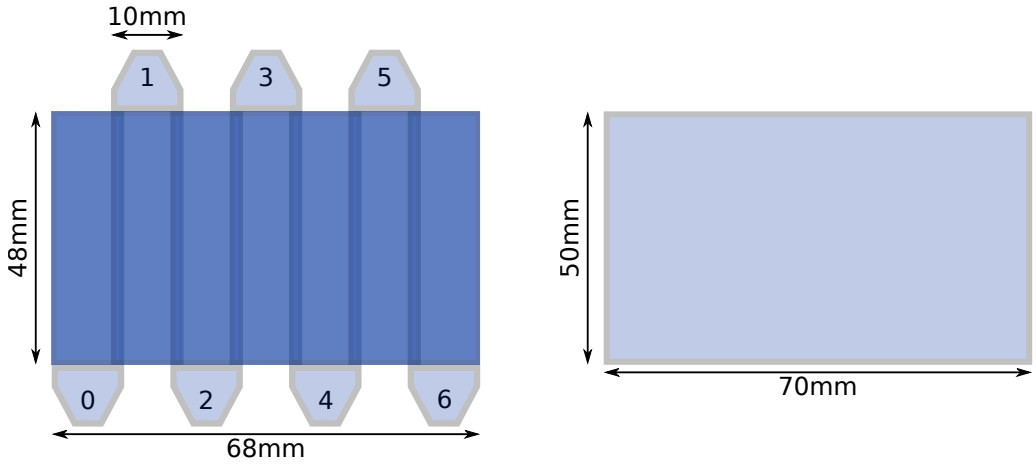

Figure 2.4: Sketch of the segmented and monolithic beam trigger elements. The segmented beam trigger element (BT1A) is shown in (a). It consists out of seven slightly overlapping (dark blue) scintillator slabs. Fishtails are used as light guides to single PMTs. The active area is marked in blue. In (b) the monolithic trigger element (BT1B) is shown. [59]

To study the influence of the beam trigger elements on the track reconstruction, the single beam trigger elements are discussed in the following. With the active area of the silicon detectors of $70 \times 50\,\mathrm{mm}^2$ (cf. Sec. 5.1) the beam trigger elements need to have a similar size to ensure a full usage of the available tracking area. For the beam trigger elements, two different types are used — a vertical segmented one and a monolithic one[2]. A sketch of the single trigger elements is shown in Fig. 2.4. The vertical segmented trigger element BT1B is placed at the very upstream position of the setup and consists out of seven single slabs each with a size of $10 \times 48\,\mathrm{mm}^2$. To avoid dead zones between, the single slabs slightly overlap. This results in an active area of about $64 \times 48\,\mathrm{mm}^2$. They are read out individually by a PMTs and the single signals slab signals are recorded in the trigger information. This segmentation allows high trigger rates of up to 2 MHz. Plexiglas fishtails are used as light guides between the scintillator slabs and the PMTs. The monolithic trigger element BT1A is located directly downstream the segmented one and has size of $70 \times 50\,\mathrm{mm}^2$. Initially, a second monolithic trigger element (BT2A) was planned similar to the BT1A element and installed at the very downstream position of the setup to select straight tracks. During the data taking, this additional trigger element was not used and only the two upstream elements are utilized to generate the beam trigger signal. [59]

An example beam profile from a single run[3] is shown in Fig. 2.5(a) using the single slab structure of the segmented trigger element. An increase of events with larger slab number is due to a not centered beam and represents the slope of the beam profile. This is also visible in the x-y-position

[2] Both scintillator are made from the plastic scintillator material BC408 [60]. [59]

[3] The used run has the number 282200.

of the extrapolated tracks, which are obtained from the reconstruction of the silicon detector information, at the segmented trigger element location shown in Fig. 2.5(b). The overlap between the single slabs becomes visible in the darker areas and also the overlap differs for the single slabs, causing a different amount of events per slab as for example the drop in slab five indicates. The precise x-y-position of each slab is not known and therefore their position information is not used for the track reconstruction.

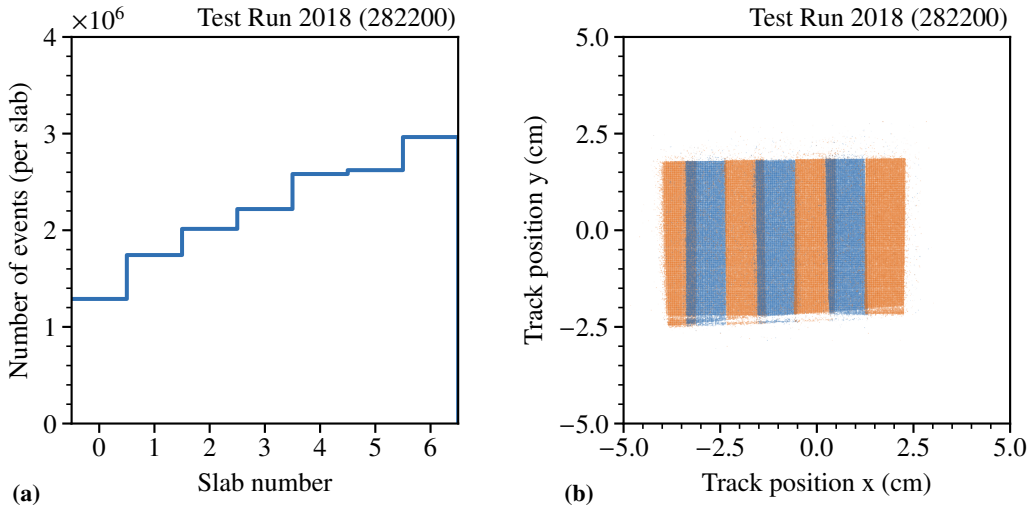

Figure 2.5: In (a) the number of events in the single slabs of the segmented trigger is shown. An increase of events with increasing slab number can be observed reassembling the not-centered broad beam profile. In (b) the x-y-position of tracks extrapolated to the position of the segmented trigger element is shown. Between the even slab numbers (orange) and odd ones (blue) an overlap between neighbors becomes visible. The data is based on the single indicated run.

The trigger geometry governs the hit and therefore track positions measured by the silicon detectors. In Fig. 2.6(a) the extrapolated track position at the location of the first silicon station is shown with the active area of the single detector planes in their UV- and XY- projection indicated (cf. Sec. 5.1). Artifacts due to the beam trigger geometry are visible as overlaps between the single trigger elements. As an example, a gap between the slabs at $x \approx 1.3$ cm can be seen. Variations in the connection between the fishtails and the single slabs and their vertical positioning can be identified. Additional pile-up tracks outside the trigger region at $y \gtrsim 1.7$ cm or $x \gtrsim 2.2$ cm can be observed. Single broken strips of the silicon detector are visible, for example at $x \approx -2.5$ cm showing also the inclination of the single strips for a projection of 2.5 degree (cf. Sec. 5.1). Overall the beam intensity varies over the area due to the non-centered beam at the test beam location during the parasitic data taking. This is even more pronounced in the x-projection of the extrapolated tracks position as shown in Fig. 2.6(b) similar to the intensity in the single slabs as presented in Fig. 2.4(a). In addition, artifacts like the gab between the slabs is also visible.

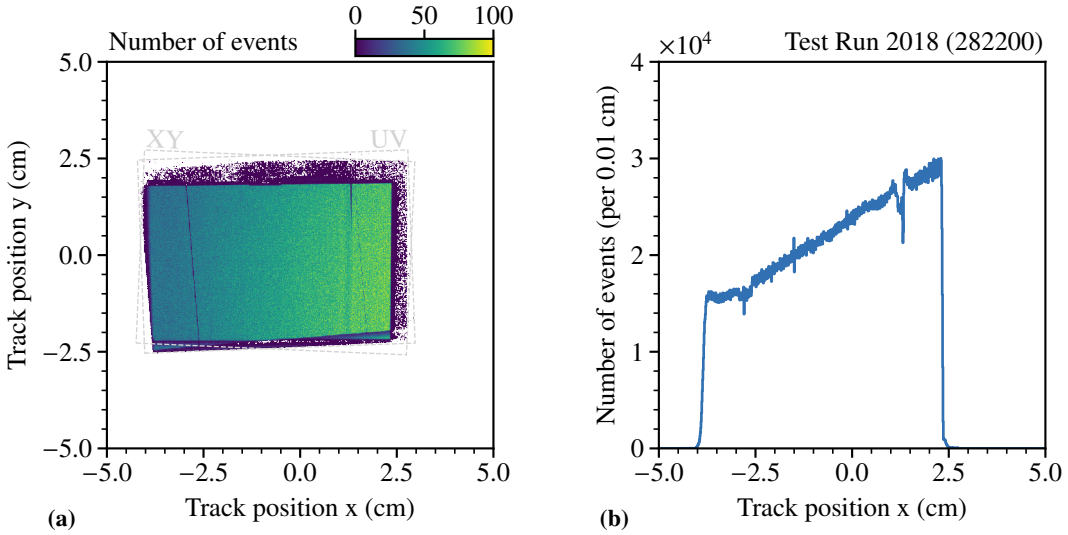

Figure 2.6: The x-y-position of the extrapolated tracks at the SI01 position is shown in (a). The detector modules in their projection are indicted. In (b) the projection in x of the extrapolated tracks at the position of SI01 is shown. The influence of the trigger elements as well as the dead zones are visible in both figures.

Table 2.1: Used trigger bits for the beam triggers, TPC and a true-random trigger. The respective prescaling and their trigger bit-mask is given.

trigger name	trigger bit-mask	value	in rate (kHz)	prescaling	out rate (kHz)
True random	0001	1	10.0	2	5.0
Beam trigger	0010	2	100–1300	1-16	20.0
TPC	0100	4	0.01–0.2	1	0.01–0.2

To identify single recorded triggers or their combination, so-called trigger bits are used. The available trigger bits are listed in Tab. 2.1. Besides a so-called true-random trigger for general calibration purposes for the detectors, the beam trigger is used. In addition, the self-generated triggers of the TPC are recorded for later study. The selected prescaling values to lower the incoming trigger rate to the maximal of the DAQ are given and the resulting trigger rates are listed. Additional information for the prescaling values and rates can be found in App. B.1.

2.1.3 TPC Prototype

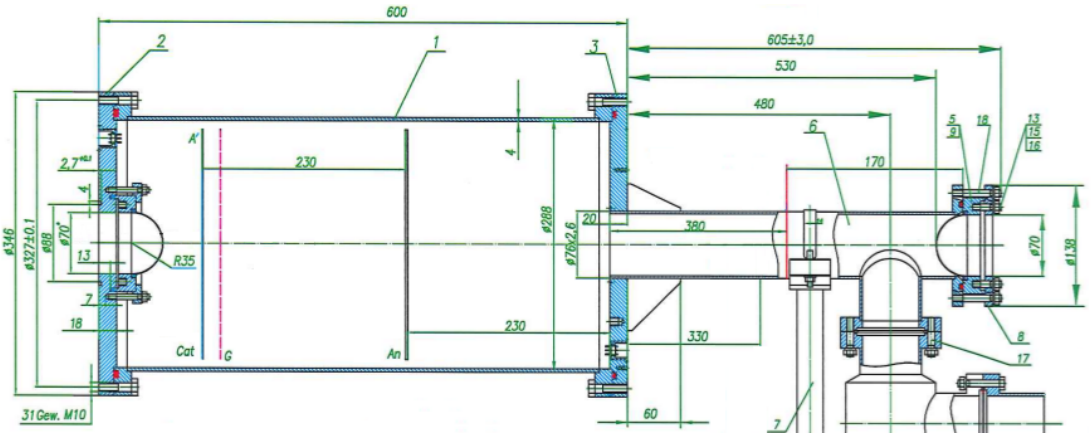

Figure 2.7: Drawing of the prototype ACTAF2 TPC. With a total length of 1 205 mm the TPC provides an active volume between anode and cathode of about 230 mm along the beam axis. The indicated size for the downstream beam window is not 70 mm, but has the size of 40 mm diameter. Figure provided by [61].

For the test measurement a prototype TPC, the so-called ACTAF2 TPC, is used. It was initially designed for the PRES experiment at MAMI to study elastic electron-proton scattering. In Fig. 2.7 a sketch of the TPC is shown. It has an overall length of 1205 mm with a 230 mm long drift volume between the anode and cathode. The anode serves as readout plane and is segmented to allow spatial information of the recoil proton measurement. The TPC is filled with hydrogen gas with a high purity level of 6.0[4] to minimize attachments due to impurities in the gas and therefore distort the drift time and the energy resolution. The maximal pressure can be adjusted up to 8 bar. A so-called Frisch grid [32] is installed about 10 mm in front of the anode to avoid induction from drifting ions. The drift voltage between the anode and cathode is 18 kV with the grid on an intermediate voltage level of 1 kV. This drift voltage setting at the nominal operation pressure results in a drift time between the anode and cathode of 64 μs. The drift volume is defines the active volume of the TPC between the anode and cathode. Field rings outside the active volume shape the drift field and guarantee a homogeneous field inside. The gas properties and the applied drift voltage defines the induced beam-ionization noise created by traversing muons (cf. Sec. 1.2.2) and the resulting energy resolution of the recoil proton energy.

To allow the beam particles to enter the TPC volume, beam windows are placed on the upstream and downstream side. They are made from Beryllium to minimize material budget along the beam axis, and therefore the effect of multiple scattering affecting the muon trajectory. The upstream window has a diameter of 70 mm and the downstream window has a size of 40 mm. They have a thickness of 0.5 mm formed in a half-sphere shape bend inwards to withstand the pressure.

[4] The gas contains 99.9999 % of the respective element.

The readout is based on a flash ADC[5] [62], which provides the amplitude, integral and time of the signal. Each channel of the modules is connected to one pad of the segmented anode structure. A schematic drawing of the pad plane is shown in Fig. 2.8(a). The segmented pad plane is visible in the inner structure of the TPC, as shown in Fig. 2.8(b). The cathode and the partially mounted field shaping rings can be seen. To allow the beam to pass through the cathode, a hole is present in the center of it. On the bottom plate, visible on the left side, the feedthroughs for readout and high-voltage are located.

Anode Structure

The segmented anode structure scheme is radial segmented into 64 pads as shown in Fig. 2.8(a). It is initially designed to be operated in a pencil-like electron beam focused in the center of the anode plane. The recoil protons of the scattering process are foreseen to originate from the center of the anode plane and travel in radial direction. The central part of the pad plane consists out of two circular pads (65 and 66). Four rings are centered around the central pad structure with an angular segmentation. Each single pad is read out by an Analog-to-Digial Converter (ADC). The beam ionization noise especially influences the energy resolution in the central pads, whereas the outer pads are less affected by the beam noise.

Signals on the single pads are used to reconstruct the recoil proton track. With the information of the most outer ring, protons leaving the active area can be identified. A future pad plane needs to be adapted to the broader muon beam to provide the required energy and spacial resolution. For calibration purposes of the energy resolution, a ^{241}Am source[6] is used. This calibration source is placed on the cathode at the opposite side of the readout anode (pad 7) as indicated in Fig. 2.8(a) and allows energy calibrations of single pads. By this, attachments on impurities in the gas can be determined and corrected for in a later step.

2.1.4 Silicon Trackers

For the tracking of the muons, so-called silicon-microstrip tracking detectors are used (cf. Fig. 5.1). The detectors were initially constructed for the COMPASS spectrometer for small-angle tracking up- and downstream of the target location. Two different types have been installed during the test measurement. Two so-called warm silicon stations and two newer cryogenic silicon stations, which were operated in the warm configuration. The warm stations have been in operation at COMPASS since 2007 and were replaced by the cryogenic version, but are expected to be fully functional, besides minor inefficiencies. They have been placed as the two upstream stations SI01 and SI02, and are operated with simplistic gaseous nitrogen cooling. The two downstream silicon detectors SI03 and SI04 are based on the later cryogenic version of the design and can be operated with liquid nitrogen cooling. During the test measurement, it was sufficient to cool all four stations with gaseous nitrogen. To control the temperature of the detector modules, temperature probes on the modules have been monitored, as further described in Sec. 2.1.4.

[5] Struck SIS3316 VME FADC

[6] It decays at about 100 % under the emission 5.486 MeV α-particles and a half-life of 432.2 years into ^{237}Np.

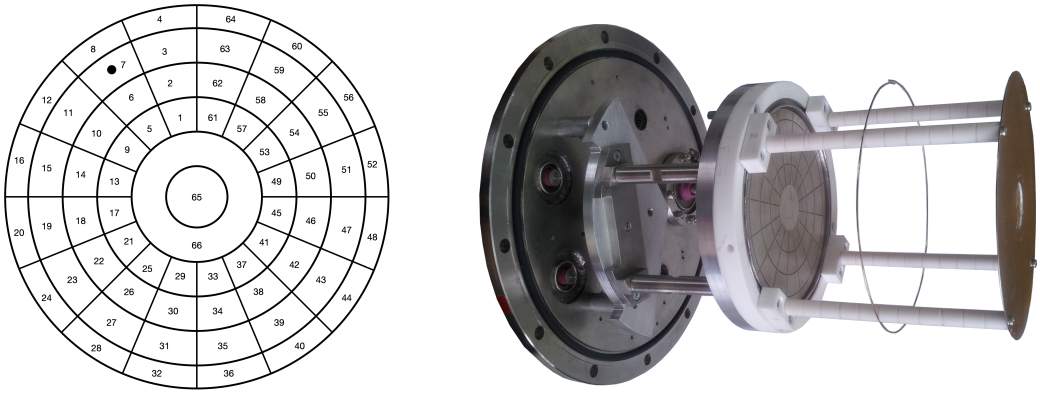

(a) **(b)**

Figure 2.8: A schematic drawing of the ACTAF2 pad plane is shown in (a). The calibration ^{241}Am source is placed at the cathode side at the same location as indicated on pad 7. In (b) the inner structure of the ACTAF2 TPC is shown. The upstream flange is visible with the holding structure for the segmented readout anode (left) and cathode (right) with the beam hole in the center. The support structure (white) for the field rings is visible with one field shaping ring attached. Figures provided by [37, 61], modified.

A silicon station provides two detector modules mounted inside a cryostat. They cover an active area of $70 \times 50\,\mathrm{mm}^2$ with $1\,280 \times 1\,024$ strips with a pitch of about 50 µm. Each module uses a double-sided silicon wafer with two coordinate planes: a X-Y-plane and a U-V-plane (cf. Fig. 5.3). The two modules have an angle of five degrees with respect to each other to allow disentanglement of single hits in the plane wires. The readout is based on the APV25 chip with 128 channels, which are directly connected to the single wires. The larger U- and X-projection require 10 chips, whereas the small V- and Y-projection require 8 chips. They provide a spatial resolution of about 14 µm and time resolution of about 2 ns. Further details on the silicon tracking detectors are given in Chap. 5. In the following, details on the operation during the test measurement are presented. Further details on the silicon detectors can be found in Chap. 5.

Depletion-Voltage Scan

To create the required depletion zone in the silicon wafer, the depletion voltage is applied. This voltage setting needs to be optimized in order to obtain a sufficient signal-to-noise ratio. Prior to the data taking of the test run, a so-called depletion-voltage scan is performed to obtain the optimal settings. The result of the four stations are shown in Fig. 2.9. For different voltages, the so-called common-mode corrected sigma (cf. Sec. 5.2) is shown. It represents the fluctuation of the signal baseline corrected for common fluctuations of all baselines per chip. It serves as indicator for the quality of the depletion.

The overall behavior of the four stations is comparable. Whereas the V- and Y-planes of each module tends to have a lower noise starting with applied voltage, the U- and X-planes show a decreasing noise starting between 50 and 100 V. Overall the difference of SI03 and SI04 as the newer cryogenic modules with respect to the older SI01 and SI02 is visible. They show a lower

noise with saturating depletion voltage. From experience, the depletion voltage does not change much over the years as long as no further radiation damage is introduced to the detector module and can be used as validation of a stable operation.

Table 2.2: Depletion-voltage settings and resulting leakage currents of the silicon-microstrip tracking detectors. The temperature of the detector modules is not stabilizes and therefore the measured current is oscillating in day-night cycles by about 10 %. The given type represents the design and not the operation mode.

Detector module (type)	V_0 (V)	i_{mes} (µA)
SI01UV (warm)	100	0.150*
SI01XY (warm)	100	0.150*
SI02UV (warm)	170	0.225*
SI02XY (warm)	170	0.233*
SI03UV (cryogenic)	120	0.080*
SI03XY (cryogenic)	120	0.081*
SI04UV (cryogenic)	120	0.070*
SI04XY (cryogenic)	120	0.071*

* averaged value due to day-night temperature cycles

The chosen settings after the scan and resulting leakage currents of the four stations are listed in Tab. 2.2. Whereas SI01, SI03 and SI04 show a quite comparable behavior for the depletion-voltage setting, SI02 requires are larger voltage. In addition, the difference between the warm and cryogenic version of the silicon modules is visible. The warm stations have a factor two increase leakage current compared to the cryogenic version. This may be caused by the age and the collected charge, causing defects in the doping of the wafer.

Temperature Readout

Due to the operation of the silicon detectors inside a cryostat, the temperature needs to be monitored and controlled. The temperature readout is based on PT100 sensors mounted on the holding structure of each wafer. During the test measurement, these probes were read out separately. For each of the larger ten-chip sides (U and X) one sensor is read out since the overall heat dissipation is expected to be larger[7]. The temperature reading is used as a soft-interlock to switch off the low-voltage of the APV25. In the cryogenic operation the temperature control is performed by a dedicated Programmable Logic Controller (PLC)-based cooling system (cf. Sec. 5.3).

[7] A heat dissipation by the APV25 chip of 2.32 mW per channel is expected [56].

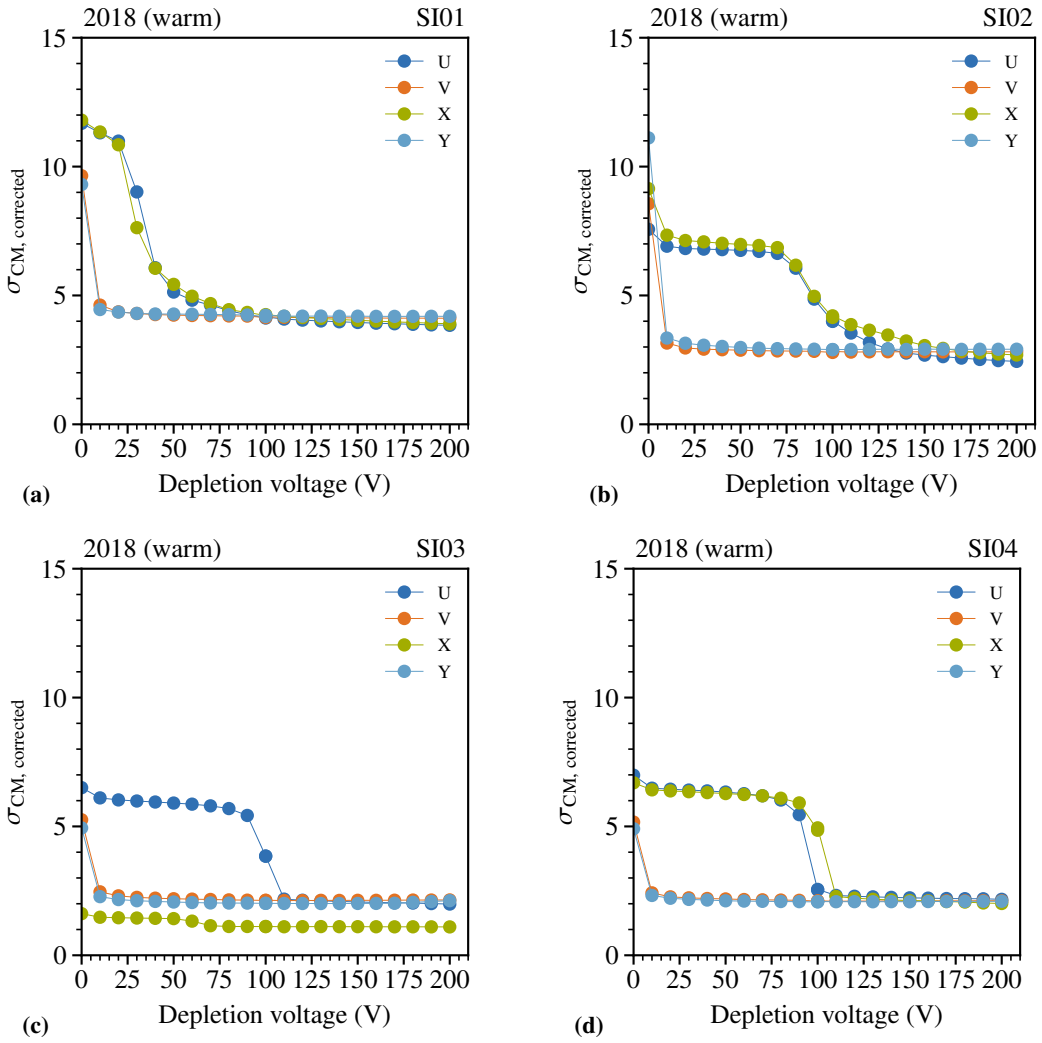

Figure 2.9: Results of the depletion-voltage scan for the different detectors modules operated in warm mode. The common-mode corrected noise is shown in dependence of the applied depletion voltage.

In Fig. 2.10(a) example results of the temperature readings of the silicon detectors are shown. During the data taking period where the detectors are active, the operation of the APV25 chip inside the cryostat causes the closed volume to heat up by about 30 K compared to the environment temperature. Since only gaseous nitrogen was flushed to the inside of the cryostat, no constant temperature of the modules could be achieved and an overall day-night fluctuation is visible. Only a minor correlation between the measured positive and negative current and the temperature fluctuation is noticeable as shown in Fig. 2.10(b). The main contribution is related to the data usage of the chip during data recording. Detailed analysis of the temperature and current correlations can be found in [63].

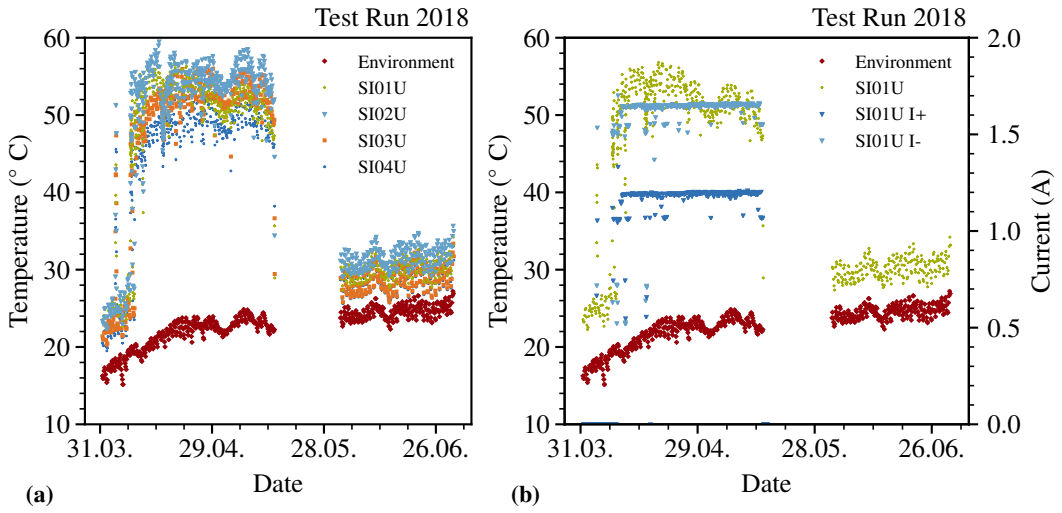

Figure 2.10: Temperature and current readings during the test run. In (a) the temperature reading of the U-planes together with the environment temperature are shown. The positive and negative current (green/blue) of the APV25 chip and the environment temperature (red) is shown in (b) for the SI01U as example.

Silicon Spatial Resolutions and Efficiencies

The silicon detectors are used as high-resolution tracking detectors during the test run. In [64] those detectors have been evaluated in detail. New calibrations for the correction of the charge-sharing between single strips (cf. Sec. 5.1) on each projection have been created, which result into an improvement of the spatial resolution. The later discussed run-by-run alignment (cf. Sec. 2.3.2) of the detectors benefits from this improvement and the obtained spatial resolution matches the expectations from the operation in previous years (cf. Chap. 5). The results of the obtained spatial resolution and detector efficiency are summarized in Fig. 2.11(a). The resolution is defined as the distance between the respective hit of the detector and the reconstructed track position at the position of the detector. The efficiency gives the ratio between this extrapolated track and the found hits in a 3σ-region around (cf. Sec. 3.3.3).

The obtained resolution is around 10 to 16 µm, which meets the expectations for the warm stations. Overall, an improvement of 5 to 22 % is achieved by applying the updated charge-sharing correction. The efficiency and its stability have been studied across three different runs from the beginning, the middle and the end of the data taking for the single detector planes. The results are shown in Fig. 2.11(b). The efficiency is around 98 % and is stable across the recorded runs apart from minor shifts for the SI01Y plane. The detector planes SI02U and SI03X showed problems during the data taking and are excluded in the overview. Since no time reference detector like scintillating fibers were present, the resulting track time is defined by the silicon hits themselves and therefore no meaningful time resolution can be extracted. Nevertheless, the so-called latency as the delay of the trigger with respect to the detector signal needed to be adjusted before (cf. Sec. 5.1).

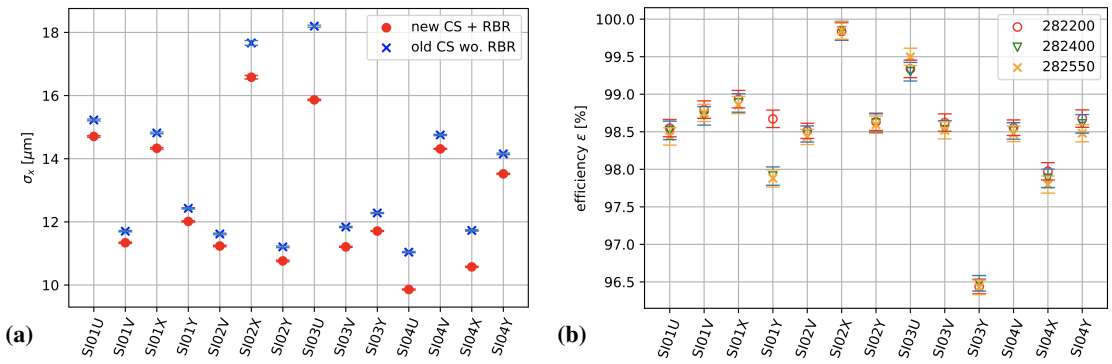

Figure 2.11: Silicon performance during the test run in 2018. In (a) the spatial resolutions for the single detector planes are shown with and without the new charge-sharing (CS) calibration and the applied run-by-run alignment (RBR). The efficiencies for three different runs along the data taking is shown in (b). SI02U and SI03X are excluded due to hardware issues. Figures taken from [64].

2.1.5 Detector Survey

The setup is located at the most downstream position of the COMPASS spectrometer in the test area. The incoming beam at this location is not following the zero-axis of the spectrometer, but is deflected due to the two spectrometer magnets upstream of the setup (cf. Fig. 1.6). The beam position is shifted about (239±2) mm towards the positive x-direction, 1.5 m downstream of the last spectrometer element (MF2). The inclination of the beam at this position is about 9.2 mrad in horizontal direction without offset in vertical direction [65]. This inclination was taken into account while positioning the detectors by introduction of a deflected beam axis as axis along the setup. For the later reconstruction, this dedicated coordinate system is used. Position measurements of the single detectors have been performed using a laser-based system. The measurement is done relative to the spectrometer coordinate system and requires a translation into the new coordinate system of the test setup.

The obtained results of the position measurement have a precision of ±0.5 mm and are listed in the respective survey report [55]. Based on these values, an initial value for the detector module position is extracted, serving as input for a later alignment of the setup based on straight beam tracks connecting all stations. Here, precision on the level of the detector resolution is obtained. To adapt for temperature-depended effects of the alignment, a so-called run-by-run alignment is applied, which is later described in Sec. 2.3.2.

2.2 Time Synchronization

The TPC DAQ utilizes the so-called Trigger Logic (TRLO) system [58]. It provides timestamps for the recorded events of the TPC. For the event time synchronization between the two dedicated TPC and tracking DAQ systems, as described in Sec. 2.1.1, the so-called heimtime or speaking clock feature of the TRLO system is used. Periodic synchronization signals containing the respective timestamp of the TPC DAQ system are broadcast, which can be recorded by external DAQ systems to obtain a common time reference. This allows to have the respective recorded events in a common time frame. This speaking time is recorded by the tracking DAQ system. To obtain a precise timing of this broadcast time, the synchronization signals of the TRLO signals are recorded by an iFTDC as is part of the tracking DAQ. It is read out with every trigger signal and the recorded synchronization timestamp is stored. The recorded signals are marked with the time in spill measured by this iFTDC as the time-reference system of the tracking DAQ. These two recorded timestamps, the time in spill of the tracking DAQ and the synchronization time stamps of the TPC DAQ, allow a time synchronization between both DAQ system. The event time of the tracking DAQ is a separate clock besides the time in spill measured by the iFTDC. The time synchronization is performed based on the iFTDC time. For the later analysis, this time reference system should be used to make use of the time synchronization. The scheme of the speaking time recording is shown in Fig. 2.12.

2.2.1 Speaking Time Format

The format of the TRLO speaking time is based on a protocol operating at 100 MHz. The protocol itself consists out of two parts — single pulses and a so-called time message. The single pulses are sent every 2^{19} clock cycles, which corresponds to 5.24288 ms. The timestamp itself is encoded in the 32-bit time message. It consists out of 32 pulses starting every 2^{26} ticks — or 128 pulses, or 0.671 s apart. With the start of the time message, two additional pulses are delivered with the encoded timestamp. Those additional pulses have a separation of either 0.16385 ms or 0.65536 ms corresponding to 0 or 1, respectively, and built up the timestamp. The encoded timestamp itself starts at local bit 24 of the time message takes into account the shift of 0.671 s between the single messages. The format of the time message is shown in Fig. B.1 with detailed information about the decoding discussed in App. B.4. [57]

2.2.2 Timestamp Extraction for Events

Each time message of the speaking time contains the timestamp t_{TPC} in the TPC DAQ system at the respective time system and is recorded with the timestamp of the iFTDC t_{TDC} in the tracking DAQ. The recorded signals are read out with every tracking DAQ trigger signal. Triggers are generated during each SPS cycle (cf. Sec. 1.2.1). Each SPS cycle starts 1 s before the 4.8 s long spill. Calibration and random triggers start 0.2 s after the start of cycle and are available only before and during the spill. Trigger generation is stopped 0.2 s before the end of spill to avoid issues during the end of the beam extraction. The iFTDC can store up to 1024 ticks with rising and falling edge of the recorded speaking time signals. The time resolution for the iFTDC is 64 ns per tick [66]. This allows up to 2 s of speaking time signals depending on the presence of time messages during this time, since its memory is read out and cleared with every trigger. With the last trigger received after about 5.6 s at the end of spill, the maximum time in spill covered is about 7.6 s in total, resulting in a maximum of 10 synchronization signals per SPS cycle. At the end of each cycle, a final trigger signal is sent and the recorded signals of the iFTDC are read out. Further details on the iFTDC decoding and timestamp processing are given in Sec. 3.4.

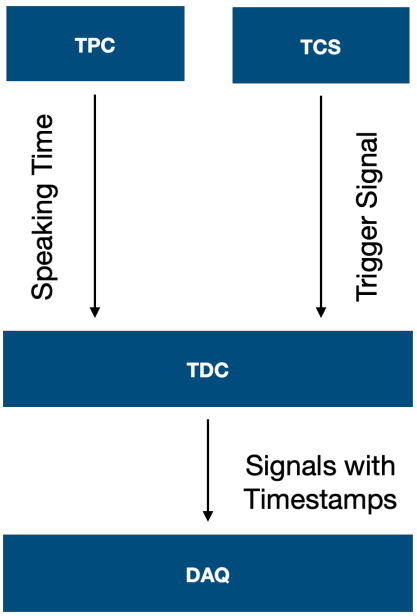

Figure 2.12: Speaking time recording layout with TDC.

The time messages are decoded for each run and spill. With the decoded time messages as the timestamp in the TPC DAQ system and the corresponding timestamp as time in spill from the iFTDC system of the tracking DAQ, a time synchronization between both systems can be performed. A linear regression is used to convert the t_{TDC} time into the t_{TPC} time and vice versa. An example for the linear regression is given as

$$b_0 = \bar{y} - b_1 \bar{x} \quad \text{with} \quad b_1 = \frac{\sum_{i=1}^{n} (x_i - \bar{x})(y_i - \bar{y})}{\sum_{i=1}^{n} (x_i - \bar{x})^2}, \tag{2.1}$$

with b_0 as the constant time offset in TRLO time for each spill and b_1 as the slope parameter resulting from the mean values $\bar{x}$ and $\bar{y}$ of the measured values x and y as time in spill and TRLO timestamp, respectively. An example for this time synchronization for one spill is shown in Fig. 2.13(a). The TRLO timestamp is obtained corresponding to the 100 MHz clock, which represents the slope of the linear regression.

2.2.3 Results in 2018

The results of the time synchronization are shown in Figs. 2.13 and 2.14. The time synchronization is available starting around run 281840. During the commissioning phase, first calibration triggers and additional off-spill triggers are used affecting the number of time synchronization signals. This phase is visible in Fig. 2.13(b) until run 281940. After this, the expected maximum of up to 10 synchronization ticks per spill are available.

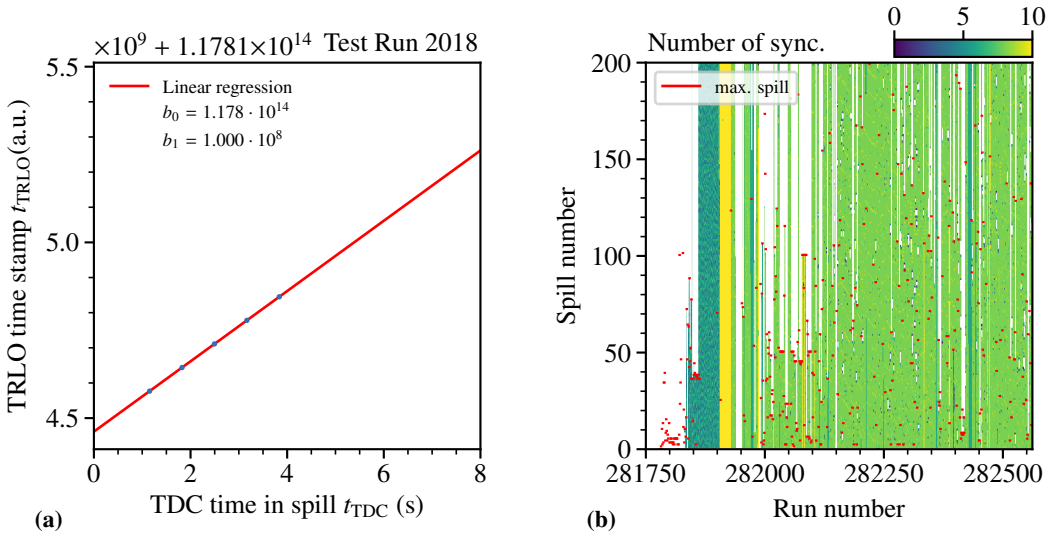

Figure 2.13: Time synchronization results during the test run. An example for the synchronization of the two DAQ systems based on a linear regression is shown in (a). An overview of the available time messages as synchronization for the recorded runs and spills during the data taking is shown in (b).

Overall fluctuations in the slope with respect to the nominal 100 MHz clock are shown in Fig. 2.14(a) together with the measured temperature in the area. About 0.1 kHz difference between day and night by the changing temperature can be observed and shows the expected precision of 10^{-6} of the clock frequency [57]. An overall shift with respect to the beginning of the data taking of about 1.3 kHz due to major temperature change is present. The difference between the TRLO and TCS event time as the second independent clock, which is not synchronized, is shown in Fig. 2.14(b). Since the TCS event time clock has a higher frequency of 125 MHz, the precision of 10 ns of the TRLO becomes visible and is uniformly distributed across the spill. Based on this, the recorded muon events from the tracking DAQ can be associated with the recorded proton events in the TPC in a later step, as discussed in Sec. 2.5.

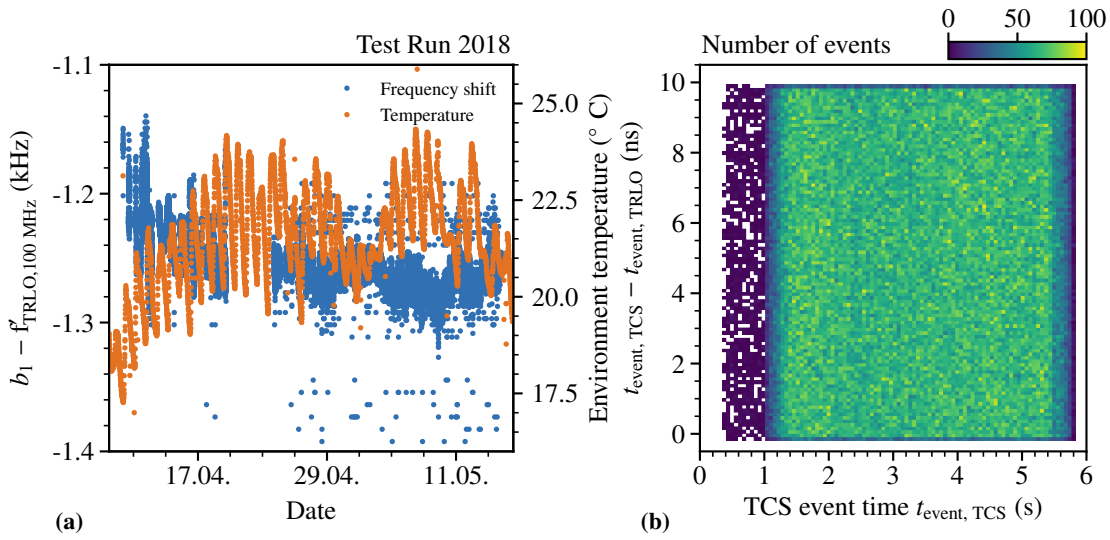

Figure 2.14: In (a) the stability of the TRLO clock operated at 100 MHz is shown. The difference between the event time provided by the TCS and the calculated one based on the TRLO depending on the TCS event time is shown in (b).

2.3 Data Reconstruction

Based on existing reconstruction software, COMPASS Reconstruction and Analysis (CORAL) used for the Compass experiment, the recorded raw data is processed and reconstructed. For the reconstruction a new coordinate system is introduced (cf. Sec. 2.1.5) and the test setup is divided into two reconstruction zones, a zone upstream of the target and a zone downstream of the target. This differs from the nominal usage of the reconstruction software for Compass with several zones due to the bending magnets in the spectrometers. Between each zone, so-called bridging of the tracks is performed to combine the tracks parts from the single zone. Here special adaptions to the reconstruction software were required in order to allow this two-zone reconstruction. The first zone corresponds to the beam track zone, whereas the second zone corresponds to the scatter track zone. This zone is starting at the TPC upstream volume in the origin along the z-axis as beam axis. Based on this definition, the respective positions for each component in the setup as listed in Tab. B.2 is obtained. The reconstructed tracks and hits obtained from CORAL can then be further analyzed. The results are stored in so-called mini-DSTs (mDSTs) files, a Rapid Object-Oriented Technology (ROOT)-based data format [67], containing information about hits, tracks and vertices and can be further processed. For example, a preselection of events can be performed by Physics Analysis Software Tools (PHAST), which can provide also a ROOT-based output. This output allows a further refined analysis with additional tools like Analysis Tool Kit (ANTOK). The single software tools are further described in the following.

During the test measurement, various runs for commissioning of the setup and tests with different settings of the TPC were recorded. Data at different TPC pressures of 4 bar and 8 bar and different thresholds are available. The TPC data taking with timestamp starts at run 281833 to

282562. An overview of the recorded runs can be found in [68]. Since the data has been recorded using the so-called standalone DAQ system of COMPASS, the runs are not linked to the normal COMPASS run logbook, but have been stored in a dedicated one located at the standalone DAQ system[8]. The recorded data has been stored on the CERN CTA. More information about the recorded data is given in App. B.3.

2.3.1 Analysis Tools

The recorded data is stored within the so-called Central Data Recording (CDR) system [69], which was first used within the COMPASS experiment and converts the raw data recorded by the DAQ into a readable data format for the reconstruction software, CORAL. This reconstruction software reads the stored data consisting of raw detector information and allows the reconstruction of the events in terms of hits, tracks and vertices. After this decoding of the detector information, so-called digits, single hits are extracted, which are then further used for the track finding, vertexing and final track and vertex fitting. The reconstructed events can then be analyzed in the next steps. The following analysis tools have been used for the event reconstruction, selection and analysis and are further described in detail in the following.

CORAL

CORAL is the main reconstruction software used for the COMPASS data and the basis for the future AMBER event reconstruction (cf. Sec. 1.2). It uses the geometry information of the setup like detector positions and material distributions for the reconstruction. The recorded events are decoded with the help of the so-called DAQ decoding library and single detector digits are extracted on an event-by-event basis. Based on this raw detector digits, so-called clusters as merged single channel information, are formed into hits in each detector. Those hits provide spatial and time information. They are used to first find possible track candidates along the setup and possible vertices. Final track candidates and vertices are used for the concluding track and vertex fitting. Propagation of those tracks through the magnetic fields of the two spectrometer magnets (SM1 and SM2), provide momentum information. In addition, the data collected by the calorimetry detectors (ECAL, Hadronic Calorimeter (HCAL))) provide information about deposited energy of particle like photons, electron, or hadrons. Multiple scattering effects due to material along the trajectories influencing the track reconstruction are taken into account via so-called material maps. Those material maps are provided via Geometry Description Markup Language (GDML) or ROOT geometries, which can be generated via the later discussed GEANT4-based simulation toolkit TGEANT[9].

[8] The used stand-alone system has been reinstalled in the mean time and the data of the logbook was unfortunately not saved. The only documentation is available in the respective COMPASS wiki [68].

[9] The underling geometry description is based on a ROOT geometry obtained by exporting the GEANT4 geometry of the simulation as GDML format and transformed into a ROOT geometry. Not all GEANT4 geometry features are available as GDML or ROOT geometry. Developments are ongoing in order to better describe the material in the setup by using directly the GEANT4 geometry within the reconstruction. As an example, CAD imported geometries like tessellated solids or triangular surface elements are not supported by ROOT (V6.2X). Currently, a persisting issue with the increased run time of selection properties along the GEANT4 geometry limits the application.

The resulting reconstructed track, vertex or single detector data, like digits and hits, is stored in so-called Data Summary Trees (DSTs). Depending on the additional information stored in this data format, the output format can be equipped with a prefix like "mini" or "mega". The latter for instanced included detector raw information for possible detector calibration or similar studies. CORAL works closely together with the PHAST toolkit to provide the ROOT-based C++ objects for, e.g., tracks and vertices in the output format as discussed in the following.

PHAST

The PHAST tool was first developed for the COMPASS experiment and used for the data analysis of the reconstructed events [70]. It will be further utilized within the AMBER collaboration for data analysis. This tool processes the so-called DST output from the reconstruction tool CORAL and uses the ROOT framework to provide access to, e.g., track and vertex objects for further analysis. Besides the general interface to the reconstructed data, additional functions useful for the analysis as track extrapolation are available. In addition, it has access to the material map stored either as GDML or ROOT geometry. Those material maps are used to generate an event display and visualization of the detector geometry. With the PHAST toolkit, a detailed event selection of the reconstructed events can be performed, providing input for further, more detailed studies. The output can also be stored in the ROOT format.

ANTOK

With the ANTOK [71] as toolkit for event-by-event basis analysis on ROOT-tree basis detailed selection of data can be performed. Initially developed for COMPASS event selection, it is continually enhanced. Preselected data available in ROOT trees as input is used to further apply selection criteria and the respective histograms with those different criteria applied can be produced to study the influence. An overview of all selection criteria, a so-called waterfall plot, is produced, which illustrates the single steps of the event selection. The output is ROOT-based and either provides the resulting histograms or selected events as an output tree for further studies.

2.3.2 Run-by-Run Alignment

Prior to the data reconstruction, an alignment of the single detectors is performed based on the initial survey results (cf. Sec. 2.1.5). For this straight tracks are reconstructed passing through the complete test setup configured as one zone. These straight lines are used to shift the single detector positions in the correct location. During the COMPASS data taking, normally dedicated alignment runs are recorded on a prior to each data taking period with dedicated magnet configuration and low intensity beam to avoid pile-up hits. This is sufficient since the setup is not expected to have large shift due to temperature fluctuations with respect to the overall detector resolution. For the test setup, only high-resolution silicon detectors are used. In this case, the expected shifts are in the same order as the detector resolution of $O(\mu\text{m})$.

For the initial alignment the survey data serves as input and the U-V-planes of the detectors are rotated such that the width of the distance between the hits in the respective projection and the two-dimensional space-point from the X-Y-plane is minimal. This is performed for each station individually. All stations are put into one reconstruction zone to reconstruct straight tracks through all sixteen silicon planes. Pivot points have to be defined as reference point. For this the x-y-position and angles as well as the x-y-position of SI01XY and SI02XY have been fixed. All z-position of the planes are fixed together with their wire pitch. The alignment itself is based on a iterative process. First iterations with factor 100 increased resolution are performed followed by iterations with only an increase by a factor 10. To finalize the alignment, the real resolution of the detectors are used. This provides in the end an initial alignment for all detectors, which then can serve as starting point for a run-by-run alignment to take even slight shifts between the single runs into account. This allows also to study the effect of temperature variations along the setup and the influence on the detector positions. [72]. The resulting detector positions for the initial alignment are given in App. B.2.

The run-by-run alignment is performed prior to the reconstruction of the full data set and uses the prior described alignment method. This run-by-run alignment is performed in the scope of [73], where further details are given. The detector position is determined and correct for every single run. In Fig. 2.15 the temperature dependence of the SI01U and SI04U plane positions during a part of the test run is shown.

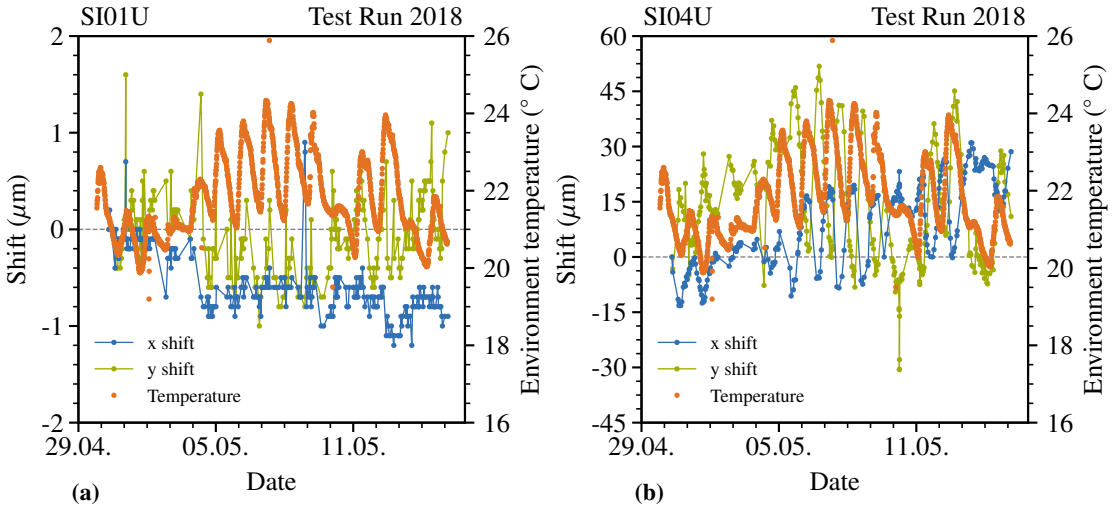

Figure 2.15: Run-by-run alignment shift results for the silicon plane SI01U and SI04U with environment temperature. In (a) the results for the upstream SI01U plane and in (b) the results for the downstream SI04U plane are shown.

The upstream station SI01 and SI02 are located in dedicated aluminum cryostats, which are positioned on an optical bench with marble rails visible on the left side in Fig. 2.1. Although the idea behind the marble and optical bench support structure is to minimize the temperature influence, a clear temperature dependence can be observed. Shifts for SI01U as shown in

Fig. 2.15(a) of about 1 µm on a day-night cycle can be observed along the y-direction and smaller ones along the x-direction, which is within the detector resolution. The partner plane (SI01XY) in the same cryostat is used as a pivot plane, but still a shift is present, which indicates that this shift is between the two detector modules.

The temperature influence is much stronger in the downstream SI04U plane. Shifts in the x- and y-direction of up to 10 µm in a day-night cycle can be observed, which is in the same order of magnitude as the spatial resolution of the detector. This is most likely related to the used support structure, which is not optimized in terms of temperature dependence. Here, a simple aluminum support is used, which was produced especially for this beam test.

The alignment is only performed with the silicon detectors. The absolute position of the TPC is not possible to align with this method. Based on the later correlated data, the rotation of the readout plane structure was performed to extract the φ-angle with respect to the tracking data. [73]

2.4 Event Selection

In the data taking of the test measurement, about $3.9 \cdot 10^6$ events have been recorded in the TPC and about $7.2 \cdot 10^9$ events have been recorded with the muon tracking. The integrated number of reconstructed events per run for the tracking and TPC data is shown in Fig. 2.16. The recorded data contains different studies resulting in various slopes along the data taking since the respective trigger rate was not constant. The recorded TPC data has been analyzed by [37] and in the following the tracking data event selection is discussed.

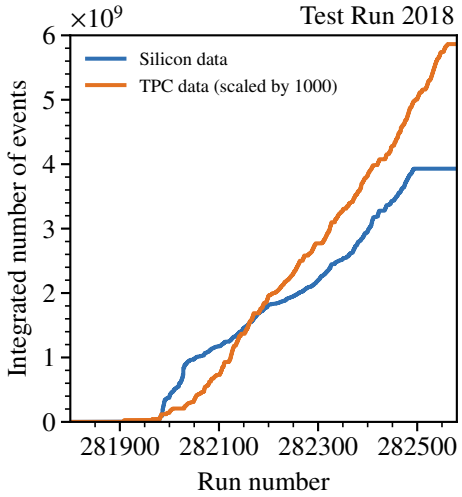

Figure 2.16: Integrated number of reconstructed events per run during the test run for the TPC and the silicon trackers. The number of events recorded by the TPC is scaled by a factor 1000.

After the reconstruction of the data using the discussed run-by-run alignment, the data is preselected to obtain an event sample for the elastic muon-proton scattering. Based on this preselected data, a more detailed selection is performed. The data contains roughly 75 % 8 bar runs and 25 % 4 bar runs. These different pressure settings of the TPC are not distinguished and treated identically at this stage. Furthermore, the TPC recorded at different thresholds between 200 and 300 keV, which were used only in TPC related studies and are not further investigated in this work.

The goal of this event selection for the test run is to obtain correlations between the muon and recoil proton tracks to study the response of the TPC. Therefore, a clean data sample of scattering events from the muon side is selected, which can then be correlated based on the recorded timestamps with the proton data set. The different steps and results are discussed in the following.

Event Preselection

Starting with $5.9 \cdot 10^9$ reconstructed events of from the tracking, a preselection of the data set is performed to reduce its size for easier handling. The preselection contains general criteria for the required event topology. For the later usage of event matching between the two dedicated DAQ systems (cf. Sec. 2.1.1) a valid time in spill and the resulting common TRLO timestamp (cf. Sec. 2.2). Each event should have a so-called primary vertex, as the single interaction point with one outgoing track to select single elastic scattering events. An overview of the applied selection criteria and their effect on the number of events and corresponding fraction is shown in Fig. 2.17. This preselection reduces the initial size by a factor of five, resulting in about $1.4 \cdot 10^9$ events.

2.4.1 Detailed Event Selection

After the preselection of the data set, a more thorough selection of events is performed. To avoid multiple scattering effects due to tracks passing through the material of the TPC, requirements on the tracks are needed. Beam and scatter tracks need to pass through the beam windows on the up- and downstream side and the beam hole in the cathode (cf. Sec. 2.1.3) of the TPC. The vertex position needs to be inside the active volume of the TPC between the anode and cathode. The scattering angle of the scattered muon affects the vertex z-resolution, and it has to be large enough to ensure a sufficient resolution of the vertex z-position.

Selection of Beam and Scatter Tracks

To minimize the effect of material along the reconstructed tracks and to improve the overall track quality by reducing multiple scattering in material, the single tracks are required to pass through the beam windows of the TPC. In addition, in the future a strict confinement of the volume between the two beam windows is required resulting in a fixed volume, which can later be used for a determination of the luminosity based on the fixed volume. As shown in Fig. 2.7, the TPC has an up- and downstream beam window with a diameter of 70 mm and 40 mm respectively. The reconstructed tracks are extrapolated to the positions of the beam windows. Those events

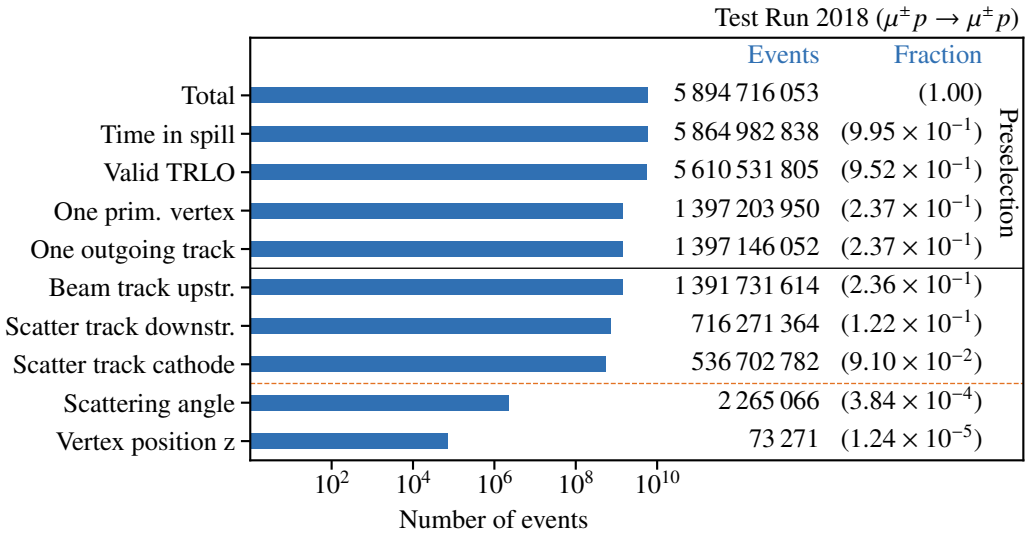

Figure 2.17: Event selection overview for the test measurement. The applied selection criteria and their resulting number of events as well as the faction is shown. After the indicated preselection a more detailed event selection is performed. The orange dashed line indicates selection part later refined for the muon-proton correlation.

with the tracks located inside the respective window position are selected. Furthermore, the inner structure of the TPC, as shown in Fig. 2.8(b), needs to be taken into account. The cathode has a dedicated beam hole in the center, which shows a slight displacement with respect to the up- and downstream windows. Therefore, those three positions need to be treated individually. The result is an overlap of three circular-shaped selections, as shown in Fig. 2.18(a).

Table 2.3: Selection criteria for beam and scatter tracks at the beam windows and cathode position. For the beam and scatter tracks a radial or elliptic selection around the given center is applied at the respective position.

Position	Track	x_{center} (mm)	y_{center} (mm)	r_1 (mm)	r_2 (mm)
Upstream window	Beam	0.30	0.0	35.0	35.0
Cathode	Scatter	3.10	−3.3	18.0	16.5
Downstream window	Scatter	2.17	0.0	20.0	20.0

For the upstream beam window, only the beam tracks should pass the circular region. The downstream window need to be passed by the scatter tracks only. In addition, the scatter tracks need to pass the cathode window. In Fig. 2.18 the x-y-position of the extrapolated tracks at the up- and downstream beam windows and the cathode for the beam and scatter tracks are shown. The overall rectangular shape is due to the active area of the silicon detectors (cf. Sec. 2.1.4).

The applied radial selection around the respective center of the windows are indicated with the values listed in Tab. 2.3. In Fig. 2.18(a) the scatter track position at the downstream window is shown. The different sizes of the windows are indicated. The walls of the TPC are clearly visible as well as internal structures like screws and nuts and cables of the anode structure. Whereas the heavier support structures are outside of the acceptance, the cables are located close the sensitive volume. Material contributions in the acceptance as present here should be avoided in the final design of the TPC. The single effects of the selection criteria are shown in Figs. 2.18(b) and 2.18(d), each with all criteria applied, except the indicated one to visualize their effect.

The coordinate system was chosen on the basis of the survey data in the way that the position of up- and downstream flanges define the z-axis. Therefore, one would expect that the central points of the beam windows are at the x-y-origin, but it can be seen that a slight shift along the horizontal axis with respect to the initial chosen coordinate system is present. This probably is caused due to external shifts of the TPC structure between survey and data taking and has no further impact on the data. Further details on the detector position are given in App. B.2.

Selection of Scattering Angle and Vertex z-Position

The angle between the incoming beam and the outgoing scatter track is defined as the scattering angle θ. In Fig. 2.19(a) the vertex z-position depending on the scattering angle is shown. The single structures of the setup are visible and indicated in the vertex z-distribution shown in Fig. 2.19(b). Here, a scattering angle of $\theta > 1$ mrad is chosen to obtain a sufficient vertex z-resolution (cf. Sec. 1.2.5) to visualize also the thin structures like the anode or cathode plane. In addition, no selection on the tracks passing through the cathode beam hole is applied for visualization of it. The active area of the TPC between anode and cathode is indicated.

The vertex z-resolution depends on the scattering angle and can be determined by evaluating the width of a thin structure with a neglectable thickness like the cathode structure. The result is shown in Fig. 2.20(a) and reassembles the expected $1/\theta$-behavior as further discussed in [47]. The used parametrization is given as

$$\sigma_z(\theta) = \frac{p_0}{\theta} + p_1. \tag{2.2}$$

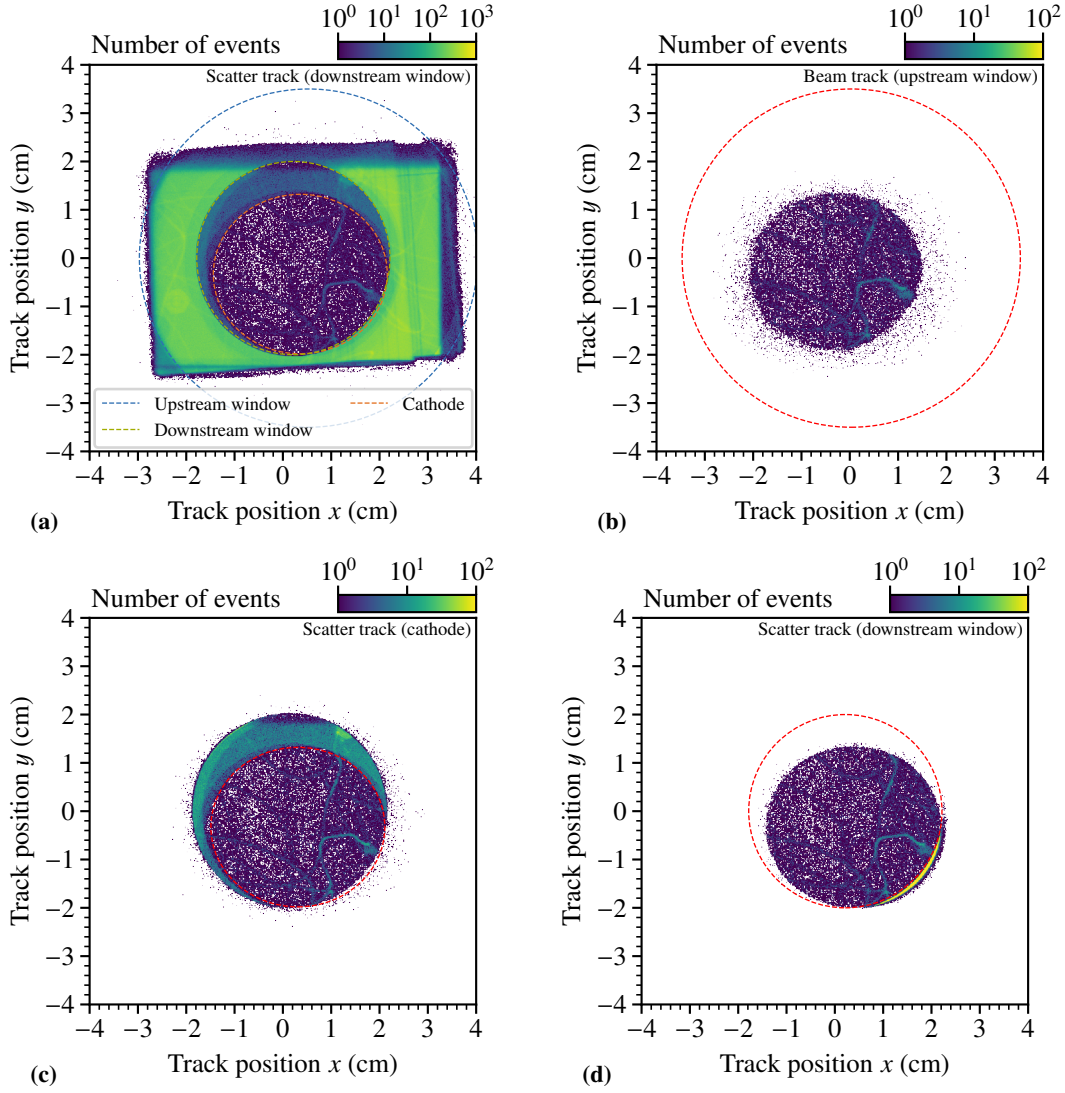

Figure 2.18: Beam and scatter track x-y-position at the up- and downstream beam window positions and the cathode of the TPC. In (a) an overview of the TPC window structures are given. In (b) the criteria on the upstream beam window position is indicated for the x-y-position of the extrapolated beam track position at this location. In (c) and (d) the cathode and downstream window selection for the scatter tracks are shown with all selection criteria except their indicated one applied.

With the Monte Carlo simulation of the test setup, a comparison of the obtained results can be performed. Those values show a good agreement with the extracted real data results. For larger scattering angles the reconstructed Monte Carlo data seems to be overestimated compared to the real data. For the vertex position inside the active volume of the TPC, events with a scattering angle of 0.2 mrad are selected. This results in about $\sigma_z = 20$ cm z-resolution. At the beam momentum of 190 GeV this corresponds approximately to $Q^2 = 1.4 \cdot 10^{-3}$ GeV$^2/c^2$. The TPC

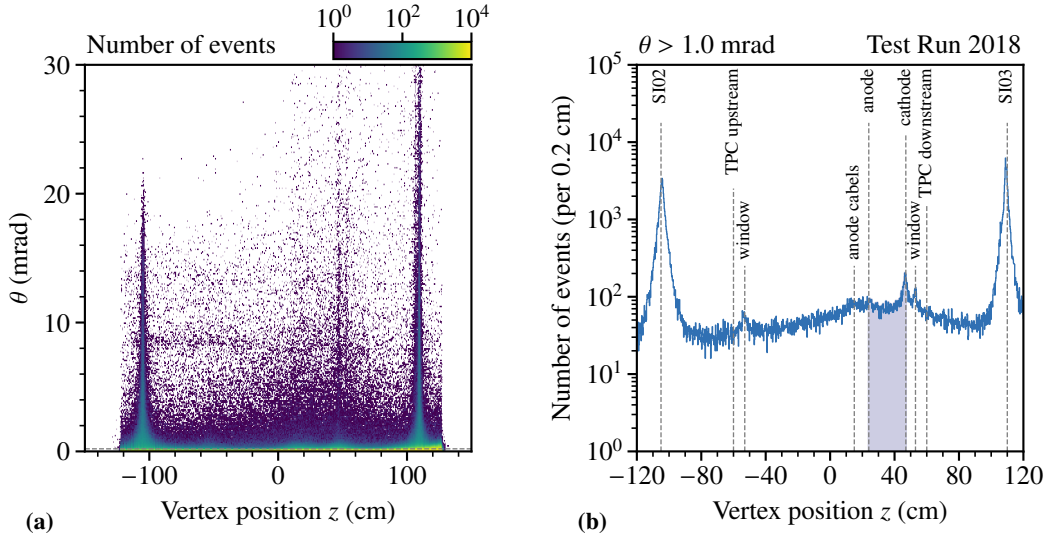

Figure 2.19: The scattering angle dependence on the vertex z-position is shown in (a). In (b) the vertex z-position is shown for scattering angles θ>1 mrad. No selection of the cathode beam hole as well as the vertex z-positions are applied to visualize the different structures. In blue the active area of the TPC is indicated.

threshold was set to about 200 to 300 keV resulting in a factor three smaller minimal Q^2 for events recorded by the TPC of about $5 \cdot 10^{-4}$ GeV$^2/c^2$. To match the kinematic range, a muon scattering angle of about 100 µrad would be required to have matching lower kinematic thresholds. This would result in a too large vertex z-resolution, larger contribution of events affected by multiple scattering and therefore would not allow a clean selecting events in the active area of the TPC. The selection of the vertex z-position and the scattering angle is adapted later for the timestamp matching between the TPC and tracking data as indicated in Fig. 2.17.

To select scattering events originating from the active area of the TPC, a selection of vertices originating from the area between anode and cathode is applied. This selection relies on the prior selection of the scattering angle. The vertex z-distribution after all selection criteria except the z-position is shown in Fig. 2.21(a). An additional contribution due to the anode structure and the cables become visible as shown in the vertex x-y-position given in Fig. 2.21(b). Furthermore, due to artifacts of the vertexing, the surrounding silicon detectors become visible at around $z = \pm 120$ cm. Based on this event selection, a data set is extracted with clean elastic scattering events, which serve as input for the matching of proton and muon events, which then results, using the correlations of both, in a cleaner data sample at a later stage.

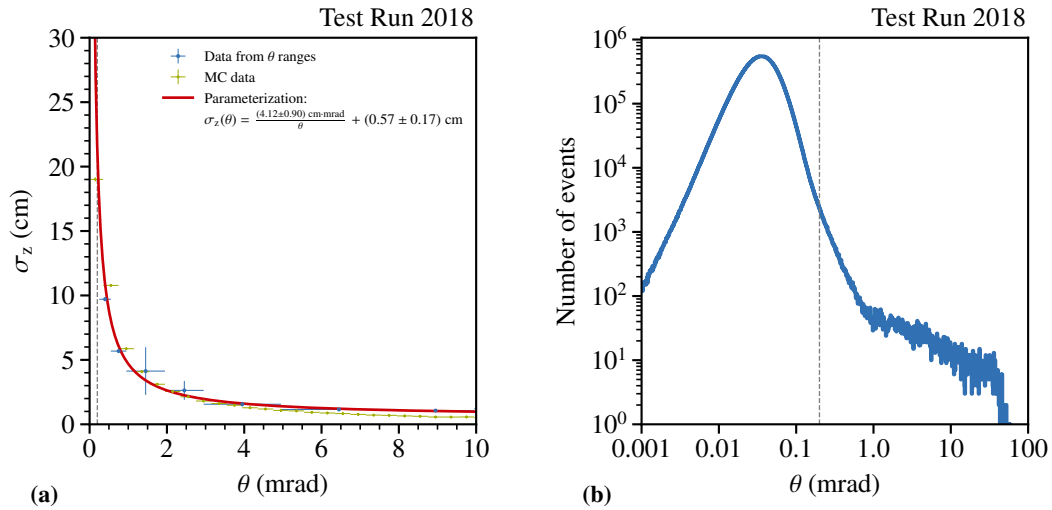

Figure 2.20: In (a) the vertex z-resolution dependence on the scattering angle is shown. A parametrization is obtained by a Gaussian fit to the vertex z-resolution in different θ-bins. The error bars along the x-axis correspond to the width of the respective θ-range and the uncertainty on the width of the extracted resolution. Results from the Monte Carlo simulation of the test setup are added as comparison. The applied selection at $\theta > 0.2$ mrad is marked in the scattering angle distribution shown in (b).

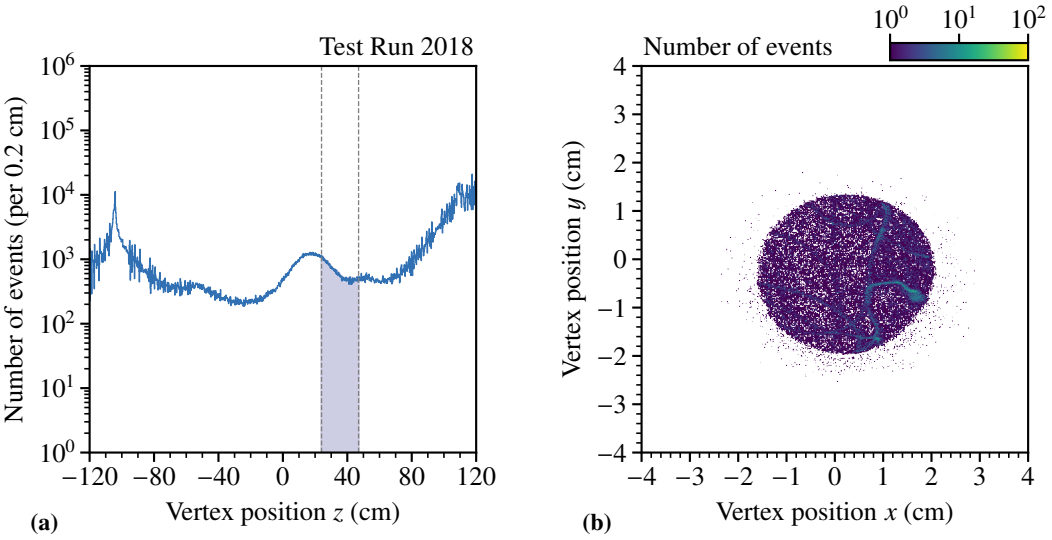

Figure 2.21: Primary vertex position of the vertex z-position in (a) with the selection criteria shown as well as the region accepted due to the vertex position z-resolution. In (b) the x-y-position of the vertex is shown.

2.4.2 Estimation of Elastic Muon-Proton Scattering Events

Based to the integrated cross-section $\sigma_{\mathrm{D}}^{\mu p \to \mu p}$ in the dipole approximation given in Eq. (1.33) the number of expected recoil proton events N_{protons} can be estimated via

$$N_{\mathrm{protons}} = \sigma_{\mathrm{D}}^{\mu p \to \mu p} \cdot \int \mathcal{L} \, \mathrm{d}t, \tag{2.3}$$

with $\mathcal{L}$ as the luminosity. The minimum selected muon scattering angle of $\theta = 0.2$ mrad at the estimated beam momentum of 190 GeV results into $Q^2 = 1.4 \cdot 10^{-3}$ GeV^2 as lower limit for the cross-section. For an upper limit, an rough estimate of a maximal scattering angle of 100 mrad ($Q^2 = 361$ GeV$^2/c^2$) is used (cf. Fig. 2.19(b)). Due to the steep fall of the cross-section with increasing Q^2 the contribution for larger Q^2 is small. In the given Q^2-range, the integrated cross-section results to

$$\sigma_{\mathrm{D}}^{\mu p \to \mu p} = \int_{0.014\,\mathrm{GeV}^2/c^2}^{361\,\mathrm{GeV}^2/c^2} \frac{d\sigma_{\mathrm{D}}^{\mu p \to \mu p}}{dQ^2} dQ^2 = 0.181 \text{ mb}. \tag{2.4}$$

Based on the number of target protons $n_{\text{target, NTP}}$ at NTP (cf. Sec. 1.2.9) at $P = 8$ bar pressure of the TPC, the target proton density is given by

$$n_{\text{target, 8 bar}} = \frac{P}{1.013 \text{ bar}} \cdot n_{\text{target, NTP}} \tag{2.5}$$

$$= \frac{8 \text{ bar}}{1.013 \text{ bar}} \cdot 5.018 \cdot 10^{25} \mathrm{m}^{-3} = 3.964 \cdot 10^{26} \text{ m}^{-3}, \quad \text{and} \tag{2.6}$$

$$n_{\text{target, 4 bar}} = \frac{4 \text{ bar}}{1.013 \text{ bar}} \cdot 5.018 \cdot 10^{25} \mathrm{m}^{-3} = 1.982 \cdot 10^{26} \text{ m}^{-3}. \tag{2.7}$$

Here, due to the 4 bar setting, the density is reduced by a factor of two. The integrated cross-section is based on the recorded number of events. Only muon events N_μ accepted by all geometrical selection criteria are used[10], namely, all criteria except the scattering angle and vertex position as shown in Fig. 2.17 (orange dashed line). Together with the target particle density n_{target} and the length of the target l_{target}, the integrated luminosity is given by

[10] In this case already the requirement of a reconstructed vertex is included, which might introduce a bias on selecting scattering events. Due to the broad distribution of the reconstructed scattering angles, especially for small values, it is assumed that the contribution of this requirement is small.

$$\int \mathcal{L}\ \mathrm{dt} = N_\mu \cdot n_{\text{target}} \cdot l_{\text{target}} \tag{2.8}$$

$$= 5.4 \cdot 10^8 \cdot 3.964 \cdot 10^{26}\ \mathrm{m}^{-3} \cdot 0.23\ \mathrm{m} \tag{2.9}$$

$$= 4.92 \cdot 10^{34}\ \mathrm{m}^{-2} \tag{2.10}$$

$$= 4.92 \cdot 10^3\ \mathrm{mb}^{-1}. \tag{2.11}$$

The expected number of recoil proton events results to

$$N_{\text{protons}} = \sigma_{\mathrm{D}}^{\mu p \to \mu p} \cdot \int \mathcal{L}\ \mathrm{d}t \tag{2.12}$$

$$= 0.181\ \mathrm{mb} \cdot 4.92 \cdot 10^3\ \mathrm{mb}^{-1} \tag{2.13}$$

$$= 890. \tag{2.14}$$

About 890 recoil proton events are expected. This estimate is still an overestimate, since it does not include detector efficiency and acceptance. It can be further refined by taking into account the rough estimate on the different pressure settings for the TPC. About 75 % of the data was recorded at 8 bar and the remaining 25 % with 4 bar. Taking into account the different pressure settings by re-weighting the initial value with the corresponding cross-section, about 780 events are estimated as a lower limit.

2.5 Muon-Proton Matching

One of the main goals of the test run is to extract correlated muon-proton pairs. A so-called matching between protons and muon candidates is performed using the time synchronization between TPC and muon tracking events (cf. Sec. 2.2). As starting point, a selected, less strict muon sample is used based on the presented event selection in Sec. 2.4. It includes only the requirement of events with a reconstructed vertex and the beam and scatter track passing through the beam windows of the TPC. There is no limitation on the minimum scattering angle and z-vertex position applied, as indicated in Fig. 2.17 (orange line). For each proton and muon event, the time difference in the TRLO time frame is calculated. Correlated events should occur within a certain time difference, which should correspond to the drift time of the TPC of about 64 µs. Possible muon candidates within the proton time-window are selected. A correlation between the time difference of the events can be verified by the kinematic relation between the vertex z-position in the TPC and the time difference as drift time of the TPC. In addition, a relation between the muon scattering angle and the measured recoil proton energy should be visible using the time correlation.

The muon-proton event matching uses the TRLO timestamp of the measured proton and the event time of the muon. The latter is translated into the TRLO time system and proton events are searched within the expected drift time window $t_{\mathrm{TPC}} = 64$ µs of the TPC. A slightly larger time window of $T_{\mathrm{win}} = 3 \cdot t_{\mathrm{TPC}} = 192$ µs is used (cf. Sec. 2.1.3). Within each time window, muon events are associated with the proton. This results in an initial mapping of muons to protons for later evaluation and is a first step to combine the two distinct data sets. The mapping is based on the TPC event number, which is unique within one run. For the muons, a unique identification would require run and spill number.

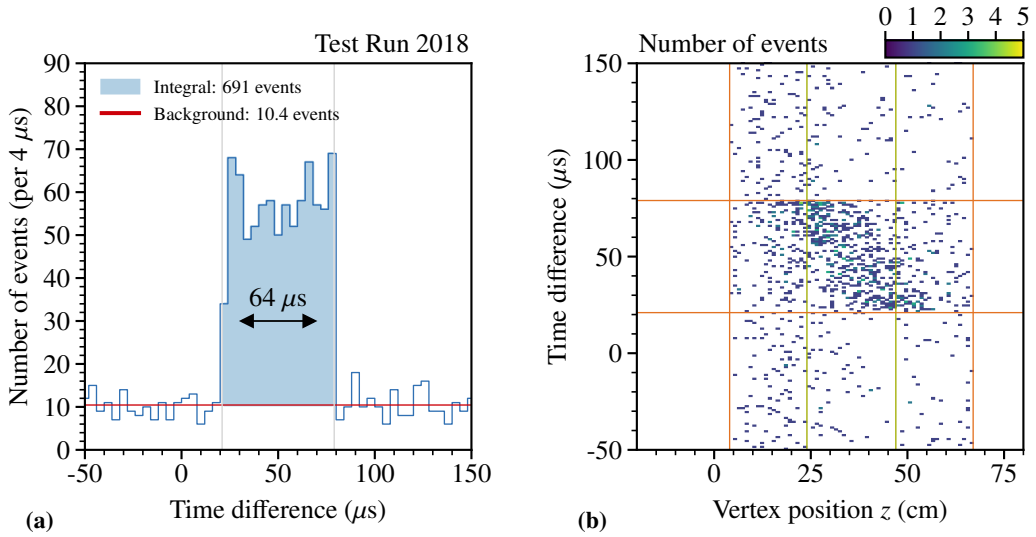

Figure 2.22: TRLO time difference between proton events and possible muon candidates. In (a) the time difference is shown. Correlated events are visible in the TPC drift-time window of 64 µs. In (b) the correlation with the muon vertex z-position is shown. The anode and cathode structure are indicates (green). In the initial vertex z-position selection is indicated together with the drift-time window (orange).

In Fig. 2.22(a) the time difference $\Delta t = t_{\mathrm{tracking}} - t_{\mathrm{TPC}}$ between the muon and TPC event in the TRLO time is shown. The initial selection of the scattering angle of 0.2 mrad as discussed in Sec. 2.4.1 is applied. Studies showed, that this value results in the cleanest selection. Furthermore, the vertex z-position of the correlated events as shown in Fig. 2.22(b) is used to further clean the spectrum. The drift time window and the more coarse selection of the vertex z-position are indicated. The correlation of the drift time with the vertex z-position is used to further select correlated events. The correlation shows about 700 events in the expected time window taking into account the subtracted background. It reassembles the expected drift time of 64 µs with its rectangular shape. The number of events is about 88 % of the expected lower limit of 780 events as discussed in Sec. 2.4.2. The missing fraction of 12 % could be due to reconstruction or detector efficiency, which was not taken into account in the calculation, but further studies are ongoing.

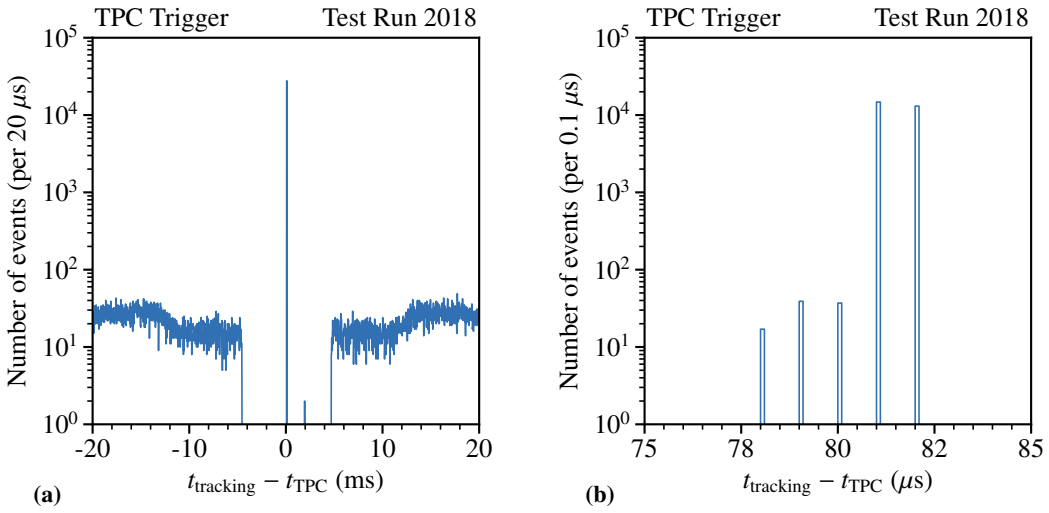

Figure 2.23: Time difference of the recorded TPC trigger events. In (a) the full time-window is shown with the coincident peak with surrounding trigger dead-time. The single discrete timing are shown in (b).

The offset of the time correlation towards zero has multiple reason. To investigate the offset of the correlated timing peak, only events triggered by the recorded TPC trigger are evaluated (cf. Sec. 2.1.1). Their time difference will give an indication of the pure technical delay between the two timestamps. In Fig. 2.23 the time difference of the TPC-trigger-based events are shown. Besides the combinatorial background, the time difference is mainly within a small time-window close to zero. It is surrounded by a window of about 4 ms where no other triggers are accepted. A closer look of the main peak results in time difference of those triggered events of about +81 µs. This indicates the overall shift between the tracking time and the TPC and the origin, why raw time difference has a positive value. With the difference calculated via $\Delta t = t_{\mu} - t_{\text{TPC}}$, one would expect a negative time difference taking into account that the TPC event should happen at the same time or later (larger timestamp) compared to the tracking time. As origin multiple factor are under investigation.

The trigger delay of the TPC readout buffer as event storage uses a safety delay for the incoming data, which could contribute to a shift between the trigger times. The data in the ADC is read backwards with a hardware discriminator issuing a trigger signal based on the incoming data. With this self-triggering of the TPC (cf. Sec. 2.1.2), the readout is initialized, and the corresponding timestamp is created and can cause an additional delay [37]. In addition, the used event time is issues by a third clock and is independent of the iFTDC time calibration. A constant time shift could be expected together with a drift between the two clocks, although it is not visible in the time difference between the event time, as shown in Fig. 2.14(b). In the future the event time is foreseen to originate from the synchronized iFTDC clock and the TRLO clock only. The delay does not affect the overall selection of correlated events, but defines the position in time, where those events are located. With introducing a third unsynchronized clock, a possible time shift within the spill could occur, but has not been observed in the test run.

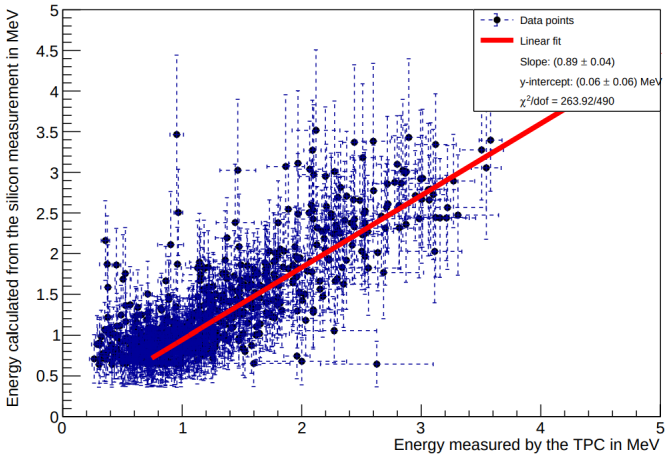

Figure 2.24: Correlation between the calculated proton energy based on the muon kinematics and the reconstructed proton energy. The linear correlation is indicated. Figures taken from [73].

Based on a preliminary energy calibration and a simple proton track reconstruction, an energy correlation is extracted and evaluated in [73]. Proton tracks are built based on pad energies, which are summed up to a total deposited energy for single events. The estimated[11] muon energy shows a clear correlation with the extracted recoil proton energy obtained from the TPC.

2.6 Muon-Candidate Likelihood-Association

A solution for the association between muon and protons using the kinematic relation has been studied. With simulated protons based a given muon as input, a probability for the energy deposition in each pad of the TPC readout plane can be extracted. Comparing these probability distributions with the measured energy deposition in each pad of a real data proton event results in a likelihood for each proton and allows estimating the most probable muon-proton pair. A dedicated Geometry And Tracking 4 (GEANT4) simulation of the TPC pad geometry is created. For each reconstructed muon multiple proton candidates are simulated taking into account the resolutions for the muon reconstruction to obtain the probability distributions for each pad. Simulation-based studies of this approach have already performed in [47] and show promising results in the first simple cases.

To apply the resolutions of the muon reconstruction for the simulation of proton candidates, they have been parameterized. Based on the simulation of the test setup, the required resolutions influencing the scattering kinematics have been extracted as a function of Q^2. In the following, these resolutions are discussed in more detail.

[11] Momentum measurement is not available in the test measurement. A fixed beam momentum of 190 GeV is assumed.

Resolution Parametrization

For the simulation of proton candidates for a reconstructed muon, the respective resolutions for the muon need to be taken into account. For this, the simulation of the test setup is used to extract those. The relative resolutions of Q^2 as well as the resolutions depending on Q^2 of the vertex x- and y-position and the azimuthal angle φ are required. They influence the distribution of the resulting simulated protons. No momentum measurement of the muon was performed during the test measurement and therefore a fixed beam momentum of 190 GeV is used for the muon kinematic and the calculation of the reconstructed Q^2. For simplicity reasons, no dedicated beam profile is used at this stage, which would include the beam divergence, positions and momenta of beam particles and also cover more surface of the setup taking into account the acceptance. Therefore, only straight central tracks are simulated.

The full detector geometry of the test setup is implemented in GEANT4 (cf. Fig. 2.2). Four silicon stations as well as the respective trigger elements have been included. The shift between the upstream-, cathode- and downstream windows of the TPC is not implemented in detail at this stage (cf. Sec. 2.4.1). Nevertheless, a similar event selection as for the real data of the elastic muon-proton-scattering as described in Sec. 2.4 is applied. For the simulation the Total Geometry And Tracking (TGEANT) toolkit is used (cf. Sec. 2.3.1). Elastic muon-proton-scattering events are generated in the Q^2 range of $10^{-5} \leq Q^2/(\mathrm{GeV}^2/c^2) \leq 10^{-1}$. The simulated data event reconstruction and selection is performed identically to real data (cf. Sec. 2.4).

The kinetic energy of the recoil proton and therefore the range inside the TPC is dictated by the respective Q^2 of the scattering process. The resolution in Q^2 affects the distance covered by possible proton candidates and the energy deposition inside the TPC. The resolutions are parameterized in terms of Q^2 and applied on an event-by-event basis. The respective quantity resolution Δi is defined as

$$\Delta i = i_{\mathrm{MC}} - i \qquad \text{for} \qquad i \in Q^2, x, y, \varphi, \tag{2.15}$$

with i_{MC} as the simulated input value and i as the reconstructed value. The parametrization of the shape, which is used as input in the simulation to obtain the respective quantity resolution Δi at a given Q^2, are given as

$$\Delta i \left(Q^2\right) = A \cdot \left(Q^2\right)^B \qquad \text{for} \qquad i \in Q^2, x, y, \varphi, \tag{2.16}$$

with A and B being the respective fit-parameters and Δi as the residuum for the respective quantity i. In Fig. 2.25 the relative Q^2-resolution is shown with the corresponding parametrizations. The relative Q^2-resolution for the test setup results in about 25 % at a $Q^2 = 10^{-3}$ GeV$^2/c^2$ and about 10 % around $Q^2 = 10^{-2}$ GeV$^2/c^2$. Since the setup is not optimized to obtain a precise values for Q^2, those resolution values are expected.

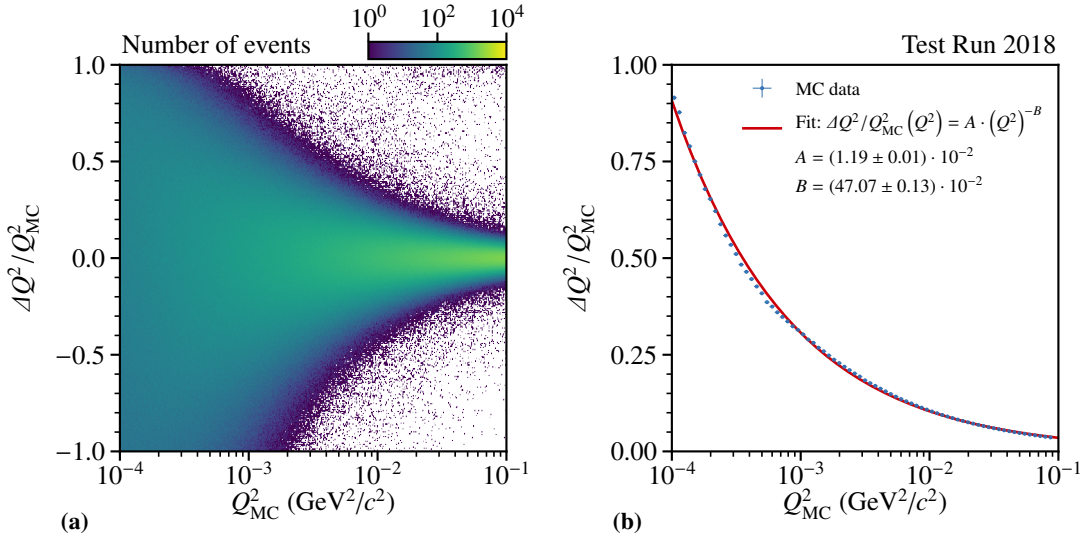

Figure 2.25: The relative Q^2-resolution is shown in (a) in terms of Q^2_{MC}. In (b) the parametrization of the relative Q^2-resolution is given.

In Fig. 2.26 the muon φ-resolution depending on Q^2 is shown. It shows a similar behavior as the relative Q^2-resolution. The φ-angle predicts the direction with respect to the pad plane. With the pad plan having 16 radial segmentation starting from the second ring on, an angular resolution of about 0.4 rad can be achieved (cf. Sec. 2.1.3). At Q^2 values below 10^{-3} GeV$^2/c^2$ the range of the proton is short compared to the pad size and if it originates from a pad center, no angular information is available. Especially those events are challenging to correlate, since here only the energy deposition and x-y-position contribute.

In Fig. 2.26(d) the vertex x-resolution depending on Q^2 is shown. The y-resolution is very similar and not shown. The resolution shows a change of slope around $Q^2 \approx 10^{-3}$ GeV$^2/c^2$due to the increasing effect of multiple scattering, especially for tracks with small scattering angles. The resolution is constant for values $Q^2 \geq 10^{-3}$ GeV$^2/c^2$ and shows a steep rise for smaller values. To take this behavior into account the parametrization is extended by a second similar term via

$$\Delta i\left(Q^2\right) = A \cdot \left(Q^2\right)^{-B} + C \cdot \left(Q^2\right)^{-D}. \tag{2.17}$$

This includes two additional parameters C and D. The extracted resolution of around 16 µm for the x-y-vertex position is influencing the starting position of the recoil proton. Besides affecting also the overall track lengths, protons close the edge of a pad may distribute small fractions of their produced ionization among other pads. The energy deposition might be below the threshold and not recorded and therefore disturb the reconstructed total energy. In the presented case, the Q^2-resolution is expected to have main effect on this uncertainty.

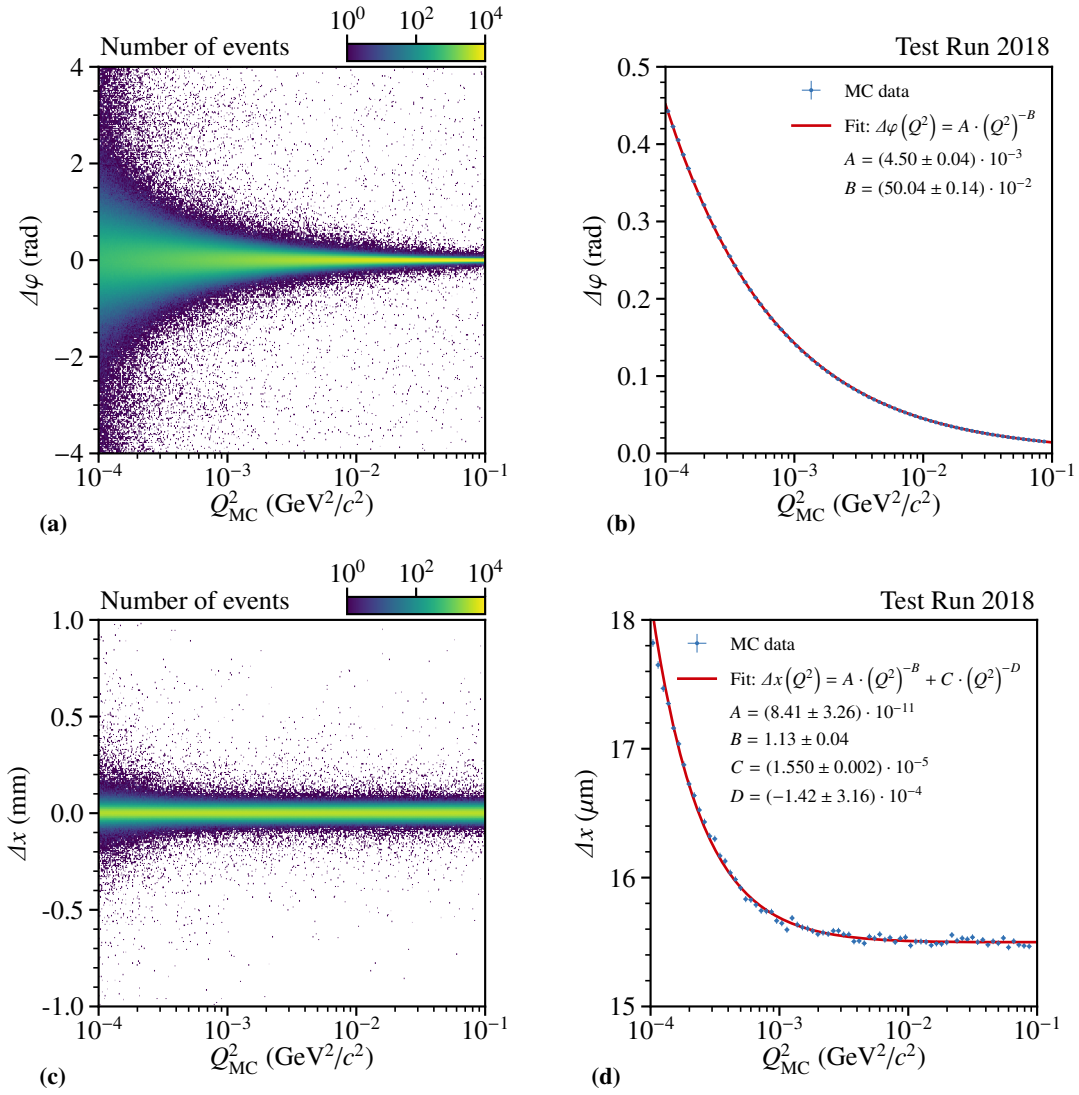

Figure 2.26: The φ-resolution is shown in (a) in terms of Q^2_{MC}. In (b) the parametrization of the φ-resolution is shown. Vertex x-resolution dependence on Q^2 is shown in (c). The corresponding parametrization is shown in (d). The values for the parametrization are given in the respective figure.

First Evaluation with Simulated Data

In Fig. 2.27 an example for the input proton event-display is shown with the respective energy deposition in the single pads. The shown simulated example event uses a Q^2 of 0.005 GeV$^2/c^2$ resulting in a kinetic recoil-proton energy of 2.66 MeV as given in Eq. (1.24), which corresponds to a projected proton range of about s_p = 6.79 cm (cf. Fig. 1.14).

Based on the resolutions of the reconstructed muon, the energy-deposition probability-distributions are generated from possible proton candidates. For the given example, those are shown in Fig. 2.28 for the single pads. Only pads with a significant contribution are shown. Neighboring pads with a very small contribution are not shown, but are taken into account to estimate the likelihood of each event.

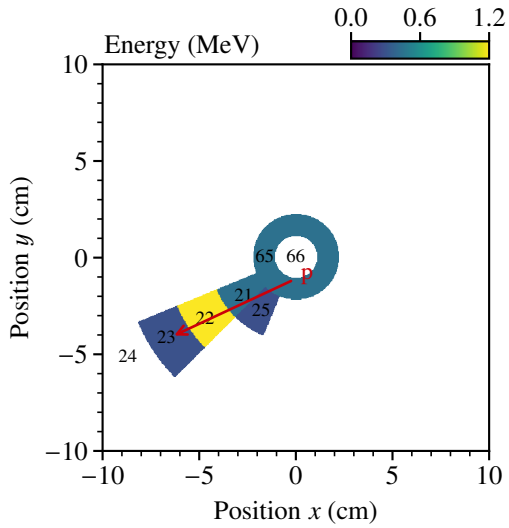

Figure 2.27: Example event candidate of proton matching for the 2018 TPC pad plane shown in Fig. 2.8(a). An example recoil proton is indicated with Q^2 = 0.005 GeV$^2/c^2$ with a corresponding range of about s_p = 6.79 cm.

The sampled probabilities for the single pads are shown in Fig. 2.28 from the given example. Based on the elastic scattering kinematics, a recoil proton candidate is calculated from the measured muon values and simulated N-times taking into account the uncertainties in Q^2, φ, x and y. For each outcome the energy deposition on each pad is saved and normalized at the end to obtain the probability distributions. The measured proton-energy on each pad is then evaluated according to the probability in single each pad and a total likelihood is calculated. Penalty terms are used in case that no energy is distributed on a pad and therefore no probability distribution is present. Each proton candidate of the TPC measurement is evaluated and the best matching initial muon and proton pair is selected. At this stage, double selections are still allowed and will be treated in the future.

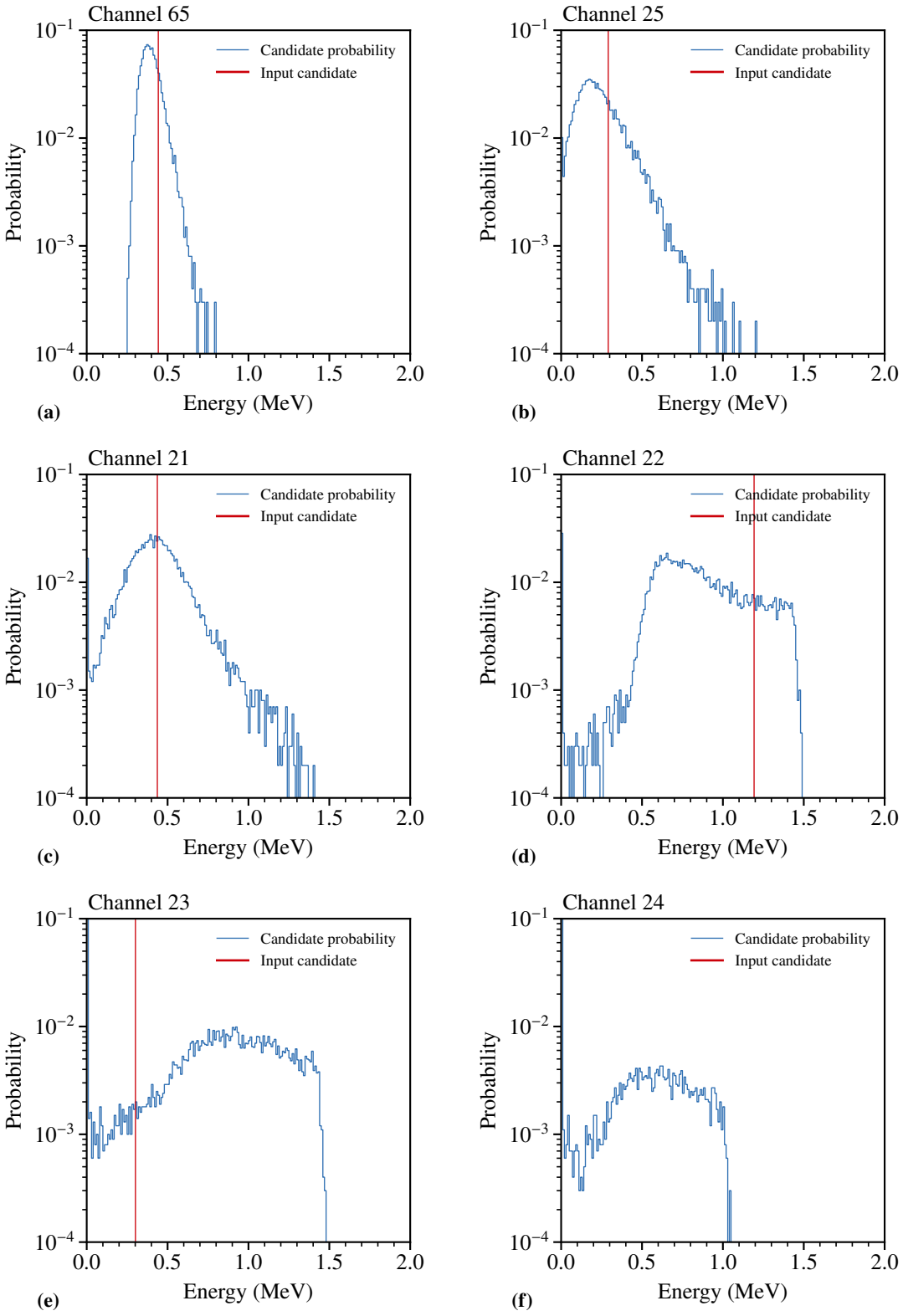

Figure 2.28: Example probability distribution for energy depositions for the single pads with the marked input of the proton candidate.

To evaluate the initial performance for the anticipated Q^2-range, a pure simulated data-set is used. Up to ten possible proton candidates are simulated according to the elastic muon-proton scattering cross-section in Q^2 (cf. Eq. (1.10)), which results in a larger fraction of events in the more challenging low-Q^2 region due to the steep slope. The simulation of each candidate takes into account the resolution of the reconstructed muon. The given probability of a correct matching $P_{\text{corr.}}$ reflects how many correct pairs are found. Each candidate can still be associated multiple times at this stage. In Fig. 2.29 the results of the simulation-based muon-proton matching for different Q^2-ranges are shown. The reduced amount of available information if only one pad has energy deposition combined with the large Q^2 uncertainty is dominating at low-Q^2. Depending on the number of available candidates per proton, the probability to associate the correct one reduces. From the 2018 test measurement real-data matching an average number of 1.6 muons per proton could be extracted (cf. Sec. 2.5). This would lead to an efficiency of more than 95 % if the full Q^2-range is covered in this simplistic example as shown in Fig. 2.29(a). In Fig. 2.29(b) different sub cross-section contributions are shown. Larger Q^2-values result in longer tracks and ensure an improved matching efficiency of close to 100 % even in the case of up to 10 muon candidates. Protons with $Q^2 < 0.005$ GeV$^2/c^2$ show a drastically decreasing efficiency starting from the second candidate. The limited range and the mostly one-pad hits are challenging.

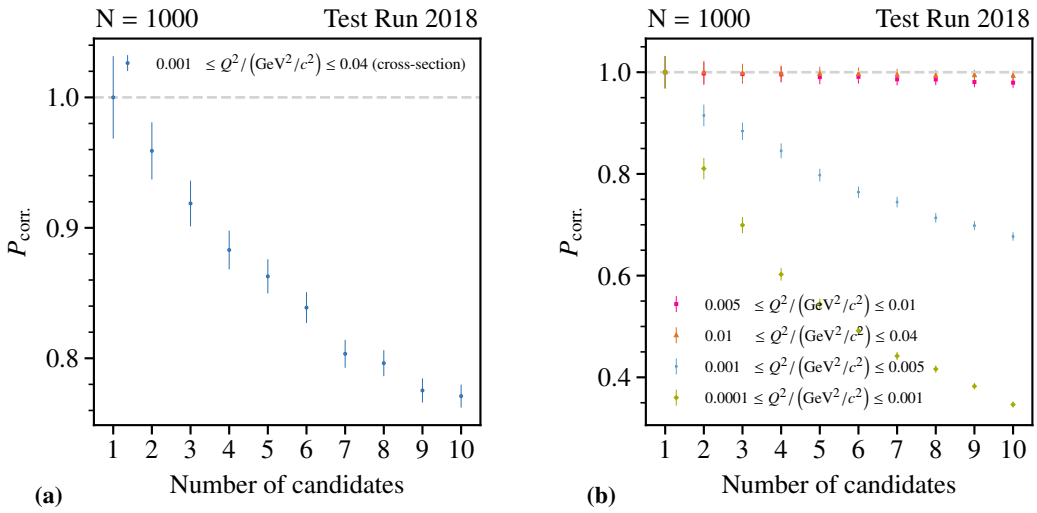

Figure 2.29: Result of simulation-based muon-proton matching for different Q^2-ranges with the statistical uncertainties indicated. The TPC pad plane geometry and the resolutions are based on the 2018 test run. In (a) the full Q^2-range according to the cross section is shown. Subsamples are given in (b).

In the future, this idea is planned to be further refined. Correlations between single pads need to be taken into account and double association will be treated. After a precise energy calibration of the proton data and an acceptance correction of the muon data, it is foreseen to test the matching based on the found correlated events. In the final version, a fast solution is required to ensure a quick data processing without starting a full GEANT4 simulation for each event. Also existing methods like the track reconstruction in the ALICE TPC [74] could be used as orientation in the simpler case for the AMBER TPC.

2.7 Elastic Muon-Electron Scattering

The elastic muon-electron scattering is a natural process arising with a comparable probability as the elastic muon-proton scattering depending on the target material. The elastic-scattering kinematic can be defined by two parameters if the target particle is at rest. This kinematics can be exploited for calibration purposes since the angular correlation between the outgoing muon and electron results in the incoming muon momentum. Using this method, the momentum measurements of the BMS stations in the M2 beam line can be calibrated (cf. Sec. 1.2.1). During the same time of the test measurement, also in a parasitic data taking, the Muon on Electron elastic scattering (MUonE) collaboration performed a test beam with the focus especially on elastic muon-electron-scattering [75]. Furthermore, this approach can be further extended towards the inverse kinematics to measure the proton radius in proton-electron scattering or even pion or kaon radii [76]. In the following, a first look into the recorded data of this channel is done and the results of both parallel measurements are compared.

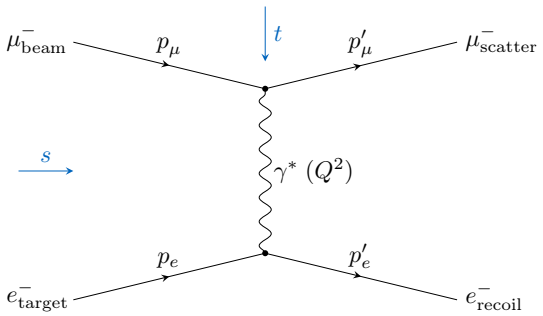

Figure 2.30: First order Feynman diagram of elastic muon-electron scattering with the momentum transfer $Q^2 = -t$ carried by the virtual photon between the scattered muon off a resting target electron and the recoiling electron. The s- and t-channel directions are indicated.

2.7.1 Kinematics

The kinematics is comparable to the elastic muon-proton scattering. The first order Feynman graph is shown in Fig. 2.30 donating the naming scheme. The angular distributions for muon and electron depend on the transferred squared four-momentum Q^2. Figure 2.31 shows the Q^2-dependence of the electron scattering angle for different beam momenta.

According to [77] the kinematic relations of elastic muon-electron scattering can be expressed as follows. The s- and t-channel of the reaction are defined as

$$s = \left(p_\mu + p_e\right)^2 = \left(p'_\mu + p'_e\right)^2 \quad \text{and} \tag{2.18}$$

$$t = \left(p_\mu - p'_\mu\right)^2 = \left(p_e - p'_e\right)^2 . \tag{2.19}$$

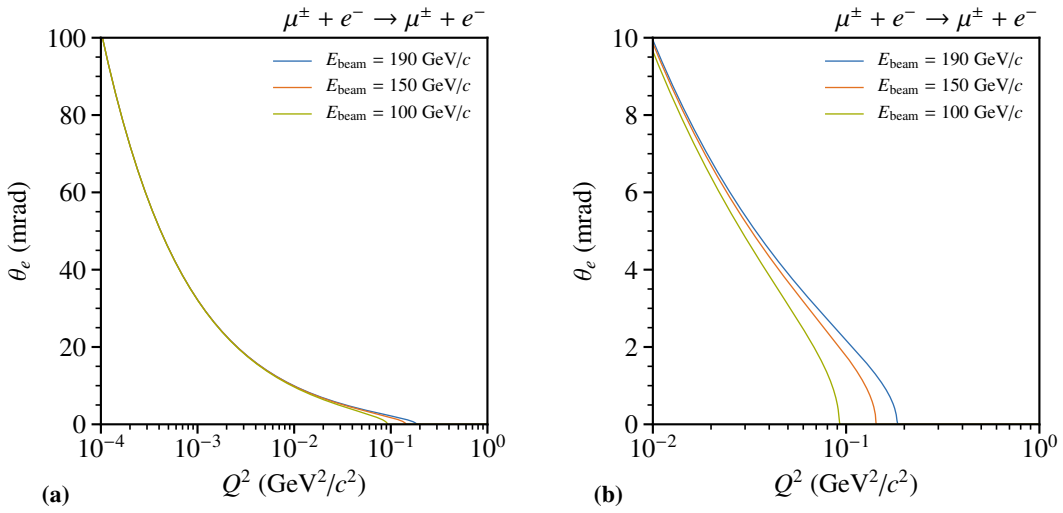

Figure 2.31: Electron scattering angle for different beam energies. In (a) the Q^2-dependence of the scattering angle is shown and in a close-up in (b).

To obtain the relation between the two scattering angles of muon and electron, the s-channel can be expressed as

$$s = (p_\mu + p_e)^2 \tag{2.20}$$
$$= 2E_\mu m_\text{e} + m_\text{e}^2 + m_\mu^2. \tag{2.21}$$

The relation between the center-of-mass system and the laboratory system is given by γ and β. Based on Eq. (2.21) the Lorentz factor γ can be expressed as

$$\gamma = \frac{E_\mu + m_\text{e}}{\sqrt{s}} = \frac{s + m_\text{e}^2 - m_\mu^2}{2m_\text{e}\sqrt{s}} \qquad \text{and} \qquad \beta = \frac{|\vec{p}_\mu|}{E_\mu + m_\mu}, \tag{2.22}$$

which can be written in a more compact way as

$$g_\mu^* = \frac{\beta_\mu}{\beta_\mu^*} = \frac{E_\mu m_\text{e} + m_\mu^2}{E_\mu m_\text{e} + m_\text{e}^2}. \tag{2.23}$$

The relation between the muon and electron scattering angle can be expressed as the so-called elastic condition, given as

$$\tan\theta_\mu = \frac{2\cdot\tan\theta_\mathrm{e}}{(1+\gamma^2\cdot\tan^2\theta_\mathrm{e})\cdot(1+g_\mu^*)-2} \tag{2.24}$$

and is shown in Fig. 2.32(b). The respective maxima[12] are defined by

$$\tan\theta_\mu^{\max} = \frac{1}{\gamma\sqrt{g_\mu^{*\,2}-1}} \qquad \text{and} \qquad \tan\theta_\mathrm{e}\Big|_{\theta_\mu^{\max}} = \frac{\sqrt{g_\mu^{*\,2}-1}}{\gamma\sqrt{g_\mu^*+1}}. \tag{2.25}$$

The beam energy can be calculated from the two scattering angles of muon θ_μ and electron θ_e. According to [23], it can be expressed as follows. With

$$f_\mu = \frac{|\vec{p}_{\mu'}|}{|\vec{p}_\mu|} = \left(\cos\theta_\mu + \eta\cos\theta_e\right)^{-1} \quad \text{and} \tag{2.26}$$

$$f_e = \frac{|\vec{p}_e|}{|\vec{p}_{\mu'}|} = \left(\cos\theta_e + \eta^{-1}\cos\theta_\mu\right)^{-1} \quad \text{with} \tag{2.27}$$

$$\eta = \frac{\sin\theta_\mu}{\sin\theta_e}, \tag{2.28}$$

the incoming beam momentum results from

$$E_\mu^2 a - 2E_\mu b + c = 0 \tag{2.29}$$

$$\text{with} \qquad a = 4f_e^2 - \left(1 - f_\mu^2 + f_e^2\right)^2 \tag{2.30}$$

$$b = 2m_e\cdot\left(1 - f_\mu^2 - f_e^2\right) \tag{2.31}$$

$$c = 4m_e^2\cdot\left(f_\mu^2 - 1\right) + m_\mu^2\cdot\left(1 - f_\mu^2 + f_e^2\right)^2 \tag{2.32}$$

[12] The formula for the maximum scattering angle $\tan\theta_\mathrm{e}$ given in [77] Eq. 9 contains a mistake in the denominator. It is written $g_\mu^{*\,2}$, but correct is g_μ^* as it is written in Eq. (2.25). The effect does only play a minor role for the electron case, but for kinematics with heavier particles like pions, kaons or protons the difference is important.

Which results in a quadratic equation for E_μ given by

$$E_{\mu,1,2} = \frac{b}{a} \pm \sqrt{\left(\frac{b}{a}\right)^2 - \frac{c}{a}}. \tag{2.33}$$

The correct solutions of the quadratic equation for the beam energy in Eq. (2.29) needs to fulfill valid kinematics. For the low-Q^2 region until $2 \cdot 10^{-4}$ GeV$^2/c^2$ it was found that only the positive solution results into the correct kinematics in this case. For larger Q^2 both solution result in a valid one. Here the calculated beam momentum can be outside of the meaningful range, but some combinations can result into a valid value and distinguishing those becomes challenging.

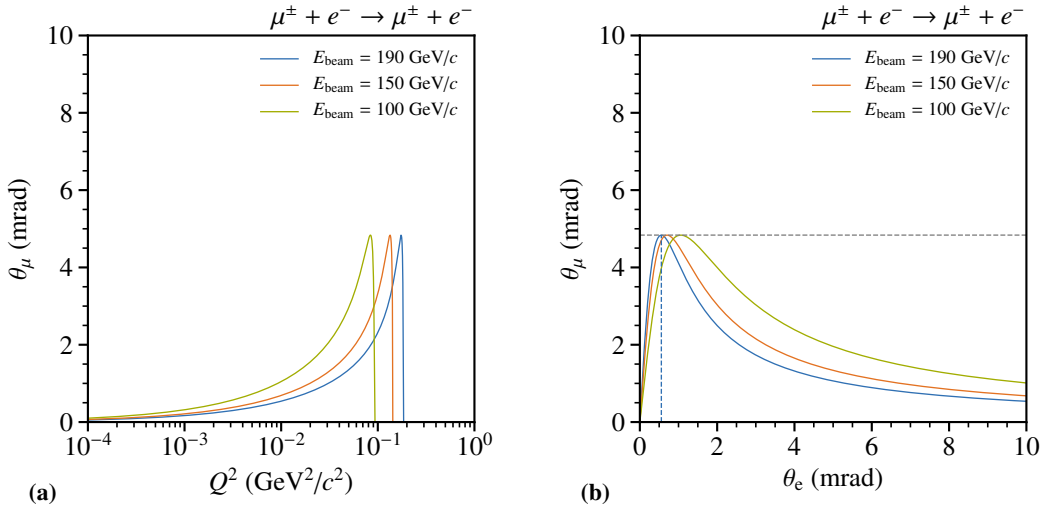

Figure 2.32: Elastic muon-electron scattering-angles for different beam momenta. In (a) the Q^2 dependence of the muon scattering angle is shown. The correlation between the muon and electron scattering angle is shown in (b) with the maximum for the muon scattering angle indicated by the gray dashed lines.

Due to the quadratic characteristics of the solution these two possible solutions are resulting, but one does not result in a valid kinematic. In addition, it can be seen in Fig. 2.32(b) that the solution for a pair of angles is not unique in terms of resulting momentum. For a certain combination two valid solutions can be extracted. Therefore, it is favorable for distinction of those solutions to measure at least one outgoing particle momentum. In the case where both resulting momenta are too close additional measures are required since no distinction between both solutions is possible.

2.7.2 Analysis of the 2018 Data

The event selection for the 2018 test run data to select elastic muon-electron scattering events is based on the initial event selection for the elastic muon-proton-scattering as discussed in Sec. 2.4. For the elastic muon-electron-scattering events, the information of the TPC is not used and therefore, the TRLO timestamp and the event correlations are not needed. Distinguishing electron and muon is not possible with pure tracking, as it is present in the test setup. Therefore, a random assumption is made that one of the tracks corresponds to the muon and the other track to the electron. The event selection is split into two stages. A preselection with basic requirements on the event topology and a more detailed selection of those events. To investigate the effect of more target material, two different event selections are performed. First, a more precise selection of events origination from structures inside the TPC is performed, followed by a more coarse selection taking into account more material as target. In the following, both studies will be discussed.

Preselection

For the preselection of the data, the basic requirement of events having a reconstructed beam track and one primary vertex with two outgoing tracks is applied. In Fig. 2.33 the overview of the applied selection criteria are shown together with the resulting number of events and their fraction.

Starting with a total of about $5.9 \cdot 10^9$ events, only about $12 \cdot 10^6$ have three reconstructed tracks including a beam track and one primary vertex. The requirement of having two outgoing tracks at this primary vertex reduces the number of events further by three orders of magnitude, resulting in about $48 \cdot 10^3$ events. This shows that one of the three reconstructed tracks is not associated to the vertex and could be due to pile up or vertexing issues. Those preselected events serve as input for the more detailed selection discussed in the following.

Event Selection

The event selection is similar to the elastic muon-proton scattering selection presented in Sec. 2.4.1 with the difference in the vertex z-criterion to select events originating from material along the TPC and the additional so-called coplanarity along φ requirement between both scattered tracks, namely the muon and electron.

First, to minimize the effect of multiple scattering in material, requirements are applied to have the incoming and all scattered tracks passing though the up- and downstream beam windows of the TPC (cf. Sec. 2.4.1). Both of the scattered tracks are required to pass the downstream beam window as well as the cathode beam hole. The resulting primary vertex x-y-distribution is shown in Fig. 2.34(a) and is comparable to the one from the elastic muon-proton scattering event selection presented in Fig. 2.21(b). Similar cable-like structures are visible (cf. Fig. 2.21(b)). The full TPC structure along the beam axis is taken into account. To select event with origin along this

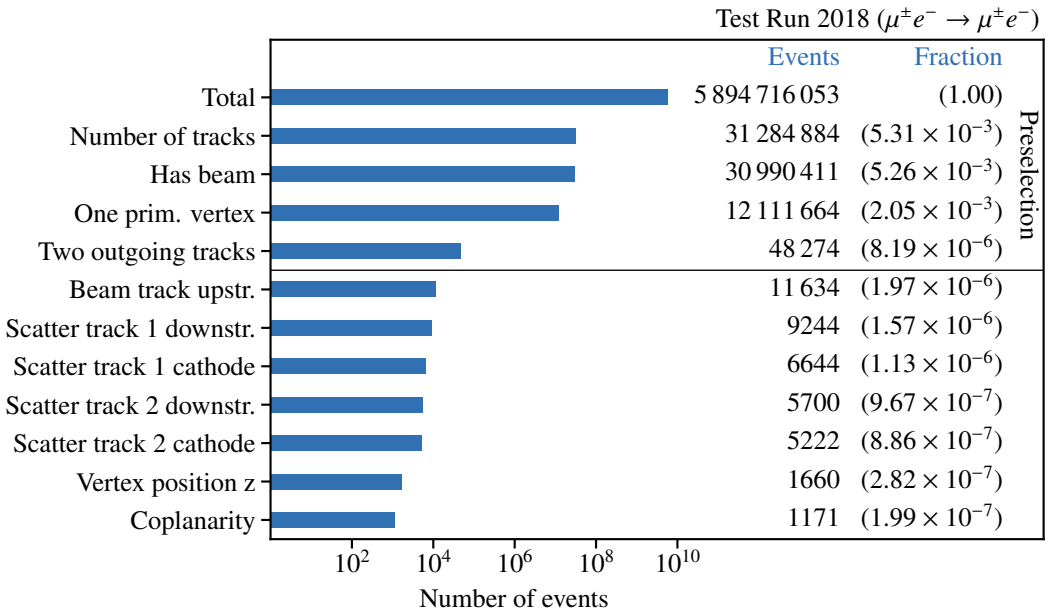

Figure 2.33: Applied selection criteria used for the elastic muon-electron event selection are shown. The preselection stage is indicated together with the resulting number and fraction of events after each stage.

axis, a selection of events along the z-direction of -95 cm $\leq z \leq +95$ cm is used. In Fig. 2.34(b) the vertex z-distribution is shown with all criteria applied except the one for the indicated vertex position. Structures along the TPC beam axis are visible, like the entrance and exit windows as well as the anode and cathode. Also, some events could be reconstructed in the material of the silicon tracking detectors.

To ensure elastic scattering, the momentum conservation needs to be fulfilled, which results in a so-called back-to-back scattering of the reconstructed muon and electron. In Fig. 2.35(a) the so-called coplanarity $\varphi_{\text{cop.}}$ with the applied selection criteria is shown. It is defined as

$$\varphi_{\text{cop.}} = \pi - |\varphi_{\mu} - \varphi_{e}| = \pi - |\varphi_{1} - \varphi_{2}|. \tag{2.34}$$

Since muon and electron cannot be distinguished their respective φ angle is arbitrarily used as φ_1 or φ_2. For the selection, only events with a coplanarity of $|\varphi_{\text{cop.}}| \leq 150$ mrad are selected. This also suppresses radiative events that lower the scattering angle of muon or mostly the electron. As an estimate according to the scattering angle relation between electron and muon shown in Fig. 2.32, scattering angles around 1 mrad or larger are expected to be reconstructed mostly. This corresponds roughly to a $Q^2 = 10^{-2}$ GeV$^2/c^2$. The expected φ-resolution of the test setup shown in Fig. 2.26 is about 50 mrad for this momentum transfer. This is in agreement with the obtained coplanarity value. No selection on the scattering angle of the two tracks is applied.

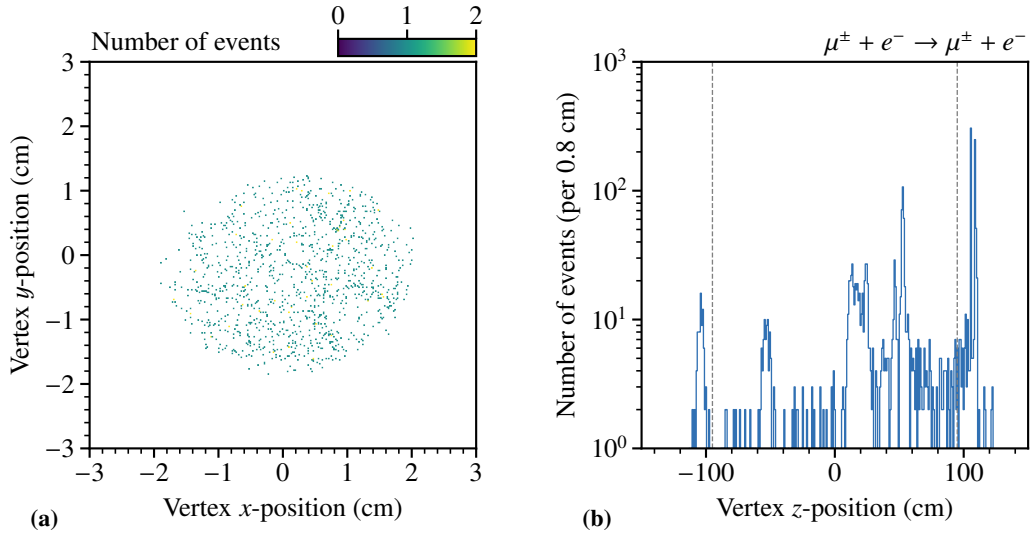

Figure 2.34: In (a) the vertex x-y-position of the selected events is shown. The exclusion of up- and downstream flanges of the TPC as well as the cathode structures is applied. Cable-like structures are recognizable. In (b) selection criteria on the primary vertex z-position is shown in (b).

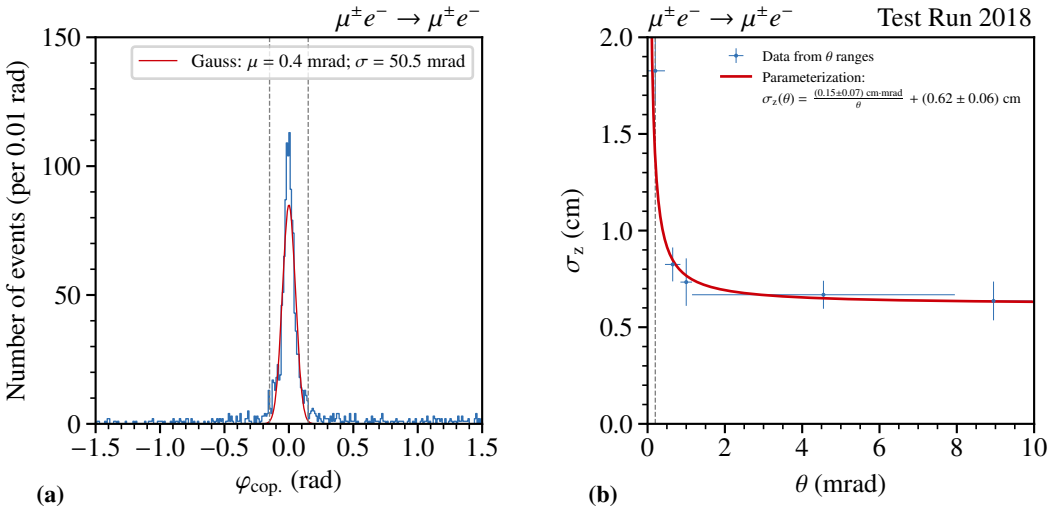

Figure 2.35: The coplanarity distribution is shown in (a) with indicated selection criteria. All criteria are applied except the indicated one. In (b) the vertex z-resolution of the selected events is shown.

In (b) the vertex z-resolution depending on the arbitrarily chosen scattering angle θ for one of the two outgoing tracks is shown. The vertex z-resolution is parameterized according to Eq. (2.2). Compared to the single outgoing track vertex z-resolution for elastic muon-proton scattering discussed in Sec. 2.4.1, the resolution is significantly improved, but shows the same asymptotic behavior for larger scattering angles caused due to possible intrinsic resolution effects.

Angular Correlation

In Fig. 2.36(a) the angular correlation distributions after the preselection stage are shown. Here a clear correlation band is visible, which is symmetric since muon and electron cannot be distinguished. Bremsstrahlung processes ($\mu^{\pm}e^{-} \rightarrow \mu^{\pm}e^{-} + \gamma$) cause bands, resulting in small reconstructed scattering angles. No electromagnetic calorimeter is present in the test setup and therefore those events cannot be studied individually. Requiring the coplanarity removes those events as well as the reduction of the traversed material by requiring the passage through the windows. The resulting elasticity curve as given in Eq. (2.24) with the estimate for a 180 GeV beam energy is shown in Fig. 2.36(b) based on the extracted result shown in Fig. 2.37. The prediction fits well with the data sample, although the correlation at angles $\theta_{1,2} \leq \theta_{1,2}^{\max}$ as given in Eq. (2.25) is not visible. This has been evaluated based on Monte Carlo. Using the cross-section behavior and simulating an identical statistic results in a comparable distribution.

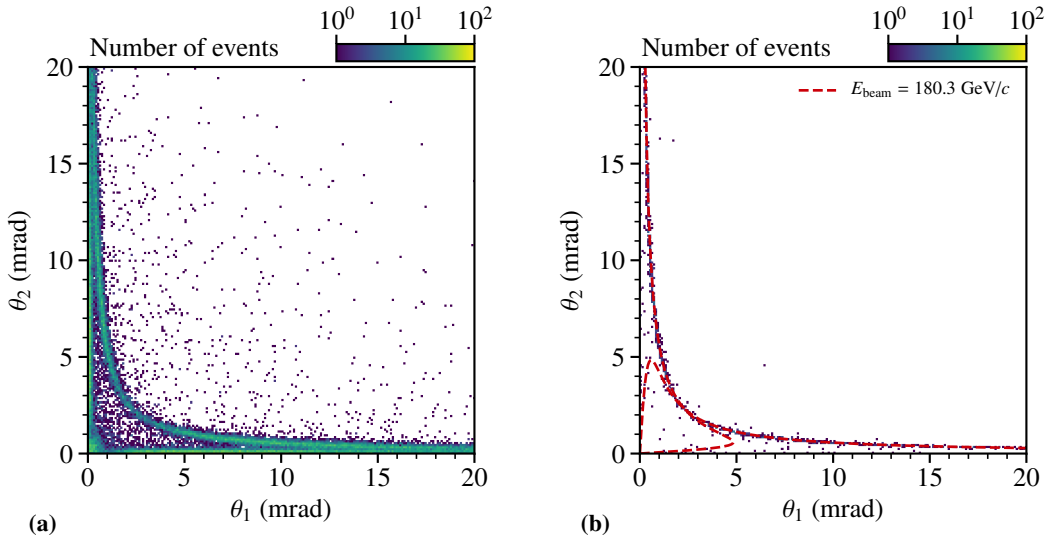

Figure 2.36: Angular correlation between the scattering angles of muon and electron. In (a) all events after the preselection are shown and in (b) all selection criteria are applied. The elasticity condition is visible in both and the calculated correlation as given in Eq. (2.24) is drawn in a mirrored way.

Beam Momentum Reconstruction

The muon beam energy can be calculated from the scattering angles as given in Eq. (2.33). The extracted beam energy is shown in Fig. 2.37. Since the data sample includes muons from a 190 GeV muon beam from pion decay along the beam line as well as muons from the COMPASS Drell-Yan measurement originating from the target region of COMPASS, the spectrum does not show a clear peak, but has multiple effects included. Muons originating from the Drell-Yan process will have a lower energy compared to the ones produced by pion decay along the beam line. In addition, all muons have to pass the whole spectrometer including the so-called muon-filter reassembled by a concrete wall. This effects the resulting muon beam energy at the location of

the test setup. Nevertheless, the expected 180 to 190 GeV can be extracted and also reassembles the angular correlation. The feature of picking the wrong solution leads to larger and calculated unrealistically large beam momenta of > 200 GeV. In addition, the asymmetric shape is caused by the indistinguishable muon and electron tracks.

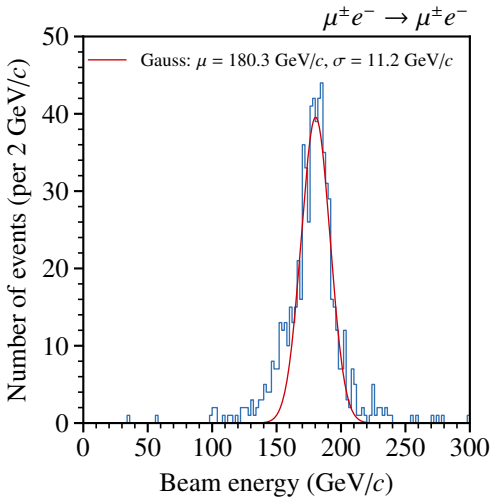

Figure 2.37: Calculated beam momentum based on the angular correlation between muon and electron.

Event Selection with more Material

To increase the number of events, more material along the TPC structure is taking into account by not requiring a passage though the beam windows of the incoming and outgoing tracks. In Fig. 2.38 the adapted selection of events is shown. The selection of tracks passing through beam windows is not applied as in the previous discussed event selection. This results into a larger number of events originating from those additional structures at the cost of a loss in precision due to multiple scattering. The reduced event selection similar to the previous one is shown in Fig. 2.38. About a factor of ten more events are obtained by taking into account the additional material.

The resulting vertex distributions are shown in Fig. 2.39. Due to the excluded beam window criteria for the tracks, more events are generated outside the beam window region. This is clearly visible in the vertex z-distribution, where the flanges contribute the most. The same holds for the x-y-distribution where also the feature of the misaligned beam windows is visible (cf. Sec. 2.4.1). The result of the additional materials is visible, especially in the coplanarity distribution shown in Fig. 2.40. The background is increased compared to the cleaner sample with window passage requirement. An increase of the resolution by a factor of four caused by the additional material can be observed. To obtain comparable results, the same 150 mrad selection is applied to the coplanarity as in the previous selection.

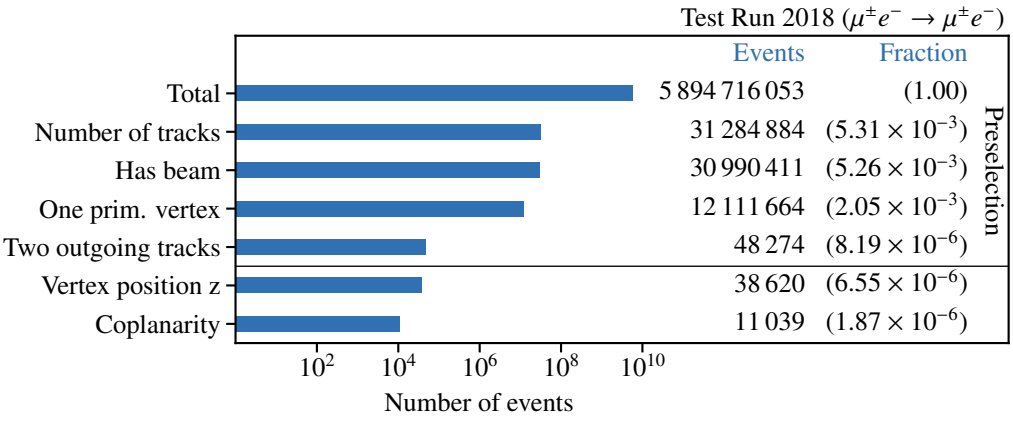

Figure 2.38: Selection used for the elastic muon-electron scattering are shown. The preselection stage is indicated together with the resulting number and fraction of events after each selection. To take more material into account, the selection of passage through beam windows are not applied.

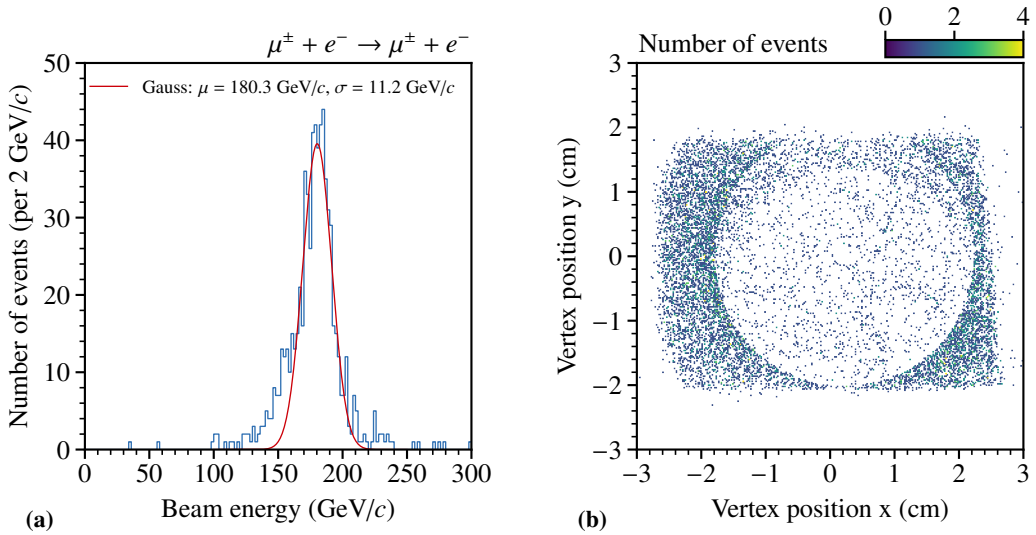

Figure 2.39: In (a) the calculated beam momentum based on the angular correlation between muon and electron is shown. The vertex x-y-position of the selected events is show in (b).

The resulting angular correlation is shown in Fig. 2.41(a) after all selection criteria applied. The estimation for a 178 GeV momentum is indicated, and the distribution is in agreement with this estimation. The extracted beam momentum shown in Fig. 2.41(b) is comparable to the cleaner sample. In addition, the spectrum is broader and shows the mix-up feature between muon and electron more dominantly. Unrealistic beam momenta of more than 250 GeV are calculated. Furthermore, the slope on the high-momentum side is steeper compared to the low momentum side. This effect could be related to the parasitic beam position.

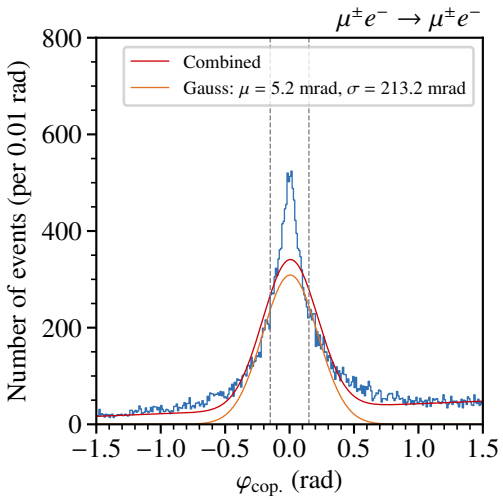

Figure 2.40: Coplanarity distribution with more material. The effect of more background events is visible.

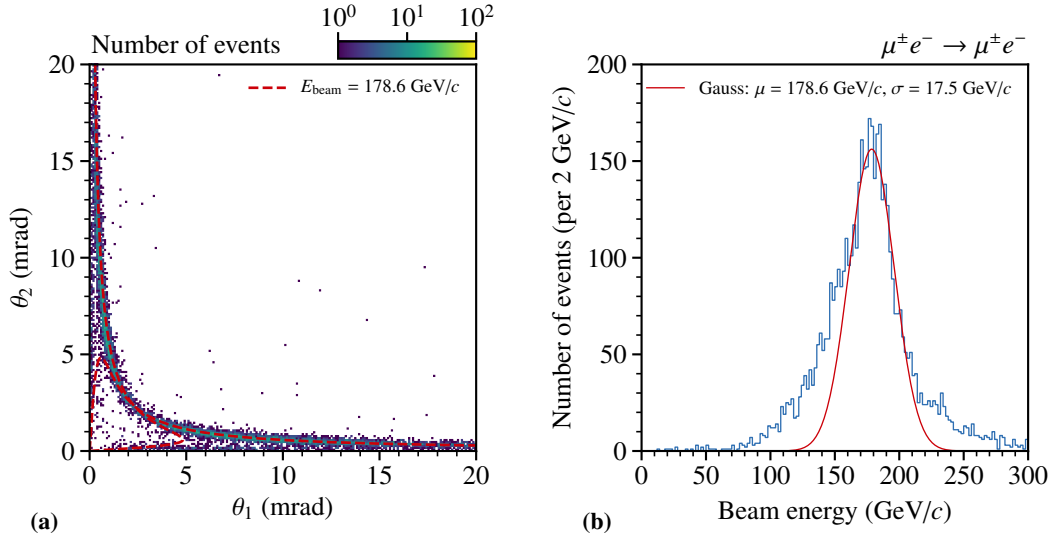

Figure 2.41: Angular correlation is shown in (a) and the extracted beam momentum is shown in (b) each with the extracted mean beam momentum is indicated.

Parallel to the test measurement, a second test setup constructed by the MUonE collaboration was present during that time. Their goal was to investigate the elastic scattering of muons on atomic electrons in a similar configuration as their proposed setup. They plan to measure the differential elastic muon-electron cross-section with a precision of $O\left(10^{-5}\right)$ [78]. The results from their test measurement are shown in Fig. 2.42(b) and are comparable to the ones extracted during the Amber test measurement shown in Fig. 2.42(a). Here, the same result as in Fig. 2.41(a) is shown, but with an adapted range. The number of events is similar and identical features can be observed like the background at lower θ_1-angles. In the MUonE data taking an identification of electrons was possible.

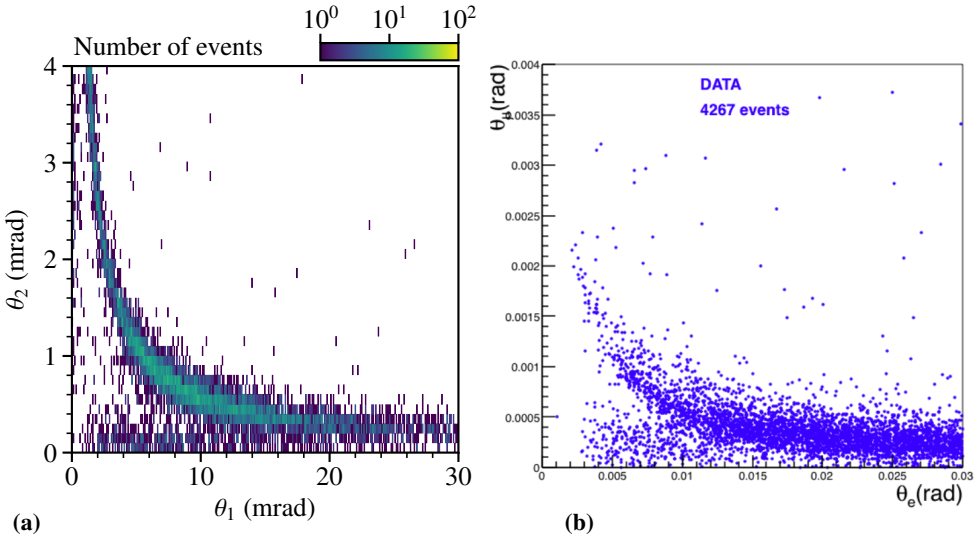

Figure 2.42: Comparison between the results of the test measurement with the MUonE test at the same time and location. In the test measurement, 6556 events in the selected range. Figure (b) taken from [75].

2.8 Elastic Hadron-Electron Scattering

The elastic muon-electron scattering as discussed in Sec. 2.7 can be more generalized into elastic hadron-electron scattering. As presented in [41] as possible extension to the intended Primakoff data-taking with hadron beams is foreseen in the AMBER Phase-2 proposal[13]. Measuring hadron radii by elastic scattering off atomic electrons is currently under investigation [76]. Using the inverse kinematic allows access also to radii of pions and kaons [79, 80]. This idea can be adapted further towards protons and to access the radius. Studies are planned to explore the systematic effects and evaluate the achievable resolutions. For the AMBER proton radius setup the TPC hydrogen volume may serve as an electron target utilizing the optimized multiple scattering properties of the setup. Simple electron target structures like beryllium discs or the beam windows of the TPC are under discussion. This would be a possible fall-back solution for the proton radius project in case of production issues or required steps depending on the current political situation.

The kinematics can be calculated as discussed in Sec. 2.7.1 by adapting the mass of the respective beam particle. The angular dependence on Q^2 for elastic proton-electron scattering is shown in Fig. 2.43. At low values of Q^2 the electron scattering angle reaches values of several mrad. With increasing Q^2, the resulting scattering angle of the electron becomes smaller and is limited by the kinematically possible Q^2_{max}. For the scattered proton, the resulting scattering angle increases towards a maximum with larger values of Q^2 and is also limited by the maximal allowed Q^2.

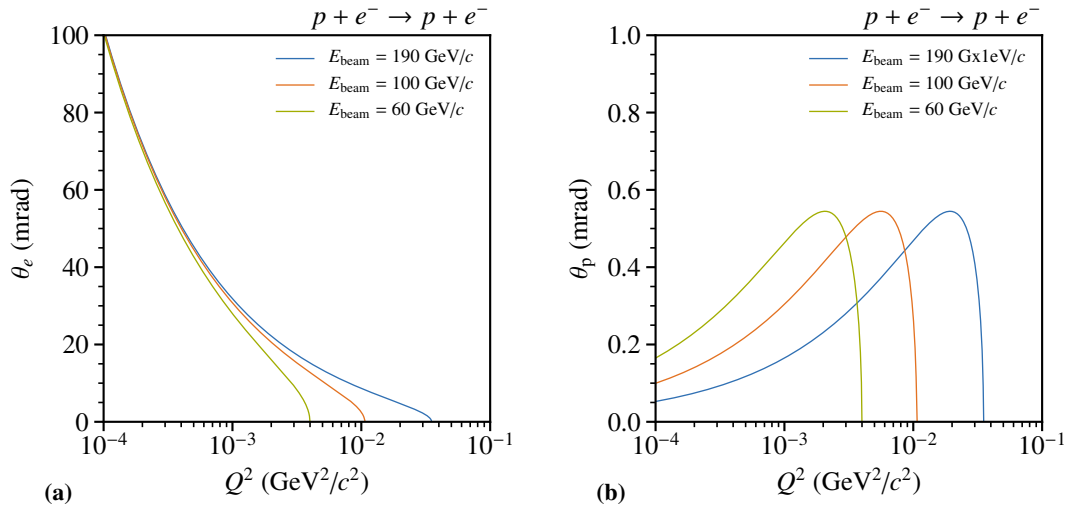

Figure 2.43: In (a) the electron scattering angle dependence on Q^2 is shown. The proton scattering angle dependence on Q^2 is shown in (b).

[13] In preparation and no yet published.

The angular correlation between the scattering angles of proton and electron is shown in Fig. 2.44(a). The maxima are indicated for the different beam energies (cf. Eq. (2.25)). The maximal accessible Q^2 based on the beam momentum is shown in Fig. 2.44(b). With a maximal beam momentum of 190 GeV/c of the M2 beam line, the maximal accessible Q^2 is about 0.035 GeV$^2/c^2$, which is comparable to the initially proposed maximal Q^2 for proton radius measurement of AMBER. Especially the extension towards pion and kaon radii becomes an interesting topic. Here, the kinematic distributions for pion and kaons are similar and can be found in Apps. B.5 and B.6.

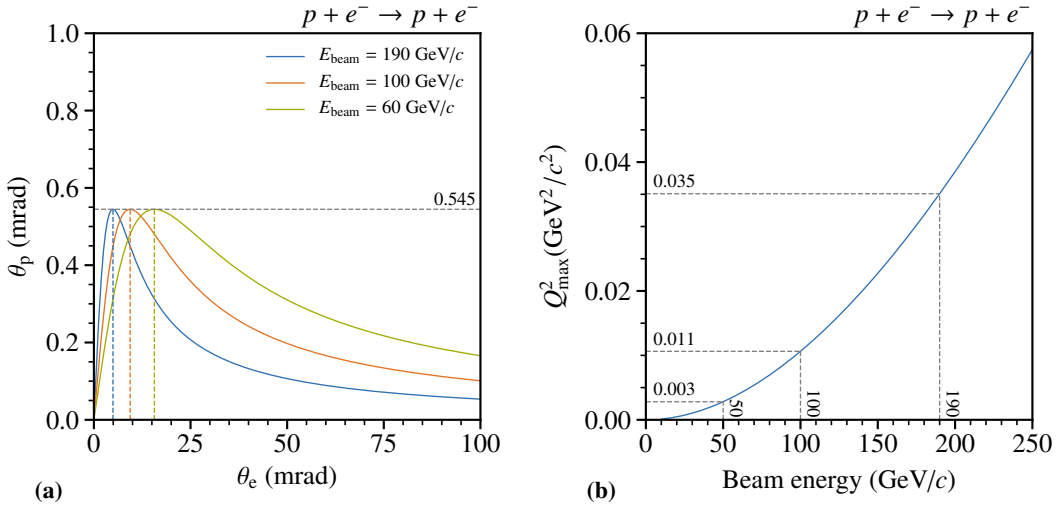

Figure 2.44: In (a) the angular correlation between proton and electron angle is shown. The maxima of the distributions are indicated. The maximal accessible Q^2 based on the beam energy is shown in (b).

With the TPC as target volume, the angular acceptance is defined by the beam windows and length of the TPC and the baseline of the setup. A schematic drawing of the TPC is shown in Fig. 1.12. With the beam windows having a foreseen radius of 35 mm and the TPC a total length of about 235 cm, a maximal angular acceptance of about 15 mrad can be achieved. A similar acceptance is obtained with the $90 \times 90\,\text{mm}^2$ size of the tracking detectors placed with a 3 m baseline. To cover the anticipated angular- and therefore Q^2-range, adaptions to the target tracking detectors are required, especially for the lower Q^2-part. The scattering angle of electrons at $Q^2 = 10^{-4}$ GeV$^2/c^2$ is about 100 mrad. This region could be accessed by increasing the tracking surface and shorten the baseline length. Events from the most downstream part of the target could be used to access the high-Q^2 region. The proton scattering angle decreases with lower Q^2 and is in region of 100 µrad similar as the lowest boarder planned of the muon-electron scattering. The Q^2 region can be extended using different beam momenta. Momenta measurements and electron identification are beneficial, which require to include the first spectrometer magnet and electromagnetic calorimetry for the larger scattering angles. In case of pions and kaons those kinematic limits differ mainly for the scattered beam particle. For kaons the maximum scattering angle is about 1 mrad and for pions it further increases up to about 3.7 mrad. Studies are foreseen to evaluate the compatibility with the proton radius setup and study possible synergies, especially for the proton-electron scattering. Since the measurement and setup requires electron identification, additional features need to be taken into account.

2.9 Summary and Outlook

The first test measurement as feasibility evaluation in the year 2018 showed the possibility of combining an active target TPC together with tracking detectors to redundantly measure muon and proton in the elastic scattering process. It served as foundation for the proton radius measurement for the at that time not yet existing AMBER collaboration. Based on an existing prototype TPC and silicon tracking detectors, a high-precision setup was constructed and was able to collect this novel type of redundant data during its few weeks of running. Besides the operation of the single detector systems, especially the TPC and studying its behavior in the broad muon beam, serves as input towards a possible main run utilizing a TPC as active target inside the muon beam at the M2 beam line combined with muon tracking.

First insights about operating this active target, initially built for a pencil-like electron beam within a much broader muon beam, were obtained. Trigger rates and energy resolution in various tests have been evaluated and agree with the expectations. The operated silicon detectors, despite their age, show a very good performance and stability. Further knowledge about their operation with respect to their temperature behavior was obtained. Not only regarding the front end, but also in the scope of the run-by-run alignment, which has been performed the first time during this measurement. The combined operation of two distinct detector measurement principles, as it is foreseen for the final measurement, brought experience for the future design.

Event matching based on timestamps obtained by a common time stamp showed that such a solution is capable of extracting kinematic correlations within the expected statistics. It serves as predecessor of the foreseen streaming DAQ system of the final measurement. About 700 events have been predicted and are extracted using this time correlation with only a minor difference towards the expected value. Clear kinematic correlations in terms of the 64 µs drift time and the respective vertex z-position as well as the energy correlation are visible and further refinements of the procedure are pursuit. During the event selection of muon candidates, knowledge regarding optimization of the structure of the TPC could be obtained. Especially the inner part is crucial for a precise measurement and possible background sources like cables or additional material should be avoided in order to meet the expected precision and minimize the effect of multiple scattering on material. Furthermore, the simulations show a good agreement with the data, which should support the simulation results obtained for the main setup. Further ideas on how to associate muon and proton pairs are under investigation, such as the Likelihood-based approach using a GEANT4 simulation. This idea shows already promising results in a yet simplistic environment.

The usage of the elastic muon-electron scattering as calibration channel for the incoming muon momenta is in agreement with the expectation. A parallel beam test by the MUONE collaboration shows similar results as extracted from the AMBER test measurement. Although, challenges are existing in terms of multiple solutions for the measured kinematics, a possible extension of this approach towards pion and kaon radii by measuring using respective beam particles and utilizing the inverse kinematics also for the proton-electron scattering are topics in reach. Developments are ongoing in terms of analysis, detectors and software, which take into account the knowledge obtained from test measurement.

CHAPTER 3

Proton-Radius Measurement Pilot Run of AMBER

For the anticipated PRM campaign at AMBER with a possible first commissioning phase starting mid of 2023, a preceding pilot run was performed end of 2021 to further evaluate the performance and feasibility of the proposed setup under conditions close to the final measurement. Based on the feasibility test measurement performed in 2018 (cf. Chap. 2), the obtained experiences and ideas are evaluated during this dedicated pilot run. This pilot run took place in the first three weeks of October 2021 and was located in the newly created test beam area within the so-called Cherenkov Detector with Achromatic Ring focus (CEDAR) region in the M2 beam line. This test area had been prepared in close work with the so-called Experimental Hall North 2 (EHN2) working group to provide the required space and infrastructure. In addition, also other experiments like NA64 [81] or MUONE [78] profit from this development [28] and construction of the new test beam area.

The pilot run was approved by the CERN research board after the recommendation by the SPSC in April 2020 [82]. Whereas the full AMBER proposal [2] was recommended by the SPSC [83] in October 2020 to be approved by the research board. With "*The proton-radius program is contingent on a successful pilot run previously approved for the first year of SPS operation after the long shutdown LS2*" [83], the SPSC requires a successful pilot run for a recommendation of the final data taking. To specify a successful pilot run, goals have been defined and split into three dedicated work packages developed in close communication with the SPSC. The pilot run is part of the beam time schedule towards 2024 as a possible year for the first physics run of the PRM. An overview of the different phases are listed in Tab. 1.6.

To obtain a close-to-final geometry of the proposed setup in the pilot run, a setup consisting out of a down-scaled version of the final TPC surrounded by silicon tracking detectors and scintillating fibers with the anticipated baseline of 3 m was installed. This reassembles the geometry of the final setup as shown in Fig. 1.6 and allows studies of the acceptance as well as energy resolutions under real conditions. Compared to the parasitic feasibility test in the year 2018 at the downstream location during the COMPASS data taking (cf. Chap. 2), a dedicated beam time of 20 days is used

with the advantage of a much more focused muon beam at the anticipated beam momentum of 100 GeV at the test beam location. This allows especially to study the TPC energy resolution under close-to-final conditions.

Construction of the full setup with the pressurized hydrogen TPC and the required tracking in a new area within 20 days turned out to be a challenging task, taking into account not only safety regulations and required formalities. Within those 20 days, the full setup was installed, commissioned and different studies have been performed. At the end, around 4 days of combined data taking could be achieved with the full setup under nominal conditions. In the following, the prepared work packages and the obtained results of the still ongoing analysis are presented.

3.1 Work Packages

To achieve the goals of the pilot run and connect with them, single tasks are split into three dedicated work packages, which were addressed prior to the 2021 beam time, during the pilot run itself and during the later analysis of the data. The main task was the study of the TPC design under high-rate muon beam conditions at the M2 beam line. In addition, the matching between muon and proton tracks similar to 2018 was foreseen. Both required a full tracking system, but due to time constraints, the UTS system of the final setup was not ready to be used for tracking as described in Sec. 1.2. Therefore, an alternative solution using silicon micro-strip detectors, which had also been used in the 2018 test measurement was chosen. Furthermore, the design and performance of the SPD and the SFH of one UTS prototype (cf.Sec. 1.2.3) was foreseen to be constructed and tested along the beam time in 2021, which was not feasible due to time constrains in the production.

The work packages have been defined in addition to the submitted proposal [2] and have been formulated mid of 2020. Due to persisting limitations[1] not all topics could be successfully addressed in the proposed time and have been delayed.

Work Package I

The testing of the new DAQ system together with the new TPC readout system was foreseen in 2021. First DAQ tests started already during the Compass commissioning phase mid of 2021. They have been performed in close communication with the Compass collaboration and the expected results could be achieved. For the TPC, the initial idea was to perform tests next to the beam line using the beam halo only. Due to time constraints, these tests could not be performed. Furthermore, tests of the new DAQ system together with the TPC during the pilot run were foreseen, but due to the fall-back solution for the tracking detectors, which are not compatible with the new DAQ system, the tests could not be performed. Testing the new DAQ system with the TPC font-end is foreseen in the close future to validate the performance in terms of readout time, structure and required data rate.

[1] COVID-19

Work Package II

Tests of the newly developed UTS were planned in 2021. Those tests could have been performed in parasitic mode at the downstream location of COMPASS, similar to the 2018 test measurement. The goal of the tests would have been to evaluate the single detector performance and infrastructure studies of the sub detector types (SPD, SFH). After verification of the single detector performance, studies were foreseen to evaluate the hit-time association between the SPD and SFH. As readout system, only the new FriDAQ structure is compatible. Furthermore, it was foreseen to test at least one UTS during the pilot run. Along 2021 dedicated tests of the free-running Intelligent FPGA-based Data Acquisition System (iFDAQ) are foreseen to evaluate the performance. The anticipated tests of the UTS could not be performed due to shortage of electronics and legal aspects of licenses for the SPD (ALPIDE). A dedicated parasitic test is now foreseen end of 2022 with a partially equipped prototype in the target area of COMPASS. Operating the new DAQ system with the UTS is foreseen to be done until end of 2022 (cf. Tab. 1.6).

Work Package III

During the pilot run, the main focus was the TPC testing. The test of the TPC in the muon beam were performed in the CEDAR location as new M2 test beam area during the pilot run. Tracking was required to evaluate the influence of the muon beam. Within the 20 days of beam time, the induced beam noise based on different rates were studies and the effect on the energy resolution was evaluated. With the chosen readout anode plane structure the reconstruction of the recoil proton kinematics is under study. First results on the combined measurement using the timestamp approach could be obtained. Based on the obtained data set, studies are ongoing to evaluate the performance.

3.2 Setup

The geometry of the pilot run setup is similar to the final setup (cf. Sec. 1.2) of the measurement and comparable to the feasibility test measurement (cf. Chap. 2). With a pressurized hydrogen TPC, the so-called Ionization Chamber for Hadronic Reactions (IKAR) TPC as prototype of the final TPC, the main beam related studies can be performed. A new designed readout plane is installed to study the energy and spacial resolution required for a later matching between measured protons and muons. For an evaluation of the energy resolution of the TPC, a tracking system is required to measure the vertex position of the recoil proton in the TPC and to compare the measured elastic scattering kinematics between proton and muon. This tracking system is a fall-back solution, since the anticipated UTS was not ready at that time. It consists out of four silicon tracking detector stations and two COMPASS scintillating fiber detectors. They are placed along the lever arm up- and downstream of the TPC together with dedicated trigger elements.

The silicon detectors are the same ones as used in the 2018 test measurement, with one additional station. The data recording is performed in the existing triggered-based DAQ. The TPC uses a dedicated DAQ system and is operated in self-triggering mode similar as in the 2018 feasibility test. By this, the TPC and tracking are independent in terms of data recording. The similar approach of utilizing a common timestamp as in the feasibility test is used to combine the data of the TPC and tracking on a later stage.

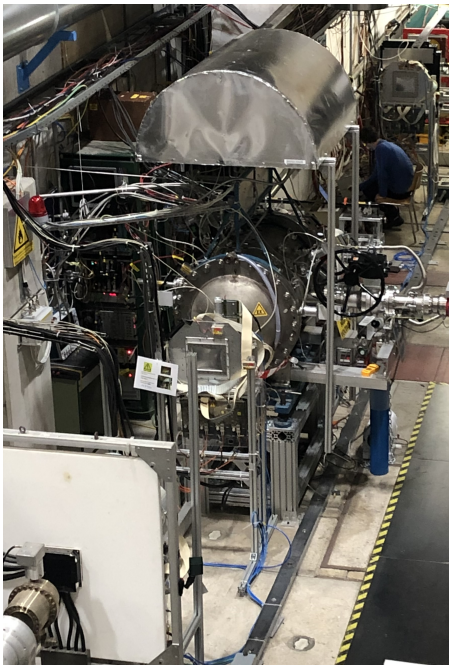

Figure 3.1: Pilot run setup at the M2 test beam location. The beam enters from the top right corner with the TPC in the center with a cover to collect possible leaking hydrogen. Silicon tracking detectors are place on the up- and downstream side of the TPC and are located inside cryostats. Scintillating fibers are visible on the most up- and downstream side (white holding structure).

For the tracking system consisting of silicon and scintillating fiber detectors, a general Beam Trigger (BT) selecting beam particles traversing the full setup is used. The beam trigger system consists out of two parts. One covers and selects beam particles passing through the full tracking surface of the silicon detectors and a second one consists out of two small elements placed with a certain distance selecting beam trajectories from the central beam region. The idea of the second element is to have beam trigger without prescaling selecting especially events centered on the readout structure of the TPC. This allows to have all muon events recorded for protons originating from the central region. The schematic layout of the pilot run setup is shown in Fig. 3.3.

Although the pilot run setup is located in the test beam area of the M2 beam line, which is about 40 m upstream of the original spectrometer location, the full spectrometer information is recorded in addition and foreseen to be merged with the data. Beam particles traversing the pilot run setup, are guided further along the beam line towards the spectrometer. Here, tracking and momentum measurement are available as well as calorimetry. The idea is to combine both measurements and obtain a momentum measurement of the scattered muon by the spectrometer. Furthermore, dedicated so-called BMS can be used to obtain the momentum of the incoming muon beam particle.

In the following, the test beam area and the single parts of the setup are presented. Besides the silicon and tracking detectors, the two beam trigger elements are discussed. In addition, the different beam optic options are evaluated.

3.2.1 M2 Test Beam Area

The pilot run setup is constructed at the so-called M2 test beam area, which is located about 40 meters upstream of the spectrometer inside the M2 beam line in a dedicated test beam area at the end of the beam tunnel. This area is also used for the installation of the CEDAR detectors if they are required for beam particle identification. In 2021 the data taking of COMPASS is performed with muon beam and no beam particle identification was needed and therefore, those detectors could be removed. By this, a space of about 13 meter is freed for various test beam setup. A full sketch of the beam line is shown in Fig. 1.10 with the indicated test beam location. It is accessible from the sides as well as from the top allowing installation of complex structures. Dedicated infrastructure has been installed to provided network, power and DAQ connections towards COMPASS. A schematic drawing of the area is shown in Fig. 3.2. For the PRM setup the 13 m long space allows a close-to final construction of the setup with the anticipated setup length of 10 m (cf. Sec. 1.2). The beam focusing at the test beam location does not have the optimal properties as in the intended target region, but has very similar properties.

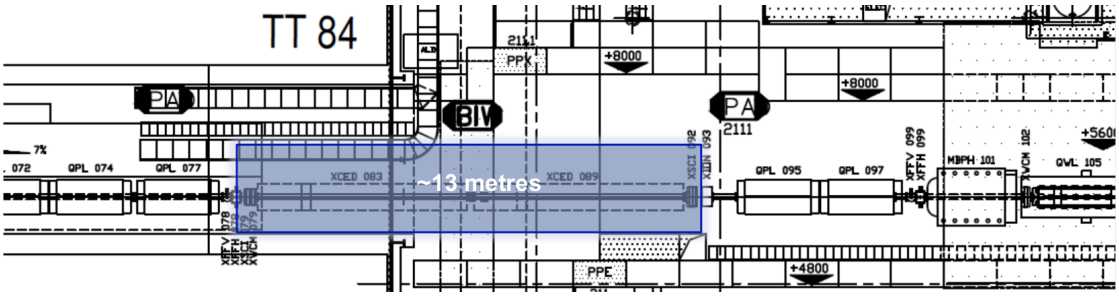

Figure 3.2: Schematic drawing of the test beam area in the M2 beam line and the indicated available space for the pilot run setup. Figure provided by [25], modified.

The test beam area is located between beam line elements required for focusing the beam towards the target area of the spectrometer. The test beam location is located in the part, where the beam is still pointing upwards before it is bent horizontal towards the spectrometer. This results in an inclination of the beam at the test location of about 3.6 mrad with respect to the spectrometer axis. This feature has to taken into account for a combined measurement of the spectrometer and the pilot run setup in the test beam location. The inclination of the beam is sketched in Figs. 1.10 and 1.11. Furthermore, due to additional focusing beam line elements between the test beam area and the spectrometer, the track association between the two areas need to be adapted accordingly, which has not been done in this configuration so far. In Tab. 3.1 the positions in the test beam area of the main components as transition between the beam line coordinates and the spectrometer coordinates are given. The test beam area starts after a MWPC used for the control of the beam optics. The center of the TPC in the setup is placed around $z = -43.2$ m corresponding to $z = 1087.2$ m in so-called beam line coordinates. Due to positioning constrains, the TPC could not be placed in the center of the test beam location, which results in a slight asymmetry of the resulting lever arms between the up- and downstream side of about 1 m.

Table 3.1: General positions in the M2 test beam area and the global spectrometer coordinates as reference also with the spectrometer target location. Positions of single beam line elements are shown in Fig. 1.10.

Location	Item	Beam line (m)	AMBER (m)
M2 test area	Start (after MWPC 15, 16)	1 079.6	−50.8
	IKAR TPC center	1 087.2	−43.2
	End (before Q34)	1 092.6	−37.8
spectrometer	target location	1 130.4	0.0

3.2.2 Layout

In Fig. 3.1 the pilot run setup is shown photographed from the downstream side towards the beam direction. The IKAR TPC is located in the center and covered with a roof, which is equipped with dedicated hydrogen sensors for safety reasons. The setup extents towards the up- and downstream sides including high-resolution silicon-microstrip tracking detectors inside dedicated cryostats and scintillating fiber detectors in white holding frames. A beam trigger system with two different elements is used. It is placed in the upstream lever arm and is not visible in the picture. In addition, a novel Gas Electron Multiplier (GEM) test detector is included in the setup, which is only used for detector and readout tests for the new front-end compatible with the new DAQ system. A sketch of the setup is shown in Fig. 3.3 with the precise positions listed in Tab. B.2. With BMS stations located upstream of the setup inside the beam line (cf. Fig. 1.10), a measurement of the incoming beam momentum is possible. The complete spectrometer is included during the data taking, allowing muon momentum measurement and muon identification together with calorimetry.

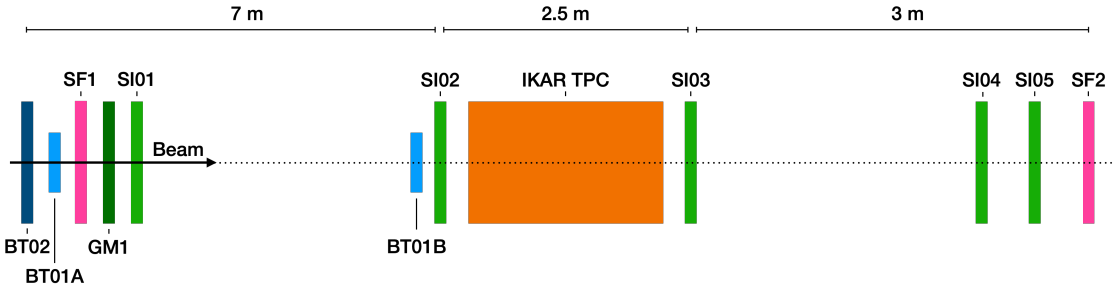

Figure 3.3: Schematic drawing of the setup for the pilot run with the beam coming from the left side. The central IKAR TPC is surrounded by silicon detectors (SI) on the up- and downstream side together with scintillating fibers (SF). A test GEM detector (GM) is positioned in the upstream part. Each side has a lever arm of about 3 m. The upstream lever arm is equipped with the BT elements.

The setup is located at the exit of the beam tunnel, with part of it still inside. It was found, that this results in a temperature gradient that influences the positioning of the detectors, which are mounted on dedicated aluminum frames instead of the original holding structures like an

optical bench, as usually used for the silicon detectors, to adapt for the beam required beam height. To take this into account, a so-called run-by-run alignment as utilized already for the test measurement in 2018 (cf. Sec. 2.3) plays an important role. Furthermore, these holding structures turned out not to be as stable as required in terms of movement, which also has to be accounted for in the alignment.

Beam optics

The inclination of the beam axis of about 3.6 mrad needs to be taken into account for the positioning of the setup. In Fig. 3.4 the simulated beam mean position and sigma values along the test beam area are shown. As coordinate system, the global spectrometer one is used. The expected focus point of the beam is located inside the central TPC volume, where a beam width of $\sigma_{x,y}$ = 15 mm is achieved. This focused beam was preferred to lower the beam-induced ionization noise (cf. Sec. 1.2.2) inside the outer parts of the TPC readout plane compared to a second, more parallel beam option, but with a larger resulting beam spot. In addition, the focused beam option benefits the usage of the dedicated small-size not-prescaled beam trigger element (cf. Sec. 3.2.2). The originally simulated beam values are given in beam line coordinates and required a translation into the spectrometer coordinate system to obtain the presented results. The expected 3.6 mrad gradient of the beam along the y-direction is added manually, since in beam line coordinates the beam has no inclination by definition since the coordinate system is chosen along the respective beam axis itself. Nevertheless, the predicted beam inclination fits well to the measured one later discussed in Sec. 3.6.

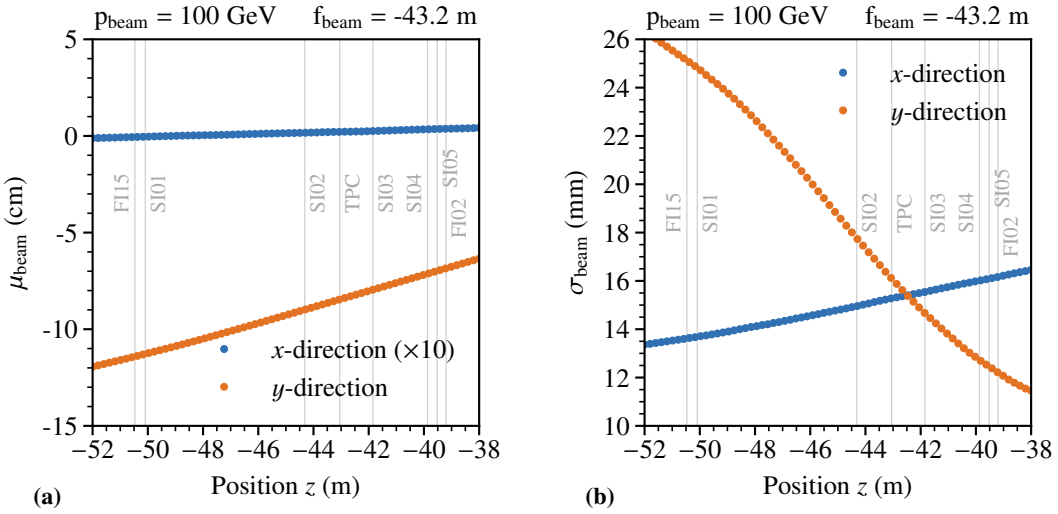

Figure 3.4: Beam mean (a) and width (b) in x- and y-direction of the focused beam option for the PRM pilot run. TPC and tracking detector positions are indicated.

To evaluate the pilot run setup, a dedicated simulation of it is performed. As input for the simulation, a realistic beam profile is required, to obtain results as close as possible to reality. This beam profile reassembles the relation between the position, gradient and respective momenta of beam particles. The beam profile takes into account the beam optics for the anticipated beam momentum of 100 GeV.

The beam optics in the test beam location are slightly different compared to the target area of the spectrometer, because additional beam optic elements are used to further enhance the beam optics towards the spectrometer target. For the beam test of the IKAR TPC, two different beam optic options have been considered:

- low divergence of the beam with the advantage of an equal-sized beam along the full length of the setup and the possibility to utilize a possible trigger on deflected muons due to the intrinsic low divergence, but with the disadvantage of a larger size of the beam spot inside the TPC disturbing the results of an energy resolution measurement, or
- a small beam spot with a larger divergence of the beam along the setup, not allowing a dedicated trigger system on deflected muons, but with the advantage of a small beam spot inside the TPC and especially in its central pad region, allowing a more close-to-final estimate of the setup's properties.

Those two different beam optics are compared in Fig. 3.5. In Figs. 3.5(a) and 3.5(b) the x-y-position of the beam spot at the target location is shown. The focused beam is well centered inside the TPC windows and the silicon tracking detectors with a width of $\sigma_{\mathrm{x}} = 10$ mm $\sigma_{\mathrm{y}} = 13$ mm, although its overall width is larger compared to the expected beam profile foreseen in the final location (cf. Sec. 1.2.6), it is much more improved compared to the feasibility test. The focused option shows a wide spread in the gradient of $\sigma_{\mathrm{d}x/\mathrm{d}z} = 0.5$ mrad and $\sigma_{\mathrm{d}y/\mathrm{d}z} = 1.5$ mrad along beam direction. Due to the beam coming from underneath the surface, the extent along y-direction is dominant. For the parallel option the beam gradients are smaller and on the level of around $\sigma_{\mathrm{d}x,\,y/\mathrm{d}z} = 0.3$ mrad. The width is broader and around $\sigma_{\mathrm{x}} = 15$ mm and $\sigma_{\mathrm{x}} = 30$ mm and only closely fitting into the openings of the TPC, which could result in an increased background due to the additional material located in the beam. Further details can be found in Apps. C.3 and C.4.

Studies regarding the beam positions in the spectrometer have been performed. The overall position along the spectrometer and the influence of the two spectrometer magnets SM1 and SM2 is investigated. Under normal data taking conditions they are operated at 2500 A and 4000 A, respectively. To adapt for the from 160 to 100 GeV reduced momentum, the magnet currents are lowered by 63 % to study the reconstruction behavior. It can be seen that a scaling of magnets results in an issue with the momentum reconstruction. The influence on the momentum reconstruction is shown in Fig. 3.6(a). Possible origin of the shifted momentum reconstruction could be the non-linear scaling of the magnetic field inside the magnet itself compared to the field map used in the reconstruction. To have the beam guided through the spectrometer along the foreseen beam axis, the first spectrometer magnet is switched off and only the second one is operated at the nominal. This option resulted in a sufficient position of the beam along the spectrometer magnets. The resulting beam spot in the most downstream GEM detector is shown

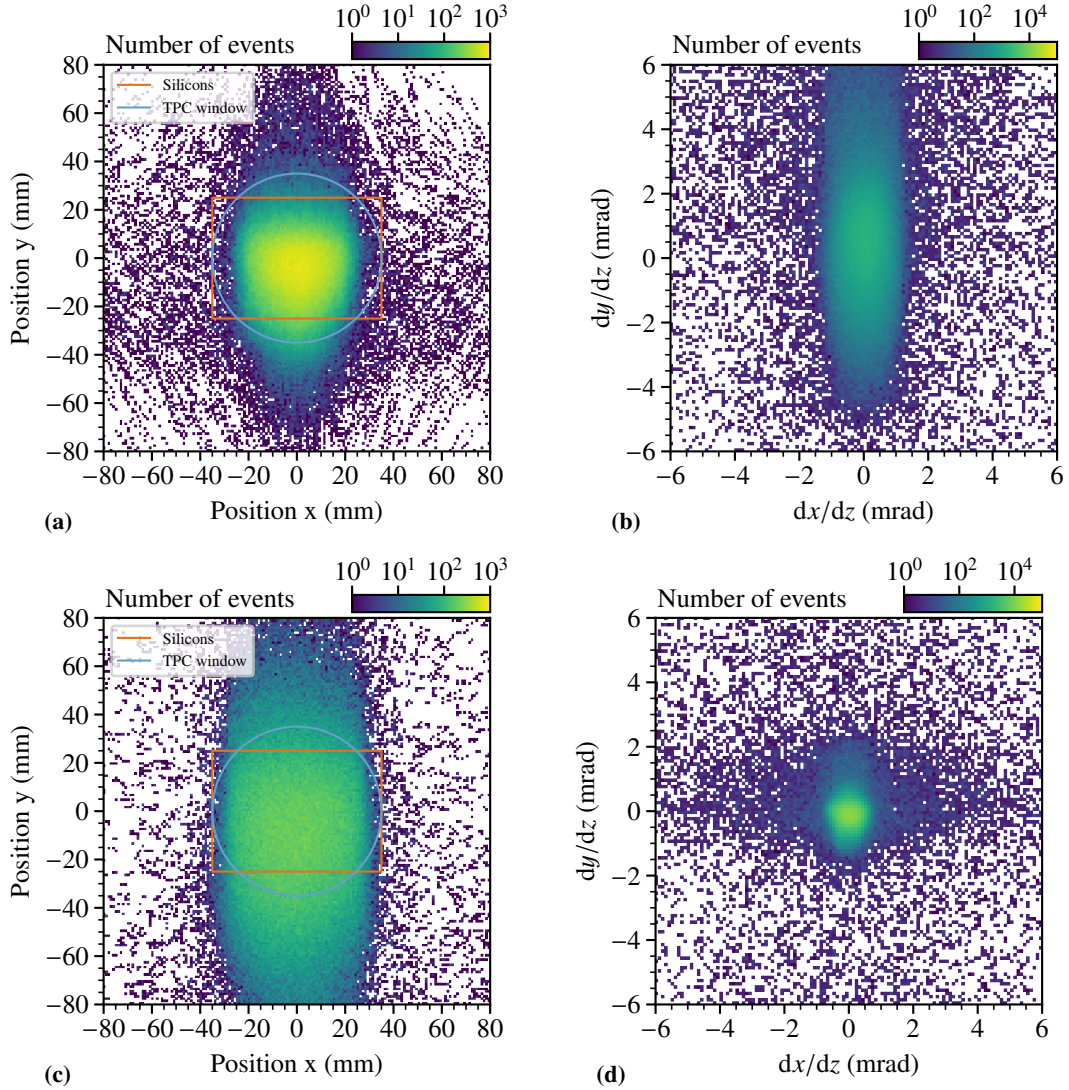

Figure 3.5: Beam optics comparison between the focused and parallel option. For the focused option in (a) and (b) the x-y-distribution with the indicated detector and TPC beam windows and the gradient along the beam axis is shown, respectively. The parallel beam option is shown in Fig. 3.5(c) and Fig. 3.5(d). Further details can be found in App. C.3 and App. C.4.

in Fig. 3.6(b) from the online event display. The beam is slightly shifted with respect to the center, but is still inside the active area of the small-angle tracking detectors. Due to the low beam rate of $2 \cdot 10^6$ Hz, the centers of the used GEM along the spectrometer could be switch on to improve the tracking during the pilot run data taking. During normal spectrometer operation with beam intensities of up to $4 \cdot 10^7$ Hz [26], the centers are switched off to avoid a high-voltage trip of the detectors. Other detectors along the spectrometer are equipped with dedicated beam holes for the non-deflected beam to pass through.

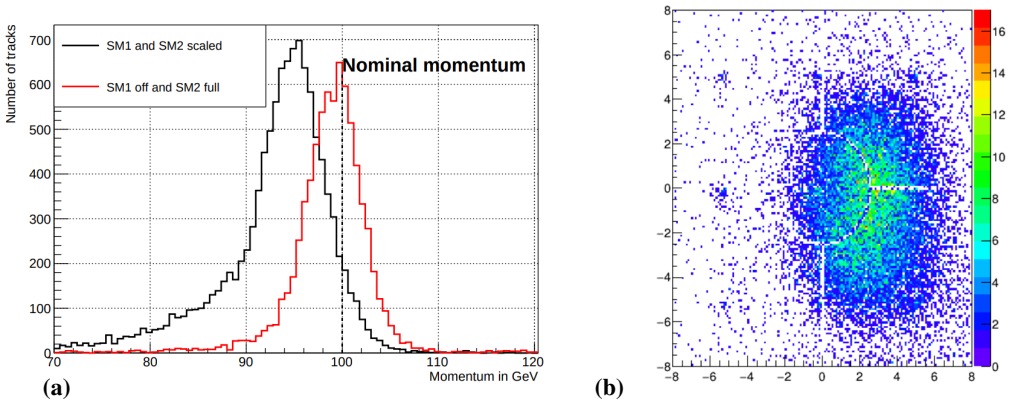

Figure 3.6: In (a) the reconstructed beam momentum during the beam commissioning with the two different settings is shown. A nominal momentum of 100 GeV is used. In (b) the beam spot measured by the last GEM detector in the spectrometer in the online event display is shown. Units are (cm). Figures provided by [36, 59].

Silicon Tracking-Detectors

For the tracking system, high-resolution silicon-microstrip detectors are installed together with a normal triggered DAQ system. The silicon detectors are the same warm stations as used during the test measurement (cf. Sec. 2.1.4). In total, five stations are placed along the setup of the measurement shown in Fig. 3.1. Two stations (SI01, SI02) are placed along the upstream lever arm with a distance of about 5 m. Three additional stations are placed along the downstream lever arm, whereas one station (SI03) is located in a cryostat directly downstream of the TPC and three two additional stations (SI04, SI05) are placed at a distance of about 2 m further downstream, combined in one single cryostat at the very downstream side. Since the TPC could not be positioned in the center of the available space, the silicon stations have been placed in a way that the remaining space matches roughly the intended 3 m baseline.

This so-called warm stations are not operated in a cryogenic mode, but are flushed and cooled with gaseous nitrogen to avoid moisture accumulating on the silicon substrate and prevent overheating of the readout chips placed in the closed volume of the cryostat. For temperature control, the PT100 sensors that are placed on the detector module are read out and their information is also used as an interlock for the power supply of the readout chips inside the cryostats. To match the beam height in the test beam area, dedicated adjustable support structures based on aluminum profiles are used. The silicon detectors provide tracking with a spatial resolution of about $\sigma = 14$ µm and a time resolution of $\sigma = 2$ ns. They are based on single strip readout and provide four planes per station. The planes are labeled as U-, V- and X-, Y- planes each combined to one silicon module (cf. Sec. 5.1). The single modules are rotated by five degrees with respect to each other and cover an active area of $70 \times 50\,\mathrm{mm}^2$. Further details on the detector concept can be found in Sec. 2.1.4 and Chap. 5.

Scintillating-Fiber Tracking-Detectors

For the tracking system two, scintillating-fiber tracking detectors are operated. The detectors, SciFi15 and SciFi02, are normally operated within the COMPASS spectrometer. In the test setup, SciFi15 is placed in the upstream lever arm and SciFi02 is placed in the downstream lever arm. The detectors are installed to provide track timing in the two regions and are used to cross-check the silicon measurement. Furthermore, the scintillating fiber detectors are more easy to install and provide beam profile information without detailed calibration purposes right from the beginning of the data taking. This feature is used to tune the beam position in the test area location in an early stage.

Table 3.2: Parameters of scintillating fiber stations used in the pilot run. [84]

detector name	projections	x-size (cm)	y-size (cm)	fiber size (cm)	pitch (cm)	channels (per projection)
SciFi15	X,Y,U	4.51	4.51	0.10	0.07	64
SciFi02	X,Y	3.94	3.94	0.05	0.04	96

The scintillating fibers can withstand rates more than $3 \cdot 10^6$ Hz per fiber and allow a precise hit-time information. Each station consists out of X- and Y-projections and in case of SciFi15 an additional U-projection rotated by 45 degree with respect to the other projections is present. To obtain sufficient high number of photo-electrons, several layers of fibers are combined in a stack in each projection and read out with PMTs. In comparison to the UTS stations where the SFH only has one layer per plane and therefore a much more reduced material budget, which is more suitable for the measurement of small scattering angles as required in the PRM. They provide an active area of around $40 \times 40\,\mathrm{mm}^2$ and are aligned with the silicon surface. The parameters are listed in Tab. 3.2. [84]

Trigger System

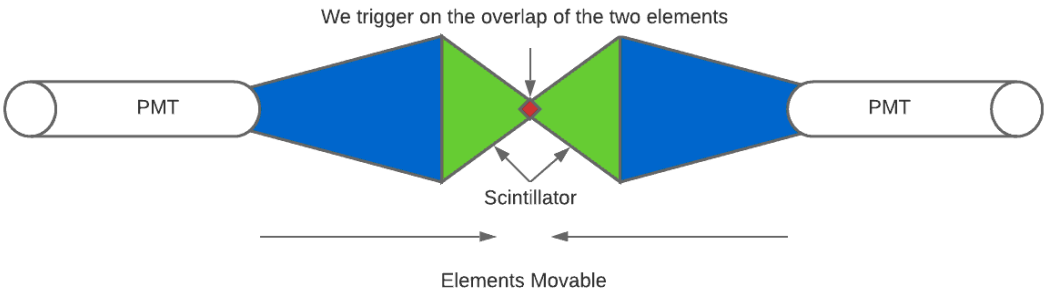

Figure 3.7: Schematic drawing of the enrichment beam trigger element to for the pilot run. Figure provided by [59].

In the pilot run measurement, two dedicated bream trigger systems are used. With the goal of reducing the trigger rate to the maximal one that the DAQ system can record without applying prescaling. The possible trigger rate is about a factor two larger compared to the test measurement in 2018. A maximum of about 40 kHz is possible from the front-end and DAQ side. To achieve a non-prescaled triggering, beam particles are selected with a low divergence from the central beam region, which then are passing through the central pad-region of the TPC. Those events are intended to be those with the recoil protons originating from the center of the radial segmented pad plane. The TPC is not using this trigger information, but the tracking detectors are selecting all tracks passing through the central pad region of the TPC. A schematic drawing of the central beam trigger element is shown in Fig. 3.7. An overlap between movable scintillators is used to adjust for the correct overlap size in order to obtain the required beam trigger rate. Two of those elements are used in a distance of about 6 m as given in Tab. B.2 with their detector label BT01A and BT01B. Both trigger elements are operated in coincidence mode to select traversing beam particles.

To evaluate the required overlap and size of the two trigger elements, preceding studies have been performed in order to estimate the resulting trigger rate. In Fig. 3.8 the results for different sizes are shown. Based on simulations it is found, that in case of a single trigger element about 5 mm edge length is required to select events from the inner part of the beam at 40 kHz trigger rate suitable for the DAQ. Using two elements in coincidence with the same size at a distance of 6 m the natural selection of a certain beam fraction with a suitable gradient to pass both elements reduces the rate further. Around 6.5 mm overlap results in a sufficient trigger rate.

The beam hit profiles are shown in Fig. 3.9. In the 1-d projection, the central beam trigger element is clearly visible. Due to a comparable trigger rate between the central and the large beam trigger element, the integrated number of triggered events in both is comparable. Furthermore, noise channels between the single APV25 chips in steps of 128 channels of the silicon detector are visible (cf. Sec. 5.1). In the 2-d projection, the sharp beam trigger element structure is visible

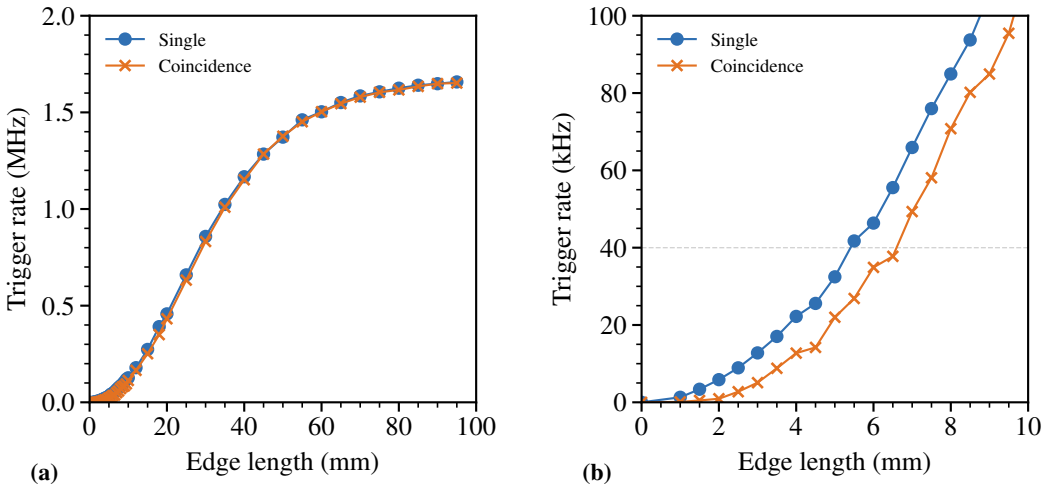

Figure 3.8: Evaluation of the rate for the central beam trigger studies depending on overlap of the elements. In (a) the full region is shown and a close-up of the small-edge region is shown in (b).

with the estimated size of about 6.5 mm. The influence of the trigger element becomes washed out along the setup due to the gradient of the beam. Whereas it is sharp in the upstream part, especially SI01 and SI02, the shape is less pronounced in the downstream stations. An overview of the 1-d planes is given in Fig. C.11 and for the 2-d planes in Figs. C.12 and C.13. An overview of the single hit profiles are given in App. C.10.

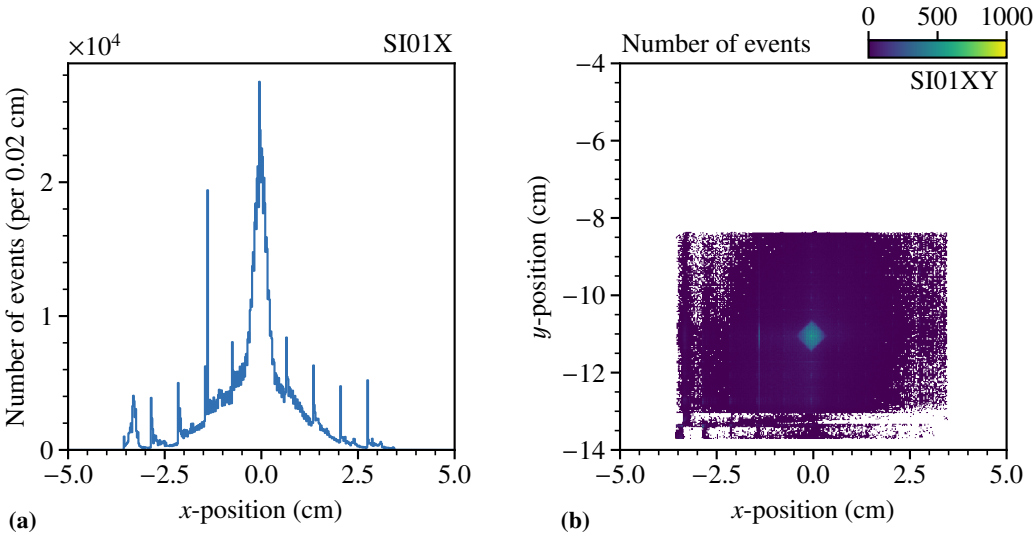

Figure 3.9: Beam profiles for SI01 are shown. In (a) the 1-d hit profile of the X-projection is given. The superposition of the central small beam trigger and the large beam trigger are visible. The 2-d projection in X-Y-plane is shown in (b) with the central beam trigger element visible as rectangular shape.

In addition, a trigger element BT02 with a comparable size of $70 \times 50\,\mathrm{mm}^2$ as the silicon tracking-detectors is used. It is the same element as used in the test measurement in 2016 as shown in Fig. 2.4(b). To distinguish the single trigger decision, so-called trigger bits are recorded and are listed in Tab. 3.3. For calibration purposes, a so-called true-random trigger based on the decay of an external radioactive source and is used. For an estimate of the trigger rate of the TPC, which is operated in the self-triggering mode, those triggers are recorded as well. Due to a technical issue, the recorded TPC triggers are recorded with a trigger-mask value of 0. For the later analysis, the beam triggers are selected by this trigger mask. Compared to the test measurement in 2018 the much more focused beam did not cover the full area of the trigger elements as well as the tracking detectors and therefore possible edge effects in the outer region that have been discussed in Sec. 2.1.2 are not visible.

Table 3.3: Used trigger bits for the beam triggers, TPC and a true-random trigger. The respective prescaling and their trigger bit-mask is given.

trigger name	trigger bit-mask	value	in rate (kHz)	prescaling	out rate (kHz)
BT01	0000 0010 0000	32	20.0	1	20.0
BT02	0000 0100 0000	64	$7 \cdot 10^3$	67	20.0
TPC	0010 0000 0000*	512*	0.04	1	0.04
True random	0100 0000 0000	1024	5.0	10	0.50

* recorded event triggers have trigger mask 0.

IKAR TPC

For the pilot run, the so-called Ionization Chamber for Hadronic Reactions (IKAR) TPC is used as active-target detector prototype. The IKAR TPC has been operated already since the 1970s at the North Area of CERN in several elastic-scattering experiments [29–31]. A schematic drawing is shown in Fig. 3.10. The gas volume can be filled with up to 8 bar. It is equipped with two 400 mm long drift cells and beryllium-based beam windows on the up- and downstream side, allowing the incoming and scattered beam particles to pass the TPC walls and traversing low material budget parts only.

The inner part is equipped with two anode structures used as readout in each drift cell and the cathode in the center. The anodes have radial size of 205 mm, allowing the measurement of the deposited energy along the recoil-proton path. A so-called Frisch grid is placed upfront each anode structure at a distance of about 10 mm to avoid induced signals by drifting ions, whereas the electrons drift towards the anode through the grid. Those vertically placed nickel-chromium grid wires have a pitch of 1.5 mm [85] and can be seen in Fig. 3.11(a). Field shaping rings are placed around the drift volume to ensure a constant and homogeneous electric field between the cathode and anodes. The TPC can be filled with helium, nitrogen or hydrogen gas for different purposes. For storage, the TPC is under helium atmosphere with slight over pressure to avoid contamination entering from the outside. In case of internal modification air and moisture depositing inside the volume and attaching to the materials need to be removed by flushing and heating. Dedicated heating belts can be mounted on the outside to enhance the evaporation of water from the inner volume. This procedure may take several days and was performed in the scope of adapting the inner structure of the IKAR TPC [85]. Due to the required internal modification, those steps have been performed prior to the pilot run to install the new anode structures.

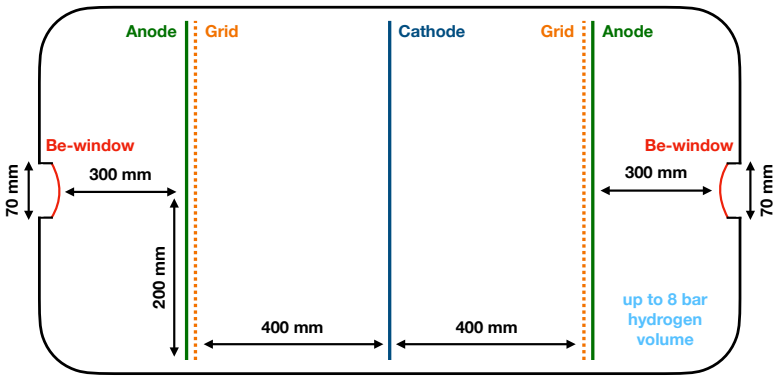

Figure 3.10: Schematic drawing of the IKAR TPC with the two 400 mm drift cells between the anode with grid and cathode. The up- and downstream beam windows are indicated. Figure provided by [37], modified.

For calibration purposes a test-pulse generator is used sending pulses to the electrodes with a fixed amplitude in a comparable scale as the recoil proton energy. The energy scale is calibrated via a ^{241}Am source emitting α-particles with an energy of 5.486 MeV placed on the grid as well as on the cathode, allowing the control of the gas properties and impurities. Further details and the full mapping of the pad plane is shown in App. C.1. To adapt for the required beam height at the test beam location of about 145 cm, an additional holding structure of the TPC itself was required. Dedicated safety tests have been performed to ensure its stability.

The IKAR TPC serves as a down-scaled version of the planned new TPC. The new design of the TPC will have twice the number of drift cells of the IKAR and will offer a larger radial size of 285 mm and therefore an increased kinematic range of the recoil proton of up to $Q^2 \approx 0.02$ GeV$^2/c^2$ corresponding to kinetic proton energies of about 10 MeV. The simulated range-values shown in Fig. 1.14(b) agree with the results quoted in [31]. A threshold of 0.5 MeV is used [85] corresponding to a $Q^2 = 10^{-3}$ GeV$^2/c^2$ and a resulting muon scattering angle of about 300 µrad. The drift time is expected to be about 140 µs [85]. In previous data taking like the test run in 2018 (cf. Sec. 2.1.3) with the ACTAF2 TPC, the drift time was smaller due to an increased electric field during those measurements.

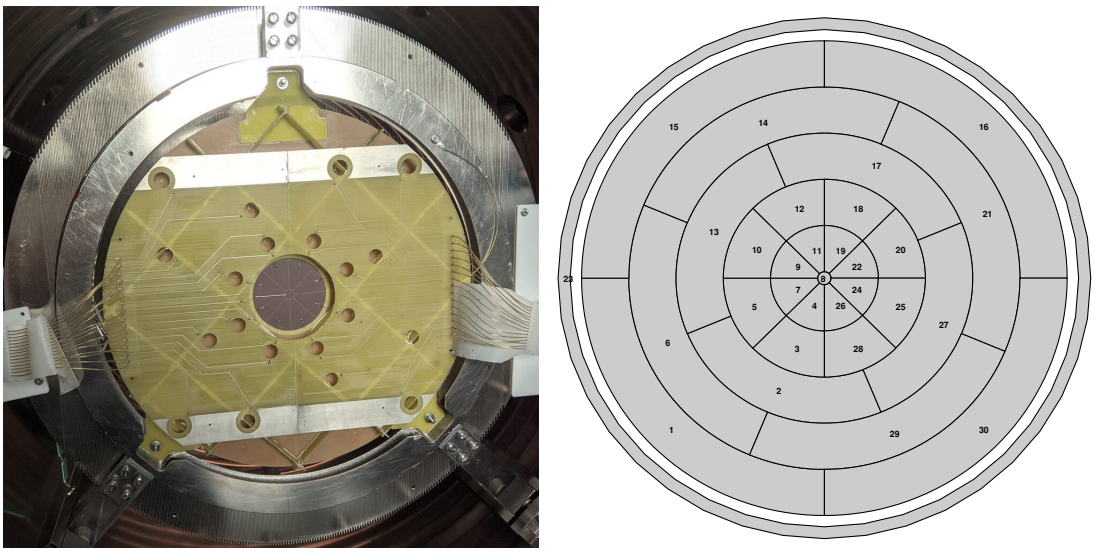

(a) **(b)**

Figure 3.11: In (a) the mounted pad plane of the IKAR TPC is shown. Besides the single pad connectors and the respective wiring the vertical Frisch grid is visible. The schematic structure and mapping of the (upstream) pad plane is shown in (b). Figure provided by [37].

3.3 Silicon Detectors

A special focus is set to the silicon-microstrip detectors used during the measurement. As already briefly discussed in Sec. 3.2.2 five stations are used during the pilot run. This required preparation work since it is the first time since 2012 where a total of five stations have been operated in parallel. Since the preceding COMPASS data taking ended with the beginning of the pilot run, the equipment in terms of power supplies, cables and front-end electronics of the installed cold silicons from the COMPASS spectrometer could be moved to the pilot run setup.

Based on the obtained knowledge in terms of operation and cooling of these so-called warm stations during the test measurement in 2018 (cf. Chap. 2), nitrogen supply for flushing together with temperature monitoring was installed for each station. In addition, new optical fibers were installed and the existing ones could be left in place to minimize the transition work between the spectrometer installation and the pilot run setup. All five silicon detectors have been tested prior to the installation to ensure their functionality and to prepare their required settings of the front-end and spot possible issues beforehand.

During the data taking, issues with the first silicon station SI01 were present. The front-end electronics were unstable and needed to be manually restarted several times during the operation. The reason is not yet fully understood. The background radiation at the position of the front-end electronics, shielded even by a beam line magnet structure, was at a level of around 2 µSv/h, and should not cause issues. The stability problems could be related to possible jitters on the TCS signal distributed to the front-end electronics of SI01. A pure hardware issue related to the attached font-end electronics were excluded by swapping those with working ones and also a dedicated power supply was tested without success.

The naming scheme for the silicon stations differs between the test measurement and the pilot run. SI01 and SI02 stayed the same, whereas SI03 was added in the pilot run and was not present during the test measurement. SI04 and SI05 are the same as SI03 and SI04 during the test measurement. In the following the preparation and operation regarding the silicon detectors for the pilot run setup are presented. The depletion voltage setting and time calibration with the obtained time resolution are discussed, as well as preliminary efficiencies of the detectors and the spatial resolutions of the five stations.

3.3.1 Depletion-Voltage Scan

Prior to the data taking, a scan of the depletion voltage for the detector modules is required to find the best working point for each module. The procedure is similar as during the feasibility test discussed in Sec. 2.1.4. To obtain the depletion zone on the silicon wafer, this so-called depletion-voltage is applied. Depending on the voltage, the common-mode corrected noise $\sigma_{\text{CM, corr.}}$ is reduced. The results are shown in Fig. 3.12. They show the expected behavior between the single planes, as described in Sec. 5.4.

Table 3.4: Depletion-voltage settings and resulting leakage currents of the silicon detectors.

Detector module (type)	2021	
	V_0 (V)	i_{mes} (µA)
SI01UV (warm)	150	0.017
SI01XY (warm)	150	0.016
SI02UV (warm)	170	0.020
SI02XY (warm)	170	0.022
SI03UV (cryogenic)	150	0.005
SI03XY (warm)	150	0.019
SI04UV (cryogenic)	140	0.005
SI04XY (cryogenic)	140	0.006
SI05UV (cryogenic)	150	0.005
SI05XY (cryogenic)	150	0.005

The obtained results are in agreement with the ones from the test measurement in 2018 for the stations that have been used at that time. The early noise decrease of SI01 is also present in 2018. The additional SI03 station also shows the expected results. Due to already existing issues with SI04X, parts of the scan are missing. In addition, a lower leakage current in the cryogenic version of the detector module can be seen as listed in Tab. 3.4. This is most likely caused by the increased radiation dose collected by the warm stations over their the operation years. The SI03UV plane was missing before the pilot run, and therefore a new spare detector module was installed. It shows a comparable leakage current as the other cryogenic modules that have been operational since 2008. During the data taking, the depletion voltage is normally not changed and is constantly applied.

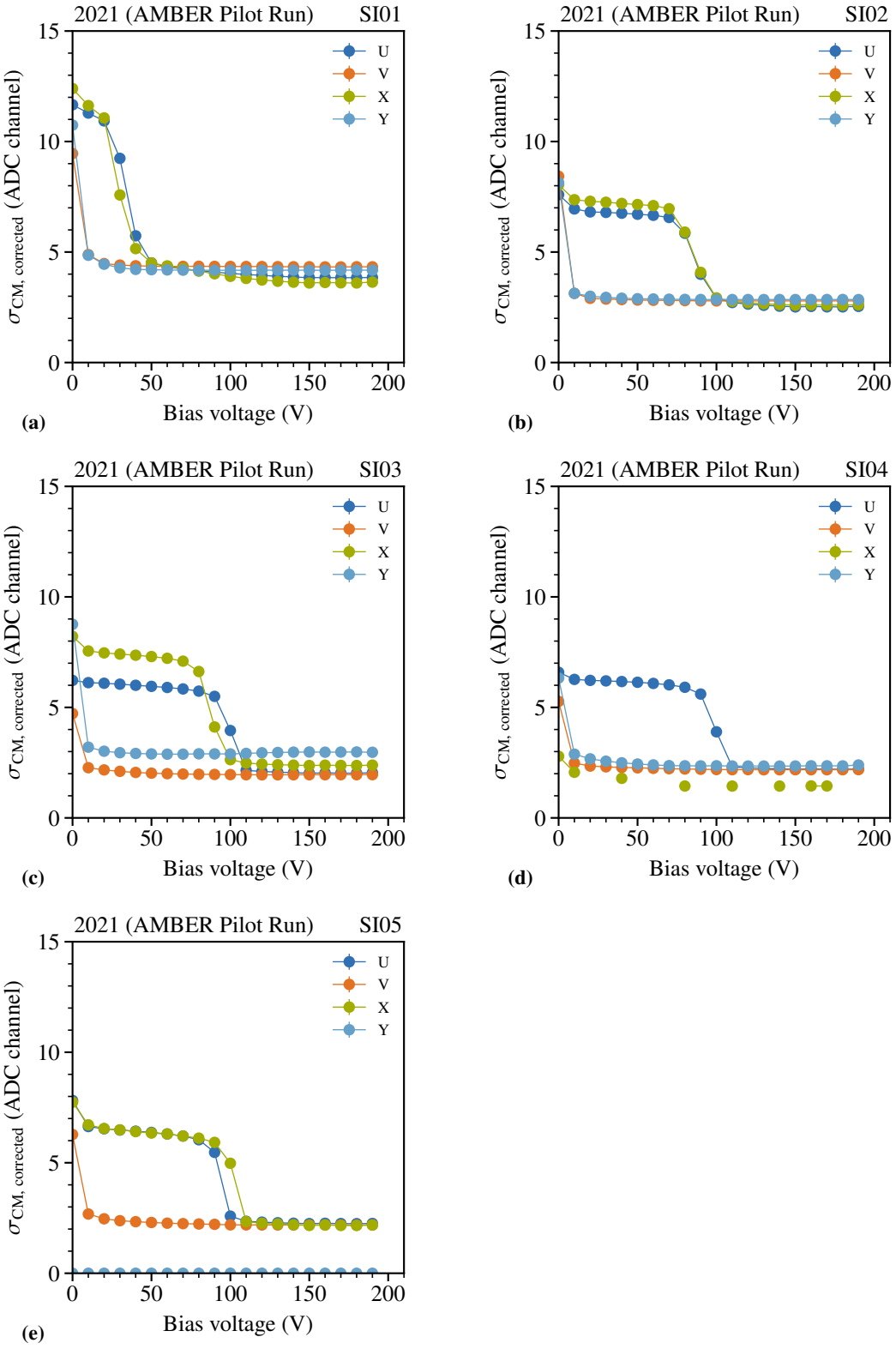

Figure 3.12: Depletion-voltage scan for the pilot run of the warm silicon tracking detector stations. The detector plans SI04X and SI05Y have been partially damaged in previous data takings.

3.3.2 Time Calibration

The silicon detectors require a so-called time-calibration, which is used to extract the time of the induced signal within each strip by the traversing particle. This is required, if other detectors are involved in the tracking, and the hit time information can be used to for the track finding. In the feasibility test in 2018 only the silicon detectors have been used, and therefore the resulting track time is determined by only those detectors, and further time selection was not applied. In the pilot run two additional scintillating fiber detectors are installed providing precise track time information. To allow a selection of the track time and also using this information for the track propagation towards the spectrometer and the BMS, a time calibration of the silicon detectors is required.

The induced signal on each strip is sampled in steps of 25.72 ns corresponding to the TCS clock cycle of 38.88 MHz [86] by the APV25 chip and attached ADCs. The APV25 chips provides amplitude information by sampling three consecutive signals as shown in Fig. 3.13. Starting with an arriving trigger signal, they extract the three consecutive signals from a 190-sample-size storage ring-buffer. The initial time difference between the arriving trigger signal and the stored signal in the ring buffer is the so-called latency. This needs to be adjusted prior to each data taking in order to read the correct hit information at a given trigger signal. Based on those three signals, the rising edge of the amplitude is reconstructed and the arrival time of the particle can be determined.

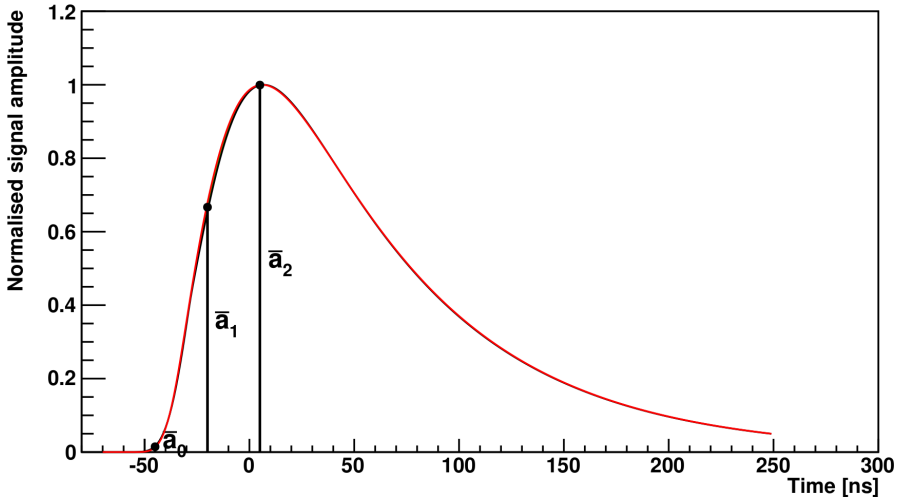

Figure 3.13: Example of a shaped silicon signal extracted from 2010 data (SI03Y). The desired position of the three sampled amplitudes is indicated. Figure taken from [87].

As comparison, the foreseen ALPIDE-based SPD for the UTS (cf. Sec. 1.2.3) only provides a hit/no-hit information for each pixel. No amplitude information is present, which could be utilize to extract a more precise timing or correlation between single planes, as it is done with the so-called mate clustering during the hit reconstruction of the silicon detectors [88]. More details as in the following performed silicon time calibration procedure can be found in [87].

The layout of the timing calibration parameters in the calibration procedure has been corrected starting with the 2016 time calibration. The single cluster time shift depending on the expected cluster sizes[2] one or two was added multiple times, resulting in a wrong single cluster timing offset. Based on these options, the so-called mate clustering, which relies on the respective partner plane of each detector, results in correct results again. New digits have been added to the detector raw information as lower and upper time error for the extracted amplitude ratios. The time calibrations have been performed for the years 2016, 2017, 2021 (COMPASS) and 2021 (AMBER) and 2022. For the time calibration the three amplitudes samples $A_i(t)$ at a given time t_{TCS}, the so-called TCS phase is defined by

$$t_{\text{TCS phase}} = t_{\text{TCS clock}} - t_{\text{trigger}}. \tag{3.1}$$

are extracted. They are written in terms of the TCS clock, defining the time steps of $\Delta = 25.7$ ns and depend on the energy-loss within the depletion zone of the detector module. The three amplitudes are defined as

$$a_0 = A(t - 2\Delta), \quad a_1 = A(t - \Delta) \quad \text{and} \quad a_2 = A(t). \tag{3.2}$$

To remove the absolute dependence of the amplitude, the ratio normalized to the last amplitude are used to extract the timing information, as

$$r_0 = \frac{a_0}{a_2} \quad \text{and} \quad r_1 = \frac{a_1}{a_2}. \tag{3.3}$$

The time dependence of the ratios r_0 and r_1 can be parameterized according to [23, 87], as

$$r(t) = r_0 \cdot \exp(\exp(-s(t')) \quad \text{with} \tag{3.4}$$

$$s(t') = \frac{a+c}{2} \cdot t' + \frac{a-c}{2}\left(\sqrt{t'^2 + b^2} - |b|\right) + d \quad \text{and} \tag{3.5}$$

$$t' = t - t_0. \tag{3.6}$$

[2] Number of strips contributing to a hit. Mostly its one or two. Sometimes cluster sizes of three or larger occur, but they are expected to be originating from delta electrons hitting additional strips.

To calculate the resulting time, the inverted functions are required, given as

$$t(r_i) = t_0 + s^{-1}\left(-\log\left[-\log\left(\frac{r_i}{r_0}\right)\right]\right) \quad \text{with} \quad i = 1, 2 \tag{3.7}$$

$$\text{and} \quad s^{-1}(x) = \frac{1}{2ac}\left[(a+c)\cdot f(x) - (a-c)\cdot\sqrt{f(x)^2 + acb^2}\right], \tag{3.8}$$

$$\text{with} \quad f(x) = x - d + \frac{|b|}{2}\cdot(a-c). \tag{3.9}$$

In Fig. 3.14 the time dependence of the amplitude ratios r_0 and r_1 at different TCS phases and their given parametrizations are shown. The full overview for all five stations in the pilot run is shown in Figs. C.4 and C.5. For each data taking, the timing needs to be adapted in case that the delay towards the trigger signal has changed. Since the time resolution is in O(ns) even a slight change in optical fiber length between the trigger signal and the detector results in a visible change. At the beginning of each data taking, the amplitude ratios are extracted using a dedicated low-intensity beam to avoid pile-up signals in the detector, which alter the extracted amplitude ratios. Within this procedure, different latency setting data is obtained by shifting the latency of the detector in steps[3] of up to $\pm 3\Delta$ to cover the full range of the amplitudes, which results in the visible areas in Fig. 3.14 each with a width of $t_{\text{TCS}} = \Delta$.

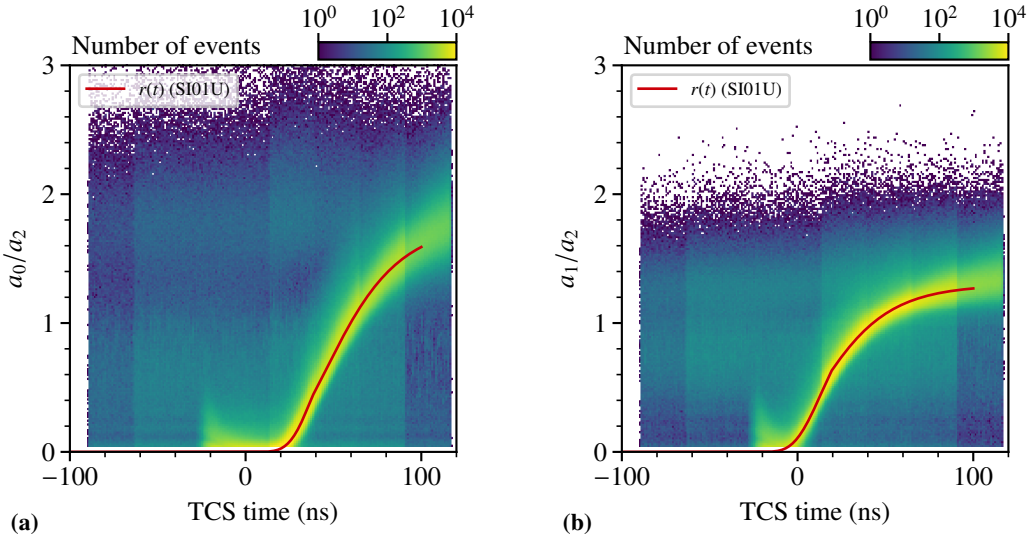

Figure 3.14: Time dependence of the amplitude ratios r_0 shown in (a) and r_1 shown in (b) as example for SI01U for the AMBER pilot run. The ratios have been obtained by shifting the detector latency in slices of $\Delta = 25.7$ ns.

[3]The latency can be adjusted in steps of 25.72 ns corresponding to the TCS phase. A fine-tuning is possible using the clock delay in the APV25 and ADC (cf. Sec. 5.1).

To adapt for time difference obtained from the two different ratios, absolute shift of the parametrization values are required. Based on the mean track time of the measurement, the uncorrected time ratios shown as example in Figs. 3.15(a) and 3.15(b) for the U- and V-plane of SI01. A calibration shift is applied to compensate the offset towards zero. In the next step, the calculated time based on the cluster size is correct and is required to be centered around zero to not widen unnecessarily the timing peak. Adaptions to the existing time calibrations have been made. The used parameters have been adapted in order to allow this shift for the single cluster shapes. Initially these parameters were wrongly implemented. This adaption is existing starting with the 2016 time calibration and allows the usage of the mate clustering using the correlation of two clusters in the corresponding mate plane. The resulting time calibrations are stored in the production database to be available for the reconstruction of the data.

The time resolution is defined by the residuum towards the track mean time calculated by the hit time of the high-resolution scintillating fibers placed in each lever arm. Results are shown in Figs. 3.15(c) and 3.15(d). With the used warm stations, resolutions of down to $\sigma = 1.7$ ns can be achieved. Corrections to the single ratio and cluster-size dependent times are indicated. Furthermore, a difference between the two wafer sides (U to V as well as X to Y) can be observed with the latter one being increased by about 20 %, which is connected to the wafer design shown in Fig. 5.2. An increased time resolution benefits from the improved charge sharing due to the intermediate strips on the respective sides shortening the travel distance by the additional electric field. The obtained single strip time is used to define the resulting cluster time and construct the final hit time.

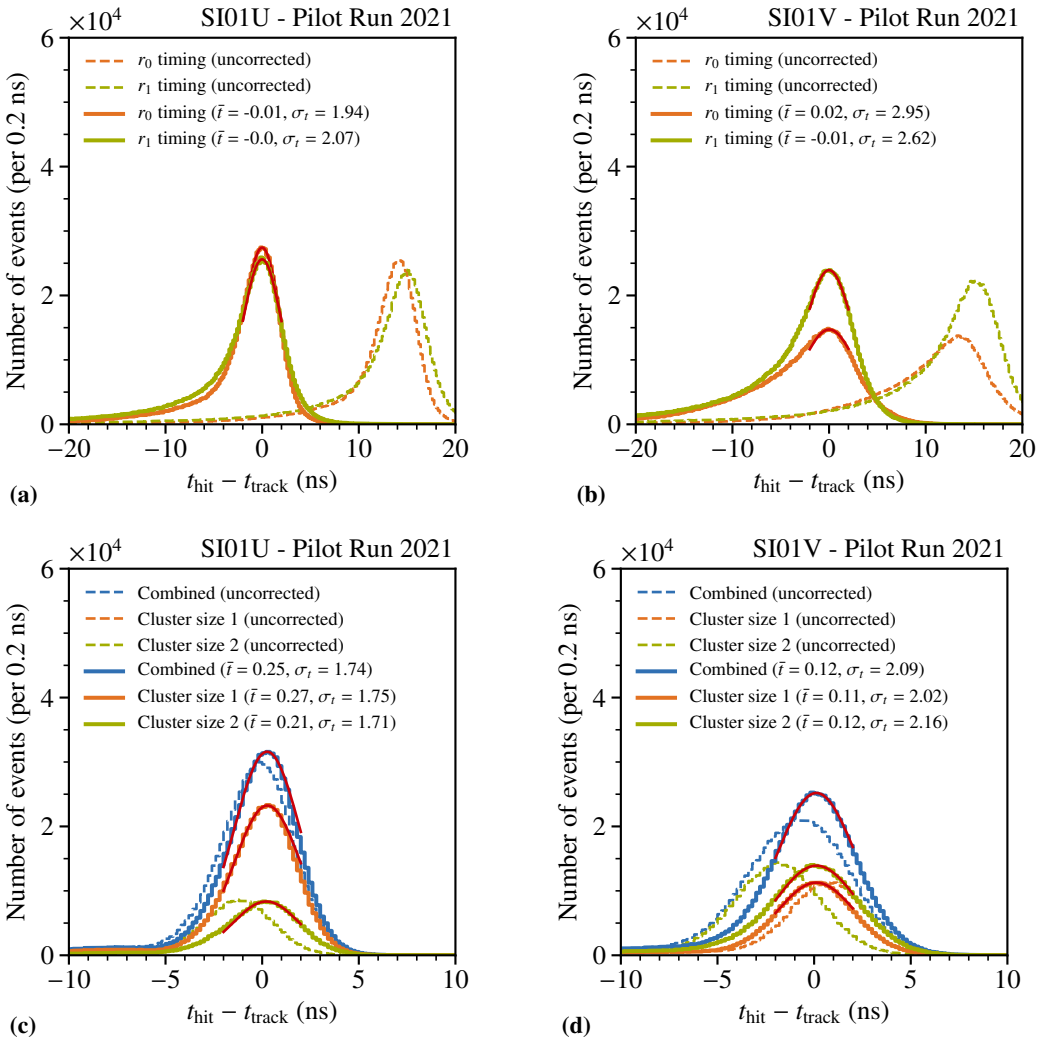

Figure 3.15: In (a) and (b) the resulting ratio time resolutions for SI01 U- and V-plane are shown with the respective Gaussian fit to the main peak. The resulting time resolution also for different cluster sizes is shown in (c) and (d). The respective uncorrected distributions are indicated as dashed lines.

3.3.3 Efficiency and Spatial Resolution

As basic characteristics the efficiency, and spatial resolution of a tracking detector are used. To determine the tracking efficiencies of the silicon detectors, the single planes have to be removed from tracking and especially track finding to not bias the results. Furthermore, using the respective plane in the track reconstruction will automatically improve the calculated residual between the hit and track position, since the track is pulled towards the hit. The basic efficiency does not take into account background hits due to noise or pile-up. This so-called apparent efficiency ϵ_{app} is given by

$$\epsilon_{\text{app}} = \frac{\text{number of found hits}}{\text{number of expected hits}}. \tag{3.10}$$

A found hit is taken into account, depending on the so-called road width, as the area around the expected hit position. Here a $3\sigma \approx 45$ µm is used as road width assuming a conservative $\sigma = 15$ µm based on the about 50 µm pitch of the detector. In case of a large background in terms of additional noise hits, the efficiency can be significantly influenced. For this, the background needs to be taken into account [26]. To determine the real efficiency ϵ uncorrelated background hits have to be evaluated that occur within the road width around the expected hit position with the background probability b and therefore artificially increase the apparent efficiency by

$$\epsilon_{\text{app}} = \epsilon + b(1-\epsilon) \quad \text{with} \quad b > 0 \quad \text{and} \quad 0 \leq \epsilon \leq 1 \quad \Rightarrow \quad \epsilon_{\text{app}} \geq \epsilon. \tag{3.11}$$

In Figs. 3.16(a) and 3.16(b) the estimated background probability for the SI01 U- and V-plane is shown. A background probability of up to 0.4 % is present during normal operation, mainly driven by the induced noise between the single APV25 chips. Nevertheless, the overall probability only has a minor contribution to the efficiency shown in Figs. 3.16(c) and 3.16(d) for the respective planes. The difference is below 0.02 % in the central region and in case of problematic chips here on the outer parts in can reach values of up to 3 %. The background effects are small and for simplicity reasons, only the apparent efficiencies are shown in the following.

The apparent efficiency in the 1-d and 2-d case for the SI01 U- and V-plane are shown in Fig. 3.17. For the U-plane the efficiency drops on the outer parts, this might be artificial due to statistical effects. The smaller V-projection is covered more. Both planes show an efficiency $\epsilon_{\text{app}} > 96$ % in the central region. Single broken strips are also visible in the 2-d projections. Taking the background contribution shown in Fig. 3.16 into account, especially the resulting difference towards the corrected efficiency, shows that the main difference rises at the outer or broken chip regions with lower efficiency. A summary of all planes and projections is given in App. C.9. From the 2018 test measurement, it is expected that the efficiencies are close to 100 % and flat over the full surface. The shown preliminary efficiencies differ from these expectations and are under further investigation. Besides the discussed possible origins of the shape, the current version of the alignment and track reconstruction might introduce possible issues in this regard.

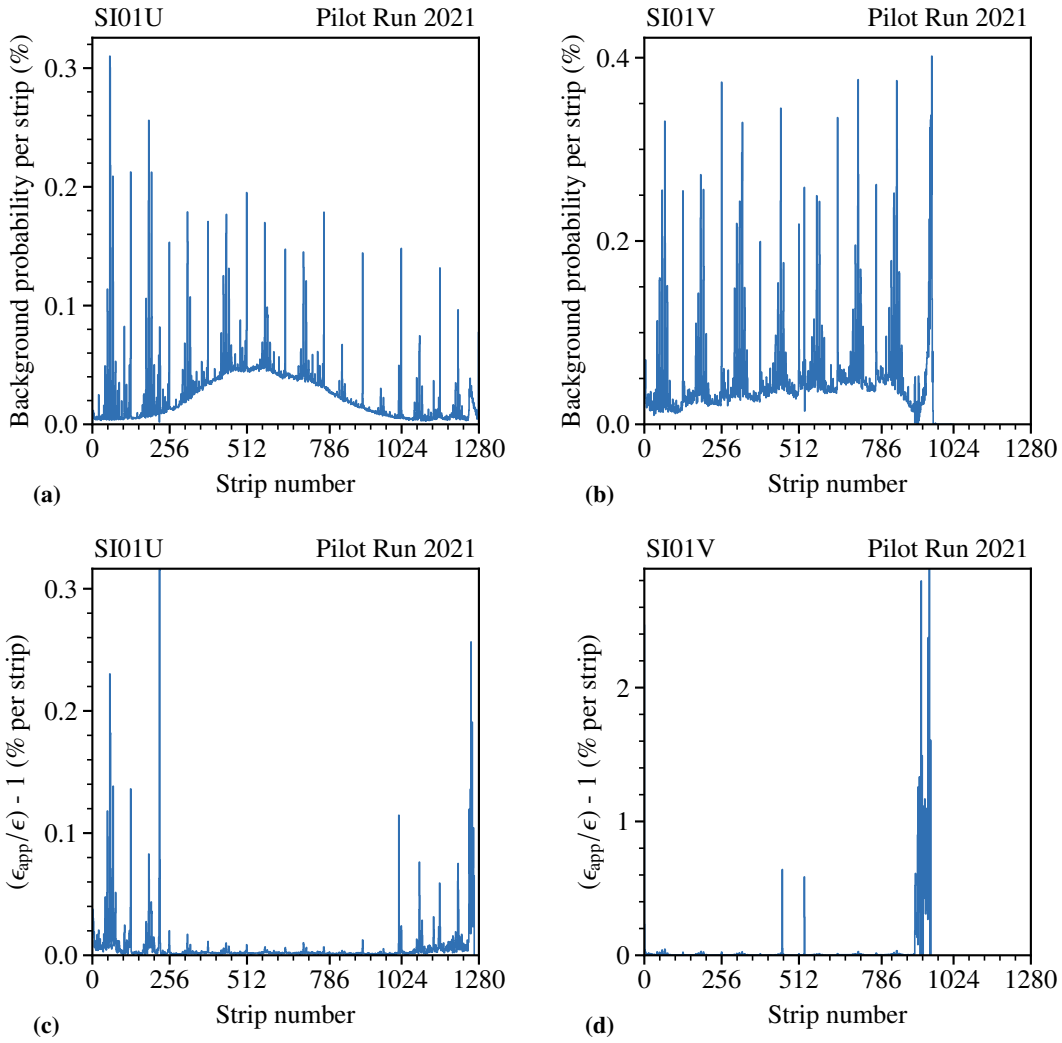

Figure 3.16: Background effects on efficiency for SI01 U- and V-plane. In (a) and (b) the background probability is shown. In (c) and (d) the ratio between the apparent efficiency and the background-corrected efficiency is shown.

The spatial resolution is defined as the residuum between the track position at the respective detector plane and the closest matching hit at this position. Since the hit is not associated to the track by excluding the respective detector plane from the track finding and fitting, the closest matching one is used. In Fig. 3.18 the spatial resolution of SI01 U- and V-plane is shown. The resolution depends on the cluster size of the respective hit. For the estimation of the hit position the Center-of-Gravity (CoG) method is used. For each strip position x_{strip} the larges sample of the amplitude a_2 is used as weight resulting in the CoG cluster position, as

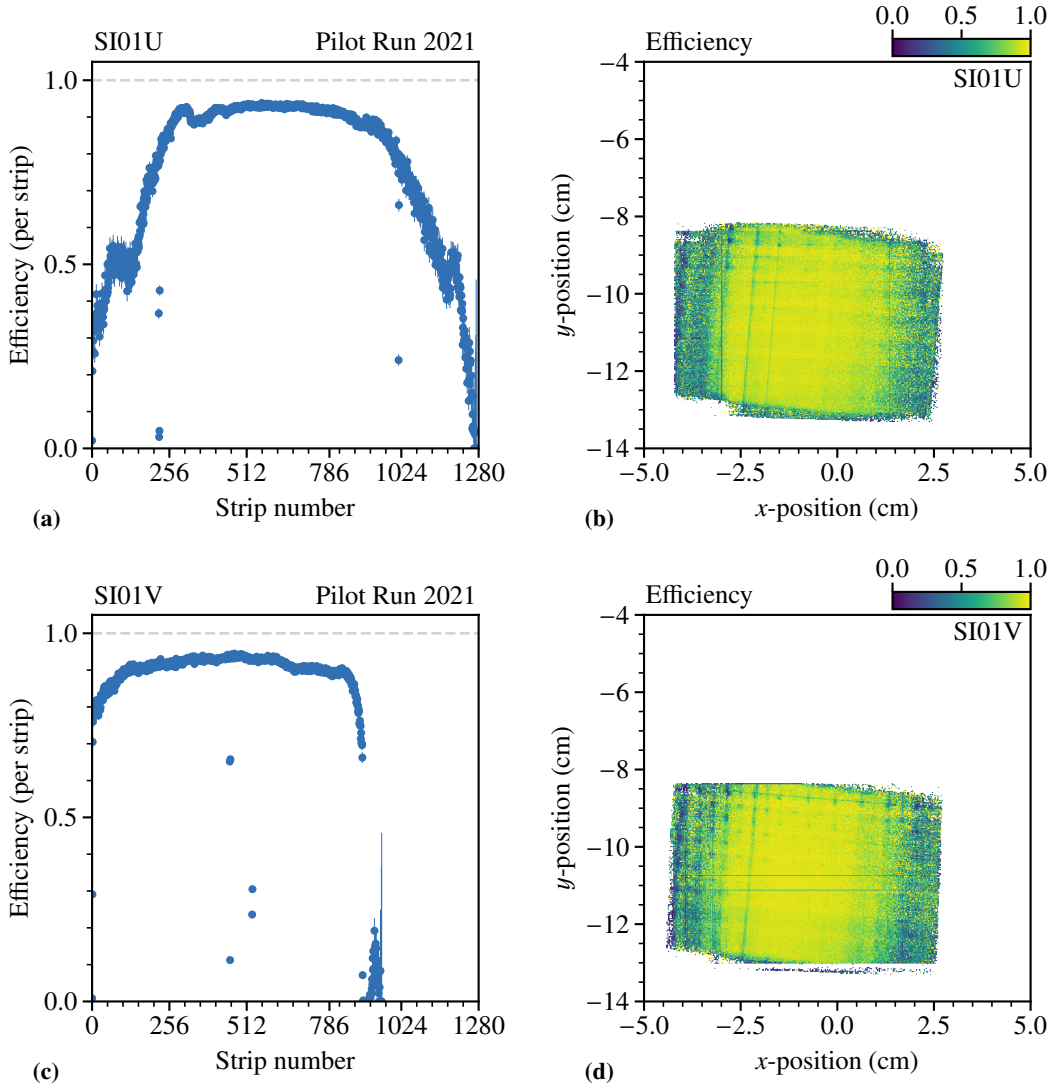

Figure 3.17: Silicon SI01 U- and V-plane efficiency in the single projections shown in (a) and (c). Uncertainties are based on Bayesian approach [67]. The respective 2-d projections are shown in (b) and (d). The plane position is given in the global coordinate system.

$$x_{\text{cluster, CoG}} = \frac{\sum_i a_{2,i} x_i}{\sum_i a_2, i}. \tag{3.12}$$

The charge sharing between the single strips varies with the hit position on the detector and therefore, additional corrections are applied to the cluster position. Due to the intermediate strips present on the V- and Y-plane, the charge sharing is improved and the overall resolution benefits. For the detectors, except SI03, the charge sharing calibration performed during the

2018 test measurement is used. Due to time constraints, a preliminary version is used for SI03, which will be adapted in the future to improve the correction of the charge sharing in this plane. The two-cluster resolution is improved by construction compared to the single-cluster resolution. In case of the shown U-plane in Fig. 3.18(a), optimizations of the alignment are still required, since the obtained resolutions are larger than the expected one. The current alignment is still a preliminary one and further work is ongoing. Some planes like the SI01U show a larger resolution of σ = 18 µm, which is about a factor two larger compared to the shown SI01V plane. An overview of all planes during the pilot run can be found in App. C.8.

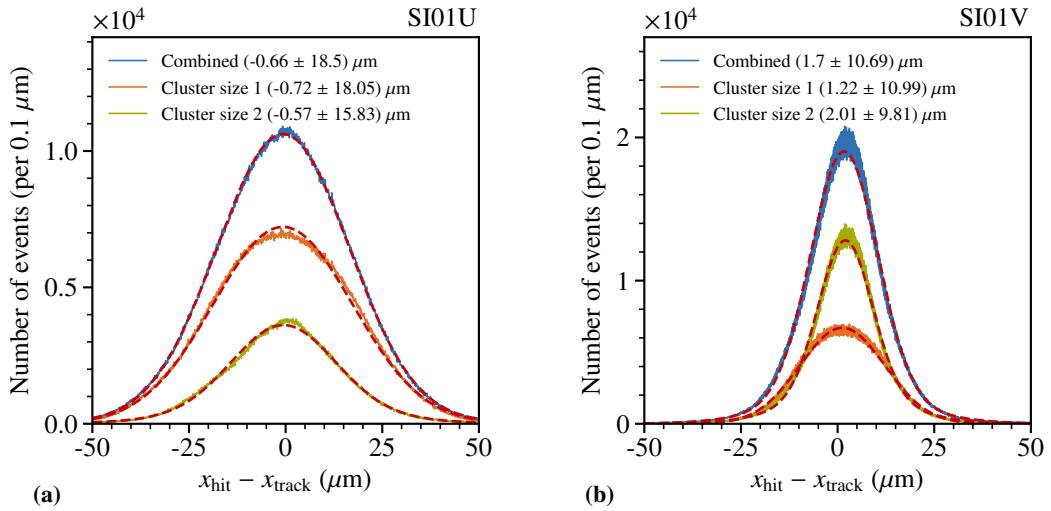

Figure 3.18: Silicon SI01 U- (a) and V-plane (b) resolutions for the combined and single cluster sizes. Four the double and combined distributions a double-Gaussian function is used to estimate the mean and sigma given here as ($\mu \pm \sigma$).

3.4 Time Synchronization

A comparable speaking time is used, as introduced in Sec. 2.2 during the feasibility test in 2018. In this pilot run, changes are applied to the operation firmware of the used iFTDC. This records besides the rising edge also the falling edge of each signal. Since the memory is limited, it can store up to 512 timestamp ticks with rising and falling end [66]. This allows up to 1 s of speaking time signals with rising and falling edge. It uses a time resolution of 32 ns for the pilot run configuration. Its memory is cleared with every trigger. With the last received trigger after about 5.6 s at the end of each spill, the maximum time in spill covered is about 6.6 s in total.

An overview of the recorded time messages for each run and spill is shown in Fig. 3.19(a). On average, 8 to 10 time messages are recorded per 4.8 s long spill during the data taking (cf. Sec. 1.2.1). For the pilot run, the time synchronization was provided starting from run 293218 spill 67[4] until the end with run 293315[5].

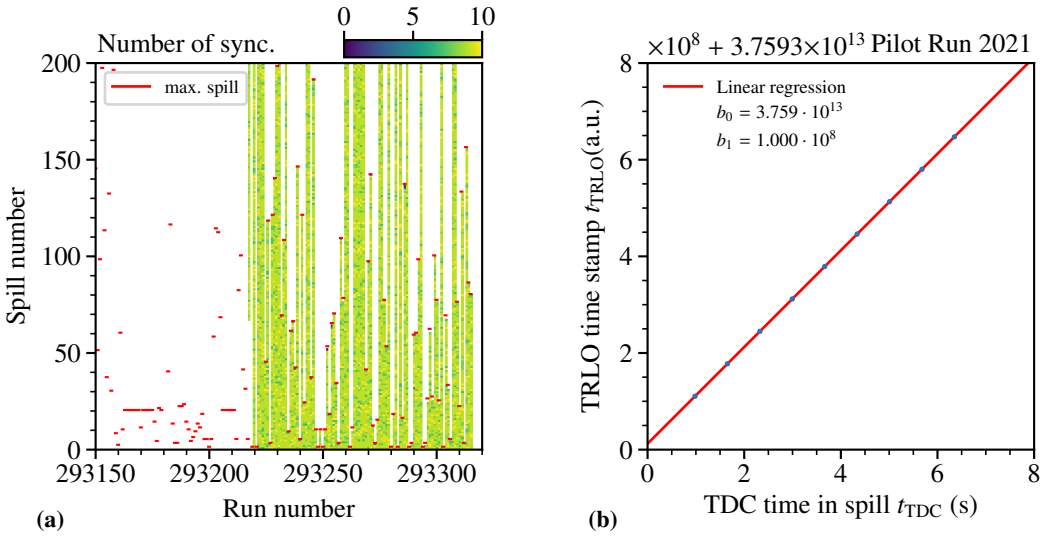

Figure 3.19: Time synchronization results during the pilot run. An overview of the available time messages as synchronization for the recorded runs and spills during the data taking is shown in (a). An example for the synchronization of the two DAQ systems based on a linear regression is shown in (b).

The extracted time messages along each spill are used to obtain a spill-by-spill time calibration based on the recorded time, when the time messages arrive. A linear regression is used to obtain this calibration. An example for a single spill is shown in Fig. 3.19(a), where time messages are used to obtain the linear function. Based on this, each event time from the tracking DAQ can be translated into the TRLO time of the TPC.

[4] The run 293218 started at 24.10.2021 07:47:19 and the spill 67 started at the same day at 08:13:51.

[5] The data taking ended at 27.10.2021 07:22:58.

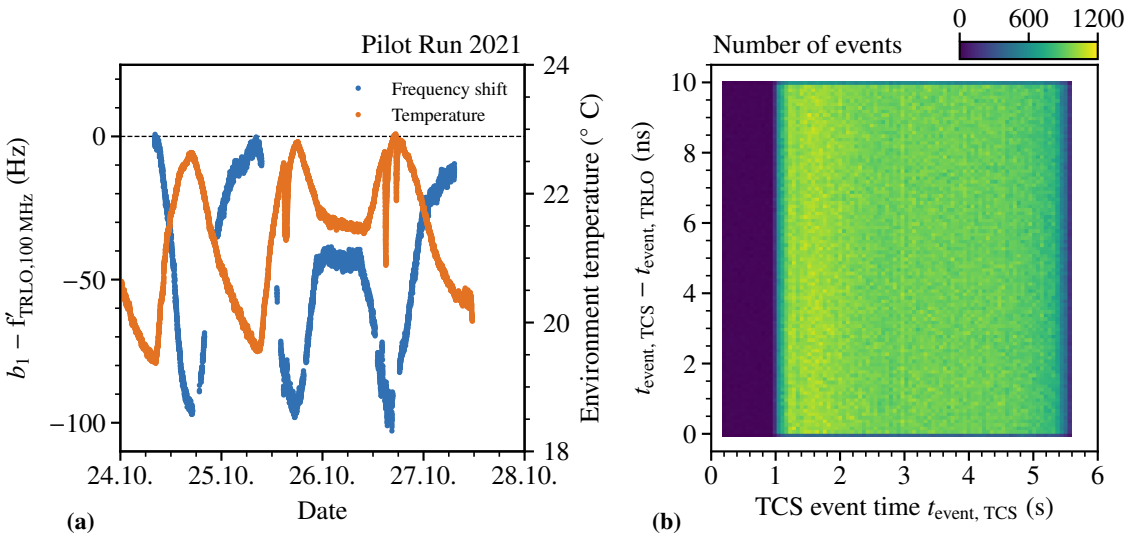

Figure 3.20: In (a) the stability of the TRLO clock operated at 100 MHz is shown. Temperature changes result in a frequency change of this clock. The difference between the event time provided by the TCS and the calculated one based on the TRLO depending on the TCS event time is shown in (b).

Figure 3.20(a) shows the clock stability of the speaking time during the pilot run as difference to its reference 100 MHz clock of the format. With the higher clock frequency of the iFTDC of 125 MHz, changes of the speaking time clock frequency due to temperature fluctuations can be observed. A clear day/night cycle is visible with a maximum frequency difference of 100 Hz within a temperature change of about 3 K. This corresponds to an overall stability of the expected 10^{-6} level [57].

The event time is given by the TCS and is based on the so-called F1 TDC operated at a clock with 155.52 MHz. Since the TRLO format is running with a 100 MHz clock, an overall difference between the event time and the TRLO time of maximal 10 ns is present as shown in Fig. 3.20(b). Although no direct calibration is present between the TRLO and event time clock as additional unsynchronized clock, a stable relation is visible. In addition, the overall spill structure as previously described can be seen, with the extraction starting at about 1 s for about 4.8 s. Further details on the time message decoding can be found in Sec. 2.2 and App. B.4.

3.5 Alignment and Coordinate System

For the reconstruction of the data, a so-called run-by-run alignment is used to compensate for shifts in the tracking detectors between single runs. A so-called alignment run[6] is taken at low beam intensities to avoid pile-up effects in the detectors and the reconstruction. This alignment run is also used to align the spectrometer at a later stage with the setup in the beam test area. For this, all magnets between the pilot run setup and the spectrometer have been switched off to ensure straight tracks along the full setup to align the detectors accordingly (cf. Sec. 1.2.1).

The alignment is performed on a run-by-run basis, similar to the 2018 test measurement by [36] (cf. Sec. 2.3.2). Already in 2018 shifts of the tracking detectors in the same order of their respective resolution have been observed. Due to the location at the beam tunnel together with the large gradient shift and the aluminum-based support structures, a larger shift is expected. For compensation, the position of the detectors is evaluated for each run and used in the later reconstruction of the data.

For the reconstruction of the events, a new coordinate system at the test beam location is introduced in a way that the beam axis is a straight line between the up- and downstream quadrupol magnet. By this, an inclination of 3.6 mrad with respect to the horizontal spectrometer axis is naturally introduced (cf Sec. 3.2.1). The x-coordinate points in the horizontal direction and the y-coordinate in the vertical direction. As origin, the downstream side of the upstream quadrupol of the test beam location is selected. Results from the survey are given in the respective survey report [89]. For the alignment together with the spectrometer, the coordinate system has to be shifted into the one of the spectrometer. The transition is expected to have uncertainties, which then can be refined by the respective straight track alignment.

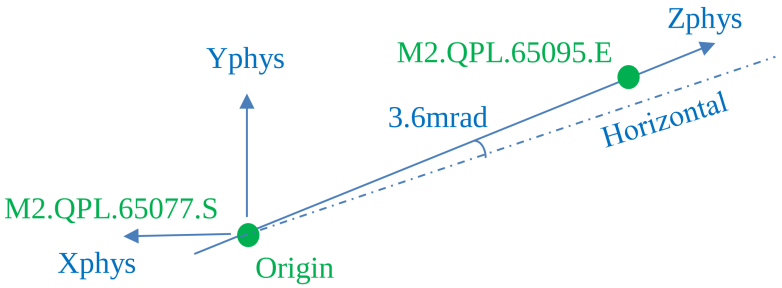

Figure 3.21: Coordinate system at the test beam location in the M2 beam line. The coordinate system is oriented between the up- and downstream quadrupol magnet (QPL) defining a 3.6 mrad inclined beam axis with respect to the horizontal spectrometer axis. Figure taken from [89].

[6] The alignment run number is 293291.

3.6 Event Selection

In the following, the event selection of the pilot run data is described to obtain an elastic muon-proton scattering event data sample. The goal of the event selection is to select candidates of elastically scattered muons inside the active volume of the IKAR TPC, similar to the 2018 test measurement as described in Sec. 2.5. Those events will later be associated with corresponding recoil protons measured by the TPC using the common timestamp. For verification purpose kinematic correlations are used. As basis the data of the very first reconstruction attempt $V1$ as so-called production is used. The initial run-by-run alignment performed by [36] as described in Sec. 3.5 has been applied for this first production. Further details on the data production are given in App. C.6. The initial alignment and reconstruction is based on the silicon tracking detectors only, except the SI04 station, which showed problems in the alignment and operation due to problematic planes. For each run a dedicated alignment file is used optimizing the position due to the overall discussed influence by the temperature fluctuations.

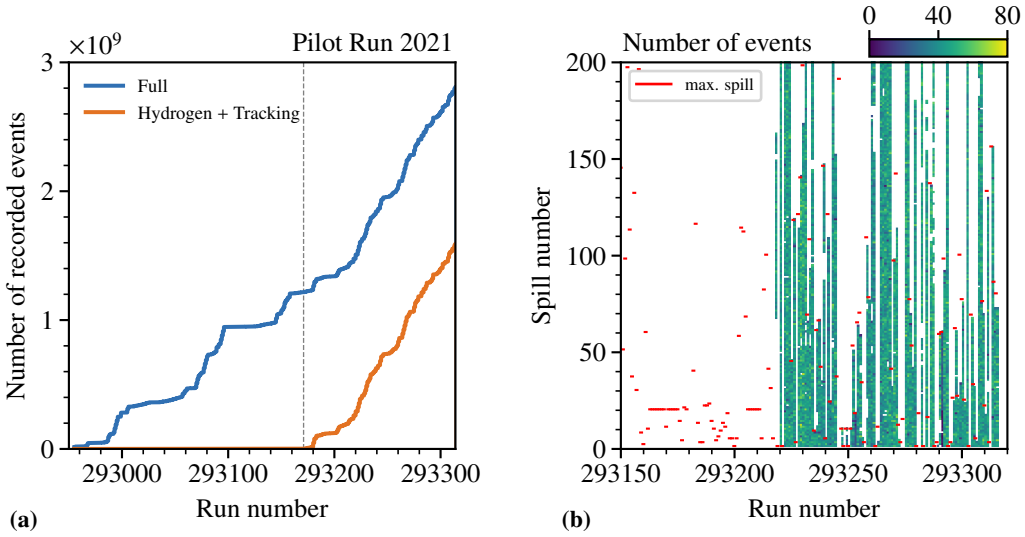

Figure 3.22: In (a) the total number of recorded events during the pilot run and the dedicated combined measurement with TPC in hydrogen mode together with tracking are shown. The selected events per run and spill with the respective maximal number of recorded spills is shown in (b).

In Fig. 3.22(a) the total number of recorded tracking data events during the three weeks of dedicated beam is shown. A total of about $3 \cdot 10^9$ events have been recorded. This data set includes not only the combined data taking with the TPC in hydrogen mode, but also calibration data sets and general beam tests for the detector systems and the TPC. The combined data taking with TPC and tracking accumulates to about $1.6 \cdot 10^9$ events during the last four days of the pilot run. Taking into account the probability of 10^{-5} for elastic muon-proton scattering (see Sec. 1.2.9) about $O(10^4)$ events are expected in the Q^2 range of $10^{-3} \leq Q^2/(\mathrm{GeV}^2/c^2) \leq 4 \cdot 10^{-2}$. A more elaborated estimate is discussed in Sec. 3.7. The runs taken into account have the number 293218 to 293315. These runs provide the TRLO timestamp as well as a common data taking of TPC and tracking in hydrogen mode.

In Fig. 3.23 the list of applied selection criteria as well as the resulting number of events is shown for the applied criteria. The event selection is similar to the 2018 test measurement described in Sec. 2.4. The selection is split into a so-called preselection of events followed by a more detailed one. It includes physics as well as technical criteria. Figure 3.22(b) shows the number of selected events for each recorded run and spill and the maximum number of recorded spills to ensure the stability of the data taking and reconstruction. With an average trigger rate of about 35 kHz over the 4.8 s long spill and the resulting reconstructed event fraction of approximately $2 \cdot 10^{-4}$, about 40 events are reconstructed on average during each spill. In some parts of the runs, tracking and vertexing is not possible in the first $V1$ production due to technical issues with the first upstream silicon tracking station (SI01). It is planned to adapt for this issue by using the installed SciFi15 detector, which is not yet included in the reconstruction due to current alignment issues with this detector [36].

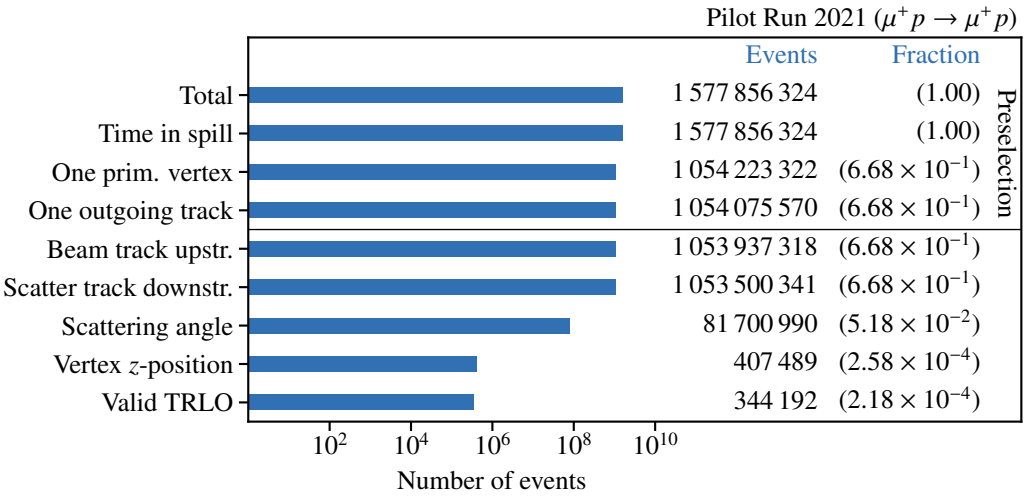

Figure 3.23: List of applied selection criteria for the pilot run event selection. The preceding preselection of the data set is indicated.

Of the recorded 8799 spills of the runs with timestamp currently 7883 have reconstructed events resulting in about 89.5 %. It is expected to increase it close to 100 % with the inclusion of the SciFi15. About 350000 reconstructed events remain after the selection as elastic scattering candidates in the active volume of the TPC. Compared with the initial $1.5 \cdot 10^9$ events reconstructed during the pilot run, the test measurement in 2018 had about a factor of four more statistics recorded. Nevertheless, the pilot run data set contains more clean events, as one obtains after applying the geometrical selection criteria to pass through the beam windows. This is the result of the used central beam trigger, which was included to obtain more events from the central part region without prescaling (cf. Sec. 3.2.2). In 2018, only around $537 \cdot 10^6$ events remain, whereas a factor of two larger data set is available in from the pilot run measurement. Furthermore, the total beam time in 2018 was about 2 months, whereas the pilot run was in total only 21 days. Based on this first production and initial alignment, a reconstruction efficiency of about 67 % is achieved.

Despite the issues with some of the tracking detectors, it is expected that the efficiency will reach the anticipated > 85 % for the main physics run.

For an easier data handling on a later stage, a so-called preselection of the data is applied. The stage is indicated in Fig. 3.23. Starting from the total number of events, fundamental criteria are applied to select meaningful event candidates. As a technical requirement, each event is required to have a respective event time in spill based on the trigger time. This criterion shows no effect, which indicates that the event recording with respect to the incoming triggers is without any problems. To select events from elastic scattering, one primary vertex is required with exactly one outgoing track. The events with those properties serve as input for the further event selection and studies.

Selection of Beam and Scatter Tracks

To avoid tracks passing through the flanges of the TPC, only beam and scatter tracks are selected that pass through the beam windows of the TPC (cf. Fig. 3.10). In Fig. 3.24 the respective selection is shown using the extrapolated track position at the up- and downstream beam window location. All criteria are applied, except the selection of the track position. Only events where the tracks are located inside the beam window size at the respective window's z-position are selected. The extrapolated beam tracks shown in Fig. 3.24(a) are centered well inside the upstream beam window of the TPC, and therefore no effect is visible. Nevertheless, a selection of beam tracks passing through the upstream beam windows is applied for completeness. The extrapolated scatter tracks at the downstream beam window position are shown in Fig. 3.24(b). On the left side parts of the holding structure of the anode are visible and are also excluded by the selection. The effect of the central beam trigger element is visible. A clearer distribution of the anode structures is shown in Fig. 3.30 discussed later.

Compared to the 2018 test measurement, the internal structures of the TPC are less pronounced. In 2018 the beam was covering the full surface of the silicon detectors and therefore the flanges and beam windows are much more visible. In this pilot run, the advantage of the beam is, that it is much more focused on the central part of the setup and therefore the surrounding structures are not visible.

Table 3.5: Selection criteria for beam and scatter tracks at the up- and downstream beam window positions. A radial criterion around the given center is applied at the respective position.

Position	Track	x_{center} (mm)	y_{center} (mm)	r_1 (mm)	r_2 (mm)
Upstream window	Beam	0.10	−8.77	34.5	34.5
Downstream window	Scatter	0.245	−8.15	34.5	34.5

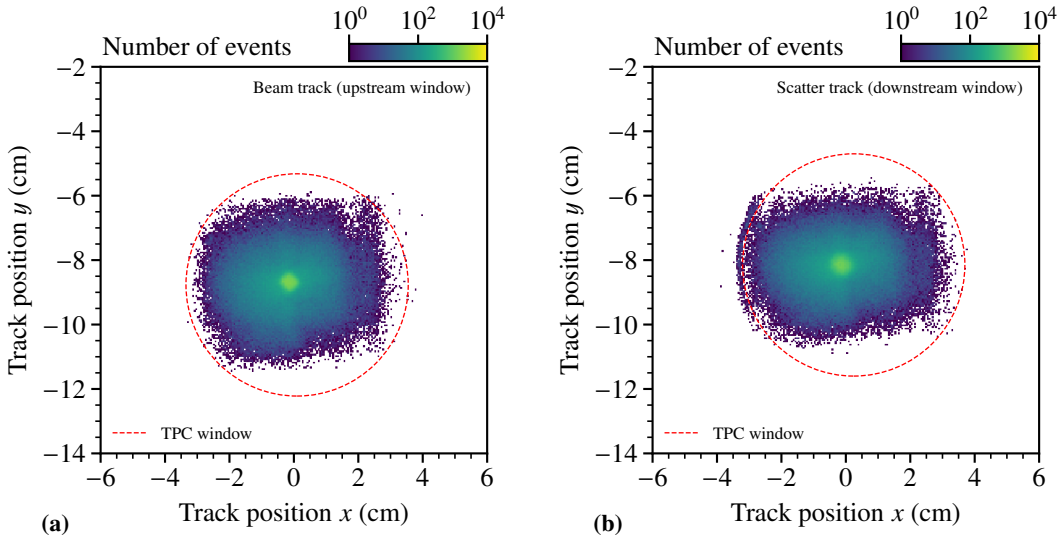

Figure 3.24: Selection of beam and scatter tracks passing through the beam windows of the TPC. In (a) the extrapolated beam track at the upstream beam window position is shown. In (b) the extrapolated scatter track at the downstream beam window position is shown. All selection criteria are applied, except the indicated one to pass through the beam windows.

The selection criteria values are summarized in Tab. 3.5. The positions of the windows are based on the initial survey [89] results of the TPC. For the downstream position, a minor offset of about -0.7 mm is applied to the y-center position as shown in Fig. 3.24(b) to take into account the anode holding structure influence. For the upstream window, the survey position is taken. No beam window structures are visible for confirmation. The radial size of the beam windows is 35 mm and a 0.5 mm smaller radial selection is used.

Selection of Scattering Angle

The scattering angle distribution is shown in Fig. 3.25(a) with the indicated selection of scattering angles larger than 300 µrad, which corresponds to the trigger threshold of the TPC of abut 500 keV (cf. Sec. 1.1.3). All selection criteria are applied, except the indicated one. An increased background due to multiple scattering can be observed at lower scattering angles. An increase is visible at scattering angles larger than exactly 2 mrad with the cut-off by the geometrical acceptance around a maximal scattering angle of 30 mrad. This rise tends to be an artifact of the reconstruction discussed later.

The vertex z-resolution can be estimated by the width of a thin structure like the cathodes of the TPC. In Fig. 3.25(b) the width of the upstream anode structure of the TPC is shown depending on the scattering angle. A vertex z-resolution σ_z of about 15 cm is achieved at the lowest scattering angles of 300 µrad. This is in agreement with the shown simulation for the lower scattering angles. Results for larger scattering angles could not been extracted due to the reconstruction artifact issue for scattering angles starting at 2 mrad, which is not present in the simulation. The reconstructed simulation data tends to be over optimistic at larger scattering angles.

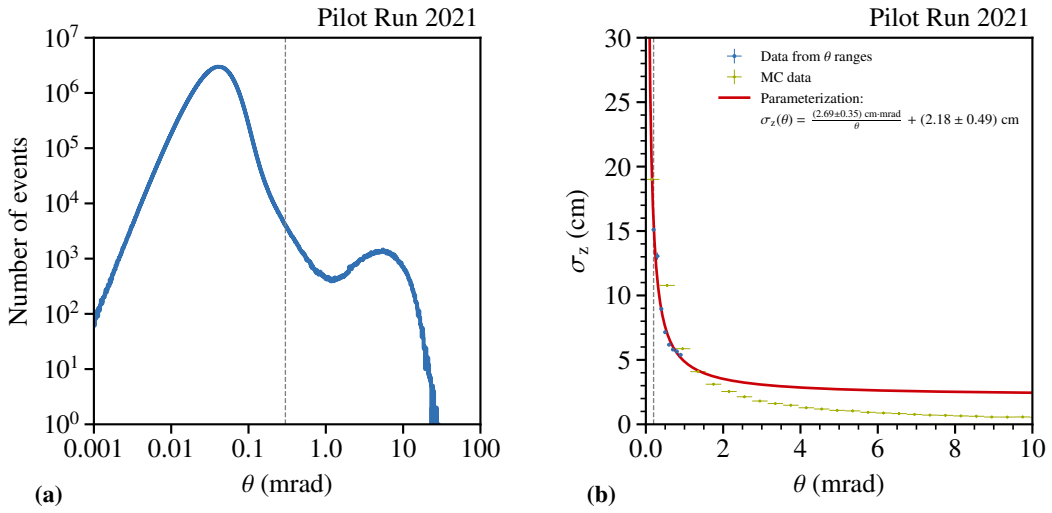

Figure 3.25: In (b) the vertex z-position resolution is shown depending on the scattering angle. In (a) the scattering angle with the indicated selection is shown.

Vertex Positions

The vertex z-position for a scattering angle range from 0.5 to 1.0 mrad is shown in Fig. 3.26(a). The structures of the setup are clearly visible. Besides the silicon detector stations, the internal structure of the TPC can be identified. Beam windows on the up- and downstream side as well as the two anode planes with the central cathode are visible. Along the active gas volume of the TPC an expected increase compared to the surrounding due to the internal 8 bar hydrogen pressure is present. The single structures are listed in detail in Tab. C.1. The dependence of the scattering angle on the vertex z-position is shown in Fig. 3.26(b). Larger scattering angles, predominantly originate from the firm structures due to the material effects like multiple scattering. The vertices in the respective tracking detector stations are mostly reconstruction artifacts and will be treated in the next version of the data production, which will also include the two additional scintillating fiber tracking detectors. This should avoid false vertex reconstruction inside the single detector planes due to minimization algorithms.

An additional artifact becomes visible in the region of above 2 mrad and at a z-position of 42.05 m. Here, sharp lines appear along those coordinate positions. The reason is unclear and further investigations are required. An enlarged view of the respective region is shown in Fig. 3.27 with indications for the artifacts. This artifact also results in a rise for the scattering angle, as shown in Fig. 3.25(a).

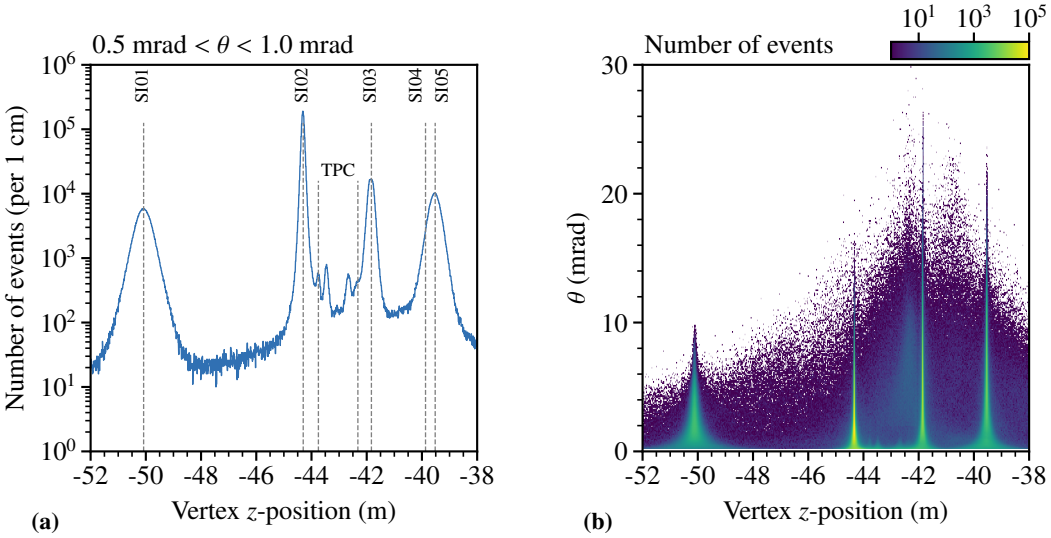

Figure 3.26: The vertex z-position along the setup is shown in (a). The single structures are indicated. The scattering angle dependency on the vertex position is shown in (b).

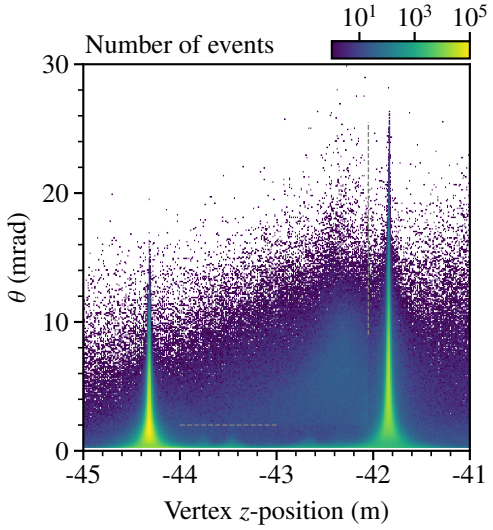

Figure 3.27: Enlarged central area of the scattering angle dependence along the vertex z-position. A reconstruction artifact in the scattering angle is visible along exactly 2 mrad and vertex z-position of $z = -42.05$ m as indicated.

The orientation of the setup along the beam axis becomes visible in the x-z- and y-z-vertex distributions. In Fig. 3.28 the vertices are shown for the respective projections. Whereas the x-position along the setup shows an expected straight behavior, the overall expected 3.6 mrad inclination becomes visible along the y-z-projection. This inclination is also similar as the given simulated beam file results shown in Fig. 3.4(a) and from the survey report sketched in Fig. 3.21. The single structures along the setup (cf. Fig. 3.26(a)) are also visible.

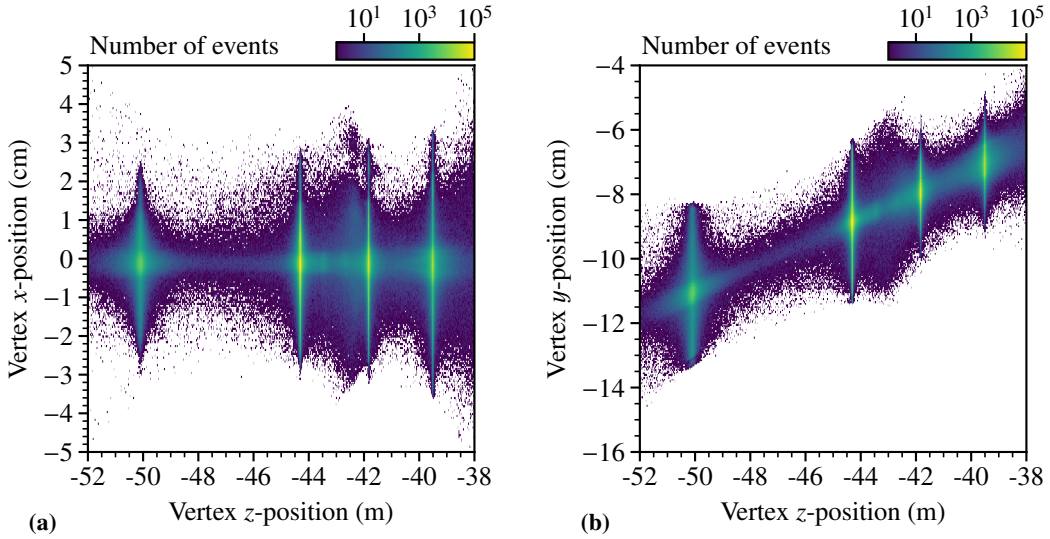

Figure 3.28: Vertex positions in x- and y-direction at their z-positions. In Fig. 3.28(a) the vertex x-position is shown depending on vertex z-position and in Fig. 3.28(a) the vertex y-position is shown depending on vertex z-position.

The applied selection criteria result in a clean data sample for elastic scattering events along the active volume of the TPC. The selected vertex z-positions are shown in Fig. 3.29(a). Events between $43.7 < z/\mathrm{m} < 42.5$ are selected, which corresponds to the inner part of the TPC. The vertex z-position will be later refined in the matching with the TPC proton data. The resulting vertex $x - y$-distribution is shown in Fig. 2.21(b). A clean distribution is visible without additional structures. The central beam trigger element result in an accumulation of events in the central spot. Due to the inclined setup and the target length, a washed-out effect is visible.

The structures of the anode planes become visible in a dedicated selection of scattering events originating from the respective z-position. In the distributions shown in Fig. 3.30 for the up- and downstream anode, the segmented structures of the anode plane is visible. The central beam trigger element is roughly positioned in the central pad. The single pads in the first ring with a radius of 45 mm can be distinguished by their respective segmentation. For the segmentation of the two pads on the left side, the connection for the central pad intersects at this position and overlaps. A picture of the mounted pad plane is shown in Fig. 3.11(a) with the discussed structures visible. In addition, the vertical wires of the Frisch grid are recognizable with a pitch of 1.5 mm and the circular holding structure of the anode plane is visible on the left side for the downstream anode, shown in Fig. 3.30(b). Furthermore, the attached pad connections can be seen close to the holding structure.

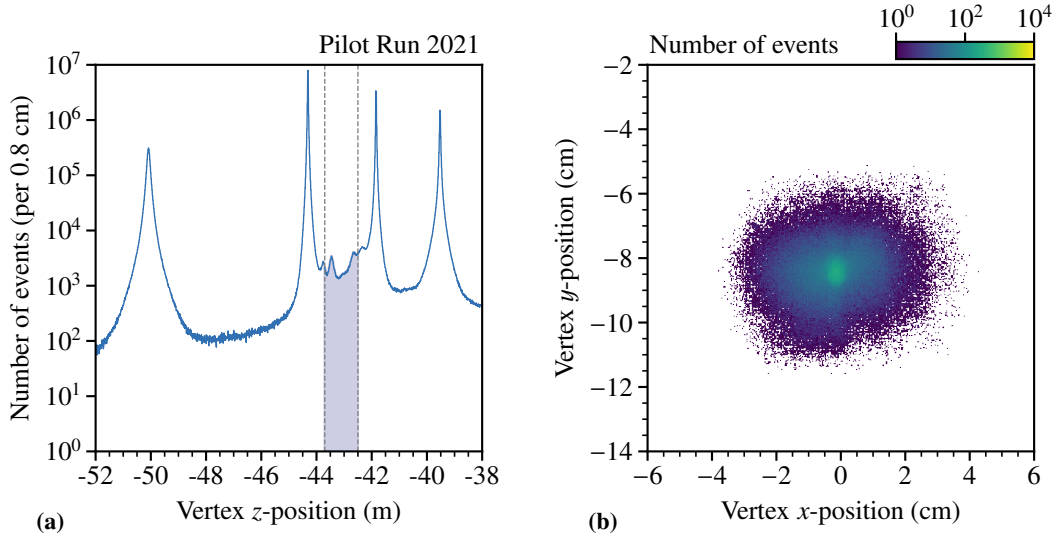

Figure 3.29: Primary vertex position of the vertex z-position in (a) with the selection shown as well as the region (blue) accepted due to the vertex position z-resolution. In (b) the x-y-position of the vertex is shown. All criteria are applied, except the indicated ones.

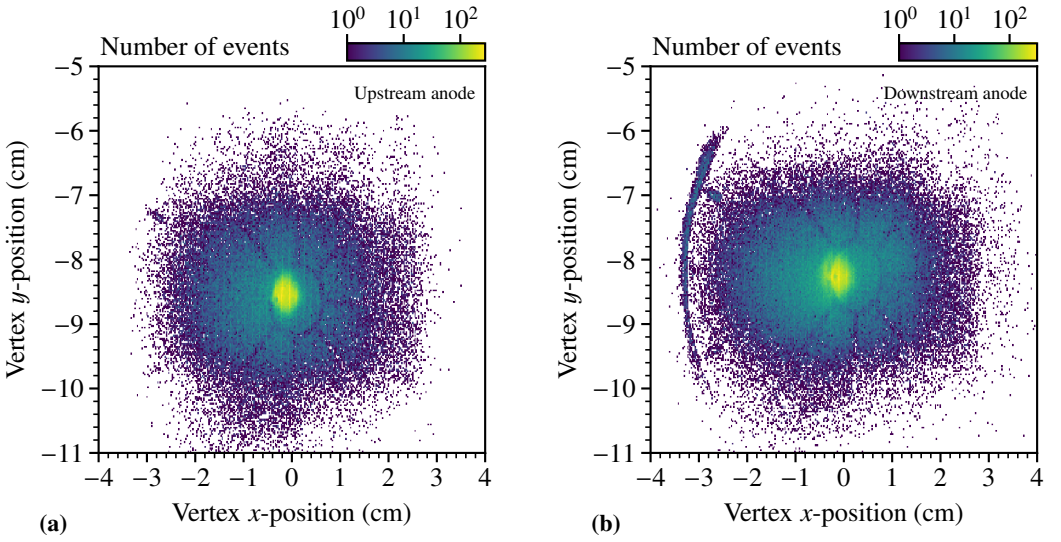

Figure 3.30: Structure of the upstream (a) and downstream (b) anode.

Beam Gradient

Using the central small BT01 trigger elements allows not only a selection of only a partial area of the incoming beam tracks to adjust the trigger rate without prescaling, but allows also to select only incoming beam tracks with low divergence. Based on the given trigger bits as listed in Tab. 3.3, the events can be selected, that passed through this trigger elements. The influence of the beam gradient for the two different triggers, BT01 as small-size trigger and BT02 covering the full silicon detector surface, can be seen in Fig. 3.31. Whereas the difference in the x-gradient direction for both selections is small, the influence on the wider y-gradient direction is larger. The resulting beam divergence using the BT01 trigger elements results in a selection of beam particles with a very small divergence in x-direction and an expected divergence in y-direction of 3.8 mrad. The extracted gradient is 0.2 mrad larger than the expected value of 3.6 mrad, which might be caused due to further beam tuning prior to the measurement. An overall gradient width of about 0.4 mrad can be observed.

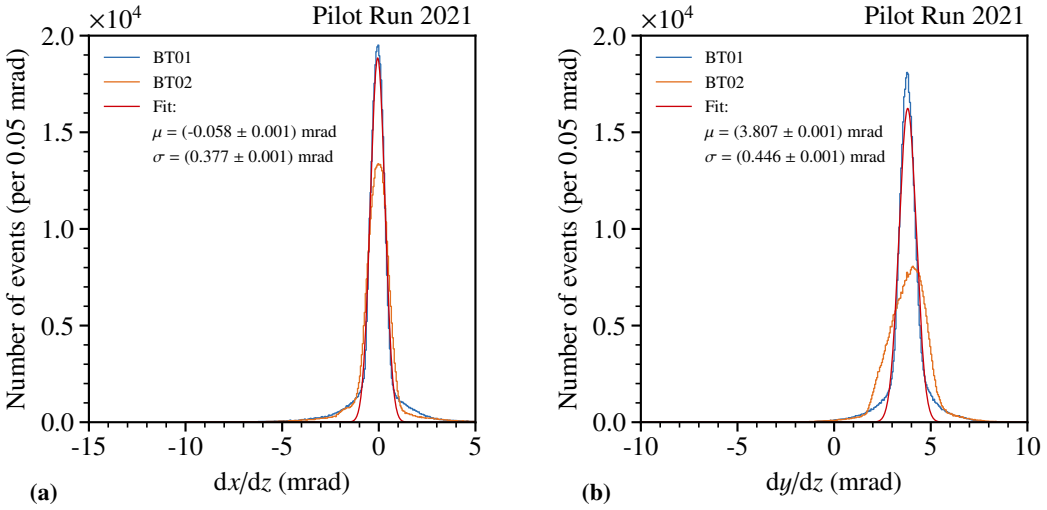

Figure 3.31: Beam gradients in dx/dz (a) and dy/dz (b) for the two different trigger elements BT01 and BT02.

3.7 Muon-Proton Time-Association

The introduced common TRLO timestamp for the tracking and TPC event recording, as discussed in Secs. 2.2 and 3.4 is used to find matching muon-proton pairs based on the respective time difference between those events. The extracted correlations of drift time and vertex z-position as well as muon scattering angle and proton energy can be used as verification. Due to the drift time of the TPC of about 140 µs a direct trigger on common events is not possible. The tracking and TPC both have a dedicated trigger on events. The TPC trigger threshold is set to 0.5 MeV protons corresponding to $Q^2 = 10^{-3}$ GeV$^2/c^2$ [85], whereas the tracking utilizes two beam trigger elements as discussed in Sec. 3.2.2.

Prior to the event matching based on timestamps, the relative time shift between the TRLO timestamp and the used event time. The event time, besides the calibrated clock of the iFTDC, is a third clock, which is used to record the time message. An event time based on the iFTDC time is not yet available for the reconstruction. Therefore, a possible shift between both system needs to be evaluated (cf. Sec. 2.2). Depending on the decoding of the TRLO time message and defining the corresponding time differences of up to 168 ms[7] can be induced additionally to hardware- and cable-induced latency, which could be in the range of additional $O(10\ \mu s)$. To calibrate the time shift, the recorded TPC triggers in the tracking DAQ are used. Each triggered event by the TPC sends a trigger to the tracking DAQ and creates a recorded event with the respective event time, which is translated into the TRLO time of the TPC data. By this, the overall shift can be evaluated.

In the first stage, the TPC data is processed and a more clean sample of events is generated [90]. In Fig. 3.32 the uncalibrated total energy measured by the TPC of the selected recoil events is shown. For the TPC data, events with meaningful signal in terms of signal time and energy deposition on pads are selected. The influence of the α-source is visible around 150 and 200 units corresponding roughly to an energy of 5.486 MeV of the ^{241}Am-source on the grid and cathode, respectively [90]. The contribution by the two calibration sources is visible in the off-spill data shown in Fig. 3.33 as the first preliminary calibration for the TPC energy spectrum. With this first calibration, the obtained raw spectrum shown in Fig. 3.32 can be converted into an energy scale. The calibrated off-spill data (green) is used to subtract the α-contribution in the on-spill data (orange) to obtain the corrected (blue) energy distribution. The off-spill data is scaled based on the duty-cycle between on- and off-spill events. Further calibrations are required to obtain a clean energy distribution. Especially, attachment processes along the drift need to be corrected based on the vertex z-position.

[7] The time message consists out of 32 ticks. Each tick is 5.24288 ms apart from the previous one and is followed by two additional ticks encoding the transmitted time message. In the tracking case the start of the time message corresponds to the respective event time. In the TPC case it seems that the arrival of the time message defines the time in the 2021 pilot run.

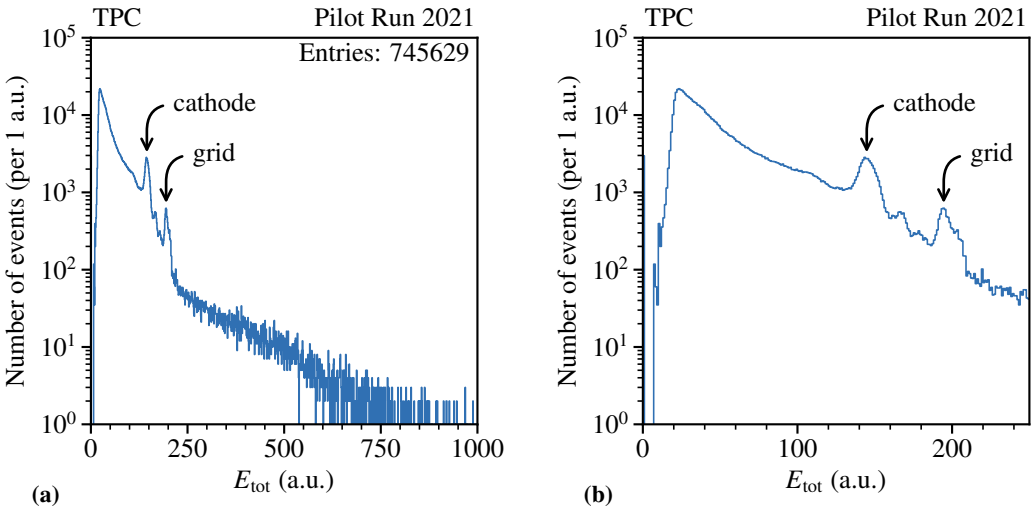

Figure 3.32: Uncalibrated total energy in arbitrary units measured by the TPC. In (a) the full energy spectrum is shown and a close-up view in the low-energy region is shown in (b). The influence of the α-source is visible around 150 and 200 corresponding roughly to an energy of 5.486 MeV of the ^{241}Am-source on the grid and cathode, respectively.

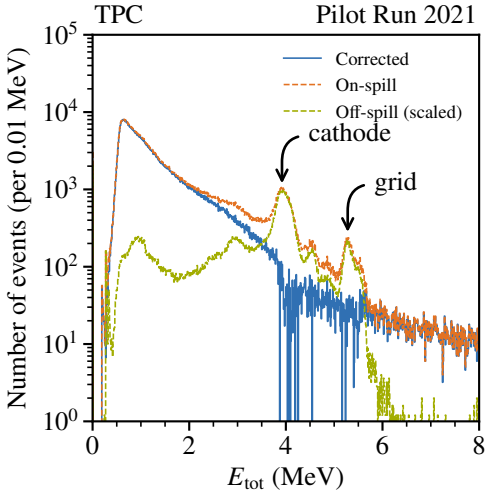

Figure 3.33: Calibrated and corrected energy spectra of the measured TPC data provided by [90]. The calibrated off-spill data (green) is used to subtract the α-contribution in the on-spill data (orange) to obtain the corrected (blue) energy distribution. The off-spill data is scaled based on the duty-cycle.

Estimation of Muon-Proton events

To estimate the expected number of events which could be extracted by the correlation of both measurements at first the TPC side is evaluated. About 745000 recoil candidates n_{TPC} have been recorded by the TPC (cf. Fig. 3.32(a)). Those events still hold a low contamination of calibration α-events. About $P_{\mathrm{recoil}} = 75$ % of the events as a rough estimate are expected to be real recoil events [90]. Taking into account the trigger rate f_{trigger} of about 35 kHz of the tracking DAQ at the 2 MHz beam rate f_{beam}, a suppression of about 55 is expected. Therefore, the expected number of correlated events from the TPC side can be estimated by

$$n_{\mathrm{correlated}} = \frac{n_{\mathrm{TPC}} \cdot P_{\mathrm{recoil}} \cdot f_{\mathrm{trigger}}}{f_{\mathrm{beam}}} \tag{3.13}$$

$$= \frac{745000 \cdot 0.75 \cdot 35\ \mathrm{kHz}}{2\ \mathrm{MHz}} \tag{3.14}$$

$$= 9778. \tag{3.15}$$

About 10000 correlated events are expected based on the measurement of the TPC as lower limit. From the muon side, the expected number of recoil proton events based on elastic muon-proton scattering can be calculated via

$$N_{\mathrm{protons}} = \sigma_{\mathrm{D}}^{\mu p \to \mu p} \cdot \int \mathcal{L}\ \mathrm{d}t, \tag{3.16}$$

with the elastic cross-section $\sigma_{\mathrm{D}}^{\mu p \to \mu p}$ for the estimated Q^2-range given as

$$\sigma_{\mathrm{D}}^{\mu p \to \mu p} = \int_{0.001\ \mathrm{GeV}^2/c^2}^{0.02\ \mathrm{GeV}^2/c^2} \frac{d\sigma_{\mathrm{D}}^{\mu p \to \mu p}}{dQ^2} dQ^2 = 0.24481\ \mathrm{mb}, \tag{3.17}$$

starting from the $Q^2 = 0.001\ \mathrm{GeV}^2/c^2$corresponding to a scattering angle of about 300 µrad to the maximal value of recoil proton stopped in the TPC of $Q^2 = 0.02\ \mathrm{GeV}^2/c^2$. For the $P = 8$ bar pressure[8] of the IKAR TPC the target proton density is given by

$$n_{\mathrm{target,\ 8\ bar}} = \frac{P}{1.013\ \mathrm{bar}} \cdot n_{\mathrm{target,\ NTP}} \tag{3.18}$$

$$= \frac{8\ \mathrm{bar}}{1.013\ \mathrm{bar}} \cdot 5.018 \cdot 10^{25} \mathrm{m}^{-3} = 3.964 \cdot 10^{26}\ \mathrm{m}^{-3}. \tag{3.19}$$

[8] During the combined data taking only the 8 bar pressure setting was used. In dedicated studies the 4 bar setting was applied in order to evaluate the beam induced noise.

Together with the target particle density n_{target} and the length of the target l_{target} the integrated luminosity is given by

$$\begin{aligned}\int \mathcal{L}\ \mathrm{dt} &= N_\mu \cdot n_{\text{target}} \cdot l_{\text{target}} && (3.20)\\ &= 1.5 \cdot 10^9 \cdot 3.964 \cdot 10^{26}\ \mathrm{m}^{-3} \cdot 2 \cdot 0.40\ \mathrm{m} && (3.21)\\ &= 4.76 \cdot 10^{35}\ \mathrm{m}^{-2} && (3.22)\\ &= 4.76 \cdot 10^4\ \mathrm{mb}^{-1}. && (3.23)\end{aligned}$$

The expected number of events is given as

$$\begin{aligned}N_{\text{protons}} &= \sigma_{\mathrm{D}}^{\mu p \to \mu p} \cdot \int \mathcal{L}\ \mathrm{d}t && (3.24)\\ &= 0.24481\ \mathrm{mb} \cdot 4.76 \cdot 10^4\ \mathrm{mb}^{-1} && (3.25)\\ &= 11653. && (3.26)\end{aligned}$$

From the tracking side about 12000 events are expected. This is about 20 % more than expected by the TPC measurement. Nevertheless, an expected lower limit of correlated events is in the order of 10000 events.

Time Shift between Recorded Events

To evaluate the shift between the two triggers of the TPC and tracking DAQ, the information of the recorded TPC trigger in the tracking DAQ is used. Each triggered event in the TPC sends a trigger to the tracking DAQ which is recorded. With the common timestamp, the time difference between the TPC event and the corresponding triggered tracking event can be evaluated. In Fig. 3.34(a) the time difference between the two trigger times is shown. A correlation is visible at around -200 ms, besides the combinatorical background of the events. An enlarged view of the region of interest shown in Fig. 3.34(b) shows the correlation peak position and its width in Fig. 3.34(c). The correlations have a time width difference of about 180 µs.

Since it is a pure technical property, it should be only one constant value. The reasons for this distribution is still under investigation. Compared to the time correlation in the 2018 test measurement data (cf. Sec. 2.2.3), no distribution of correlated trigger-only events was found, but a discrete distribution at single values. The drift time can not influence the time difference, since it is a pure hardware-based property. The temperature dependence of the timing clock results in shifts of about 100 Hz as shown in Fig. 2.14(a) is too small to contribute significantly. For the time correlation an overall shift of time difference of 200 ms is taken into account for the further matching of the events. As origin for the 200 ms time shift multiple ideas are possible. It could

be related to a different decoding of the time message, or related to the fact of using the event time, as a third clock besides the recorded time timestamp by the iFTDC. Investigates are ongoing and a possible connection towards the feasibility test procedure is on under study. The overall time shift is accounted for, and the respective time difference is shifted by the found value.

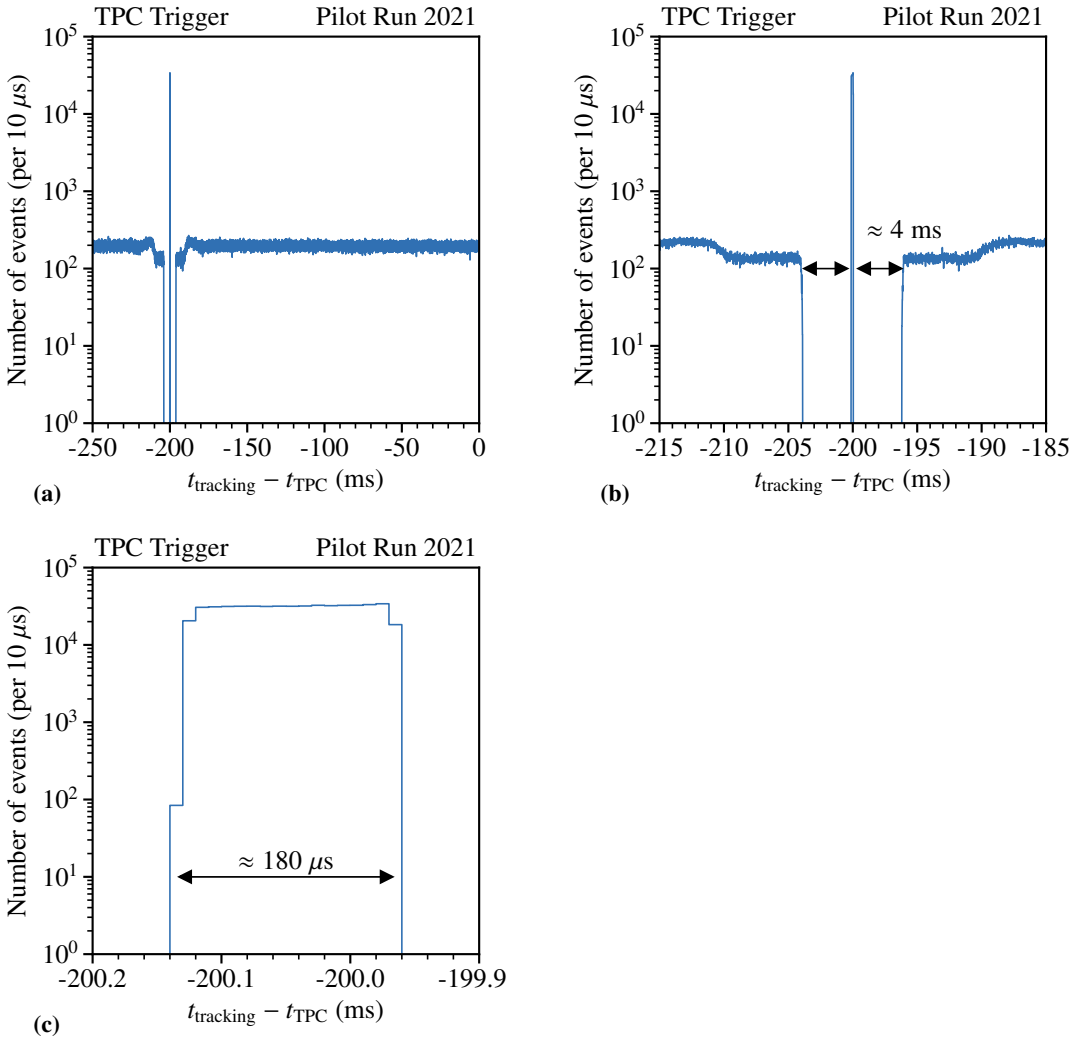

Figure 3.34: The time difference between the TPC triggers recorded by the TPC DAQ and the tracking DAQ. In (a) the large time window from 250 ms to 0 ms is shown containing the correlated trigger events. In (b) the region of interest is enlarged showing the indicated trigger dead time window of the TPC. In (c) the width of the trigger coincidence peak is shown.

From the muon side, events are used based on the discussed event selection. Muon and proton data is then combined on a run-by-run basis and the time difference for each event combination is evaluated within a defined time window to keep the number of possible combinations at a reasonable level. The drift time of the IKAR TPC is assumed to be about $t_{\text{drift}} = 100$ µs. Matching events are assumed to be in a window of $\pm 5 t_{\text{drift}} = \pm 500$ µs. The time shift of 200 ms is applied to the time difference.

Associated Muon-Proton Events

By applying the discussed time shift of 200 ms for the time difference between the TPC and muon-tracking events, a time correlation is extracted. The muon events are selected based on the previously discussed event selection (cf. Sec. 3.6). For the TPC data an event selection based on signal time and energy deposition on pads per event is performed by [90] to select meaningful events. The resulting time difference of those events is shown in Fig. 3.35(a). A correlation peak is visible between -250 ms and +20 ms. From the 2018 data discussed in Sec. 2.5, the drift time window of the TPC should be reassembled. For the IKAR TPC, a drift time of about 140 µs is expected [85]. In addition, a rectangular shape of the spectrum according to the drift is expected. The resulting shape and overall width of 270 µs is investigated in the following. This feature is also visible in the vertex z-correlation of the events shown in Fig. 3.35(b). Events close to the anode structure position on the up- and downstream side of the TPC at roughly $z_{\text{up}} = -43.45$ m and $z_{\text{down}} = -42.66$ m have the shortest drift and therefore the smallest drift time, those closer to the central cathode at $z_{\text{cath}} = -43.05$ m have the longest drift.

A clear correlation between the muon events and the recoil-proton events in scattering angle and total energy is shown in Fig. 3.35(d). The scattering angle is given in terms of $\sin^2(\theta/2)$ as it is proportional to the Q^2 (cf. Eq. (1.8)). For the conversion into the reconstructed Q^2 (cf. Eq. (1.7)), the momenta of the incoming and scattered muon are required, which are not yet reconstructed within this production. Furthermore, the used TPC data is not yet calibrated in the shown data and given in arbitrary units. The correlation shows the expected accumulation at lower values. As lowest value a scattering angle of 300 µrad is chosen corresponding to the energy threshold of the TPC data of 0.5 MeV ($Q^2 = 10^{-3}$ GeV$^2/c^2$) recoil protons. A rough maximum of the scattering angle distribution corresponds to about $Q^2 = 0.008$ GeV$^2/c^2$.

Using the angle-energy correlation shown in Fig. 3.35(d), a cleaner sample can be obtained. Selecting events within this region as shown in Fig. 3.36(c) results in a lower background in the time correlation as well as the vertex z-distribution shown in Figs. 3.36(a) and 3.36(b). For the current selection of events about 2000 correlated events of muon and recoil-proton can be identified and can be used for further studies. The difference towards expected number of 10000 events as discussed in Sec. 3.7 is still subject of investigation.

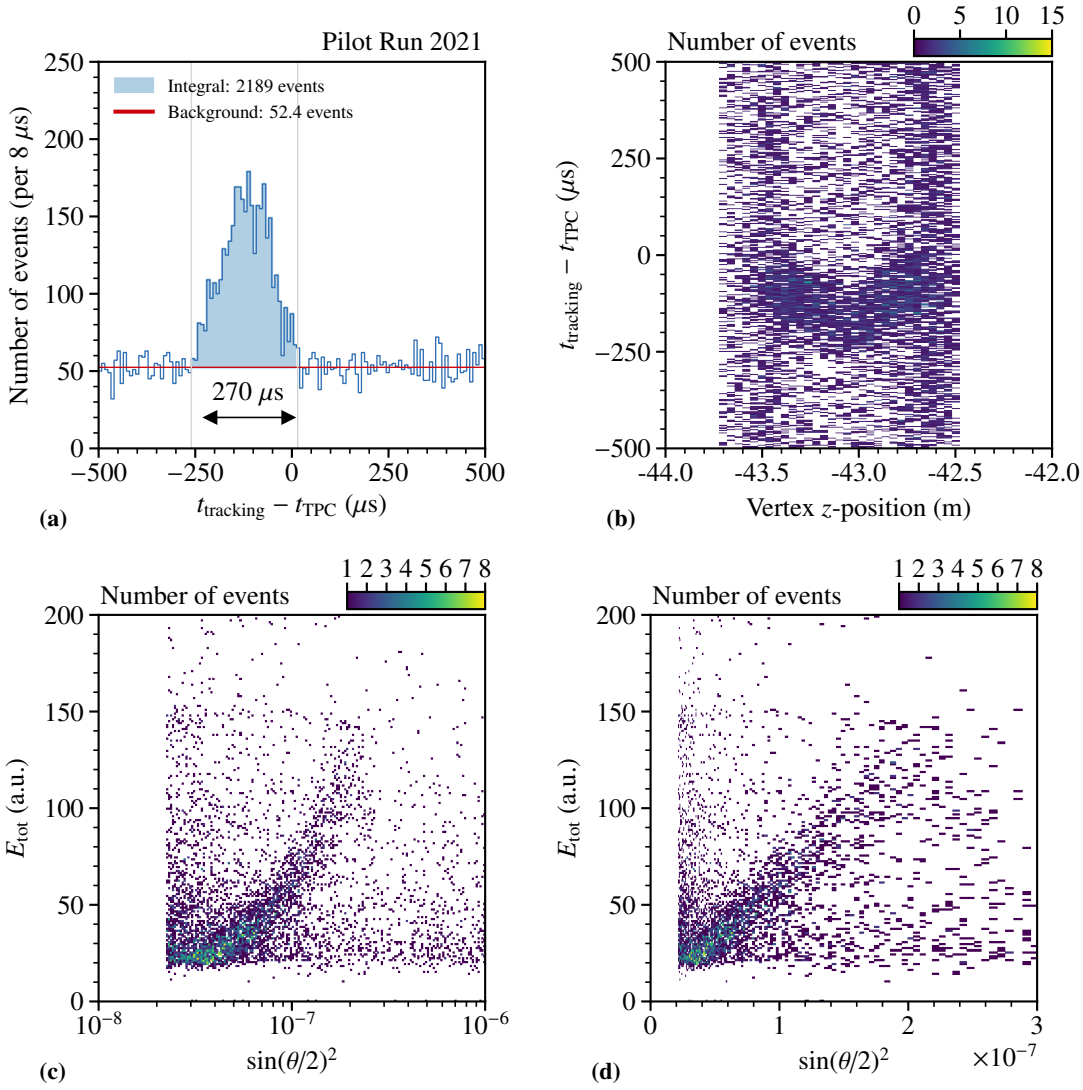

Figure 3.35: Result of the event-time correlation of muon and proton data from tracking and TPC. In (a) the time difference between both events with the background subtracted number of events is shown. The time-difference correlation along the vertex z-position is shown in (b). The correlation between muon scattering angle (cf. Eq. (1.8)) and deposited recoil-proton energy is shown in (c) in logarithmic and in (d) as linear scale.

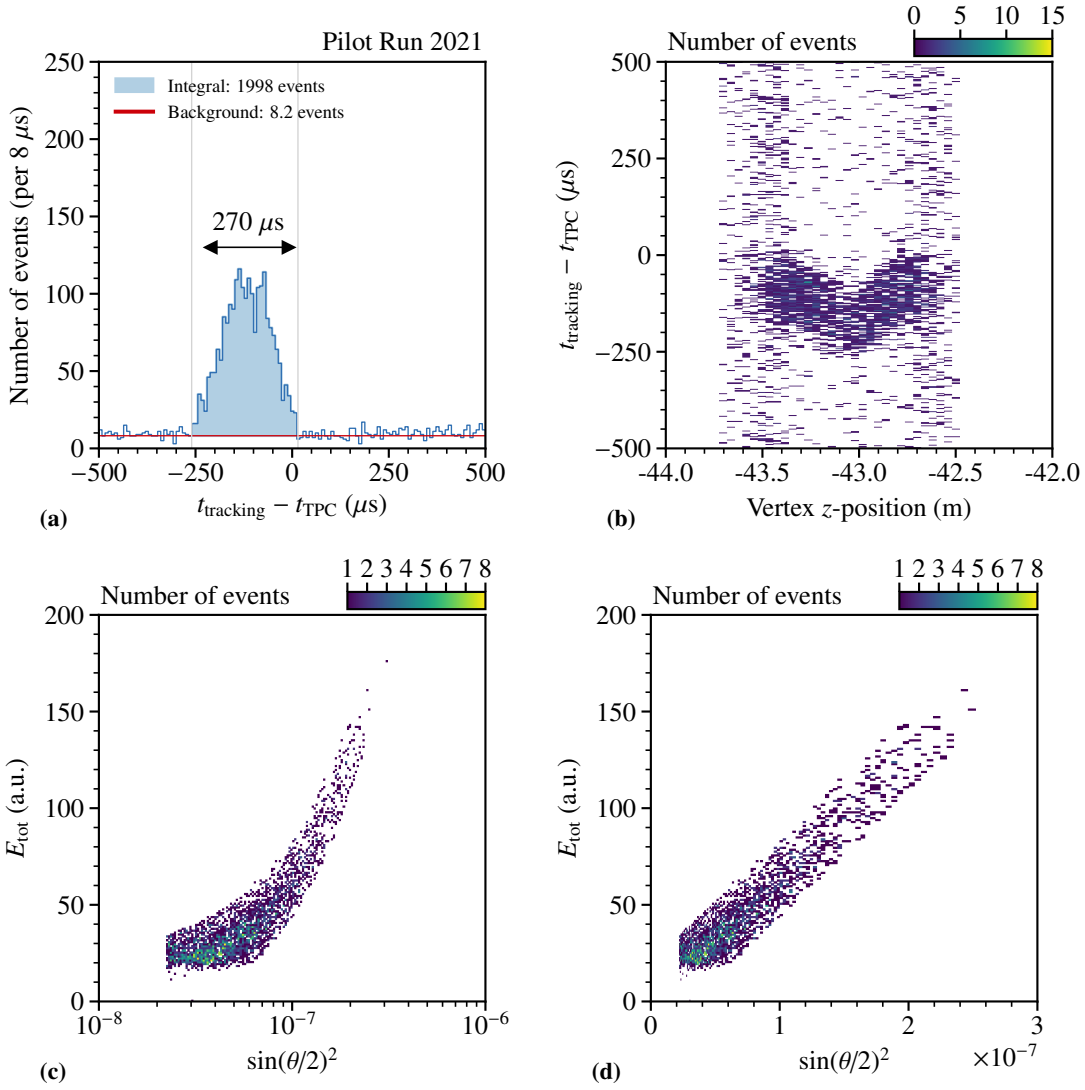

Figure 3.36: Result of the event-time correlation of muon and proton data from tracking and TPC after selecting events within the scattering angle and deposited energy correlation. In (a) the time difference between both events with the background subtracted number of events is shown. The time-difference correlation along the vertex z-position is shown in (b). The correlation between muon scattering angle and deposited recoil-proton energy is shown in (c).

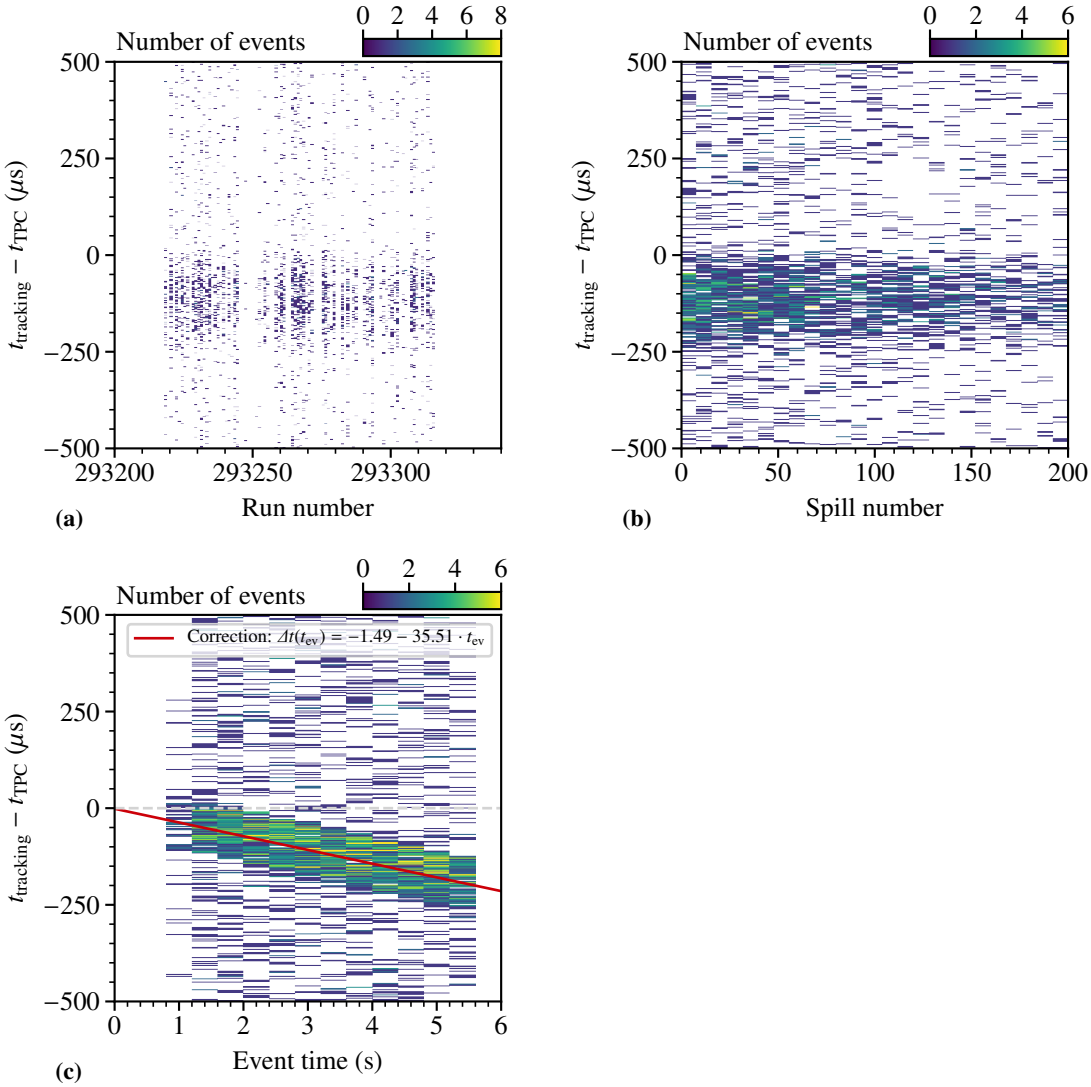

Figure 3.37: Stability of matched events during the data taking. The distribution across single runs is shown in (a), for single spills in (b) and during each event in (c). An additional time-correction is indicated based on the shown event time.

The stability of the matched events during the data taking is shown in Fig. 3.37 for the single runs, single spills and within those single spills. A stable recording of events and no indication of possible missing reconstructed data could be found. Single gaps for single runs shown in Fig. 3.37(a) are understood and correspond to very short or calibration runs. For the single spills shown in Fig. 3.37(b) the contribution of the majority for shorter runs can be seen by the accumulation of events at lower spill numbers. Nevertheless, the correlated events are stable over the default maximum of 200 recorded spills per run.

An overall shift of the time difference depending on the event time is visible inside the single spills as shown in Fig. 3.37(c). This shift is introduced artificially by using the time of the iFTDC recording the time message for synchronization and the event time for each event, which is provided by a third time system. In the future, a dedicated event time given by the synchronization iFTDC is foreseen. For now a correction shown in Fig. 3.37(c) at this stage is applied to compensate the drifting of the two clocks.

Applying the correction of the selected events as shown in Fig. 3.37(c) compensates the drift during the single spill time and corrected the artificially broadened time-difference of the correlated events. The result of the correction on the time difference is shown in Figs. 3.38(a) and 3.38(b) for the raw selected events and the events fulfilling the discussed $\theta - E_{\text{tot}}$-correlation. The initial number of events is slightly increased as shown in Fig. 3.38(a) and 1974 events can be extracted. An artifact by the applied time correction of the events is visible starting at -500 ms due to the fixed time window of ±500 ms, shifting events from the lower edge along the time difference. The initial background is slightly decreased by about 4 % compared to the data set without the correction. The expected rectangular shape due to the drift time of the TPC is visible as well as the corresponding drift time of 145 µs. Using the $\theta - E_{\text{tot}}$-correlation, a clean spectrum is obtained as shown in Fig. 3.38(b). The drift-time correlation along the vertex z-position given in Fig. 3.38(c) shows now a clean structure with discussed features.

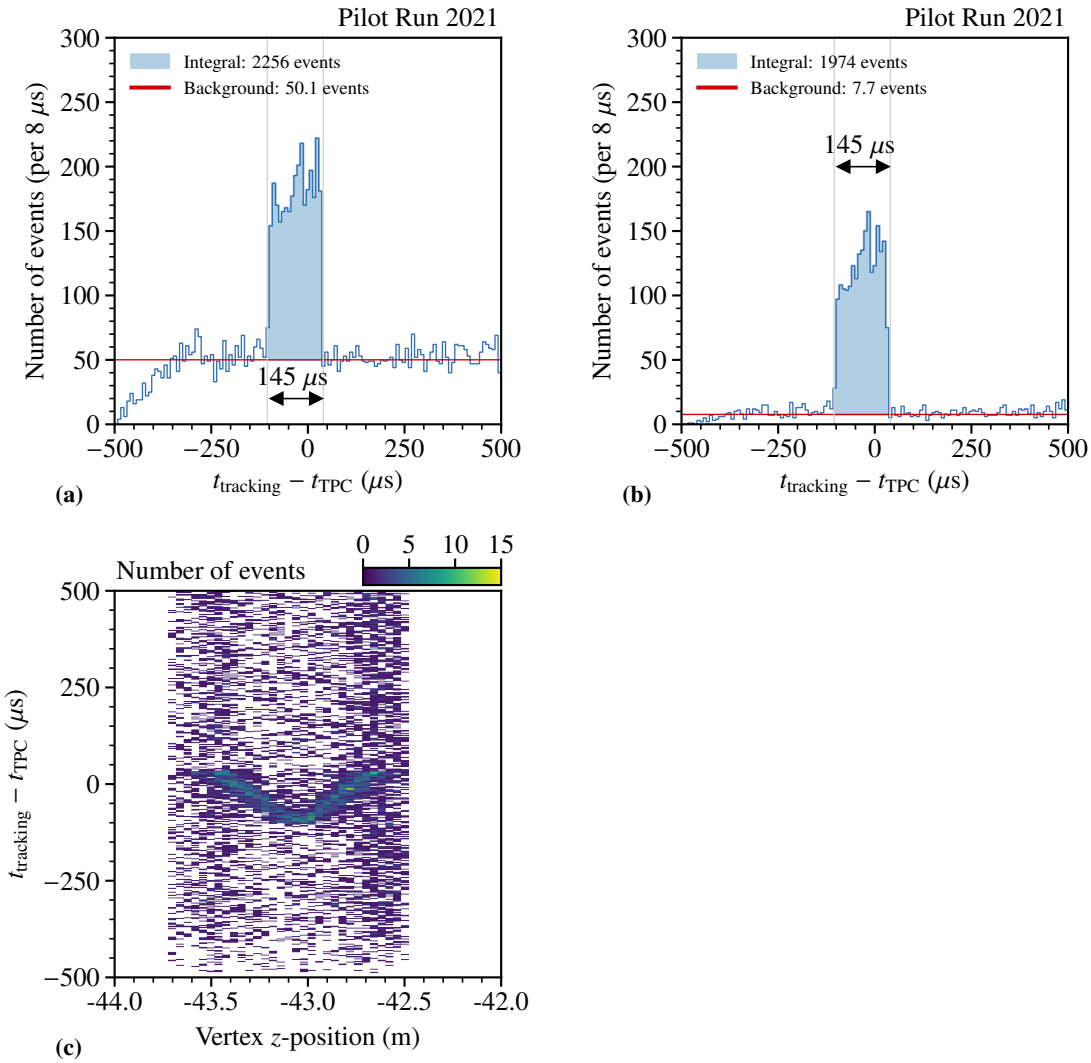

Figure 3.38: Result of calibrated the event-time correlation of muon and proton data from tracking and TPC. In (a) the time difference between both events with the background subtracted number of events is shown. In Fig. 3.38(b) the result using the correlation between muon scattering angle and deposited recoil-proton energy is shown. The resulting drift-time dependence on the vertex z-position is shown in (c).

3.8 Summary and Outlook

The pilot run measurement performed in October 2021 was the first measurement under the umbrella of the new AMBER collaboration. It is used to evaluate the performance of the setup for the anticipated measurement of the proton radius starting 2023/2024. To verify that the expectations of the measurement can be fulfilled, a close-to-final setup was recommended by CERN's SPSC as a requirement for a following physics run. Prior to the measurement, goals have been formulated as dedicated work packages to allow a later evaluation. Due to persisting limitations[9], not all topics could be addressed in the proposed time and have been delayed. Nevertheless, the main goal was to study the TPC performance in terms of energy resolution and induced beam noise under close-to-final conditions.

Within 20 days, a full setup consisting out of five silicon tracking stations, two scintillating fiber trackers and a beam trigger system has been constructed around the IKAR TPC at a novel 13 m long test beam location in the M2 beam line. Commissioning and calibration of the single detectors, especially the TPC and the silicon detectors has been performed. The beam conditions are comparable to the final position, but they are expected to be slightly more improved at the target position of the spectrometer. Nevertheless, evaluation of the TPC energy resolution is within the expectations. During the measurement with the pilot run setup, the full spectrometer was read out as well. First studies of the momentum and track reconstruction with the adapted layout of the spectrometer to the lowered beam momentum showed issues with the momentum reconstruction in case of scaling single magnets. Therefore, no magnet scaling is foreseen, but a single-magnet operation is planned.

To obtain a clean data set, a new beam trigger system was constructed and operated to select events from the central part of the beam with low divergence. This results in a non-prescaled beam trigger and recording of all events passing through the central part of the TPC. Preceding simulation studies to evaluate this trigger elements agreed with the obtained real data. Compared to 2018, the inner structure of the TPC has been adapted, and no additional material was found in the acceptance that might disturb the trajectories of the traversing muon. The used silicon detectors showed an expected good performance and resolutions. This precise tracking will be used in the analysis to further evaluate the recoil proton events in the TPC. The same event time stamping is utilized as in the 2018 feasibility test, which served as predecessor for the new streaming DAQ system. It showed comparable results as expected from the 2018 data. Adaptions to the data format have been made with respect to 2018 and have been implemented in the data decoding. The resulting event selection of muon tracks and proton events from the TPC are used to find correlations in both systems. After applying additional time corrections required due to introducing a third uncalibrated clock, expected correlations between the drift time and the vertex z-position as well as the measured energy in the TPC and the muon scattering angle could be found.

[9] COVID-19

In the future, a new implementation of the event time by using only the two respective clocks that are calibrated with respect to each other will remove the required additional calibration. About 2000 events have been identified, which is a factor of five lower than the expected value of 10000 events. Investigations are ongoing to clarify this results. Nevertheless, already those clean events can be used to further develop a matching procedure that can be applied in the future to the lowered beam momentum streaming DAQ system. Based on those events, the energy calibration of the TPC can be performed in the future and position dependent relations can be studied. A new alignment which includes the so far not included scintillating fiber detectors is foreseen. In addition, a combination with the spectrometer data is planed to allow momentum measurement of the scattered muon. Also, the measurement of the BMS is of interest, especially for the elastic muon-electron scattering as calibration channel. Currently, first studies and analysis are performed on a preliminary real data set and together with simulations for further evaluation [91].

CHAPTER 4

Summary and Outlook

The proposed measurement of elastic muon-proton scattering at a beam momentum of up to 100 GeV at the M2 beam line using an active-target pressurized-hydrogen TPC combined with the muon measurement using a magnetic spectrometer can contribute to a solution of the persisting proton radius puzzle, especially in terms of different systematics compared to elastic electron-proton scattering.

As first preparation, a test measurement in the year 2018 was used as feasibility test of the principle to redundantly measure the elastic muon-proton scattering in a pressurized-hydrogen TPC and silicon-microstrip detectors. The measurement was performed in a parasitic mode during the COMPASS data taking at the downstream test beam location. A main task was to study the TPC in a muon beam to evaluate the energy resolution. For the test measurement, the prototype ACTAF2 TPC was used. Originally, this TPC was constructed to be used in a pencil-like electron beam and the design, especially of the readout plane, was not optimized. The induced ionization noise in the TPC was studied, which affects the energy resolution of the reconstructed kinetic energy of the recoil proton. Thresholds of about 200 keV proton energy could be used to measure the recoil proton events. The measurement of the TPC was combined with muon tracking based in silicon-microstrip detectors to determine the incoming and scattered muon trajectory. The measurements of the proton in the TPC and the muon trajectory were recorded by two distinct DAQ systems. Using a common event time allowed to associate events measured by both systems based on their time difference. This procedure was used as predecessor to the planned streaming DAQ system foreseen for the final measurement. Based on this, about 88 % of the expected 780 combined events could be identified, which show a correlation in the drift time and vertex z-position as well as in the energy between recoil proton and scattered muon. To allow a calibration of the incoming muon beam momentum in the final measurement, the angular relation in the elastic muon-electron scattering was studied. First promising results could be extracted and serve as starting point to calibrate the incoming muon momenta based on the BMS measurement in the beam line. Furthermore, studies are ongoing to extend this approach towards the inverse kinematic of measuring the proton radius in elastic proton-electron scattering. This idea could also be expanded towards radii of pions and kaons.

With the proposal for the proton radius measurement, a dedicated pilot run in the year 2021 was requested by the SPSC to validate the expected resolutions and behavior of the experiment and especially the TPC. Dedicated 20 days of beam time in the test area of the M2 beam line was used to study the energy resolution of the prototype IKAR TPC in a close-to-final configuration of the setup and beam optics. Similar to the 2018 test measurement, silicon detectors and scintillating fibers for muon tracking were used. It was found, that the energy resolution of about 40 keV of the TPC due to induced beam noise matches the expectations. Evaluation of the data is ongoing, but first results already show about 2000 timestamp-based correlated events between both systems. Further work to combine the data of the pilot run setup with the spectrometer information are ongoing and results are expected soon.

A novel pressurized-hydrogen TPC offering pressured up to 20 bar is planned for the final measurement. It will consist out of four drift cells as active-target volume. The segmented readout plane in each volume will allow covering a Q^2-range of $10^{-3} \leq Q^2/(\mathrm{GeV}^2/c^2) \leq 4 \cdot 10^{-2}$. Studies have been performed to further extend the range up to $Q^2 = 0.08\ \mathrm{GeV}^2/c^2$ with a relative precision of around 4 % based on energy loss inside along the proton path. For muon tracking, a combination of SFH and SPD will be combined in four UTS up- and downstream of the TPC providing a precise measurement of the scattering angle. It allows disentanglement of pile-up events in the SPD up to ten times larger rates as the anticipated one.

Optimizations of the material budget, especially of the SPD and dedicated helium beam pipes have been performed, which results in a total material budget of 4 %. The planned setup will have lever arms of 3 m on the up- and downstream side between the UTS to obtain the required angular resolution of about 25 µrad for the scattered muon, resulting in a relative Q^2-resolution of 15 % at the lower end of the Q^2-range. A novel streaming DAQ system will be used to compensate the time resolution differences between fast tracking detectors and the TPC. The combination of TPC proton measurement and muon tracking in the spectrometer allows the novel approach this redundant measurement. First estimations of the required number of events show, that about 33 million events are required to obtain the anticipated precision of 1 % on the extracted proton radius, depending on the used model.

A first physics data taking could take place starting mid of 2023. After the transition phase from the previous data taking, the PRM setup could be installed. After a commissioning of the setup, first physics data could be recorded afterwards. Nevertheless, ongoing developments and construction of the new TPC as well as the foreseen novel four UTS are pursued. The first full physics data taking could take place starting 2024.

Further ideas like elastic proton-electron scattering are under investigate to access the proton radius using a proton beam as a different approach. The idea of this inverse kinematic can be further extended towards pion and kaon radii. Especially, the current political situation could affect the contribution from groups of the collaboration, which might require different steps in the future.

Part II

Instrumentation

CHAPTER 5

Silicon-Microstrip Detectors at COMPASS

For the COMPASS collaboration, three cryogenic silicon-microstrip tracking detectors are used as beam telescope and two additionally ones have partially been used as detectors for particles scattered at small angles. The first operation of those detectors took place during the 2008 data taking. Since then, they have been used regularly until 2012. From 2016 until 2022 they have been operated during various measurements with the spectrometer. As first version, so-called warm stations have been used until 2007 prior to the cryogenic one.

Those warm detectors have been put back to operation for a feasibility test measurement in 2018 as preparation for a possible proton radius measurement (cf. Chap. 2) within the new AMBER collaboration. The goal was to evaluate the measurement principle of operating an active-target high-pressure hydrogen TPC in a muon beam and combine the recoil proton measurement with the results obtained from muon tracking. As preparation for a physics run for the proton radius measurement, anticipated in 2023/2024, a preceding 20-days pilot run was performed in 2021 (cf. Chap. 3), with the goal to evaluate a similar setup as in the previous 2018 feasibility test measurement, but with a close-to-final geometry of the layout. Five of the warm silicon stations served as tracking detectors during this data taking. These detectors offer a precise tracking with a spatial resolution of $O(\mu\text{m})$ and a time resolution of $O(\text{ns})$ (cf. Sec. 5.5.1).

The cryogenic version of the detector require a PLC-based cooling system to allow the operation at temperatures of 200 K achieved by using liquid nitrogen. The warm stations can be operated with a simpler gaseous nitrogen, cooling and require less infrastructure. The operation of the cryogenic and the warm version during their respective data taking periods as part of this thesis is described in the following or in the dedicated sections (cf. Secs. 2.1.4 and 3.3) for the feasibility test measurement and the pilot run.

A main focus is given to the operation of the cooling system of the cryogenic stations. These stations have been operated along this thesis starting in 2016 and are foreseen to be further used also within the first AMBER data taking to measure the anti-proton cross-section [2]. These detectors are not suitable for the novel streaming DAQ due to their APV25-based readout system (cf. Sec. 5.1), which requires a dedicated trigger signal synchronized to the interaction.

5.1 Detector Modules

The wafer design was done for the HERA-B experiment by the Halbleiter Labor (HLL) of the Max-Planck-Institute in Munich and produced by the Norwegian company Stiftelsen for Industriell og Teknisk Forskning (SINTEF) in Oslo. It has a double-sided strip-readout design to reduce the material budget compared to single-sided wafer designs. The 280 µm thick n-type wafer has an active area of $70 \times 50\,\mathrm{mm}^2$. On the n-side it has 1280 strips with a pitch of 54.6 µm and perpendicular 1024 strips on the p-side with a pitch of 51.7 µm. In this configuration two spatial coordinates are covered with one detector module. The strips are tilted by 2.5 degree with respect to the wafer edge as shown in Fig. 5.3. Two additional detector modules are placed in one detector station with an inclination of ±2.5 degree towards the main reference system. By this the projections U, V and Y, X are measured as ordered along the beam axis. In Fig. 5.2 the cross-section schematic of the silicon wafer design is shown. The single strips with their respective pitch are indicated on the n- and p-side. The p-side is equipped with additional so-called intermediate strips. Those enhance the charge sharing between two neighboring strips and increases the spatial and time resolution. The modules are mounted in that way, that the n-side features the U- and X-plane and the p-side the V- and Y-plane. Therefore, the respective two planes show slightly different properties, due to the wafer design, which can be seen in the later evaluation. [92]

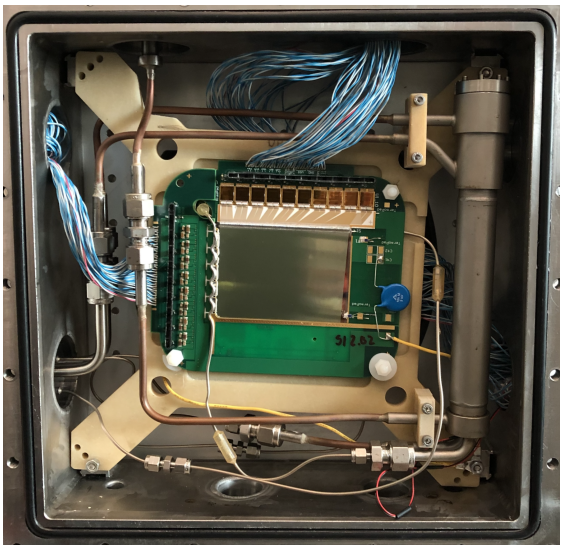

Figure 5.1: Inner view into the cryogenic silicon station. The detector module is placed in the center with green support structures providing cooling and electrical connections. The phase separator for the liquid nitrogen is visible on the right.

In Fig. 5.1 the inside of a cryogenic silicon station is shown with the module in the center mounted on the respective holding structure. The larger U-side with 70 mm can be identified by the ten bonded APV25 chips connected on the top. The V-plane is located on the back of the U-plane. The second module for the X- and Y-plane is positioned on the other back side and not visible in the picture. Feed-throughs towards the outside of the cryostat are connected to so-called repeater cards, which provide amplification as well as power and data connections. They are connected via the visible blue wires on the top and left side and serve as connection to the detector module. The shown cryogenic version of this module is equipped with cooling pipes mounted close to the silicon wafer itself and allow a reliable cooling of the wafer and the electronics. The detector module is cooled down to 200 K by circulating liquid nitrogen through those cooling pipes. Lower operation temperatures have been tested [93], but it was found that the operation at this temperature ensures a safe operation of the detector module due to the different expansion coefficients of the used materials [94]. This operation principle makes use of the so-called Lazarus effect [95] as

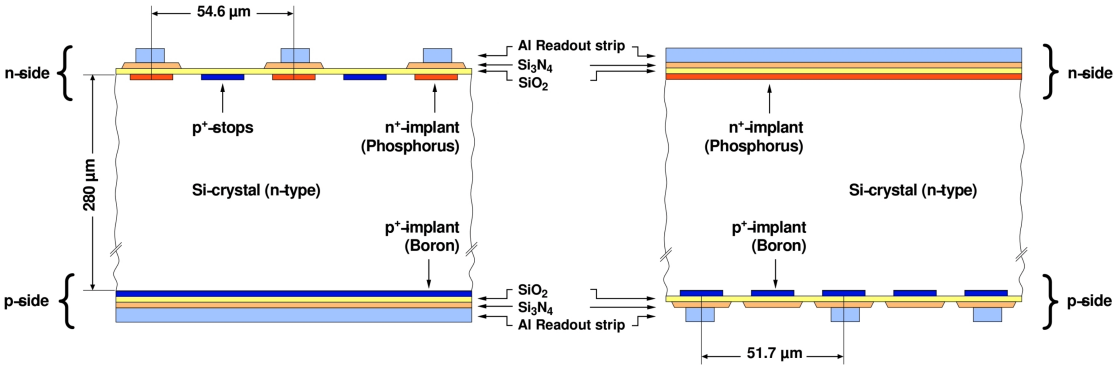

Figure 5.2: Cross-section schematic of the silicon wafer design. Stops and implants are marked. The pitch of the different strips on the n- and p-side is indicated as well as the intermediate strips on the p-side. Figure taken from [92].

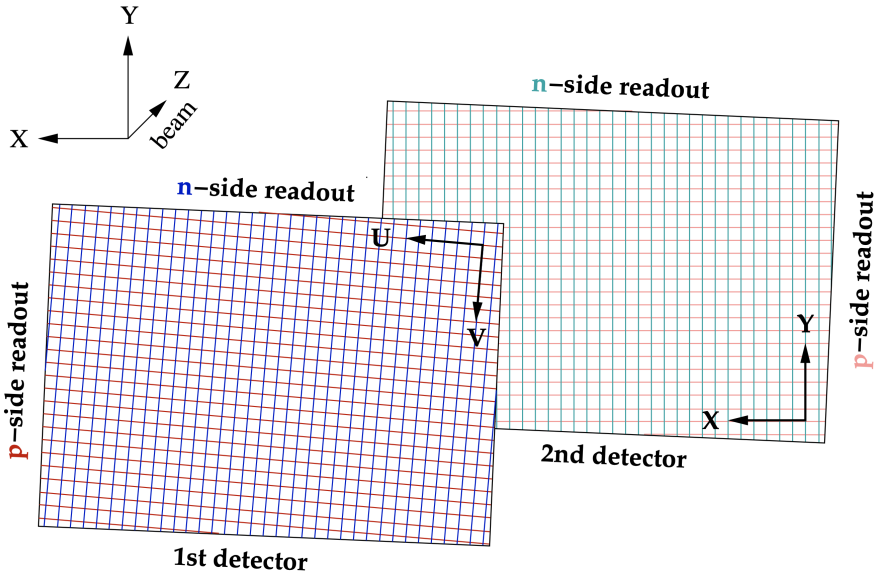

Figure 5.3: Schematic view of the silicon wafer orientation as installed in the cryostats in the given coordinate system. Figure taken from [92].

well as reduces the thermal noise and thus improves also the time and spatial resolutions. The phase separator required for the liquid nitrogen operation is visible on the right. It is filled from the outside by nitrogen supply tubes in a continuous flow. The two detector modules mounted in each station are connected separately to the separator allowing an independent cooling of each. The respective output flows and therefore the temperature is controlled by flow meters and valves on the outside of the cryostat.

APV25 Chip

As readout for the individual strips, the APV25 chip [56] is used. In Fig. 5.4 the scheme of a single chip is shown. It is an analogue-pipeline Application-Specific Integrated Circuit (ASIC) and has a total size of $8\,055 \times 7\,100\,\mu m^2$. It was initially designed to read out silicon strip detectors in the Compact Muon Solenoid (CMS) tracker, and is also used at the COMPASS experiment for the readout of silicon and GEM detectors. The chip is based on the Inter-Integrated Circuit (I^2C) standard for configuration. Each chip provides 128 channels with preamplifier and shaper connected to a 192 column analogue memory which stores samples with the common 38.88 MHz Large Hadron Collider (LHC) clock. This allows an overall coverage 4.89 µs as latency, but values in the column memory larger than 160 will reduce the pipeline efficiency at larger trigger rates. These delay or latency values between the trigger and writer pointers can be adjusted according the required incoming trigger latency. [56]

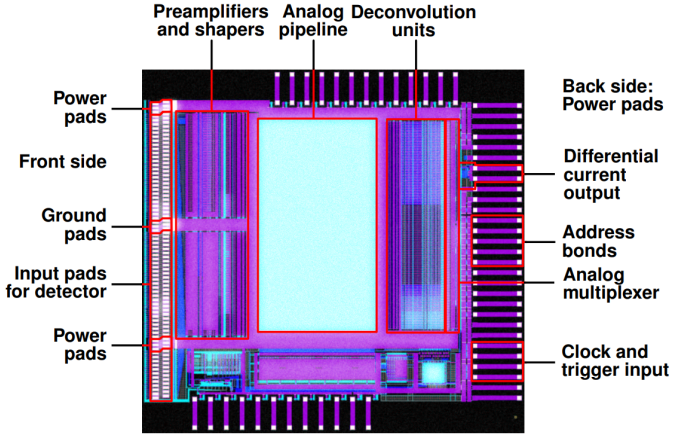

Figure 5.4: Layout of the APV25 chip. The single detector strips are connected via bonding wires on the left side. Connector pads on the right are used for the output, clock, trigger and power lines. Pads on the top and bottom side can be used as probe pads. Figure taken from [96].

The chip can be operated in different modes, which can be adjusted via the respective mode register as listed in Tab. 5.1. Depending on the operation on the silicon wafer, an inverted or non-inverted mode to set the preamplifier polarity for the incoming signal shape is required. The readout frequency and clock can be set to either 20 MHz or 40 MHz and the amplitudes are recorded with either one or three samples. For the silicon U- and X-planes, a mode value of 13 (00001101) is used, and for the V- and Y-plane a mode value of 45 (00101101). The operation mode is results to a 3-sample peak readout at 20 MHz. This mode is adjusted for the respective plane. For testing the single sample readout, the delay between the ADC and APV25 can be checked and adjusted on the ADC side by correcting the delay clock or delay trigger value.

In the COMPASS spectrometer, the used cryogenic silicon detectors have the so-called S1 version of the chip installed. The previous warm detector stations use the S0 version chip. These two versions need a different default setting for the reset polarity of the chip. Further information about the chip can be found in [56].

Table 5.1: The APV25 mode settings for the respective bit number. [56]

Bit number	Function	Value = 0	Value = 1
7	Not used	-	-
6	Not used	-	-
5	Preamplifier polarity	Non-inverting	Inverting
4	Read-out frequency	20 MHz	40 MHz
3	Read-out mode	Deconvolution	Peak
2	Calibration inhibit	OFF	ON
1	Trigger mode	3-sample	1-sample
0	Analogue bias	OFF	ON

Table 5.2: Silicon detector operation during the years 2003–2022. The type defines different detector stations and operation modes. The operation in respective beam times are given.

.

Detector name	Type/Mode	APV	Operated
SI01UV (new) SI01XY (new)	cryogenic	S1	2008–2012^{C}, 2016^{C}, 2017^{C}, 2021, 2022^{C}, 2023^{A*}
SI02UV (new) SI02XY (new)	cryogenic	S1	2008–2012^{C}, 2016^{C}, 2017^{C}, 2021, 2022^{C}, 2023^{A*}
SI03UV (new) SI03XY (new)	cryogenic	S1	2008–2012^{C}, 2016^{C}, 2017^{C}, 2021, 2022^{C}, 2023^{A*}
SI04UV (new) SI04XY (new)	cryogenic/warm	S1	2008–2012^{C}, 2018^{A}, 2021^{A}
SI05UV (new) SI05XY (new)	cryogenic/warm	S1	2008–2012^{C}, 2018^{A}, 2021^{A}
SI01UV (old) SI01XY (old)	warm	S1	2003^{C}, 2004^{C}, 2006^{C}, 2007^{C}, 2018^{A}, 2021^{A}
SI02UV (old) SI02XY (old)	warm	S0	2003^{C}, 2004^{C}, 2006^{C}, 2007^{C}, 2018^{A}, 2021^{A}
SI03UV (old) SI03XY (old)	warm	S1 S0	2003^{C}, 2004^{C}, 2006^{C}, 2007^{C}, 2021^{A}

^{A} AMBER
^{C} COMPASS
* planned

An overview of the silicon detectors of COMPASS and AMBER is listed in Tab. 5.2. In total eight stations are available with cryogenic or warm design. The cryogenic version of the detectors has been used for the COMPASS spectrometer starting from 2008 and uses the S1 APV25 chip. These detectors are planned to be used for the AMBER data taking in 2023. The warm stations were recently used in the 2018 feasibility test measurement for the proton radius measurement and the pilot run in 2021.

5.2 Read-out System

A schematic overview of the readout chain is shown in Fig. 5.5. The induced signal is processed and the analog output is passed through short flat-band cables towards the repeater card. Power supply for the APV25 chips as well as trigger, clock, data and temperature readout connections are fed through the card. Furthermore, it amplifies the analog digital output signals of the APV chip and passes it to the so-called Silicon and GEM ADC (SGADC), where the data is digitized. One ADC card supports up to 12 APV chips. The incoming data is processed by two FPGAs, where each is connected to six ADCs. Inside each ADC, the data is processed in parallel allowing the so-called zero- and common-mode noise suppression and the handling of the pedestals for each channel. Only signals that exceed a given threshold of the overall baseline fluctuation are further processed and sent out to the so-called GEM-Silicon Control and Acquisition (GeSiCa), which is connected via optical fiber. Up to four ADCs can be connected to one GeSiCa. Due to the depletion voltage of the detector module, it is required to use those optical connections. The TCS clock as well as reset and trigger signals are distributed across the GeSiCa towards the front-end cards. The serial data stream is sent via optical fibers to the DAQ. Further details can be found in [86, 92].

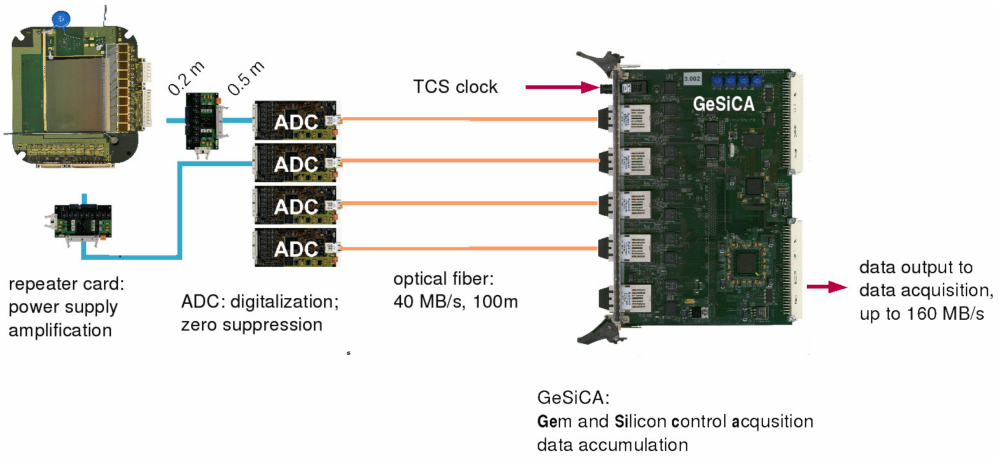

Figure 5.5: Silicon readout chain is shown. The detector module is connections to the frond-end electronics are indicated towards the transmission to the DAQ. Figure taken from [92].

5.3 Silicon Detector Operation at COMPASS

The silicon detectors are operated since 2003 as beam telescope. Starting with 2008 two additional silicon stations were installed to measure the scattered particles, especially during the runs in 2008 to 2012 [97]. From 2016 on, only the beam telescope stations are installed and operated. The required angular acceptance downstream of the target for the physics programs at COMPASS required a larger angular acceptance, which the silicons could not provide, or the required space downstream of the target location is not sufficient. Since the silicon stations are used as a beam telescope located on the so-called target platform, they have to be disassembled each year for the transition between each target configuration. Therefore, a full re-installation is required for every year.

In Fig. 5.6(a) the recent installation during 2022 is shown. The silicon stations are located inside dedicated cryostats visible with the beam entering from the right side passing through the respective beam windows (visible as white frames) of the stations. To avoid the deposit of water and ice on the windows during the operation, they are flushed with gaseous nitrogen. The silicons are operated at a temperature of 200 K using a liquid nitrogen cooling system. The detector modules are placed in a vacuum inside the cryostats. Liquid nitrogen is provided via dedicated transferlines (top to left) connecting the single stations to the so-called valve box as nitrogen distribution box. A schematic view of the cooling circuit is shown in Fig. 5.6(b).

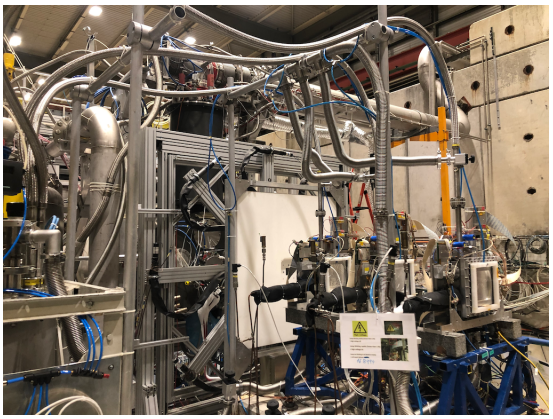

(a)

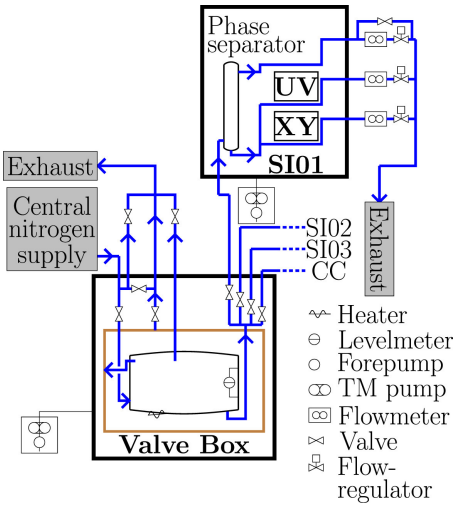

(b)

Figure 5.6: The silicon setup at COMPASS is shown (a). The three detector stations are visible on the right with the beam passing from right to left. Vacuum and liquid nitrogen connections are attached to the stations. Transferlines for liquid nitrogen connect the so-called valve box on the right with the single stations. In (b) a schematic drawing of the valve box and the first station located inside the cryostat. Figure taken from [98].

The cooling of the system is fully automatized and based on a PLC. Detailed information about the cooling system can be found in [94]. The cooling system is based on Proportional-Integral-Derivative (PID) algorithms using feedback loops to control the temperatures and pressures of the system. For this, multiple pressure and temperature sensors are installed as input for the control of the pressure and flow valve.

According to [94], for a control variable y the input of variable x is used. The difference to the set point w of x is used as error $e = w - x$. The regulation is then based on a proportional term, and integral term and the derivation of the error as given in [94] as

$$y = \underbrace{K_\mathrm{P} \cdot e}_{\text{proportional}} + \underbrace{K_\mathrm{I} \int e \,\mathrm{d}t}_{\text{integral}} + \underbrace{K_\mathrm{D} \frac{\mathrm{d}e}{\mathrm{d}y}}_{\text{derivative}} . \tag{5.1}$$

The respective non-negative coefficients K for the respective terms results in the contribution and is used to regulate possible overshoots or oscillations around the set point. As example, temperature probes attached to the detector module give feedback of the current temperature value and serve as input for the nitrogen control valves to regulate the flow.

The cooling system itself is controlled via the MUSCARDE® system [99]. A screenshot is shown in Fig. 5.7[1]. As shown in the schematic view presented in Fig. 5.6(b) the single components are visible. Control units for the valve box in the center as well as the three stations (white boxed) on the left are visible (C300 to C500)[2]. Temperature probes as well as pressure sensors and flow meters are indicated at the respective location. Since the cooling operation of the system is fully automated, the basic operations of the single components are accessible as shown on the left side — *COOLING*/*HEATING* for the single stations and *START*/*STOP* for the valve box operation. Under regular conditions, no manual interventions are required. For testing purposes, each value can be set by hand and single tests of the modules can be performed. In case of problems the PID values can be adapted. If a failure of single sensors arises, the system can be controlled by hand[3].

Prior to each cooling operation of the stations, the valve box needs to be filled with liquid nitrogen. This is mostly done in an automatic mode, but requires some manual adjustments to compensate for the large pressure rise in case of the fully warmed-up liquid nitrogen reservoir. In Fig. 5.8(a) the automatic refilling of the valve box is shown during the data taking in 2022. As soon as it reaches a fill level (pink) below 35 % the system starts to cool down the inlet transferline as well as the bypass and the attached exhaust to avoid large pressure spikes during filling. The temperature of the bypass (light blue) rises as soon as the inlet valve (green) is opened. During cooling, a constant pressure (blue) of about 1450 mbar is used to avoid sudden pressure spikes. As soon as the temperature of the bypass is below 90 K for a sufficient time the liquid nitrogen is filled into

[1] In the software a minor issue is present for the indication of the bypass for the phase separator. Here the bypass status indication is inverted. It is indicated as *open*, but is closes in reality in this case.

[2] C600 is the conical cryostat, which is not operated since 2012.

[3] Only if the operator is experienced enough.

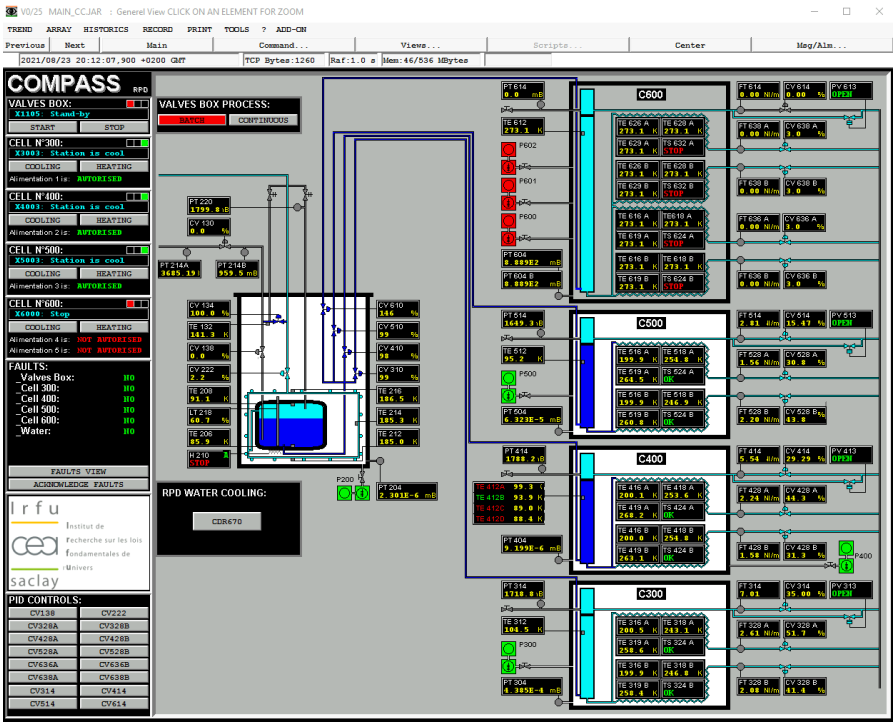

Figure 5.7: Screenshot of the MUSCARDE® control system during 2021 data taking. The tree detector stations are depicted on the left (C300 to C500) with the valve box in the center.

the reservoir. This results in a pressure rise (red) inside the valve box, which is regulated that the pressure inside the valve box (yellow) stays at a constant 1800 mbar. This is the optimized value to operate the attached stations. The filling is performed until the fill level reaches 70 % leaving some safety margin. A total of 50 liters are stored. This process usually takes about 30 to 90 minutes, depending on the inlet pressure (black) from the main transferline. As soon as the filling is finished, the nitrogen is guided through the bypass and all inlet valves are closed. The circuit part between the main transfer line and the exhaust stays fully open to avoid building up pressure. The refilling cycle is performed every 16 hours. During the data taking, the single silicon modules are held at a constant temperature of 200 K.

The APV25 dissipates 2.31 mW per channel, resulting in about 10 W[4] for the four planes inside each cryostat. In Fig. 5.8(b) the cooling procedure for the station SI01 is shown as example. At first, the phase separator is cooled down (blue) and the pressure inside the phase separator (black) rises to 1750 mbar. Oscillations of the pressure are present and are interconnected within the whole system. If the temperature reaches 200 K the two detector planes (pink, brown) are slowly cooled down with about 0.1 K/s to avoid large temperature gradients. The flow meters (red, light blue) regulate the flow through the detector module and control the resulting temperature. The resulting temperature of 200 K is reached within about 30 minutes and is kept at a constant level

[4]Each APV25 chip has 128 channels. The X- and U-planes are equipped with 10 APV chips, and the Y- and V-plane has 8 chips each.

of ±0.5 K. In case of failure, the detectors are heated up in a similar manner to avoid stress due to too large temperature gradients across the different materials. This procedure is also foreseen in case of a too low nitrogen level in the nitrogen supply.

In case of failures during the operation the cooling system is designed in that way, that automatically a safe state is achieved. For this, safety valves and bypass valves are installed. An upgrade of the cooling system for the 2021 data taking was performed together with CERN Experimental Physics - Detector Technologies (EP-DT). Initially the cabling of the single components were directly connected to the PLC, which introduces a lot of cabling work. Furthermore, new pressurized-air based safety valves for the stations have been introduced. Initially so-called Lucifer electronic valves are used, requiring separate power lines. In Fig. 5.9(a) the new sensor hub is indicated. It consists out of two parts and provides the connections for the vacuum pump indicator, pressure, temperature and vacuum sensors as well as the interlock for the detector low voltage in case of cooling issues. It can be directly connected to the PLC via a patch panel mounted on the valve box close to the detectors. In Fig. 5.9(b) the upgrade for the new pressurized-air based safety valves is shown. In addition, a new distribution box is introduced to connect the flow meters and valves for the station.

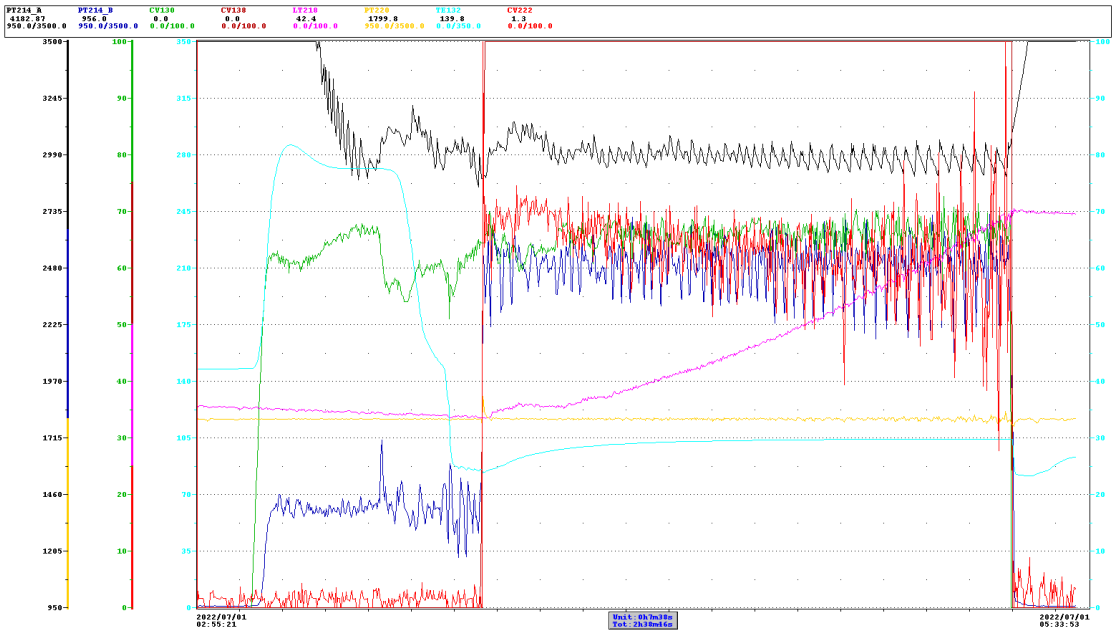

(a)

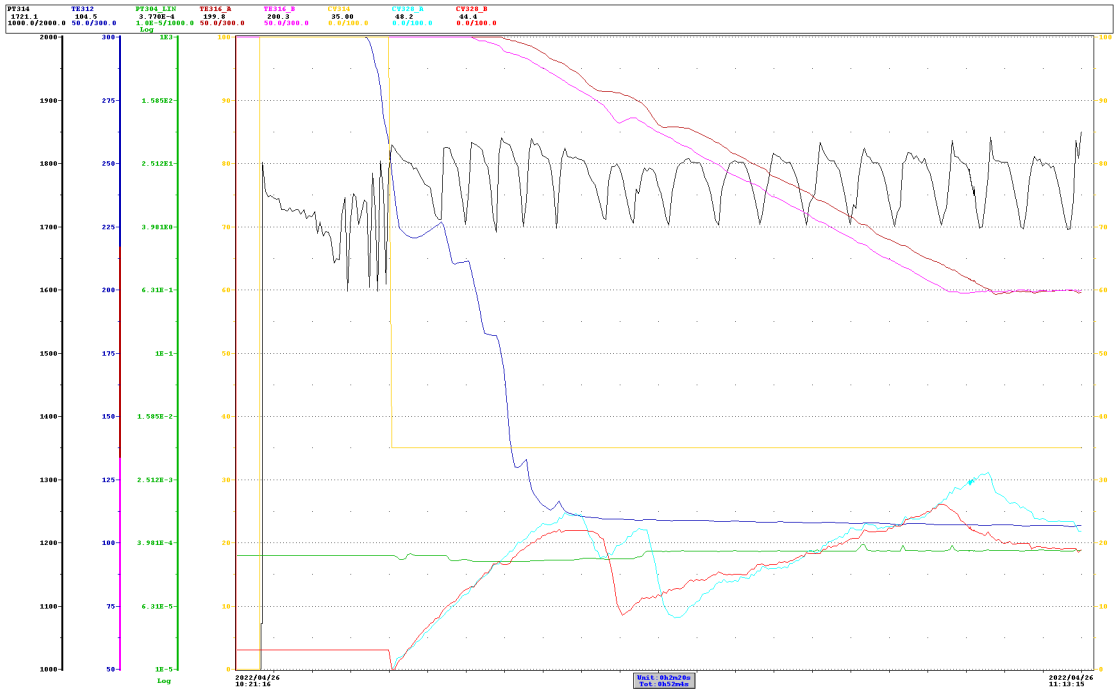

(b)

Figure 5.8: In (a) the refilling procedure of the the valve box is shown. The cooling procedure of SI01 is shown in (b). The respective description of the single colors/quantities is available in the text.

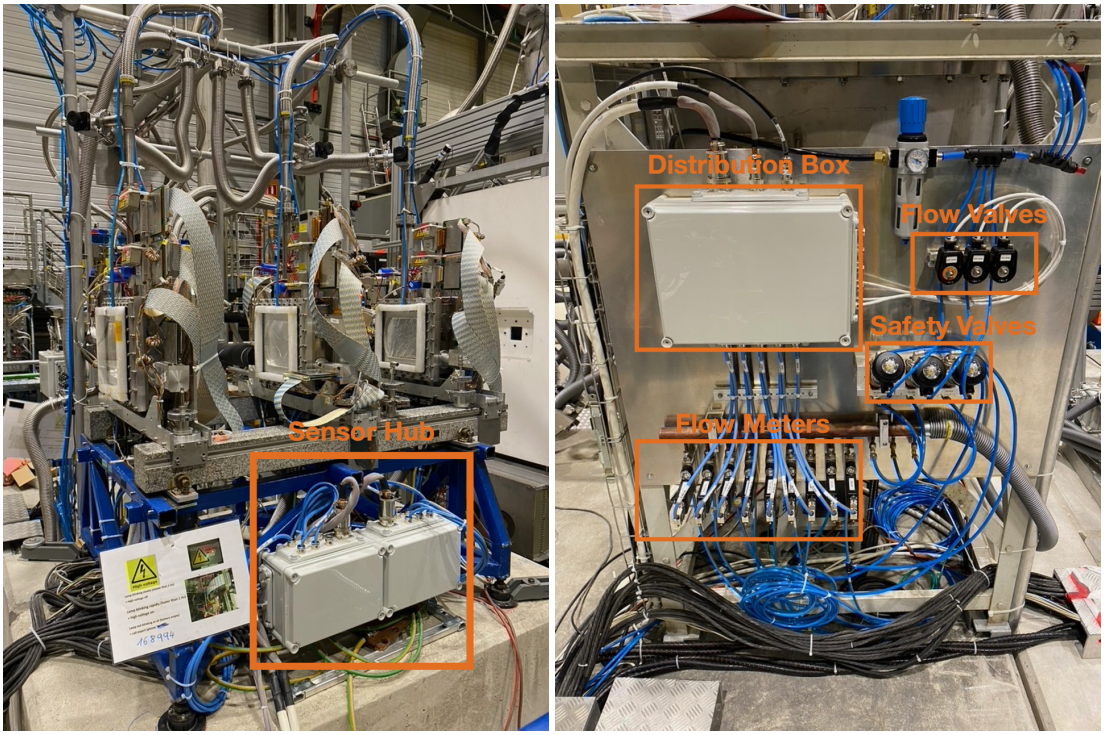

(a) **(b)**

Figure 5.9: Cooling system upgrades for 2021 data taking. In (a) the new sensor hub is shown. In (b) the upgrade for the safety valves as well as the new distribution box is show.

5.4 Depletion Voltage

To generate the depletion zone in the doped silicon material between the n- and p-side, the so-called depletion voltage is applied. This depletion zone is generated in the silicon n-type crystal between the p-n-sides as shown in Fig. 5.2. For the COMPASS silicon-microstrip detectors, a maximum design value of up to 250 V can be set. For each data taking period, the depletion voltage is adjusted to obtain an optimum working point in terms of applied voltage and noise. FPGAs are used to perform zero suppression and to apply the so-called common-mode noise correction of the incoming data. The common-mode noise σ_{CM} is the noise that is induced with the same amplitude in all channels per APV25 chip. Therefore, the baseline of the APV25 chip fluctuates with this common-mode noise and needs to be corrected before further threshold cuts are applied. Induced electronic noise by capacitances, thermal and electronic noise from the amplifiers is individual for each channel and not corrected. [86]. Normally a bias voltage between 100 to 150 V is used. Due to aging effects of the detector modules caused by radiation damages, the required bias voltage for a low common-mode noise level can vary. This effect is more visible for the warm stations used during the AMBER feasibility test and pilot run in 2018 and 2021 as further described in Secs. 2.1.4 and 3.2.2 that are not operated in cryogenic mode, which tends to lower radiation-induced damages due to the Lazarus Effect.

The leakage current resulting from the depletion voltage through the silicon wafer and capacitors is expected to be below µA-level. The results of the common-mode corrected noise at different depletion-voltage settings are presented in the following for the COMPASS data taking periods from 2016 to 2022 with a summary of the settings listed in Tab. 5.3. Due to the construction of the wafer as shown in Fig. 5.2, the U- and X-plane as located on the n-side of the wafer show an increased common-mode noise compared to the V- and Y-plane. The noise level on the p-side decreases much faster due to the increased resistance between the p^+-implants on this side. Compared to the n-side, the p^+-stops planted between the n^+-implants are used to increase the resistance there, but only with sufficient large depletion voltage reaching from the p-side towards the n-side the full substrate is completely depleted.

2016 and 2017

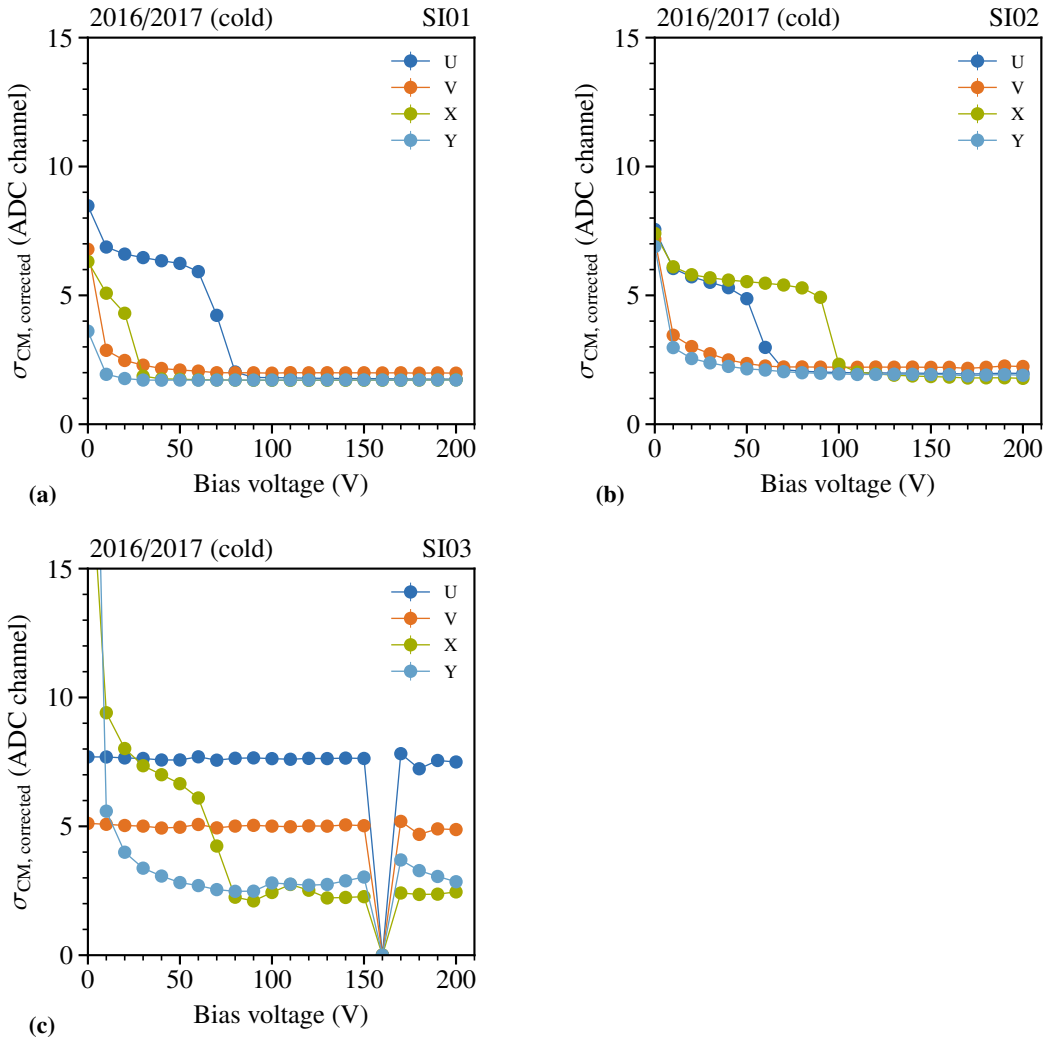

Figure 5.10: Silicon depletion-voltage results during the 2016 and 2017 data taking period. SI03 U- and V-plane showed problems during the measurement. Data from the 160 V measurement is missing for SI03.

During the data taking in 2016 and 2017 the detector installation stayed in place and the settings for the two years are expected to be identical. In Fig. 5.10 the results of the depletion-voltage results for 2016/2017 are shown. With increasing voltage, the common-mode corrected noise decreases further until it reaches the expected plateau. This expected behavior can be observed for all planes. Whereas it tends to be higher in case of U- and Y- planes of the corresponding due to the doping of the module. In general, the noise drops to a constant value below two ADC-channels around 100 V for each plane. For SI03 (cf. Fig. 5.10(c)) the 160 V measurement result is missing for all plane. A problem with the U- and V-plane of SI03 during the measurement was present and the voltage setting was set manually. The operation settings for the bias voltage and the respective leakage currents are listed in Tab. 5.3.

2021

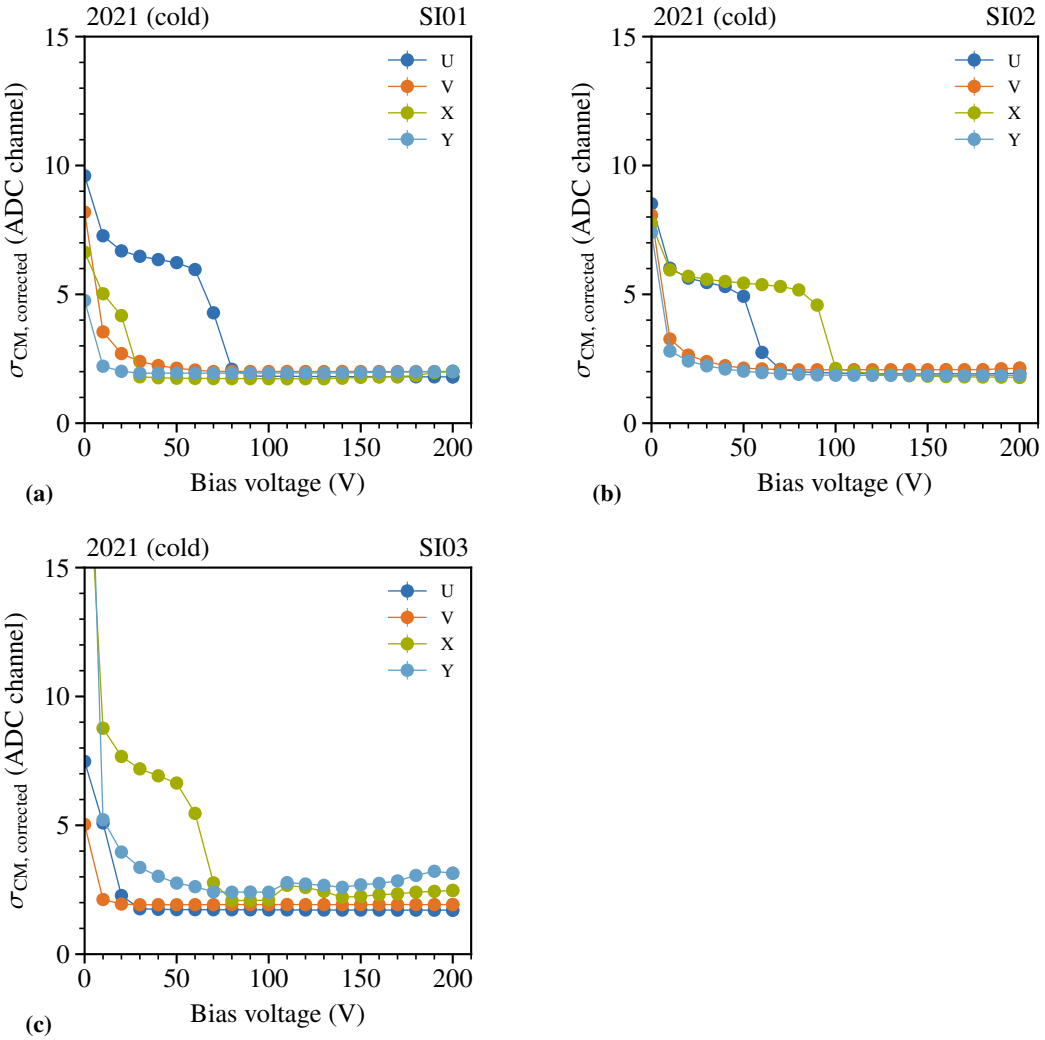

Figure 5.11: Silicon depletion-voltage scan of cold station for the 2021 COMPASS data taking .

The result of the depletion-voltage scan for the data taking period in 2021 are shown in Fig. 5.11. For SI01 (Fig. 5.11(a)) and SI02 (Fig. 5.11(b)) the behavior is as expected and similar to the previous results from 2016/2017. The common-mode noise reaches a stable level around 2 ADC-channels above a voltage of 100 V for those planes. The feature of the U- and X- plane noise being increased compared to the other two planes is visible. SI03 (Fig. 5.11(c)) shows slightly lower and more stable common-mode corrected noise on the X- and Y-plane compared to 2016/2017. In addition, those two planes show an increase with rising voltage around 100 V which is only slightly visible in the 2016/2017 data. In addition, the X- and Y-plane show structures at larger voltages, which are also present in the previous year. The operation settings for the bias voltage and the respective leakage currents are listed in Tab. 5.3.

2022

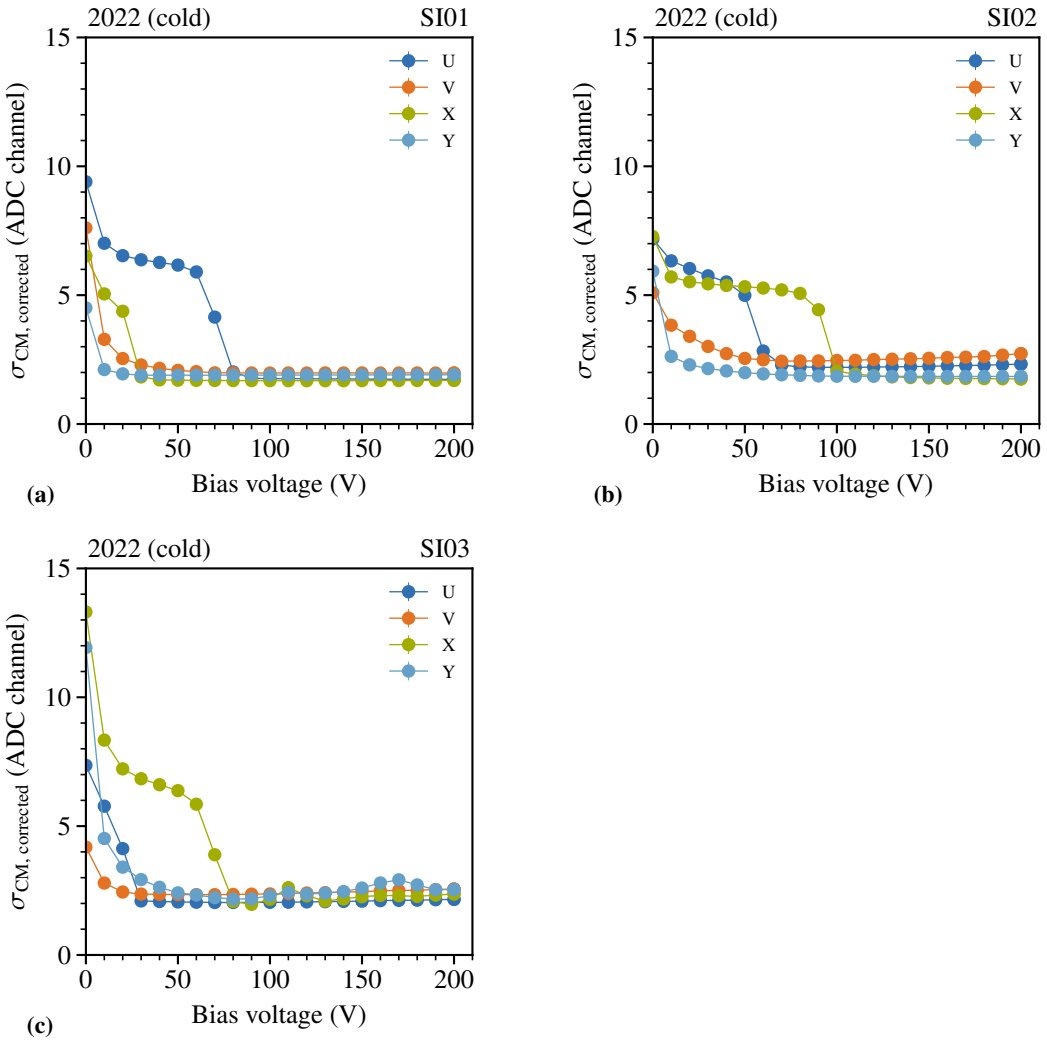

Figure 5.12: Silicon depletion-voltage scan of the cold stations during the 2022 COMPASS data taking

The data taking of COMPASS in 2022 is a continuation of the one performed in 2021. The silicon detectors are in the same location as in 2021 and the installation is similar. They were disassembled for the target material unloading during the winter break and also part of the equipment was used for the AMBER pilot run in October 2021 (see Sec. 3.2). The results are comparable to the previous years. Noticeable is the slow increase of the noise in SI02 (Fig. 5.12(b)) with increasing voltage. The results of the voltage scan are shown in Fig. 5.12.

Settings Overview and Leakage Current

In Tab. 5.3 the overview of the used depletion-voltage settings are listed. Since the detectors were operated only using muon beams during the given periods, no radiation damage effect is expected also the noise behavior is foreseen to stay constant. The results show that the same depletion-voltage settings and comparable leakage currents are obtained during the four years of operation in the COMPASS data taking.

In 2022 a dedicated lab power supply (Rohde & Schwarz HMU4040) was installed to replace the current Deutronic DN35W for the ADC operation of SI02U and SI03U due to a too low power output of these modules causing the ADC to fail during data taking. The resulting leakage current is much lower compared to the other planes and the overall measured current is governed by the power supply of the ADCs. For the operation with the Deutronic modules a leakage current of about 20 µA at 100 V is expected, which corresponds to a 5 MΩ resistance to ground.

Table 5.3: Depletion-voltage settings and resulting leakage currents of the silicon-microstrip tracking detectors in the years 2016, 2017, 2021, 2022.

Detector module	2016/2017		2021		2022	
	V_0 (V)	i_{mes} (µA)	V_0 (V)	i_{mes} (µA)	V_0 (V)	i_{mes} (µA)
SI01UV	90	0.020	90	0.019	90	0.019
SI01XY	90	0.021	80	0.020	80	0.020
SI02UV	110	0.025	110	0.026	110	0.000*
SI02XY	140	0.033	140	0.030	140	0.030
SI03UV	80	0.019	80	0.023	80	0.000*
SI03XY	80	0.019	80	0.017	80	0.017

* Lab power supply installed for the respective planes.

5.5 Detector Properties during COMPASS data taking

To evaluate the detector performance, the time and spatial resolution as well as the efficiency of the detector modules is determined. In the following, the detector properties in the years 2016 and 2017 and the most recent ongoing data taking in 2022 are presented. Details on the time calibration as well as resolution and efficiency are discussed in Sec. 3.3 within the scope of the AMBER pilot run. For the efficiency and resolution studies, events have been reconstructed where the respective plane under study has been removed from track finding and reconstruction. This gives an unbiased result, since the respective plane does not participate in the tracking itself. Especially for the efficiency studies, this is required to determine an unbiased efficiency. A brief overview and discussion is given in the following.

5.5.1 Time and Spatial Resolutions

The time and spatial resolution are evaluated based on the reconstructed tracks. The time resolution is given by the difference between the hit time of the respective detector of the hit associated to the track and the corresponding track time, which is defined by scintillating fiber detectors with time resolutions of about 400 ps [84]. Details on the time calibration and resolution are discussed in Sec. 3.3.2. The spatial resolution is obtained by the residuum between the track position at the respective detector plane and the associated hit position of this plane.

2016/2017

The time resolutions have been evaluated within [63] for the years 2016 and 2017. During both years the detector installation stayed in place and have identical calibrations. It is expected to obtain similar results in both years. The results are shown in Fig. 5.13. All planes show a time resolution of around 1.8 ns besides minor differences at SI03X in 2016. Furthermore, the difference between the two wafer sides with and without intermediate strips is visible. The U- and X-planes show an improved time resolution compared to the V- and Y-planes.

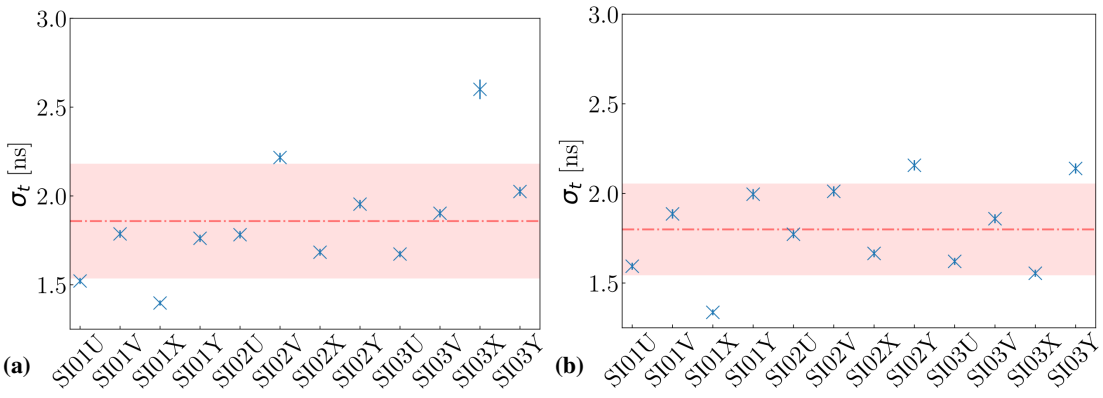

Figure 5.13: Silicon time resolutions for 2016 (a) and 2017 (b). The 1σ-region is indicated and the uncertainties are scaled by a factor three. Figures taken from [63].

The spatial resolutions for the years 2016 and 2017 are shown in Fig. 5.14(b) and have been evaluated in [63]. Based on the respective alignment of the detectors for each data taking period, the resolution can change depending on the respective alignment. The results are shown in Fig. 5.13. All planes show a spatial resolution of around 7 µm besides minor differences. In 2017 as shown in Fig. 5.14(b) the detector alignment differs from 2016. Whereas SI01 and SI03 show an increased resolution about 11 µm with respect to 2016, SI02 shows the resolution of 2016. The influence of the intermediate strips not dominant and mostly governed by the alignment precision of the single detectors, although the two-strip cluster hits are more likely and dominate the detector resolution. Overall the stability during the data taking in 2016 and 2017 have been found to be very stable [63].

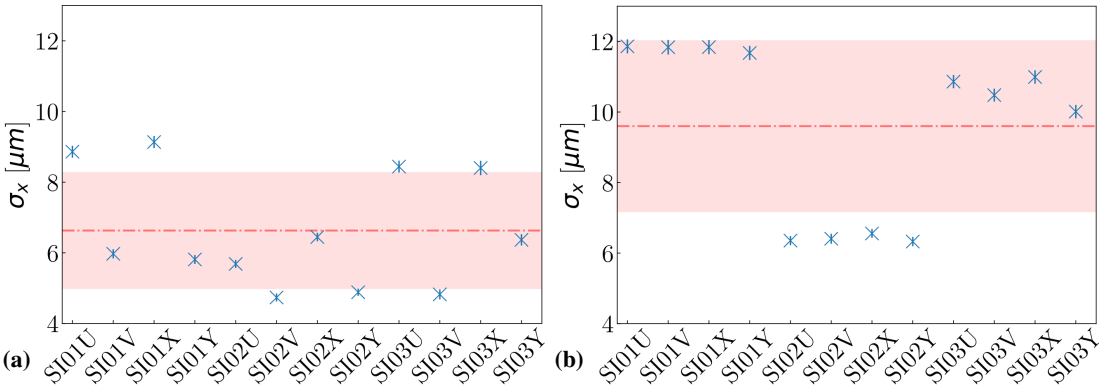

Figure 5.14: Silicon spatial resolutions for 2016 (a) and 2017 (b). The 1σ-region is indicated and the uncertainties are scaled by a factor five. Figures taken from [63].

2022

For the 2022 data taking, the detectors are reinstalled. Nevertheless, the installation differs to the years 2016 and 2017 in terms of position and connections to the DAQ system. Furthermore, a preceding data taking took place in 2021 already, but due to many failures along the spectrometer no usable physics data has been obtained. Nevertheless, the setup in 2022 is expected to be comparable and for the time calibrations the preliminary ones from 2021 are used.

In Fig. 5.15 the results of the time resolution for the two planes SI01 X- and Y-plane are shown exemplary. The expected improved time resolution for the wafer side with intermediate strips is visible. For the X-plane a resolution of about 1.5 ns is achieved, whereas for the side without intermediate strip, a slightly larger resolution of about 2 ns is extracted. A constant offset of the time residual is visible of about -0.5 to 1.5 ns, which requires further tuning of the preliminary time calibration. Although no changes have been made for the trigger timing as well as cable length this time offset is visible. These preliminary time calibrations are taken from the 2021 run and no differences are expected.

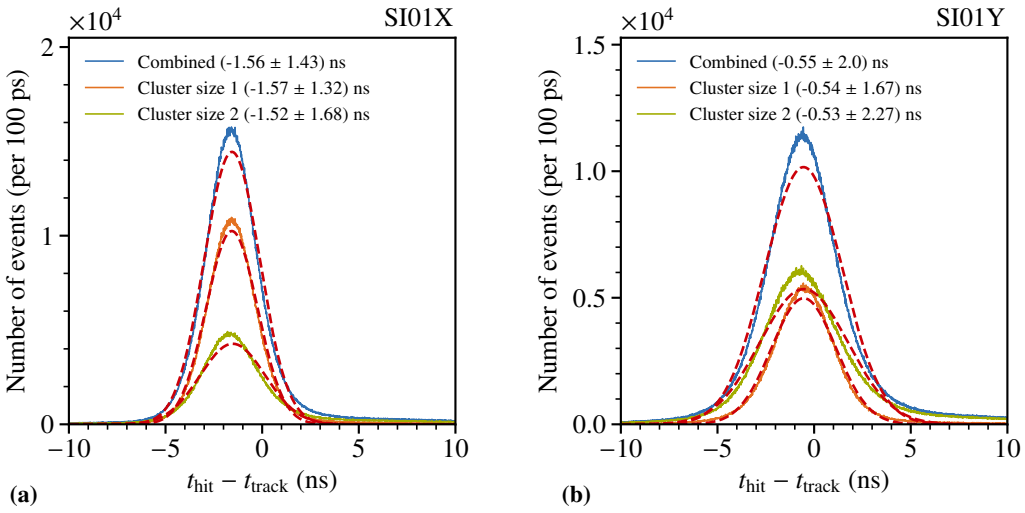

Figure 5.15: Silicon time resolution in 2022 for SI01X (a) and SI01Y (b). The combined time resolution as well as the single and two-size cluster contributions are shown.

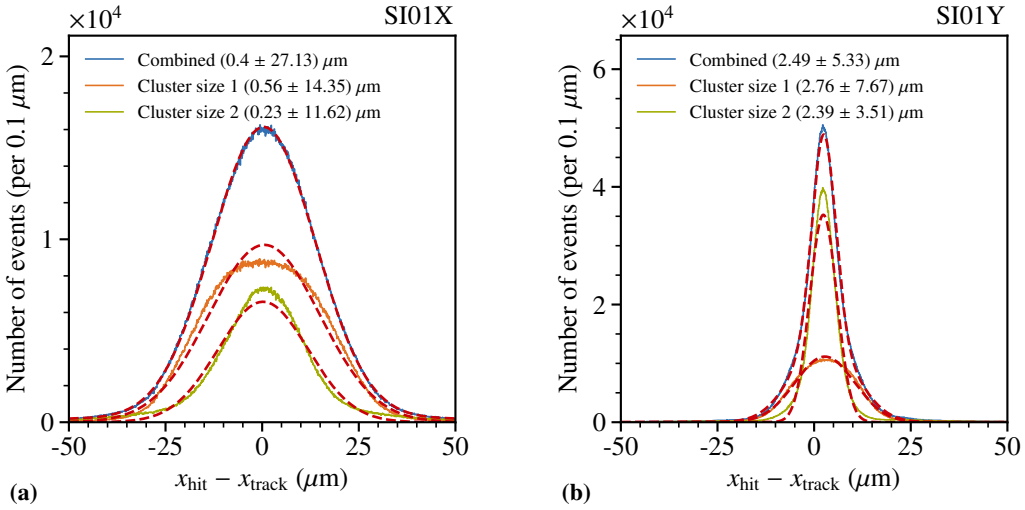

Figure 5.16: Silicon spatial resolutions in 2022 for SI01X (a) and SI01Y (b). The combined spatial resolution as well as the single and two-size cluster contributions are shown.

With a preliminary alignment for the run 295169 the current spatial resolution is determined. The results are shown in Fig. 5.16. The plateau from the single cluster resolution in visible as well as the improved resolution for the hits with cluster size two. For SI01X, the extracted resolution of about 27 µm is about a factor five larger than the expected value of about 6 µm. The current preliminary alignment shows still issues at this point and further optimization is required. SI01Y shows the expected results and achieves a resolution of about 5 µm predominantly due to the two-cluster size events. An overview for all planes is given in App. D.2 for the spatial resolutions and in App. D.1 for the time resolutions.

5.5.2 Efficiencies

The efficiency is determined by the ratio of found hits in a 3σ-region and the extrapolated track position at a given position within the respective detector plane. The detector plane under study is excluded from the tracking to not bias the results. Details on the efficiency calculated are given in Sec. 3.3.3. The influence of background hits in those detectors has been evaluated and is considered to be small and therefore neglected in the results. The efficiencies in the 2016/2017 COMPASS data takings have been evaluated in [63] and are briefly summarized.

2016/2017

The efficiency for the data taking in 2016 and 2017 is shown in Fig. 5.17 as summary for all three stations. For all stations an expected efficiency of more than 90 % is obtained in both years. In 2016 an issue related to the trigger signal for SI03X was present during that run and results in a lowered efficiency. In 2017 the spread of the efficiency is smaller compared to 2016 since the installation was not redone and further improvements on the electronic noise and positioning have been performed.

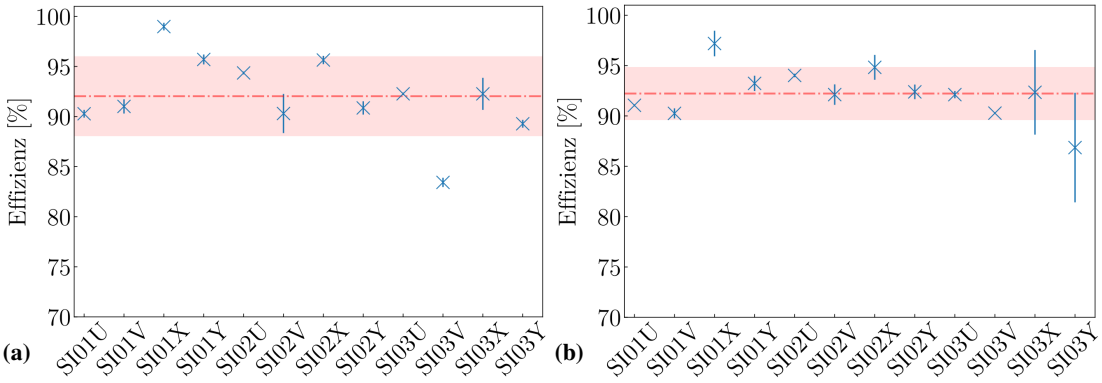

Figure 5.17: Silicon efficiency for 2016 (a) and 2017 (b). The 1σ-region is indicated and the uncertainties are scaled by a factor three. Figures taken from [63].

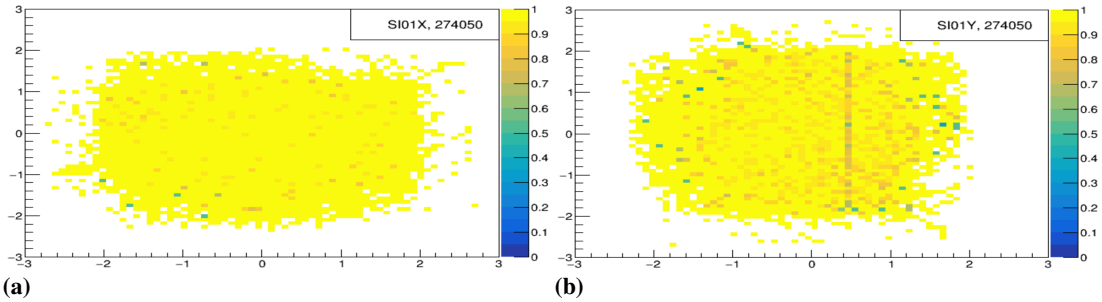

Figure 5.18: Silicon 2-d efficiency for 2016 for SI01X (a) and SI01Y (b). Units are (cm). The y-plane is presented in the detector-reference system. Figures taken from [63].

In Fig. 5.18 an example for the 2-d efficiency is shown of the SI01XY planes during the 2016 data taking. A homogeneous efficiency is visible, with a slight beam profile (cf. Fig. 5.19). In addition, a broken wire can be seen for SI01Y in Fig. 5.18(b).

2022

The efficiency of the single projection for the SI01 X- and Y-plane are shown in Fig. 5.19. The overall efficiency is above 98 % and comparable to the previous results. To visualize the effect of the beam profile due to radiation damage, the z-axis range is adapted. It is slightly lower in the center due to the influence of the beam profile. This drop to around 98 % is also visible in the 2-d projection shown in Figs. 5.19(c) and 5.19(d). The influence of the not-fully-covered surface of the silicon detector by the surrounding scintillating fibers results in a cut-off on the edges due to tracking requirements. In total, it is slightly improved compared to 2016/2017.

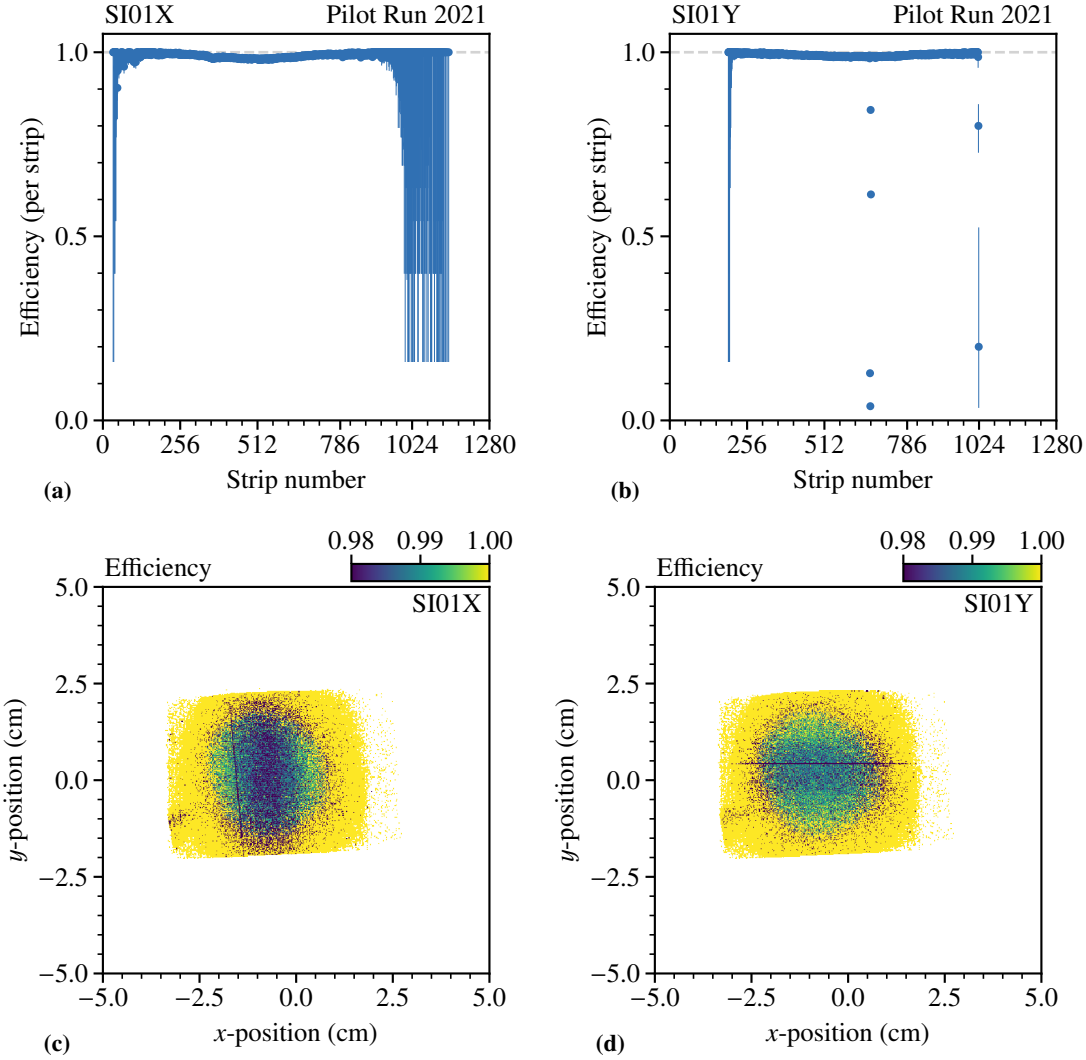

Figure 5.19: Silicon SI01 X- and Y-plane 1-d efficiency in the single projections are shown in (a) and (b), respectively. Uncertainties are based on Bayesian approach [67]. The silicon SI01 X- and Y-plane 2-d efficiency are shown in (c) and (d), respectively

5.6 Summary and Outlook

The used cryogenic silicons have been operated in the scope of this thesis since 2016 and show a stable performance during the operation during several data taking campaigns at COMPASS. They have been installed, commissioned and maintained in the years 2016, 2017, 2021 and 2022. Furthermore, an operation during the AMBER anti-proton cross-section measurement beginning of 2023 is planned. The installation involves not only setting up the detectors themselves, but also the connection of the required DAQ infrastructure and especially the cooling system. Thorough testing of the cooling system is required prior to the fully automatic operation. The complete system including the full infrastructure had to be installed for each year of operation and is operated during the full data taking period. A stable and reliable operation is required for the COMPASS data taking, which requires a constant monitoring of the system, including a fast response in case of arising issues.

After the installation of the required infrastructure, the detectors calibrations like the depletion-voltage study and time calibrations have been performed. Those are necessary steps in order to obtain the expected performance in terms of stability, efficiency and resolution. Despite their age of about 14 years, the expected spatial resolutions of up to $\sigma = 5$ µm and time resolution of about $\sigma = 2$ µs could be obtained during the years of operation. The same holds for the efficiency, here expected values of around 98 % are achieved. For the year 2021, improvements for the cabling of the cooling system has been installed and commissioned together with CERN EP-DT to allow a more simplified installation of the system.

CHAPTER 6

Own Contributions

Starting from 2016 I took over the responsibility for the silicon-microstrip tracking detectors of COMPASS and gained experience in this detector system. I prepared and operated the detectors for the COMPASS measurements in 2016 and 2017. Starting with the first calibrations, improvements to the time reconstruction have been implemented, which enhance the existing clustering algorithm of the detector. A master's thesis [100] was written on the topic of silicon hit clustering under my supervision. The gained knowledge of this detector system was then an indispensable help for the feasibility test in the year 2018 of the PRM project. This idea was the foundation for the transition between the ending COMPASS experiment and the planned successor, AMBER. I was in charge of the preparation, organization and run coordination of this test measurement. Besides preparing the older version of this detector system, the so-called warm silicon station, for the setup, which were used for the last time in 2007, I took over the coordination with the COMPASS side during the parasitic measurement. I structured the data taking and was on-site during the full measurement time from March to May 2018 and took care of occurring issues. The result was the very first data set of a combined measurement with a prototype TPC and muon tracking.

Based on the obtained knowledge during the data taking, I started the analysis of the taken data and I supervised various bachelor's [63, 64] and master's theses [73] contributing to my data analysis. I was responsible for the so-called timestamp matching of the two detector systems starting with the decoding of the recorded time messages, the muon event selection and the later combination of the two data sets. Based on the initial LoI [1] for the AMBER collaboration with the measurement of the proton radius as one of the three physic parts, I took a leading role in the writing of the proposal for this measurement [2]. As a leading role in terms of analysis, I started with the organization of the PRM group within AMBER by chairing weekly meetings. Since no full simulation of the setup was available and neither a dedicated person, I took over the additional task of the GEANT4 simulation of the setup and built up experience in implementing various scenarios on a detailed level. This also improved the existing simulation for the COMPASS experiment, i.e., detector and event descriptions. These simulations also serve as a basis for new developments as the HLT, detector designs and evaluation of the anticipated setup. Adaptions and improvements of the reconstruction software have been performed by me due to the different geometry and

requirements of the proposed setup, including new implementations for the reconstruction of the UTS detectors. This also led to the formation of the AMBER *Analysis and Software group*, which I initiated and organize in bi-weekly meetings. Additional theses [47, 91, 101] have been performed or are in preparation on the topic of the PRM project under my supervision.

Further discussion on the proposal in the scope of the SPSC referees in order to be accepted by the CERN research board lead to a creation of a *Question and Answer* document[1] with a detailed examination of the project. I contributed with additional material in close work with our created PRM working group. The result of those discussions was the request to perform a dedicated pilot run similar to the first feasibility test measurement, but with a close-to-final geometry in the M2 beam line to provide real data that can verify the expected properties of the planned final setup. With the knowledge of the silicon detectors, I organized and commissioned the muon tracking system consisting out of five stations for the evaluation of the TPC performance. With knowledge obtained during the test measurements, I contributed to the realization of the pilot run. For this data taking, I was responsible for the timestamp decoding as well as and additionally for the muon event selection and the correlation of muon and proton events.

I also took part in composing applications[1] for the BMBF and DFG for the contributions by the Technical University of Munich (TUM) group and provided the material and results obtained from simulation and real data.

The silicon detectors within COMPASS have been used besides 2016/2017 in the year 2021 and in 2022 they are currently in operation (cf. Tab. 5.2). Together with the CERN EP-DT group, I improved the existing liquid nitrogen cooling system of silicon detectors and simplified the electrical cabling and connections. During the whole time of silicon operation, I was the main responsible for the system and provided the on-call duties during the whole time of the different data takings.

[1] not published

CHAPTER 7

Acknowledgements

First of all I would like to thank Prof. Stephan Paul who gave me the possibility to work on those exiting subjects. His support and encouragement is fulfilling. His ideas and engagement on the different topics are the foundation for this work.

My sincerest thanks to Jan Friedrich, who fully supported me in many ways and guided me through this work. His continuous encouragement and trust in the various projects helped to accomplish many goals. Together with Boris Grube, who was always supportive and inspiring with many great ideas and an open ear, they built the foundation of this work over the years.

Furthermore, I would especially thank Igor Konorov for his patience and helpful ideas through the years not only with the silicon detectors, but also other various topics.

Over the time, many people took part in this work. I would direct special thanks to Prof. Bernhard Ketzer, Sebastian Uhl, Florian Haas, Stefan Huber, Charly Bicker, Sergei Gerassimov for their support and help during the time.

Furthermore, I would like to thank Vincent Andrieux, Karina Bernhard, Sverre Dørheim, Alexei Dzjuba, Dominik Steffen/Ecker, Karl Eichhorn, Daniel Greenwald, Alexander Inglessi, Martin Hoffmann Florian Karspar, Max Lamparth, Martin Losekamm, Mikhail Mikhasenko, Thomas Pöschl, Johannes Rauch, Benjamin Moritz Veit and Stefan Wallner as close colleagues and friends for the support, fruitful discussion and amazing time.

During my work at CERN I had the opportunity to meet great people. Without them, this work would not have been possible. Therefore, many thanks go to friends and colleagues: Maxim Alekseev, Vladimir Anosov, Dipanwita Banerjee, Johannes Bernhard, Laurent Deront, Nori Doshita, Stefano Levorato, Christoph Menezes, Pires, Cedric Peron, Michael Pešek, Jean-Yves Rousse, Pascal Sainvitu, who helped in every possible way. With special thanks to Oleg Denisov, Barkur Parsamyan, Fulvio Tessarotto, and the members of the COMPASS and AMBER collaboration. To all of you, I am really thankful for the amazing and inspiring time. Besides the productive work, I am confident to say that we also shared a good time also along the rest of the time.

In addition, I had the pleasure to work with many students, to whom I also owe to say thank you for working with me on many interesting theses and the great time. Huge thanks go to Simon Helbing and May Mynther

Special thanks go to Karin Frank and Katharina Langosch for taking care of the organizational issues and motivation, especially towards the end.

I want to express my special gratitude to my family and friends for their continuous support and encouragement during the time.

APPENDIX A

PRM Main Run

A.1 TPC Pad Plane

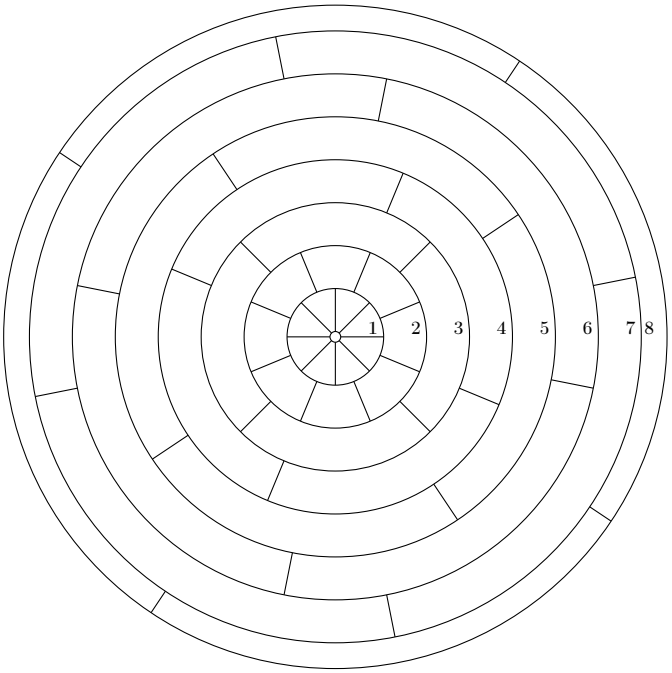

Figure A.1: Segmented TPC readout anode plane. With the central pad and the single rings indicated. Details can be found in Sec. 1.2.2.

A.2 Muon and Proton Scattering Angles

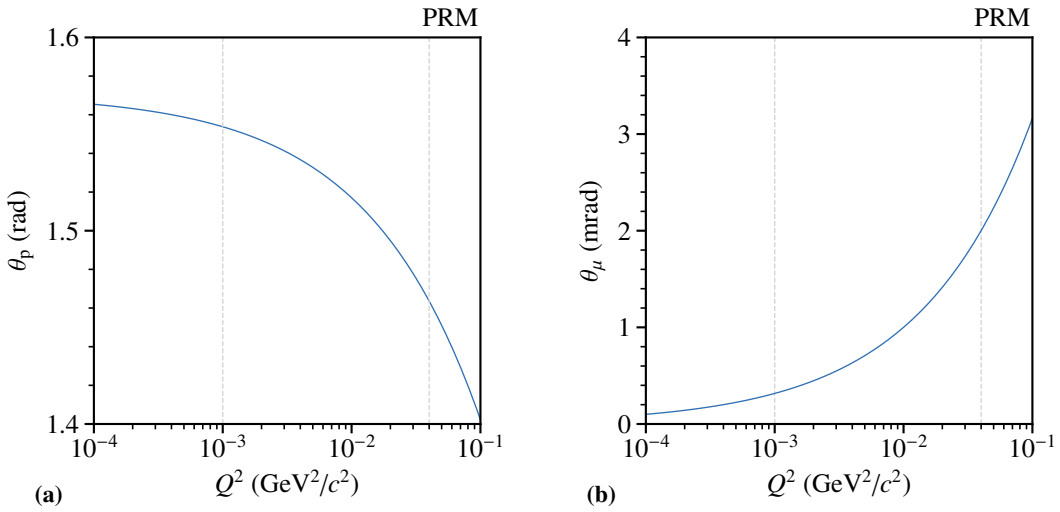

Figure A.2: Scattering angles for muon (a) and proton (b) based on kinematic calculation.

A.3 TPC Inner Component Properties

Table A.1: Different component properties of the planned TPC. [2]

Component	Value
cathode-grid distance (drift zone)	400.0 mm
grid-anode distance	10.0 mm
grid-wire diameter	0.1 mm
grid-wire spacing	1.0 mm
grid transparency	1.8 ‰
anode diameter	600 mm
hydrogen pressure	4 bar and 20 bar
electron field in drift space $\lvert\vec{E}\rvert/p$	0.116 kV/(cm bar)
electron field in grid-anode zone $\lvert\vec{E}\rvert/p$	0.340 kV/(cm bar)
electron drift velocity in drift zone	0.41 cm /μs
electron drift velocity in grid-anode space	0.70 cm /μs

A.4 Resolution Parametrizations

Table A.2: Results for the different parameterisation for the resolutions shown in Fig. 1.23.

Type	Baseline (m)	A $(10^{-3}(\mathrm{GeV}^2/c^2)^B)$	B
$\Delta Q^2/Q^2_{\mathrm{MC}}$	0.5	8.352 ± 0.093	0.444 ± 0.002
	1	7.816 ± 0.085	0.438 ± 0.002
	2	7.730 ± 0.084	0.436 ± 0.002
	3	7.726 ± 0.084	0.436 ± 0.002
	4	7.662 ± 0.084	0.436 ± 0.002
	5	7.521 ± 0.085	0.440 ± 0.002
Type	Baseline (m)	A $(\mathrm{cm} \cdot (\mathrm{GeV}^2/c^2)^B)$	B
Δz	0.5	0.391 ± 0.005	0.494 ± 0.002
	1	0.340 ± 0.004	0.491 ± 0.002
	2	0.321 ± 0.004	0.490 ± 0.002
	3	0.315 ± 0.004	0.491 ± 0.002
	4	0.315 ± 0.004	0.489 ± 0.002
	5	0.315 ± 0.004	0.489 ± 0.002
Type	Baseline (m)	A $(\mu\mathrm{rad} \cdot (\mathrm{GeV}^2/c^2)^B)$	B
$\Delta\theta$	0.5	30.70 ± 0.03	-
	1	26.48 ± 0.03	-
	2	25.65 ± 0.03	-
	3	25.60 ± 0.03	-
	4	25.53 ± 0.03	-
	5	25.63 ± 0.03	-

A.5 Beam Simulation Coordinates

The beam position is simulated in the beam line coordinate system and needs to be translated into the experiment coordinate system. For this known beam line elements as the SM1 and SM2 are used where the position is known in both systems. Furthermore, the beam line coordinates are always with respect to the nominal beam axis and do not show the overall inclination, but only the one with respect to that axis. The positions for the 2023 PRM setup are listed in Tab. A.3.

Table A.3: Positions in beam line and AMBER coordinates for the final measurement in the AMBER target location and the M2 test area location. A more detailed sketch of the complete beam is shown in Fig. 1.10

Location	Item	Beam line (m)	AMBER (m)
M2 test area	Start (after MWPC 15, 16)	1 079.6	−50.8
	IKAR TPC center	1 087.2	−43.2
	End (before Q34)	1 092.6	−37.8
AMBER	Q36 (QUAD36)	1 123.3	−7.1
	PRM target	1 129.4	−1.0
	origin	1 130.4	0.0
	Beam file focus	1 130.7	0.3
	SM1 (BEND10)	1 134.0	3.6
	SM2 (BEND11)	1 148.7	18.3

A.6 Detector Positions in the Simulation

Table A.4: Positions of the core elements in the target area.

Detector	Type	Size (z-axis) (cm)	Position (z-axis) (cm)
FT01 (4 planes)	fiber tracker		−570.5
SP01 (3 planes)	silicon tracker		−555.5
HT01	helium tube	270.0	−413.0
SP02 (3 planes)	silicon tracker		−255.5
FT02 (4 planes)	fiber tracker		−270.5
TPC	active target	236.0	−130.0
SP03 (3 planes)	silicon tracker		−4.5
FT03 (4 planes)	fiber tracker		105.0
HT02	helium tube	270.0	153.0
SP04 (3 planes)	silicon tracker		295.5
FT04 (4 planes)	fiber tracker		310.5

A.7 Alternative Parallel Beam Properties

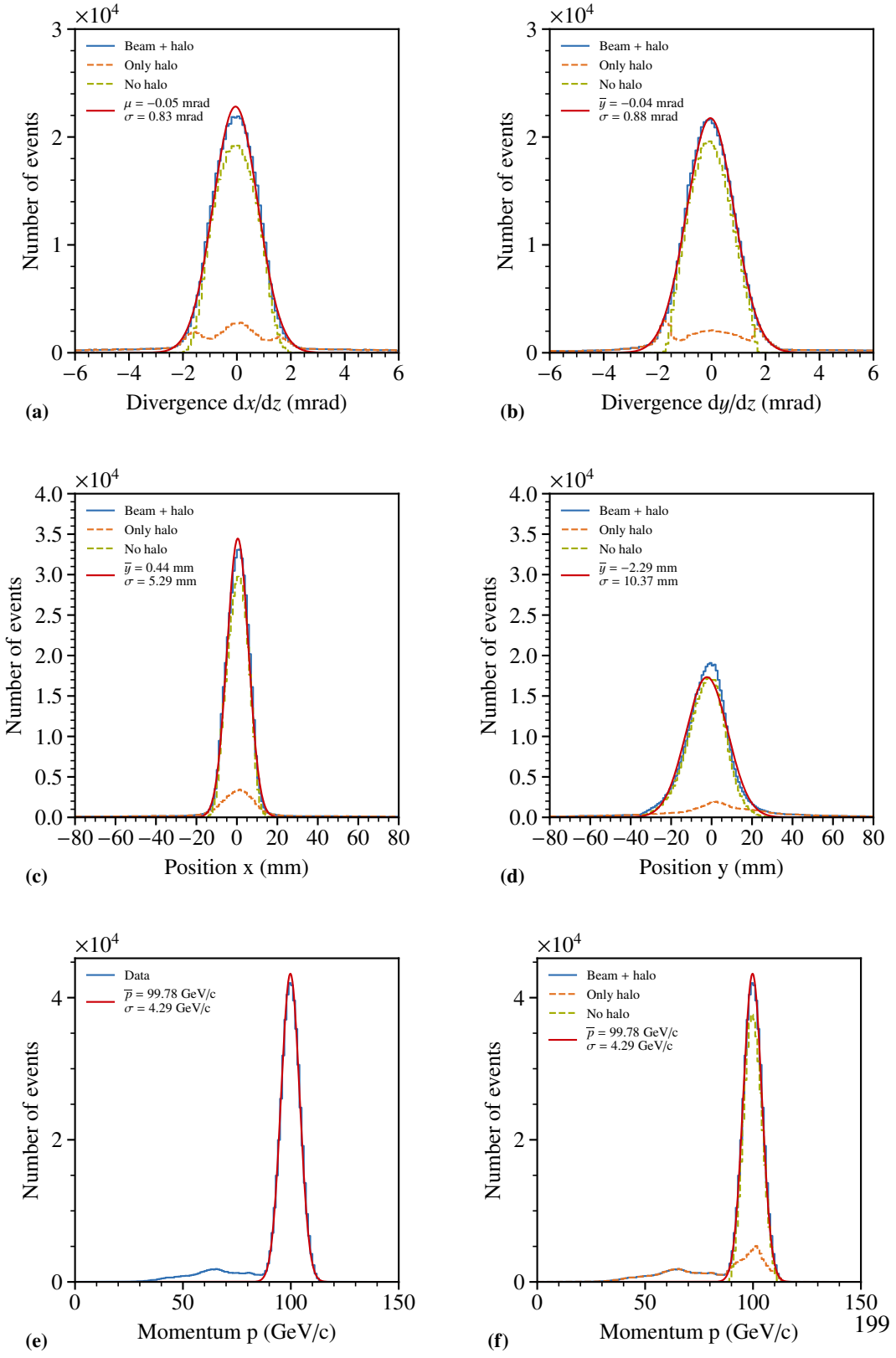

Figure A.3: Beam properties

A.8 Fiber Halo Studies

In Sec. 1.2.3 the beam halo influence is studied. The additional first planes are given in the following figures. Due to the long lever arm between the stations a change in beam profile distribution on the respective planes can be observed.

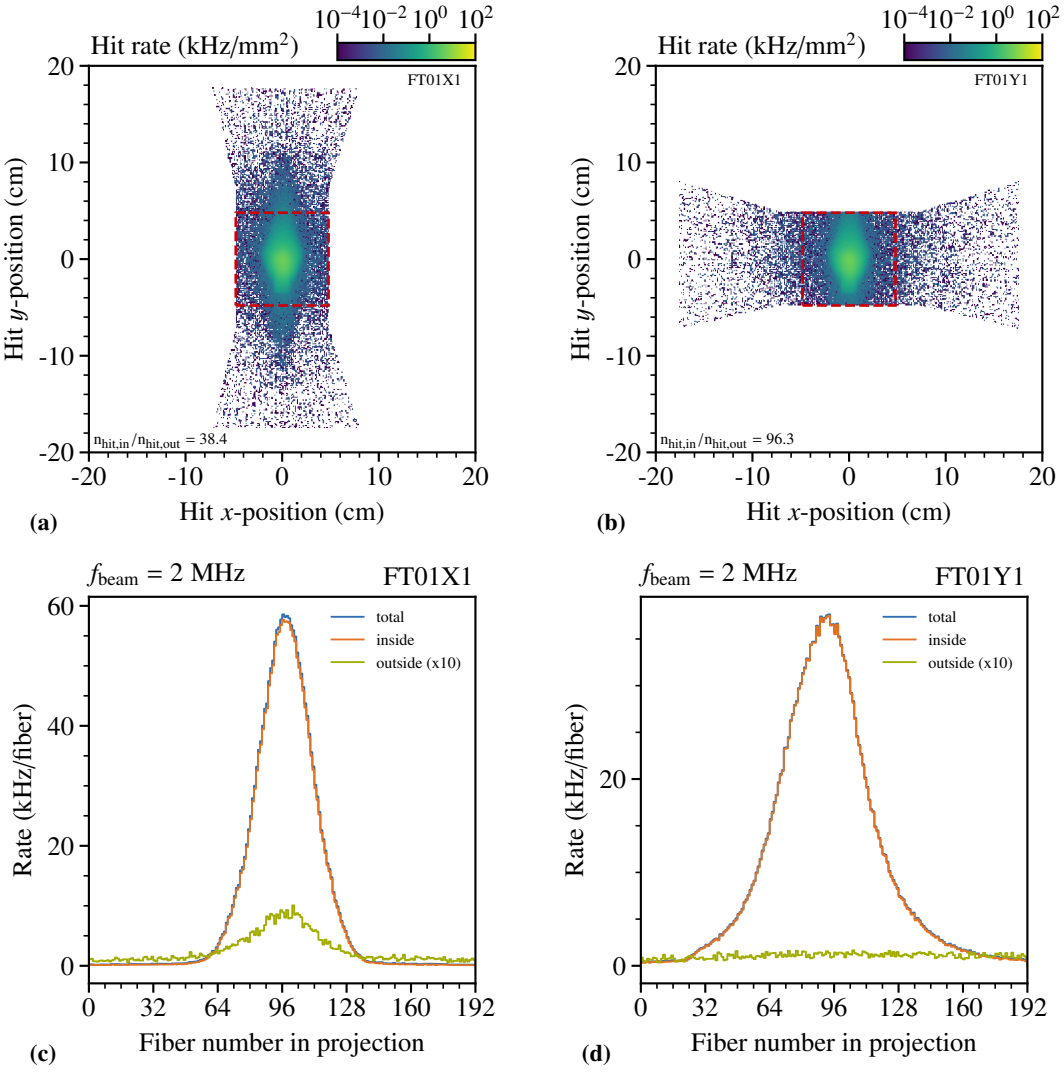

Figure A.4: Fiber hit positions and rate for the x- and y-projection of the FT01 station. In (a) and (b) the respective position with the central $96 \times 96\,\mathrm{mm}^2$ area marked in red. The overall ratio between inner and outer hits is given in the figure. In (c) and (d) the corresponding rates per channel are shown. The different contributions between the inner and outer part.

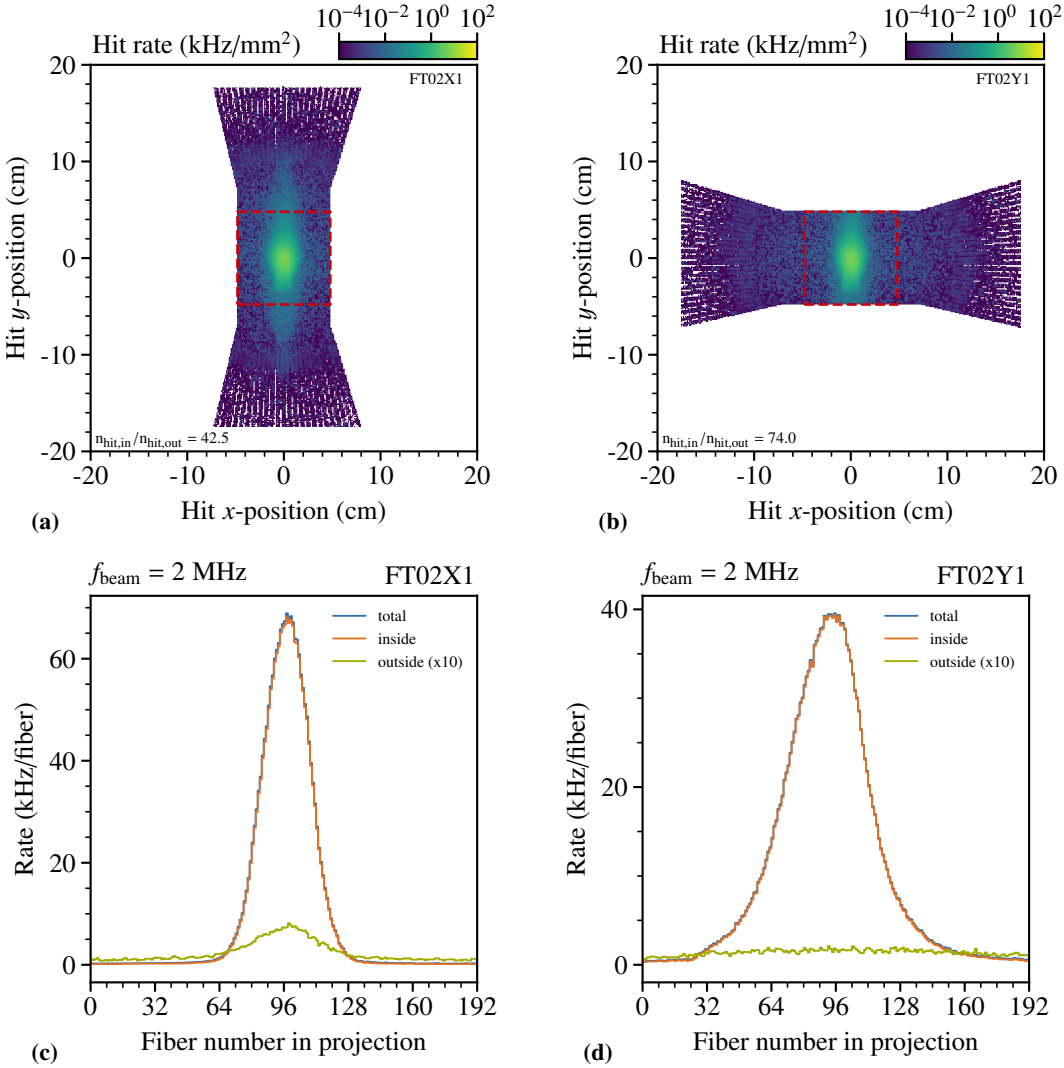

Figure A.5: Fiber hit positions and rate for the x- and y-projection of the FT02 station. In (a) and (b) the respective position with the central $96 \times 96\,\mathrm{mm}^2$ area marked in red. The overall ratio between inner and outer hits is given in the figure. In (c) and (d) the corresponding rates per channel are shown. The different contributions between the inner and outer part.

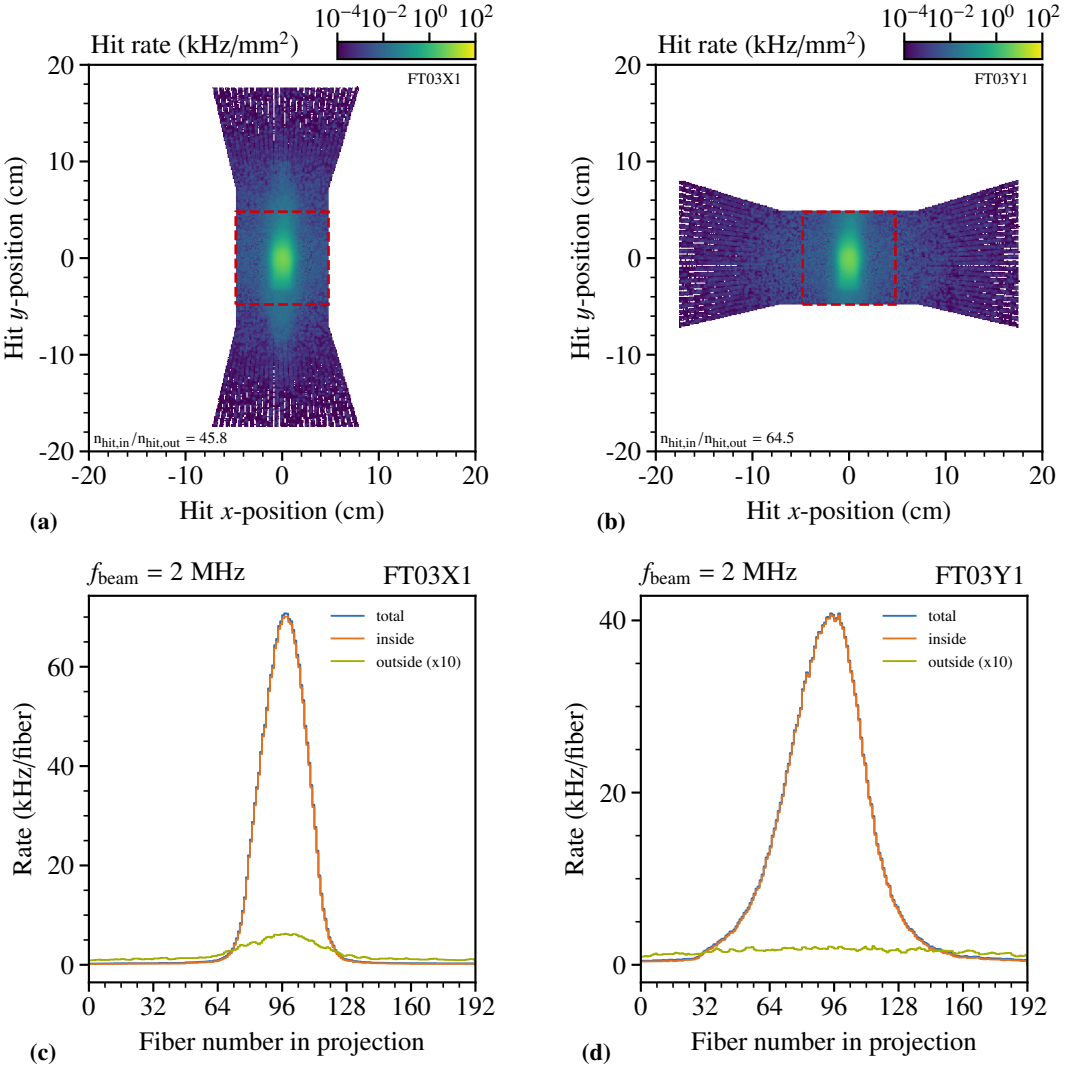

Figure A.6: Fiber hit positions and rate for the x- and y-projection of the FT03 station. In (a) and (b) the respective position with the central $96 \times 96\,\mathrm{mm}^2$ area marked in red. The overall ratio between inner and outer hits is given in the figure. In (c) and (d) the corresponding rates per channel are shown. The different contributions between the inner and outer part.

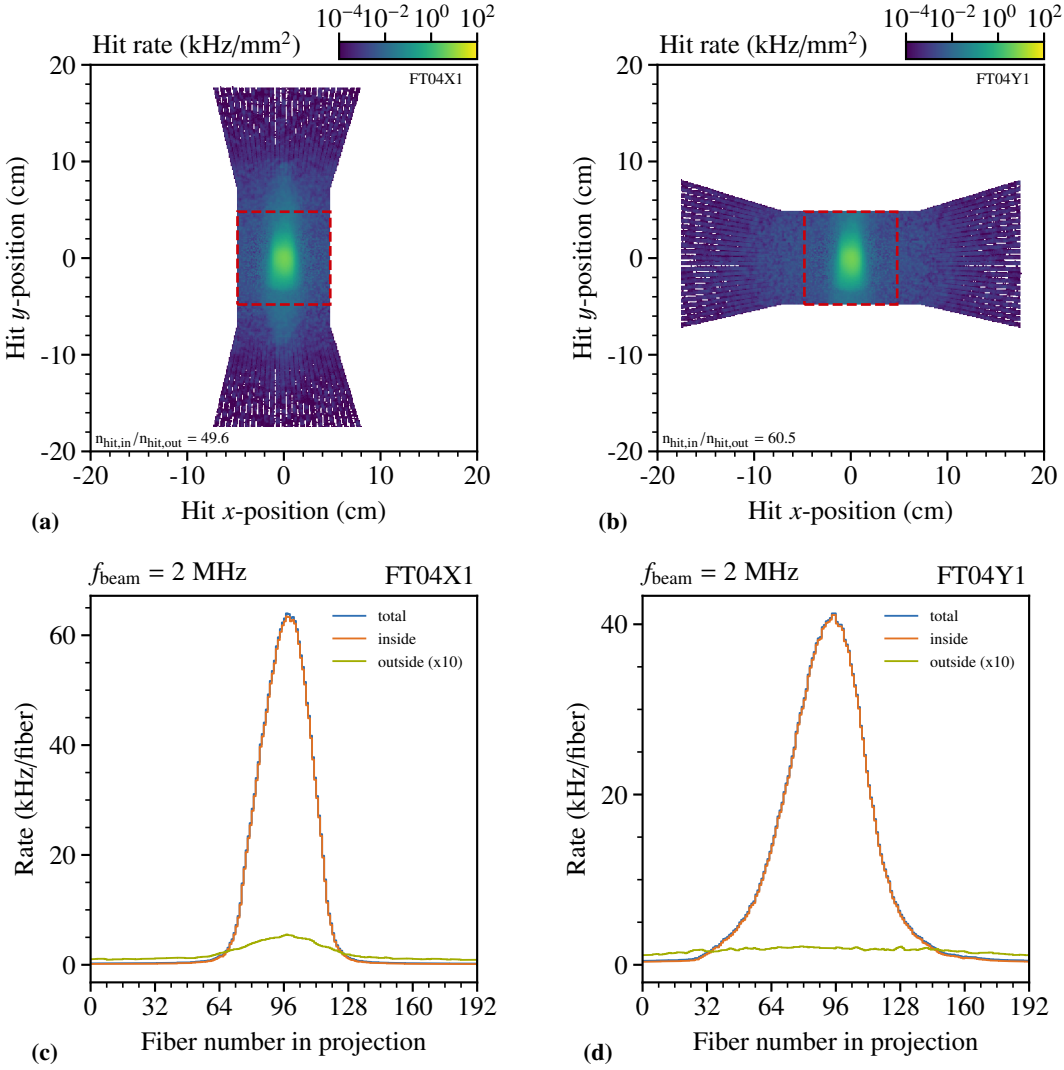

Figure A.7: Fiber hit positions and rate for the x- and y-projection of the FT04 station. In (a) and (b) the respective position with the central $96 \times 96\,\mathrm{mm}^2$ area marked in red. The overall ratio between inner and outer hits is given in the figure. In (c) and (d) the corresponding rates per channel are shown. The different contributions between the inner and outer part.

APPENDIX B

PRM Test Run

B.1 Prescaling Values

During the data taking of the Proton Radius Test Measurement (PRTM) the prescaler has to be set manually to adapt for the respective beam conditions. In Tab. B.1 rough values as orientation are given. Those values can serve as rough orientation. The required settings heavily depend on the beam optics and used DAQ system.

Table B.1: Prescaler values during the PRTM. The values are chosen according to the respective conditions to obtain a trigger rate which is sufficient for the stand-alone DAQ.

Beam type	T6 Units ($\times 10^{11}$)	T6 thickness (mm)	Prescaler value
π^-	40	40	2
	100	40	1
	100	100	1
	100	180	2
	100	300	2
	100	500	2
	120	500	4
μ^-	100	40	1
	40	100	2
	120	40	4
	100	100	1
	100	180	2
	100	300	2
	100	500	8
	120	500	16
(alignment)	120	500	1

B.2 Detector Positions in the PRTM Setup

Table B.2: Detector positions in the PRTM reference frame. The position for each detector is calculated based on the measurement from the survey [55]. The most upstream position of the TPC volume serves as origin point for the coordinate system. Positions are based on the initial alignment and are refined by the run-by-run alignment. The origin is located at COMPASS position $(x, y, z) = (50.3142\ \text{m}, 0.2760\ \text{m}, 0\ \text{m})$. The center is located 60 cm upstream of the downstream flange. The z-direction is defined by the connecting the up- and downstream flange [72].

detector name	x position (cm)	y position (cm)	z position (cm)
BT1B (segmented)			−200.0000[b]
BT1A (monolithic)			−195.0000[b]
SI01U	−0.61795	0.09151	−184.1144
SI01V	−0.61795	0.09151	−184.1144
SI01X	−0.63906	0.06989	−183.0744
SI01Y	−0.63906	0.06989	−183.0744
SI02U	0.03452	0.06151	−105.2260
SI02V	0.03452	0.06151	−105.2260
SI02X	0.01722	0.05909	−104.1860
SI02Y	0.01722	0.05909	−104.1860
TPC upstream flange	0.00000[a]	0.00000[a]	−60.0000
TPC upstream window			−53.5000
TPC upstream volume	0.00000[a]	0.00000[a]	0.0000[a]
TPC anode			24.0000
TPC cathode			47.0000
TPC downstream window			53.5000
TPC downstream flange	0.00000[a]	0.00000[a]	60.0000
SI03U	0.48599	0.04811	109.0506
SI03V	0.48599	0.04811	109.0506
SI03X	0.50262	0.16059	110.0906
SI03Y	0.50262	0.16059	110.0906
SI04U	0.80710	−0.10831	143.0491
SI04V	0.80710	−0.10831	143.0491
SI04X	0.71164	0.01153	144.0890
SI04Y	0.71164	0.01153	144.0890
BT2A (monolithic)			240.0000[b]

[a] by definition of the coordinate system

[b] not measured, estimated position

B.3 Raw Data

The raw data of the PRTM is stored on the tape archive CTA at CERN. 1065 runs from the stand-alone DAQ with the tracking data are stored under the following directory:
`/eos/ctapublicdisk/archive/compass/data/2018/SDAQ/tmp/`

The raw data from the TPC DAQ system is stored under the following directory:
`/eos/ctapublicdisk/archive/compass/data/2018/SDAQ/tpc_data/`

The run-by-run alignment production output as mDSTs can be found under the directory:
`/eos/ctapublicdisk/archive/compass/PRdata/martin/alignedProduction/output/mDST`

The produced TPC data for the single runs is stored under:
`/eos/ctapublicdisk/archive/compass/PRdata/tpcdata/analyzed`

B.4 Timestamp Synchronisation

In the following section, further information regarding the speaking time message decoding described in Sec. 2.2 can be found. A sketch of the speaking time format is shown in Fig. B.1. The single ticks followed by the 32-bit time message is shown.

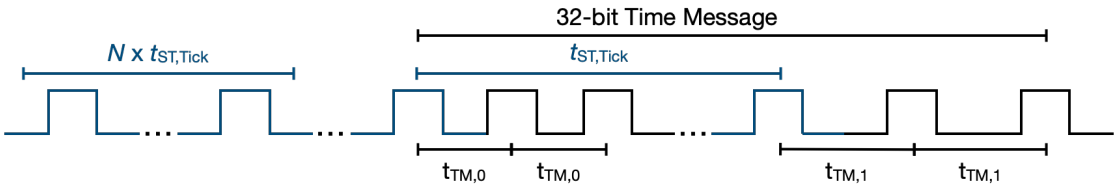

Figure B.1: TRLO speaking time format with 32-bit time message. The single ticks are indicated, as well as the decoding ticks of the time message.

During the pilot run, the operation mode of the used iFTDC was set in a way that the rising and falling edge of the recorded signal are stored with a separate timestamp. For the decoding of the data, only the timestamp of the rising edges are used. The iFTDC collects the signals of the speaking time until a trigger by the TCS of the tracking DAQ arrives. With every trigger, all collected signals are sent to the tracking DAQ system and deleted from the iFTDC. Since the time distance between two triggers is mostly smaller than the length of the full time massage, it is often split across several recorded events in the tracking DAQ. In addition, the tracking DAQ distributes the recorded events in up to four different separate files, so-called chunks. Those chunks are defined by a maximal file size of 2 GB. As a result, the time message is distributed among consecutive events and in up to four different files. For the decoding of the full time message, this has to be taken care of. First, the raw data files are processed. For each decoded event in the raw files, the following information are stored:

- Basic:
  - Chunk number
  - Run number
  - Spill number
- Event:
  - Event number
  - Event time in spill
- Digit/Data word:
  - Channel number (as rising/falling edge identifier)
  - Time stamp (time of the recorded signal)
  - Coarse time (time of the trigger signal)

The identifier for the rising and falling edge of the pulse as given as rising = 0 and falling = 1. The respective timestamps when the trigger arrives as so-called coarse time and the single recorded pulses are stored. To sort the events, the corresponding run, event and spill number are stored. For bookkeeping the respective chunk number of the event is also stored which allows reconstructing the file together with the run number. The extracted raw information of the iFTDC is further processed by a separate software, where the event sorting and decoding of the data words takes place. The events are first sorted in a way that the event number is ascending and each event starting from the first event in spill has a following event candidate. If no signal is recorded and only the trigger signal as coarse time is recorded by the iFTDC the digits of this triggered event is not stored for the decoding.

The format of the iFTDC raw digits is given in Tab. B.3. The format during the pilot run differs from the common format. Since only one port is used on the iFTDC the rising and falling edge was measured with the previously used channel number is used to tag the rising and falling edge measurement of the signal. In addition, the Cyclic Redundancy Check (32-bit) (CRC32) checksum is calculated differently compared to the default settings of the iFTDC firmware. Here the leading bit is always set due to the S-Link format and therefore the CRC32 checksum only has the remaining 31 bits.

For V1 the coarse time does not have the lowest 4 bits are not in the data stream in the data format. In addition, one has to be careful if the trigger time as coarse time is subtracted from the digit time or not. In V2 this is not the case, for V1 this setting can be used.

The decoding of the speaking time message in 2018 is done on an event-by-event basis, whereas in 2021 the time message is distributed across several events. This mainly affects the extraction of the time message itself and the correct handling of consecutive events.

Since the TRLO time is measured via a 100 MHz clock the precision is 10 ns and therefore each tick of the TRLO timestamp corresponds to 10 ns.

The timestamp is given in so-called iFTDC ticks. Each tick corresponds to 32 ns during 2021 and for the 2018 setup the setting was set to 64 ns per iFTDC tick.

The spill duration within a SPS cycle can vary between 4.8 s and 9.6 s and is always a multiple of the 1.2 s accelerator cycle. The timing of each spill, defined by the arrival of particles in the beam lines, is given by three hardware National Instrument Module (NIM) signals. First the Warning Warning Extraction (WWE) signal arrives about 1 s before the particles arrive, followed by the Warning Extraction (WE) signal arriving a few hundreds microseconds before the beam. The spill ends with the Extraction End (EE) signal. [102] The combination of these are used to for the TCS signal at AMBER to generate the control signals Beginning Of Spill (BOS), End of Spill (EOS) and End of Cycle (EOC) signals for the readout electronics. Together with the BOS signal a global reset signal is sent, which also resets the time counters, while the readout electronics accept any kind of triggers like physics, calibration or random.

Table B.3: Data format for the iFTDC during the pilot run. Two different versions V1 and V2 are shown. V1 is used for the standard iFTDC decoding as is present in the 2018 test run and V2 is used during the pilot run.

31										20								10								0

S-Link Header

0	trigger (5)	source ID (10)	event size (16)
0	spill number (11)	event number (20)	
0x0000		TCS error byte (8)	0x01

iFTDC Header (in V1)

0	port (15)	event size (16)
1	event number (31)	
1	coarse time (27)	0x0

iFTDC Header (in V2)

0	port (15)	event size (16)
1	event number (31)	
1	coarse time (31)	

Data Word (in V1)

1	channel (7)	timestamp (24)
⋮		
1	channel (7)	timestamp (24)

Data Word (in V2)

1	edge type (1)	timestamp (30)
⋮		
1	edge type (1)	timestamp (30)

Trailer

1	CRC32 checksum (31)

B.5 Elastic Pion-Electron Scattering

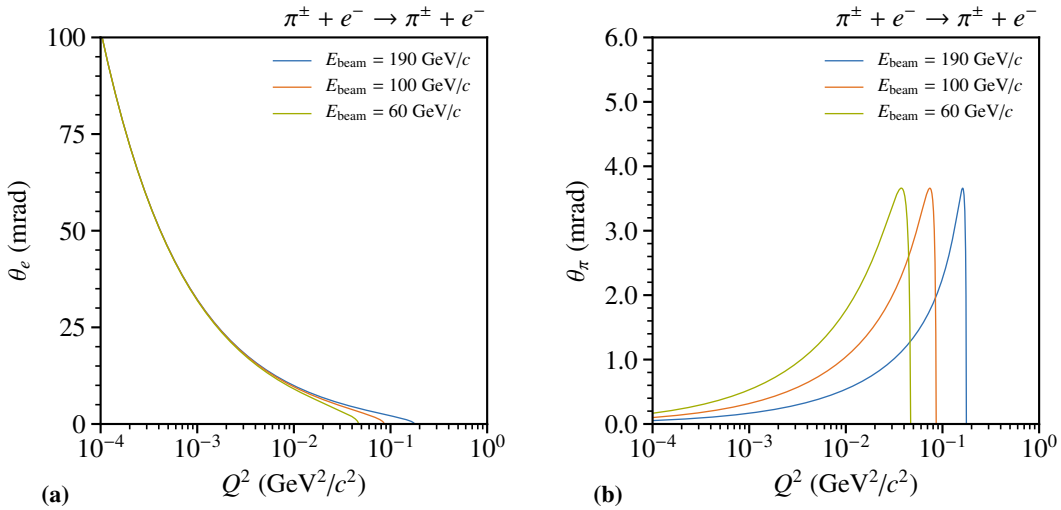

Figure B.2: In (a) the electron scattering angle dependence on Q^2 is shown. The pion scattering angle dependence on Q^2 is shown in (b). Further information can be found in Sec. 2.7 and Sec. 2.8.

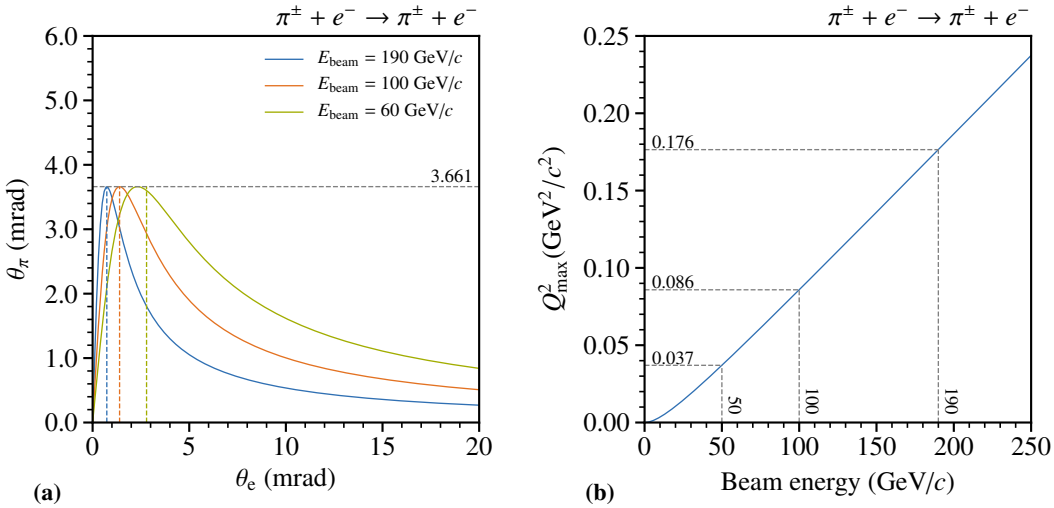

Figure B.3: In (a) the angular correlation between pion and electron angle is shown. The maxima of the distributions are indicated. The maximal accessible Q^2 based on the beam energy is shown in (b). Further information can be found in Sec. 2.7 and Sec. 2.8.

B.6 Elastic Kaon-Electron Scattering

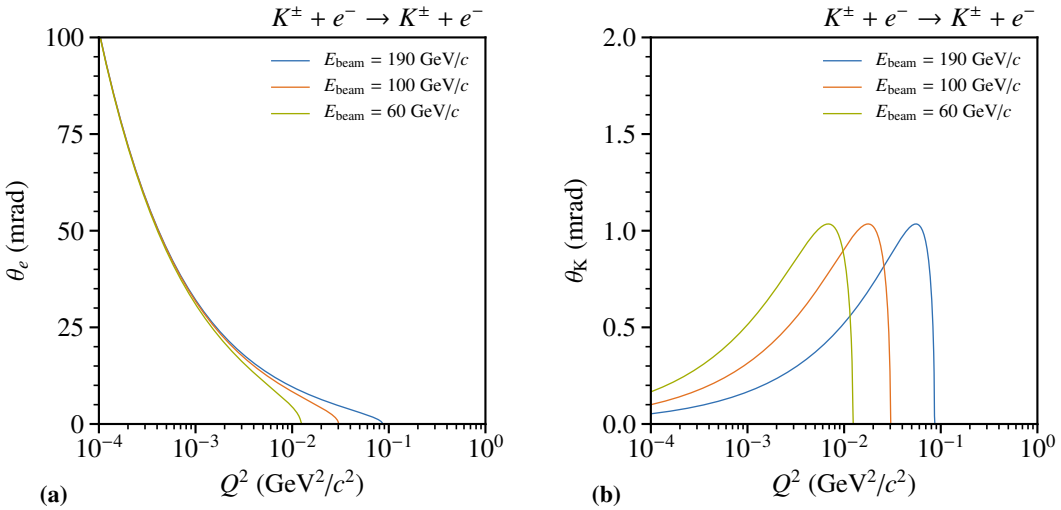

Figure B.4: In (a) the electron scattering angle dependence on Q^2 is shown. The kaon scattering angle dependence on Q^2 is shown in (b). Further information can be found in Sec. 2.7 and Sec. 2.8

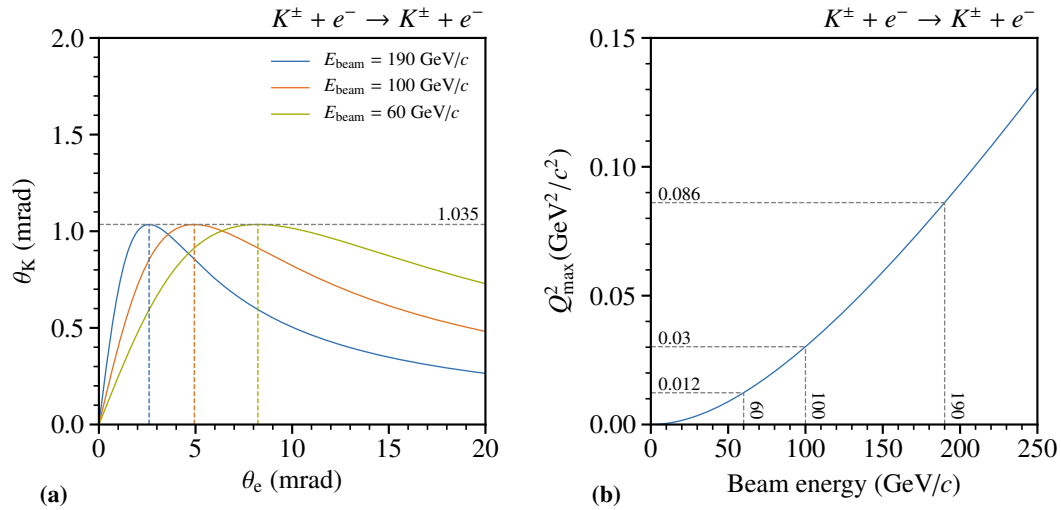

Figure B.5: In (a) the angular correlation between pion and electron angle is shown. The maxima of the distributions are indicated. The maximal accessible Q^2 based on the beam energy is shown in (b). Further information can be found in Sec. 2.7 and Sec. 2.8

APPENDIX C

PRM Pilot Run

C.1 IKAR TPC Pad Plane

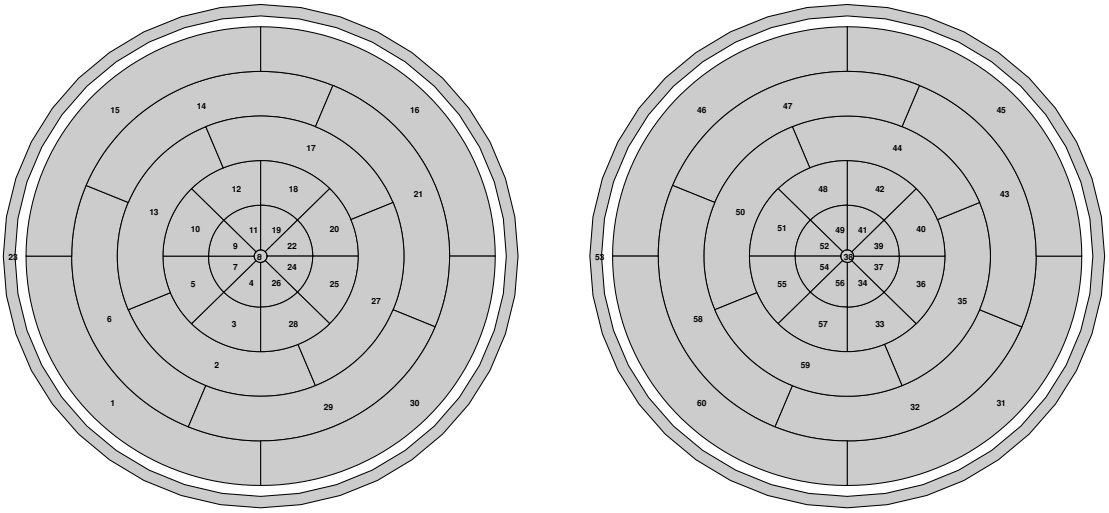

Figure C.1: The IKAR TPC pad plane mapping for the upstream (left) and downstream (right) anode structure.

C.2 Detector Positions in Spectrometer Coordinates

Table C.1: Detector and trigger element positions along the beam axis using the spectrometer reference coordinate system. Details are discussed in Sec. 3.2.2.

detector name	detector id	z-position [m]
BT02	1704	−51.360000
BT01A	1700	−51.100000
FI015U	601	−50.464000
FI015Y	602	−50.462000
FI015X	600	−50.460000
SI01U	701	−50.090025
SI01V	702	−50.089725
SI01X	703	−50.079325
SI01Y	704	−50.079624
BT01B	1702	−45.35000
SI02U	705	−44.317150
SI02V	706	−44.316850
SI02X	707	−44.306450
SI02Y	708	−44.306750
TPC upstream window		−43.754600
TPC upstream anode	1925	−43.450000
TPC center		−43.050000
TPC downstream anode	1926	−42.657300
TPC downstream window		−42.325000
SI03U	709	−41.845975
SI03V	710	−41.845675
SI03X	711	−41.835275
SI03Y	712	−41.835575
SI04U	713	−39.870950
SI04V	714	−39.870650
SI04X	715	−39.860250
SI04Y	716	−39.860550
SI05U	717	−39.530951
SI05V	718	−39.530651
SI05X	719	−39.520251
SI05Y	720	−39.520551
FI02X	115	−39.199500
FI02Y	117	−39.195500

C.3 Focused Beam Properties

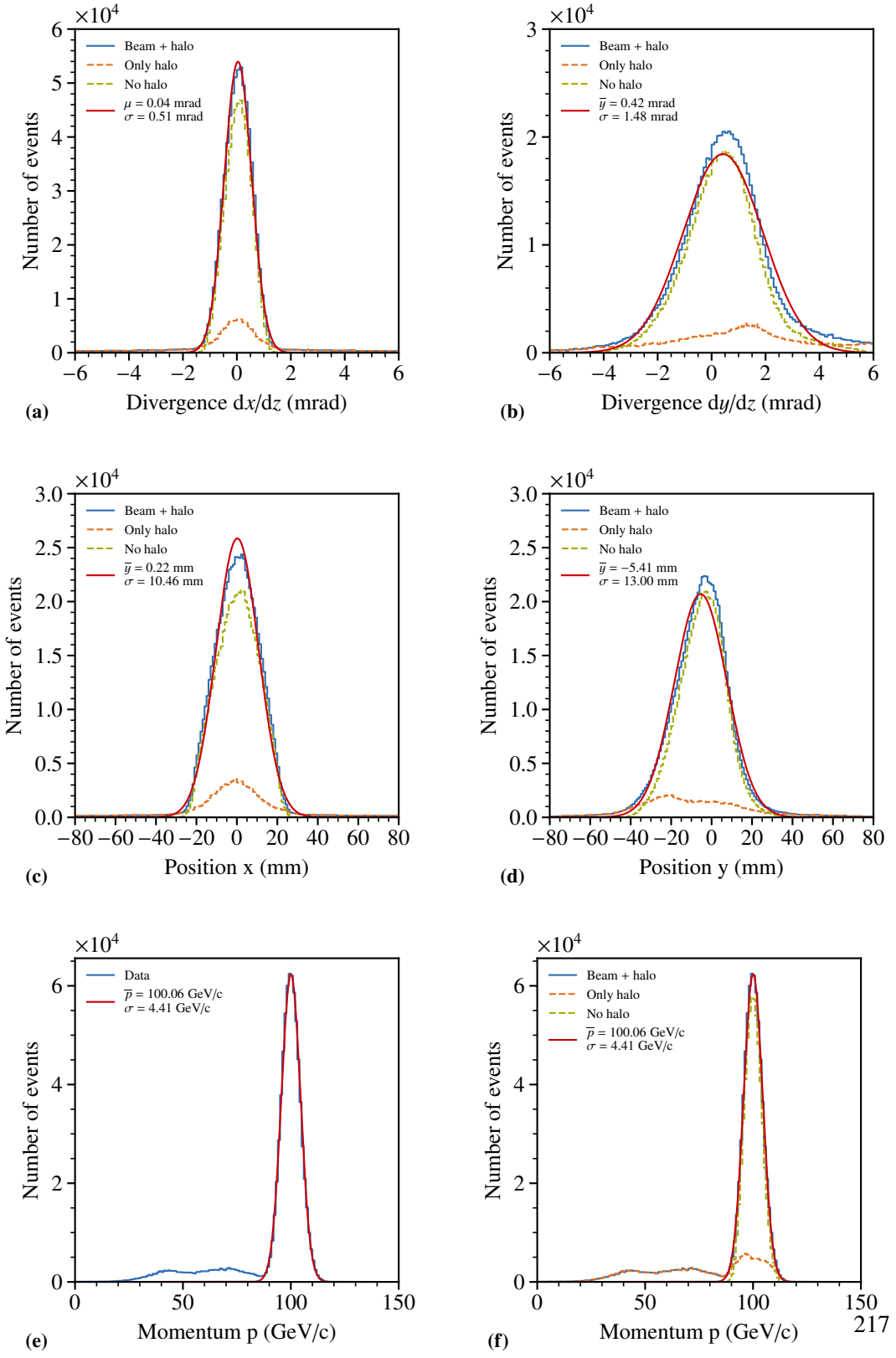

Figure C.2: Beam properties for the focused option. Details can be found in Sec. 3.2.2.

C.4 Parallel Beam Properties

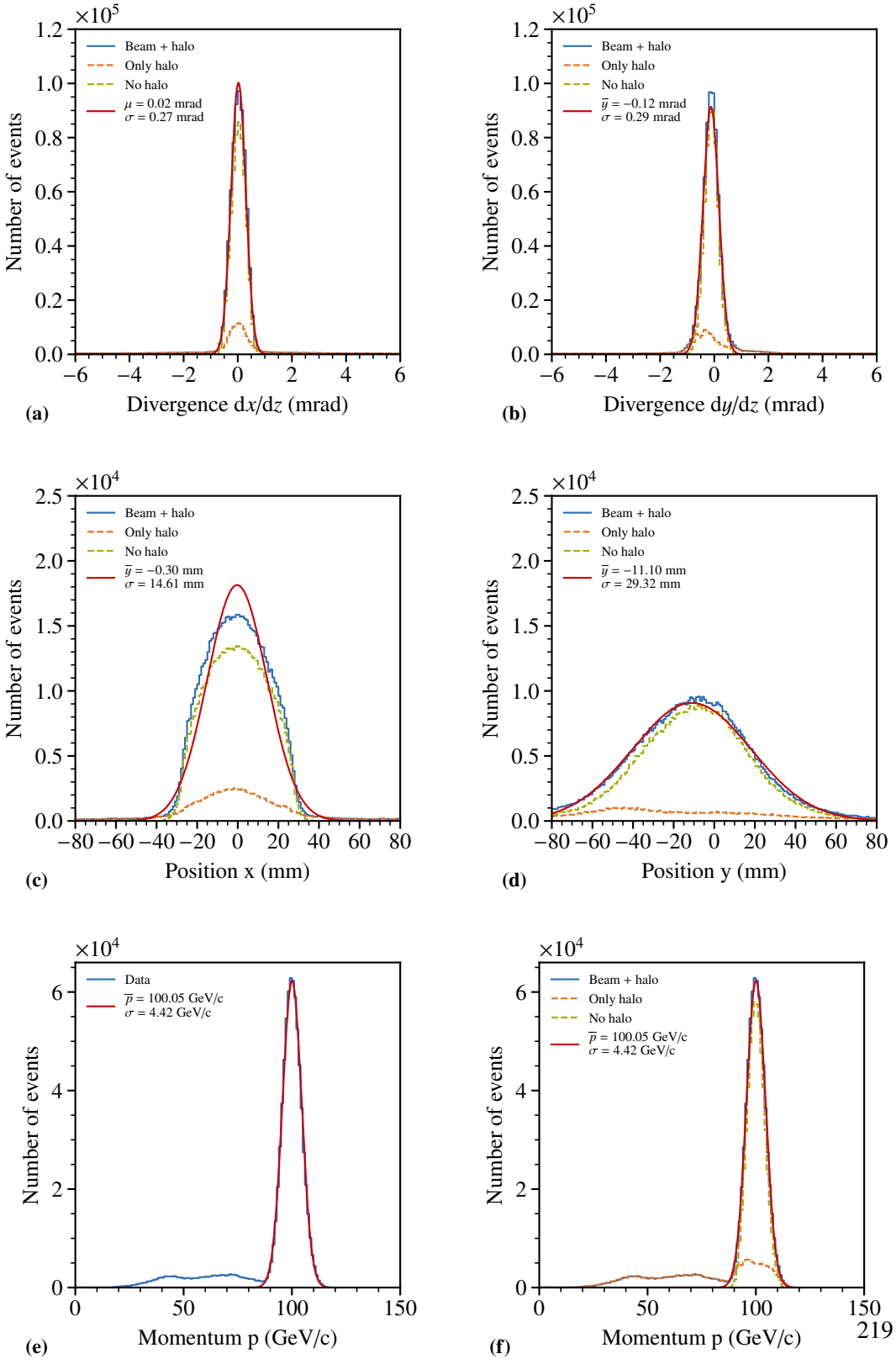

Figure C.3: Beam properties for the parallel option. Details can be found in Sec. 3.2.2.

C.5 Raw Data

The raw data is stored on the tape archive CTA at CERN. 361 runs with racking data are stored under the following directory:
`/eos/ctapublicdisk/archive/compass/data/2021/amber/raw/T09/`

The run-by-run alignment production output as mDSTs can be found under the directory:
`/eos/experiment/compass/PRdata/christian/PilotRun2021/ProductionV1.2/histograms/U7000`

The raw and produced TPC data for the single runs is stored under:
`/eos/ctapublicdisk/archive/compass/PRdata/tpcdata/analyzed/`

A latest version is stored under:
`/eos/experiment/compass/PRdata/tpcdata/analyzed/03`

C.6 Production

For the so-called production of the data the run-by-run alignment is required as well as the decoding for the TRLO timestamp. Productions are performed on demand. With a first production focused on having combined data of tracking and TPC a following production with a focus on a larger tracking data set is performed.

Production V1

For the first production of the data the initial run-by-run alignment is used. With the first goal to obtain combined TPC and tracking data runs were reconstructed starting from the first run with a valid TRLO timestamp (293218) until the last run taken with the pilot run setup (293315).

Production V1.3

In a following production the usable tracking data is produced starting from the first run with correct latency settings of the silicon tracking detectors. This is the case starting with run 293215.

C.7 Silicon Timings

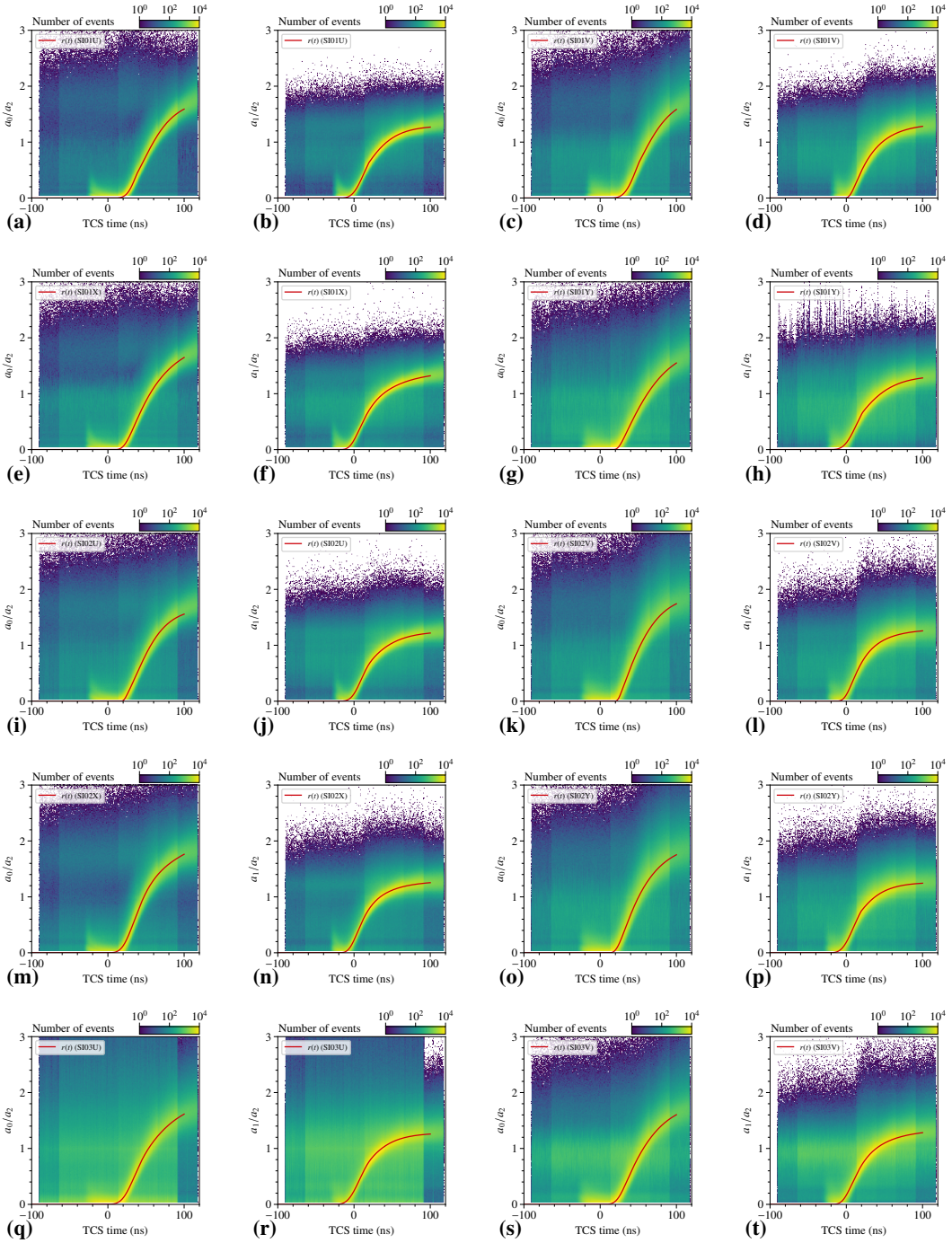

Figure C.4: Amplitude ratios for SI01, SI02, SI03U and SI03V for the time calibration. Details can be found in Sec. 3.3.2.

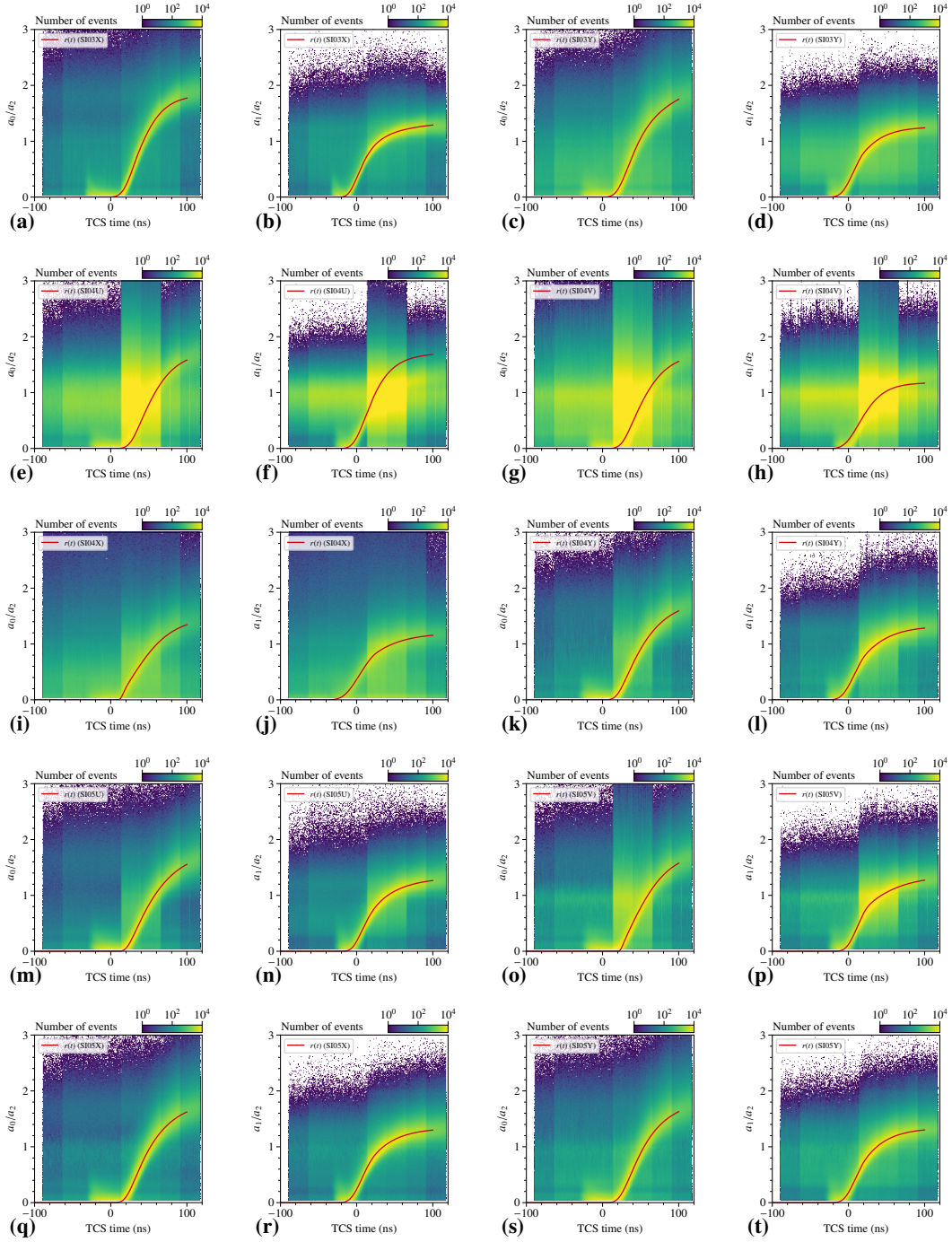

Figure C.5: Amplitude ratios for SI03X, SI03Y, SI04, and SI05 for the time calibration. Details can be found in Sec. 3.3.2.

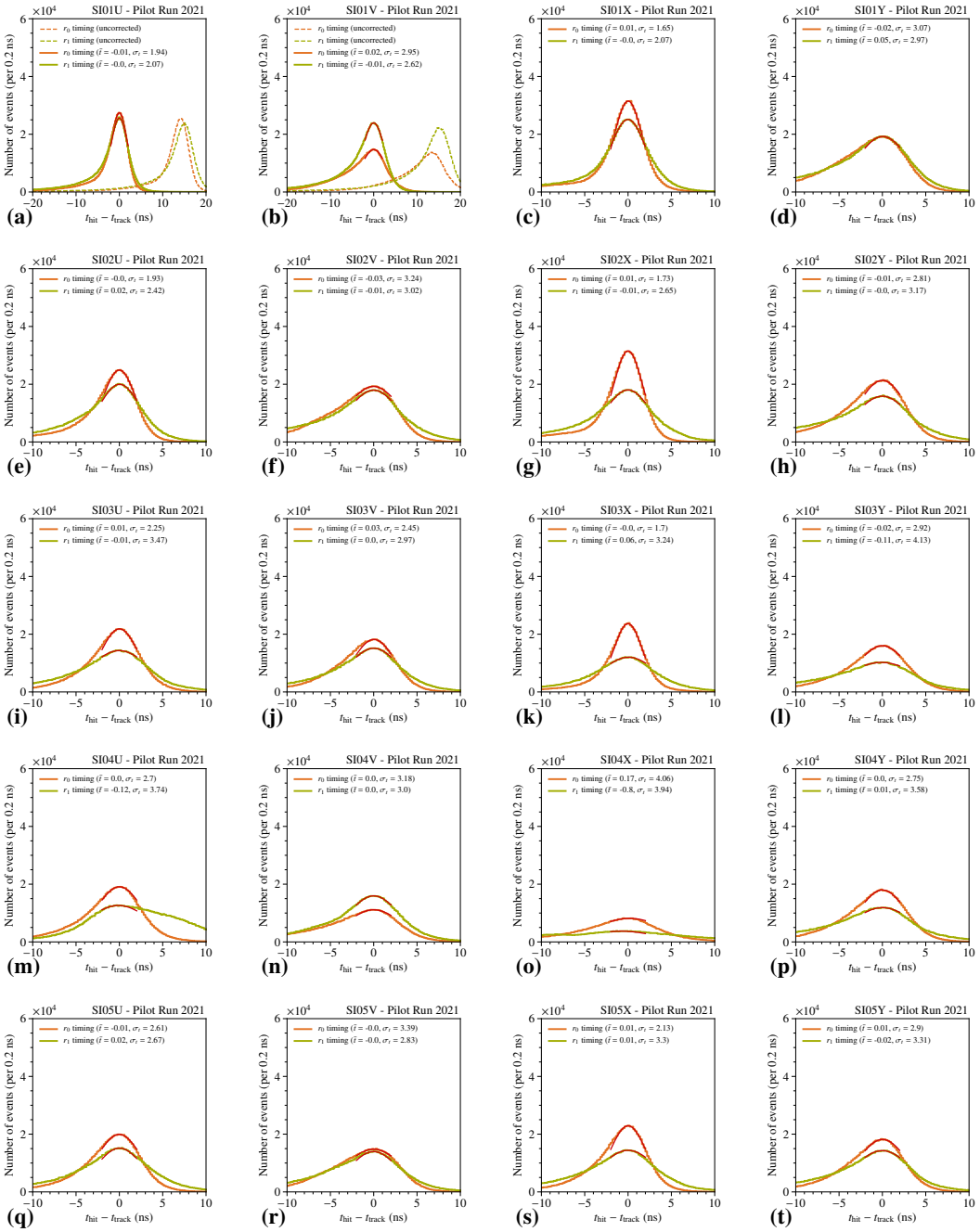

Figure C.6: Amplitude ratios for SI03X, SI03Y, SI04, and SI05 for the time calibration. Details can be found in Sec. 3.3.2.

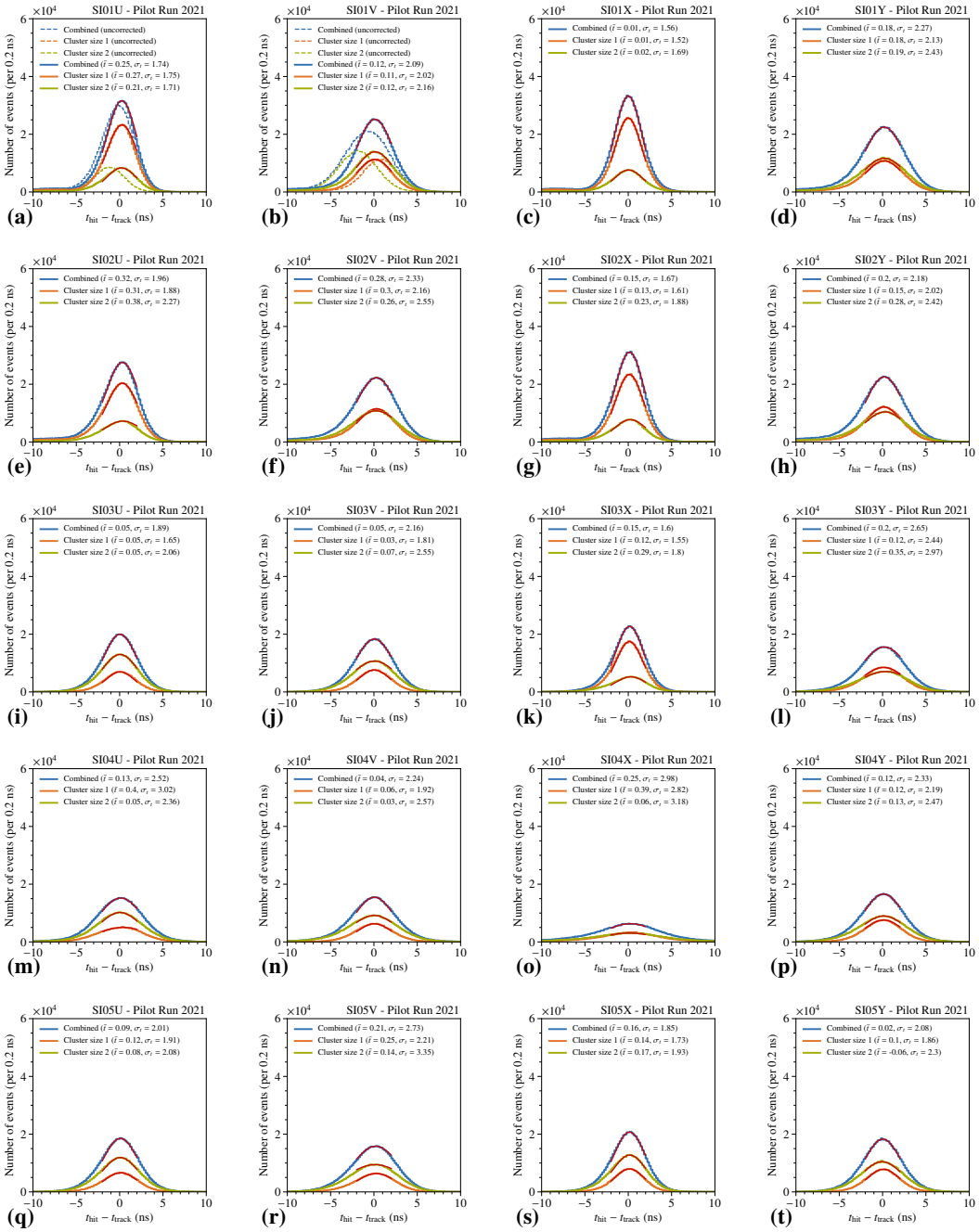

Figure C.7: Silicon time resolutions for different cluster sizes during the pilot run. Details can be found in Sec. 3.3.2.

C.8 Silicon Spacial Resolutions

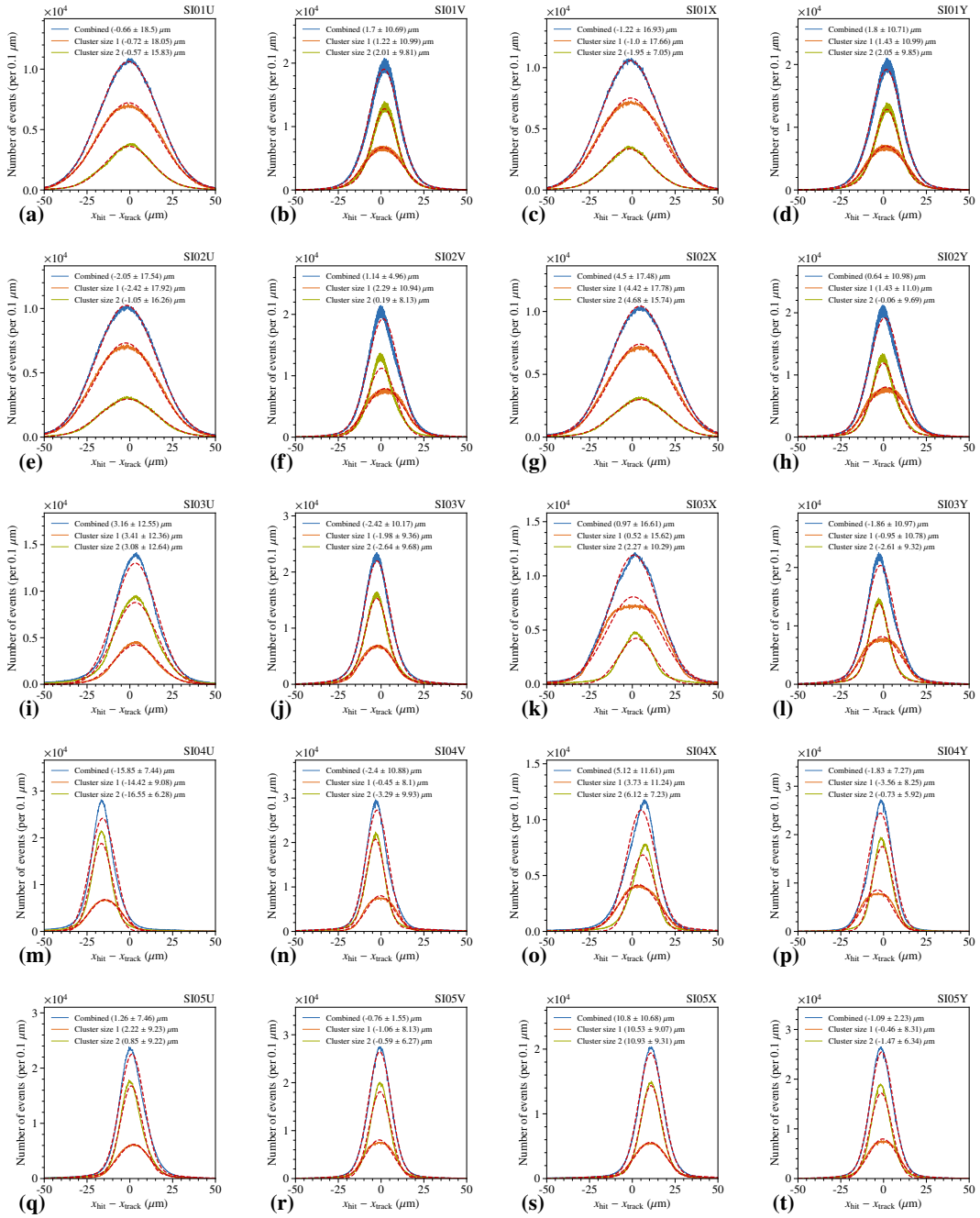

Figure C.8: Silicon resolutions for the combined, single and double cluster size events. Details can be found in Sec. 3.3.3.

C.9 Silicon Efficiencies

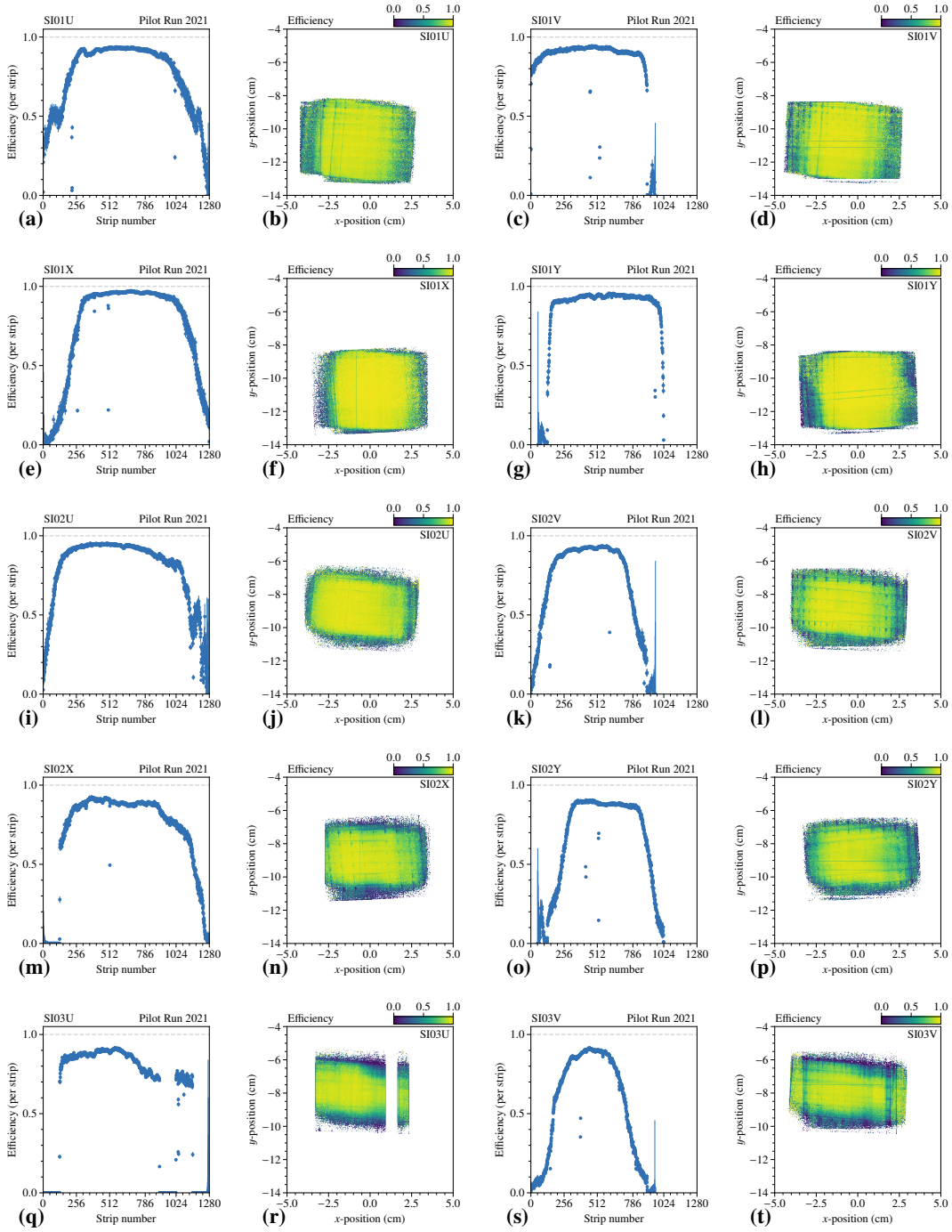

Figure C.9: Silicon efficiencies in 1-d and 2-d projection. Details are discussed in Sec. 3.3.3.

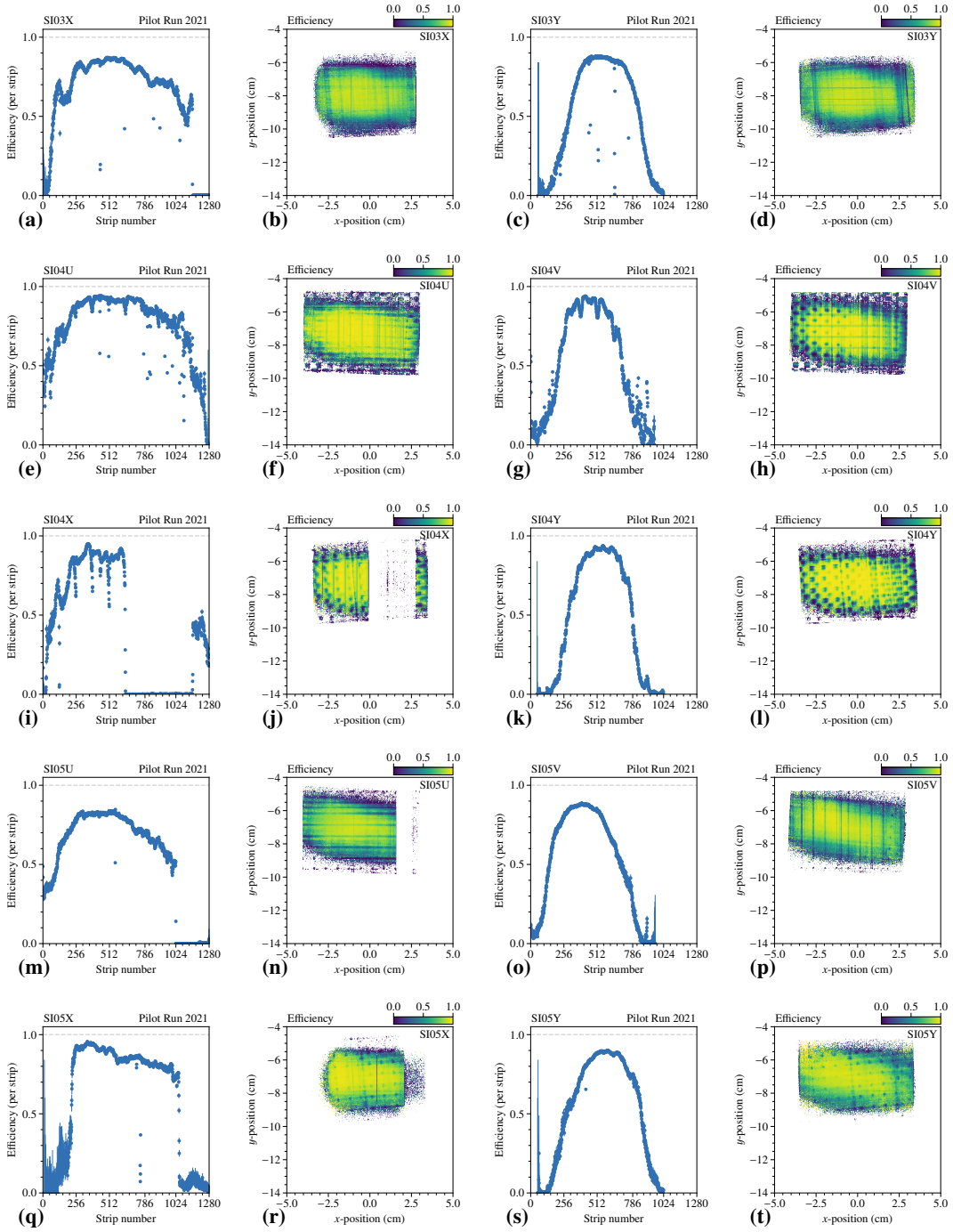

Figure C.10: Silicon efficiencies in 1-d and 2-d projection. Details are discussed in Sec. 3.3.3.

C.10 Silicon Profiles

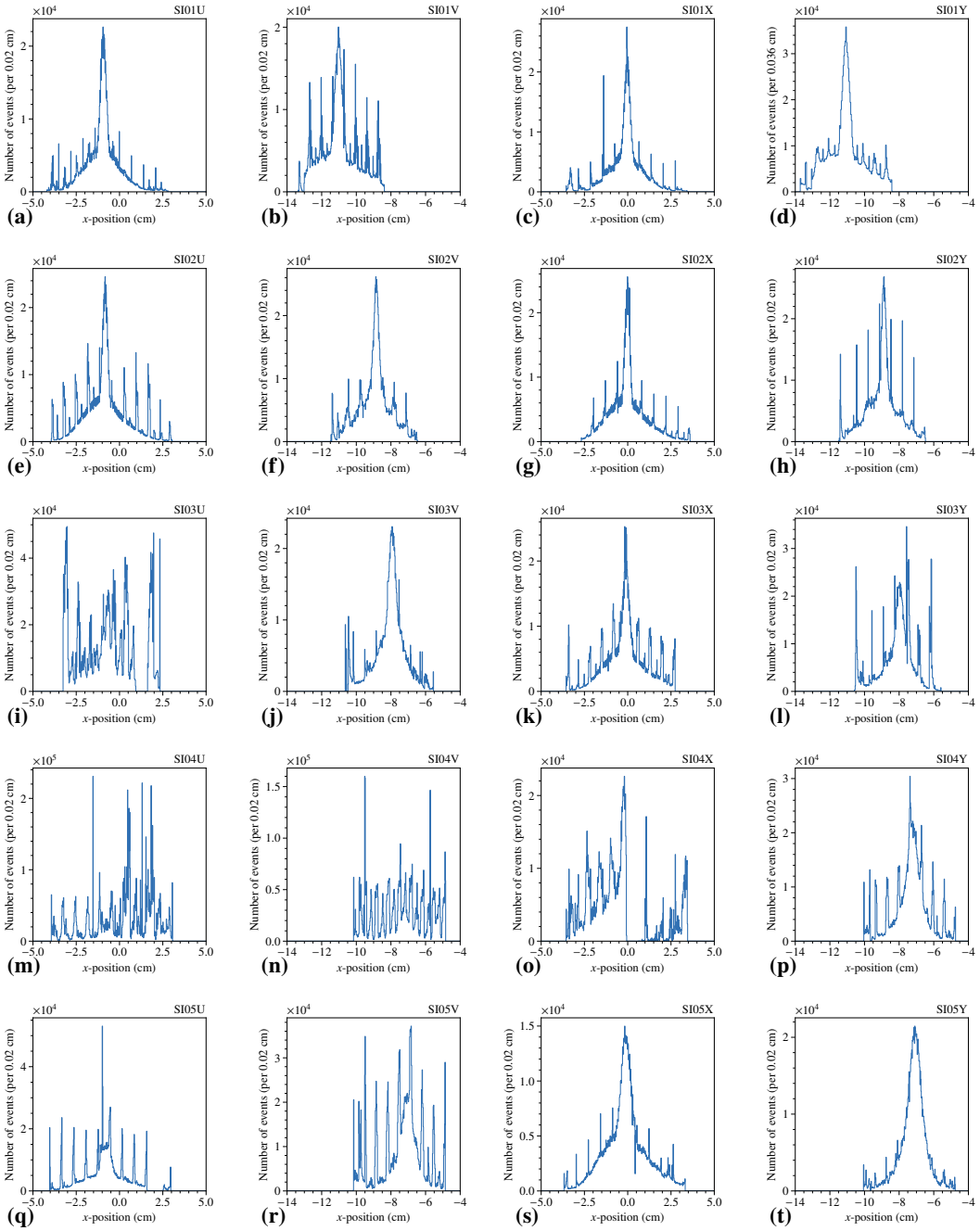

Figure C.11: Silicon 1-d profiles of the single projections. Further information are given in Sec. 3.3.

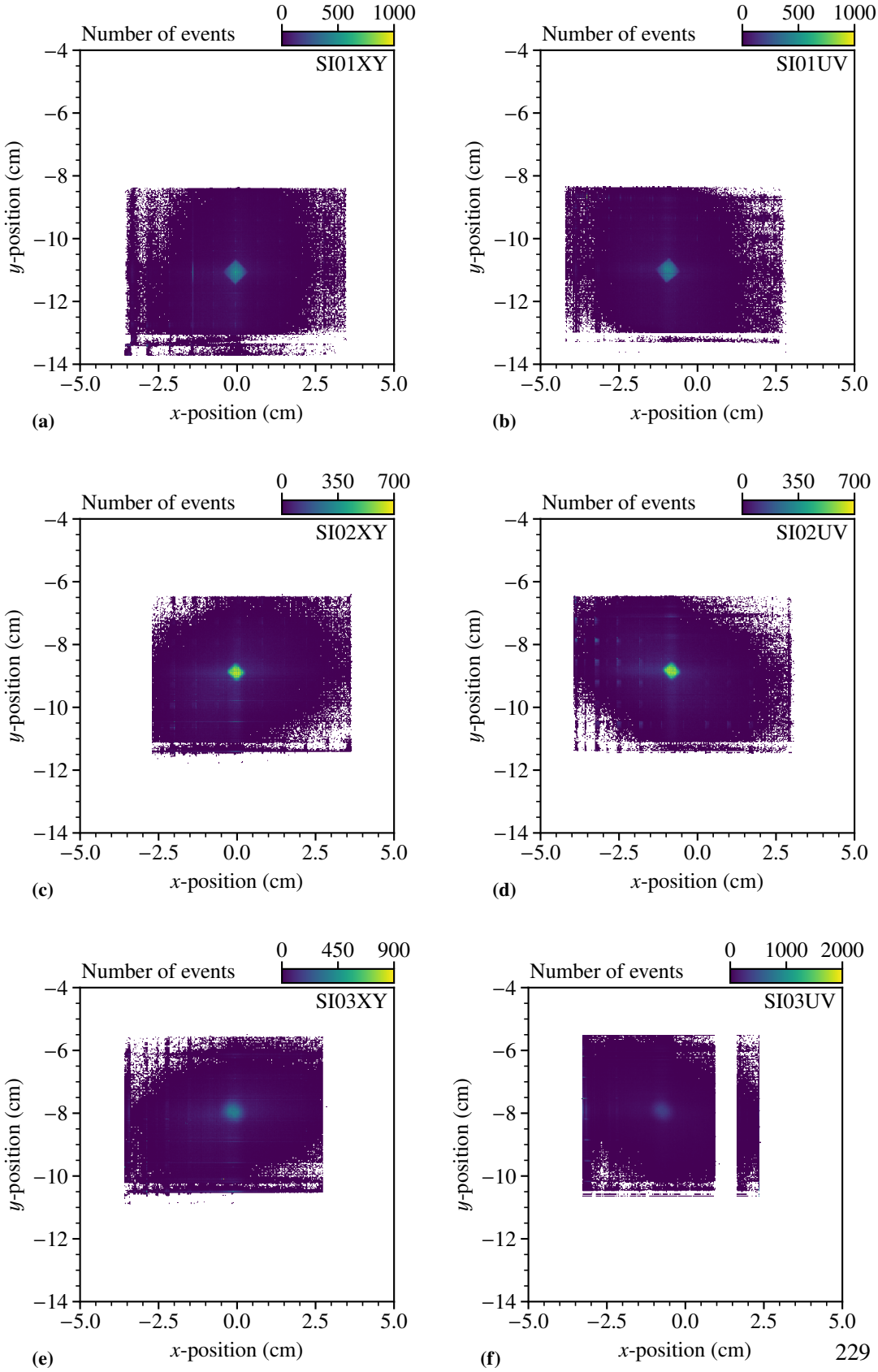

Figure C.12: Silicon 2-d profiles of the single projections for SI01, SI02 and SI03. Further information are given in Sec. 3.3.

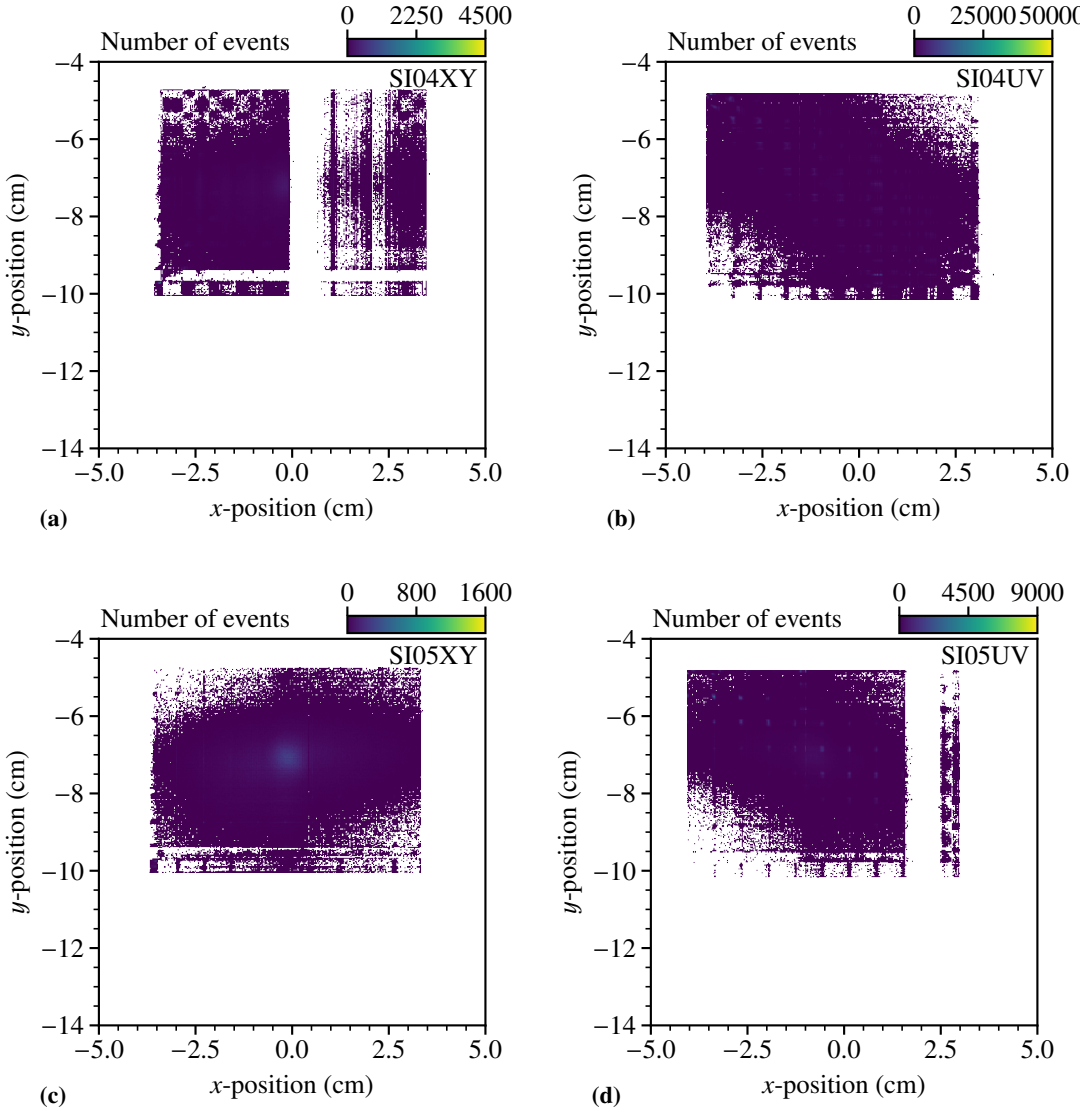

Figure C.13: Silicon 2-d profiles of the single projections for SI04 and SI05. Further information are given in Sec. 3.3.

APPENDIX D

Silicon Detectors at COMPASS

D.1 Silicon Time Resolution

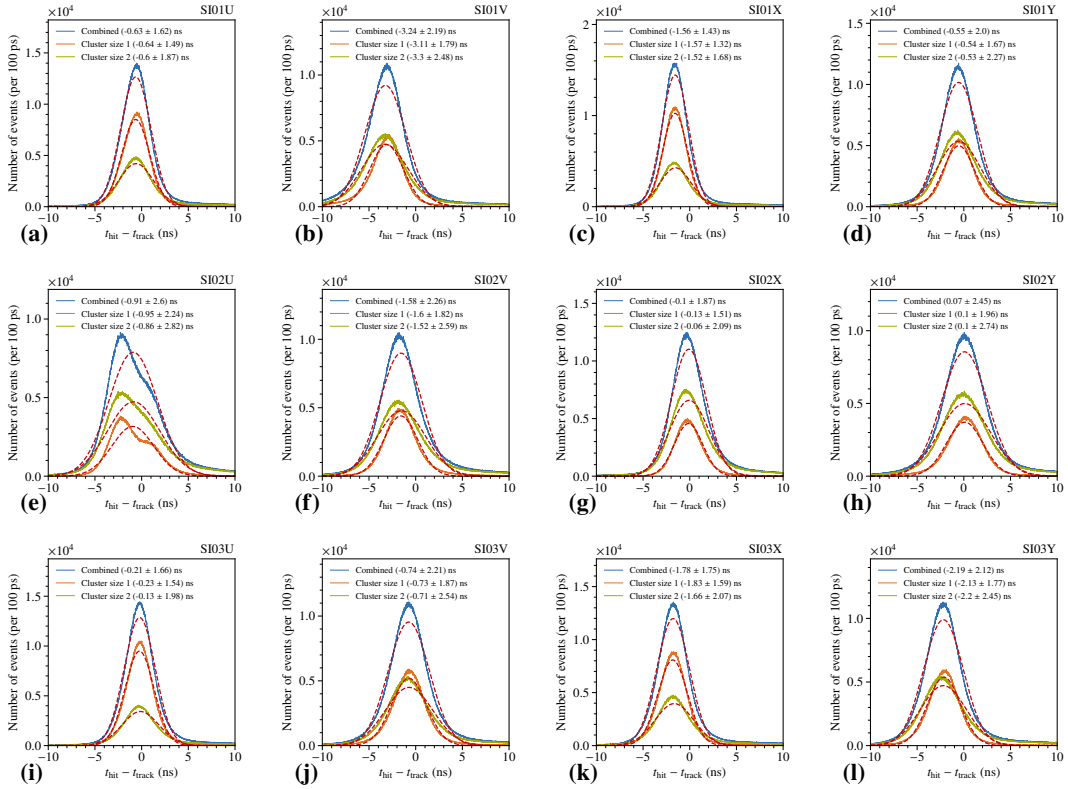

Figure D.1: Silicon time resolution for the single planes. The single and double cluster-size events are shown together with the combined distribution. Details in Sec. 5.5.

D.2 Silicon Resolution

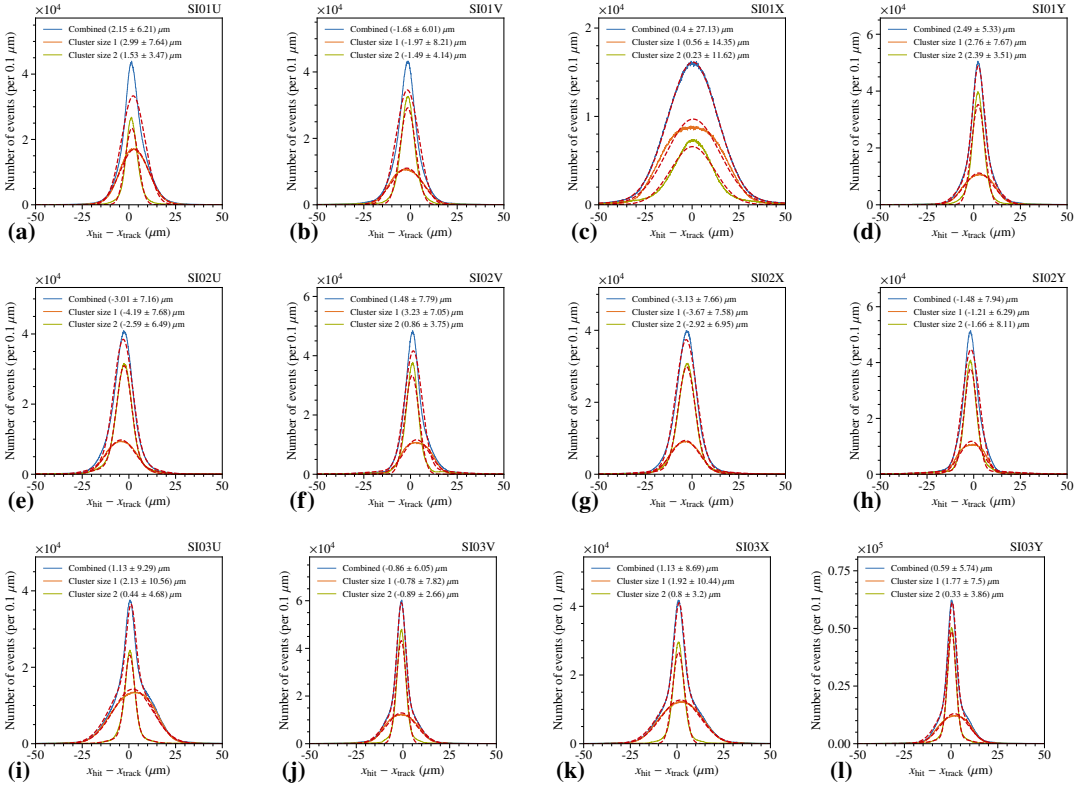

Figure D.2: Silicon spatial resolution. The single cluster as well as the two-cluster events together with the combined distribution are shown. Details can be found in Sec. 5.5.1.

D.3 Silicon Efficiency

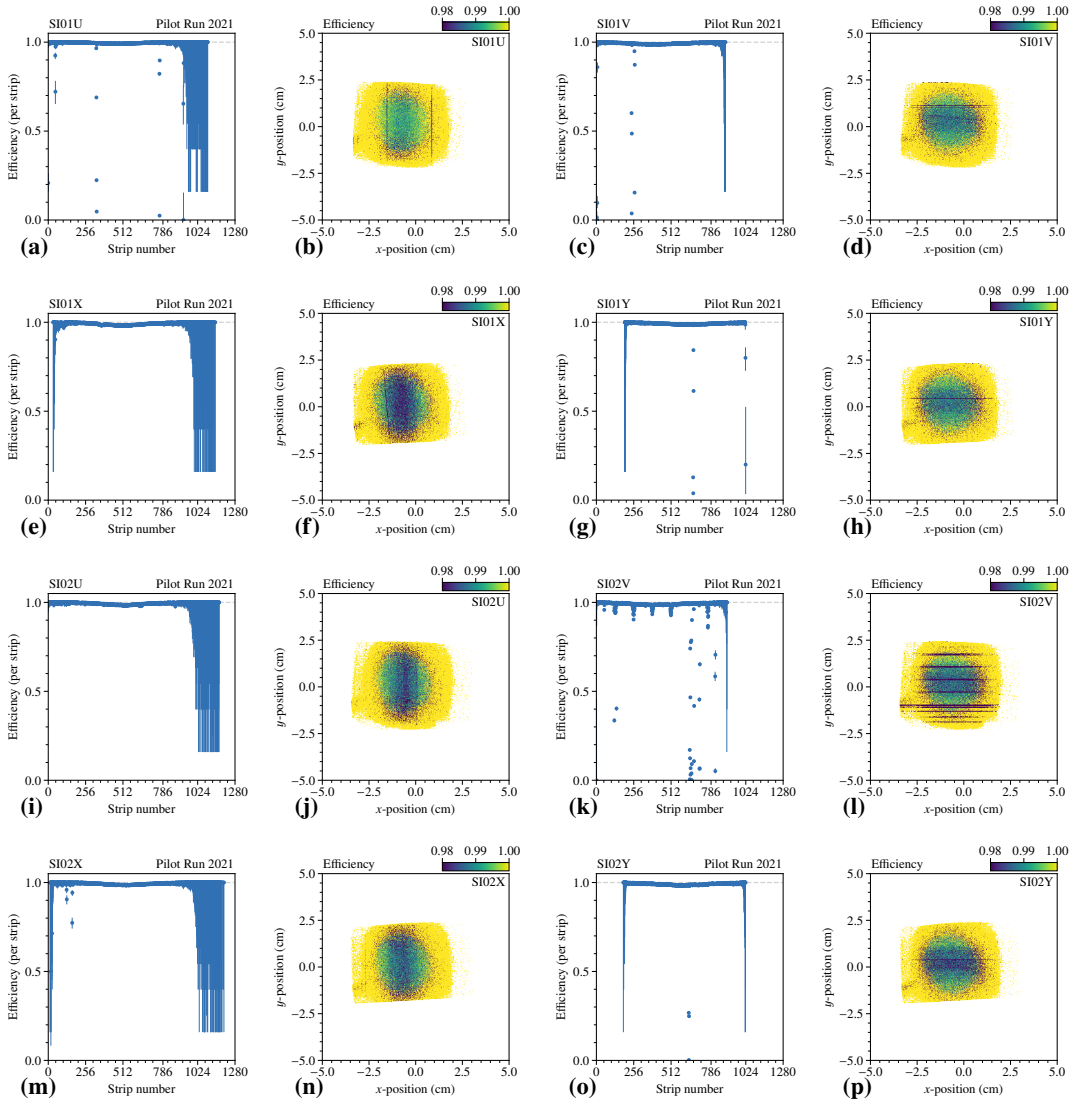

Figure D.3: Silicon efficiencies in 1-d and 2-d projection for SI01 and SI02.

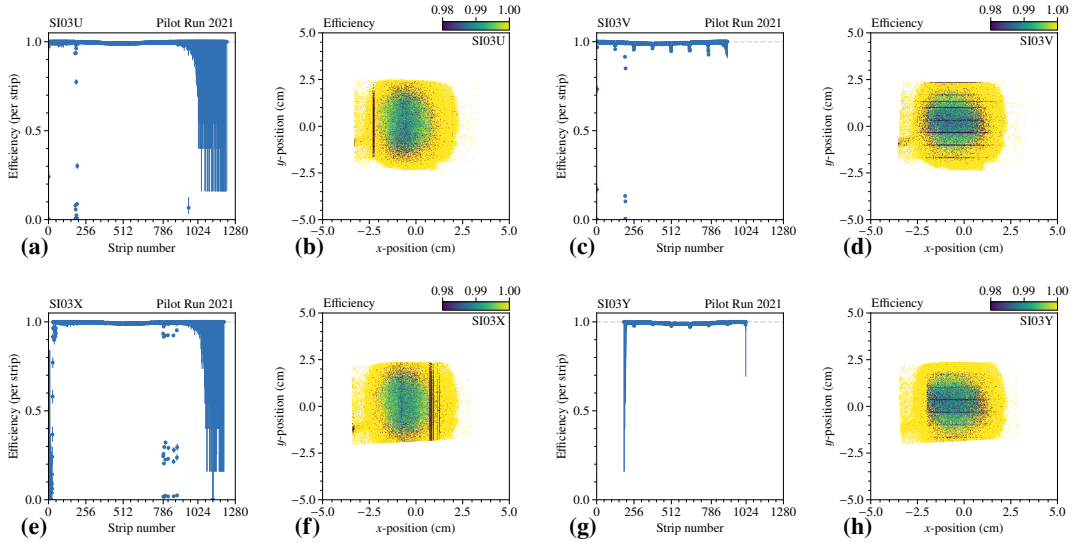

Figure D.4: Silicon efficiencies in 1-d and 2-d projection for SI03.

Bibliography

[1] B. Adams et al., *Letter of Intent: A New QCD facility at the M2 beam line of the CERN SPS (COMPASS++/AMBER)*, 2019, arXiv: 1808.00848 [hep-ex]
(cit. on pp. 3, 9, 12, 51, 189).

[2] B. Adams et al., *COMPASS++/AMBER: Proposal for Measurements at the M2 beam line of the CERN SPS Phase-1: 2022-2024*, tech. rep. CERN-SPSC-2019-022. SPSC-P-360, The collaboration has not yet constituted itself, thus instead of a Spokesperson currently the nominated Contact Person is acting in place.: CERN, 2019,
URL: http://cds.cern.ch/record/2676885
(cit. on pp. 3, 6, 12, 18, 19, 25, 40–42, 44, 46, 47, 52, 107, 108, 165, 189, 194).

[3] E. E. Chambers and R. Hofstadter, *Structure of the Proton*, Phys. Rev. **103** (5 1956) 1454,
URL: https://link.aps.org/doi/10.1103/PhysRev.103.1454 (cit. on p. 4).

[4] N. d'Hose, *private communication*, URL: nicole.dhose@cea.fr (cit. on p. 4).

[5] Jan C. Bernauer, *private communication*, URL: jan.bernauer@stonybrook.edu
(cit. on p. 4).

[6] W. Xiong et al.,
A small proton charge radius from an electron–proton scattering experiment,
Nature **575** (2019) 147, URL: https://doi.org/10.1038/s41586-019-1721-2
(cit. on pp. 4, 6).

[7] J. C. Bernauer et al.,
High-precision determination of the electric and magnetic form factors of the proton,
Phys. Rev. Lett. **105** (2010) 242001, arXiv: 1007.5076 [nucl-ex] (cit. on pp. 4, 9).

[8] Bernauer, Jan C., *The proton radius puzzle - 9 years later*,
EPJ Web Conf. **234** (2020) 01001,
URL: https://doi.org/10.1051/epjconf/202023401001 (cit. on pp. 5, 6).

[9] S. Bifani et al., *Review of lepton universality tests in B decays*,
Journal of Physics G: Nuclear and Particle Physics **46** (2018) 023001,
URL: https://doi.org/10.1088%2F1361-6471%2Faaf5de (cit. on p. 5).

[10] Y.-H. Lin, H.-W. Hammer, and U.-G. Meißner,
High-precision determination of the electric and magnetic radius of the proton,
Physics Letters B **816** (2021) 136254, ISSN: 0370-2693, URL: https://www.sciencedirect.com/science/article/pii/S0370269321001945
(cit. on p. 6).

[11] H.-W. Hammer and U.-G. Meißner, *The proton radius: from a puzzle to precision*, Science Bulletin **65** (2020) 257, URL: https://doi.org/10.1016%2Fj.scib.2019.12.012 (cit. on p. 6).

[12] G. Höhler and E. Pietarinen, *Electromagnetic radii of nucleon and pion*, Physics Letters B **53** (1975) 471, ISSN: 0370-2693, URL: https://www.sciencedirect.com/science/article/pii/0370269375902208 (cit. on p. 6).

[13] P. Mergell, U.-G. Meißner, and D. Drechsel, *Dispersion-theoretical analysis of the nucleon electromagnetic form factors*, Nuclear Physics A **596** (1996) 367, URL: https://doi.org/10.1016%2F0375-9474%2895%2900339-8 (cit. on p. 6).

[14] W. E. Lamb and R. C. Retherford, *Fine Structure of the Hydrogen Atom by a Microwave Method*, Phys. Rev. **72** (3 1947) 241, URL: https://link.aps.org/doi/10.1103/PhysRev.72.241 (cit. on p. 6).

[15] N. Bezginov et al., *A measurement of the atomic hydrogen Lamb shift and the proton charge radius*, Science **365** (2019) 1007, eprint: https://www.science.org/doi/pdf/10.1126/science.aau7807, URL: https://www.science.org/doi/abs/10.1126/science.aau7807 (cit. on p. 6).

[16] A. Antognini et al., *Proton Structure from the Measurement of 2S-2P Transition Frequencies of Muonic Hydrogen*, Science **339** (2013) 417, eprint: https://www.science.org/doi/pdf/10.1126/science.1230016, URL: https://www.science.org/doi/abs/10.1126/science.1230016 (cit. on p. 6).

[17] *Physics program of MAGIX, Magnetic Radius of the Proton*, URL: http://magix.kph.uni-mainz.de/ (cit. on p. 6).

[18] R. Gilman et al., *Studying the Proton "Radius" Puzzle with μp Elastic Scattering*, 2013, URL: https://arxiv.org/abs/1303.2160 (cit. on p. 6).

[19] A. A. Vorobyev, *Precision Measurement of the Proton Charge Radius in Electron Proton Scattering*, Physics of Particles and Nuclei Letters **16** (2019) 524, URL: https://doi.org/10.1134%2Fs1547477119050303 (cit. on pp. 6, 17, 18).

[20] E. Voutier, *ProRad@PRAE*, URL: https://indico.him.uni-mainz.de/event/14/contributions/147/attachments/128/130/HERAEUS-Voutier.pdf (cit. on p. 6).

[21] T. Suda, *Elastic electron scattering off protons using 60 MeV electron linac of Tohoku University*, URL: https://indico.mitp.uni-mainz.de/event/132/contributions/552/attachments/420/451/24_1_Suda_PRP_2018.pdf (cit. on p. 6).

[22] M. N. Rosenbluth, *High Energy Elastic Scattering of Electrons on Protons*, Phys. Rev. **79** (4 1950) 615, URL: https://link.aps.org/doi/10.1103/PhysRev.79.615 (cit. on p. 9).

[23] J. M. Friedrich, *private communication*, URL: jan@tum.de (cit. on pp. 9, 93, 127).

[24] N. Kaiser, Y.-H. Lin, and U.-G. Meißner, *Radiative corrections to elastic muon-proton scattering at low momentum transfers*, Physical Review D **105** (2022), URL: https://doi.org/10.1103%2Fphysrevd.105.076006 (cit. on pp. 12, 40).

[25] D. Banerjee, *private communication*, URL: dipanwita.banerjee@cern.ch (cit. on pp. 14, 17, 33, 35, 111).

[26] P. Abbon et al., *The COMPASS Setup for Physics with Hadron Beams*, Nucl. Instrum. Methods Phys. Res., A **779** (2014) 69, URL: https://cds.cern.ch/record/1950827 (cit. on pp. 15, 16, 115, 131).

[27] H. W. Atherton et al., *Precise measurements of particle production by 400 GeV/c protons on beryllium targets*, CERN Yellow Reports: Monographs, CERN, 1980, URL: https://cds.cern.ch/record/133786 (cit. on p. 16).

[28] J. Bernhard et al., *Studies for New Experiments at the CERN M2 Beamline within "Physics Beyond Colliders": AMBER/COMPASS++, NA64μ, MuonE*, AIP Conf. Proc. **2249** (2019) 030035. 7 p, MENU 2019 Proceedings, 7 pages, arXiv: 1911.01498, URL: https://cds.cern.ch/record/2702256 (cit. on pp. 17, 33, 107).

[29] J. Burq et al., *Measurements of the total π-He and p-He cross sections and the slopes of the forward diffraction peak at energies from 50 to 300 GeV*, Nuclear Physics B **187** (1981) 205, ISSN: 0550-3213, URL: https://www.sciencedirect.com/science/article/pii/0550321381902704 (cit. on pp. 17, 121).

[30] J. P. Burq et al., *Determination of the absolute momentum of a high-energy hadron beam using elastic scattering of hadrons from a helium target*, Nucl. Instrum. Methods **177** (1980) 353, URL: https://cds.cern.ch/record/133912 (cit. on pp. 17, 121).

[31] A. Vorobyov et al., *A method for studies of small-angle hadron-proton elastic scattering in the coulomb interference region*, Nuclear Instruments and Methods **119** (1974) 509, ISSN: 0029-554X, URL: https://www.sciencedirect.com/science/article/pii/0029554X74908015 (cit. on pp. 17, 121, 122).

[32] O. Frisch, *British atomic energy report br-49*, Atomic Energy Research Establishment: Harwell, UK (1944) (cit. on pp. 18, 59).

[33] F. Metger,
Simulations of an active-target TPC for a measurement of the proton charge radius,
Master's Thesis: HISKP, Rheinische Friedrich-Wilhelms-Universität Bonn, 2020,
URL: https://wwwcompass.cern.ch/compass/publications/theses/2020_mst_metzger.pdf (cit. on p. 18).

[34] ANSYS, *ANSYS webpage*, 2022, URL: https://www.ansys.com/ (cit. on p. 18).

[35] R. Veenhof, *GARFIELD++ webpage*, 2022,
URL: http://garfieldpp.web.cern.ch/garfieldpp/ (cit. on p. 18).

[36] M. Hoffmann, *private communication*, URL: martin.hoffmann@cern.ch
(cit. on pp. 18, 116, 137–139).

[37] A. Inglessi, *private communication*, URL: alexander.inglessi@cern.ch
(cit. on pp. 19, 54, 61, 73, 83, 121, 122).

[38] A. A. Vorobyov, *private communication*, URL: vorobyov_aa@pnpi.nrcki.ru
(cit. on p. 19).

[39] M. B. et al., *Stopping-Power and Range Tables for Electrons, Protons, and Helium Ions*,
2011, URL: http://www.nist.gov/pml/data/star/index.cfm (cit. on pp. 19, 21).

[40] M. Mager, *ALPIDE, the Monolithic Active Pixel Sensor for the ALICE ITS upgrade*,
Nuclear Instruments and Methods in Physics Research Section A: Accelerators, Spectrometers, Detectors and Associated Equipment **824** (2016) 434, Frontier Detectors for Frontier Physics: Proceedings of the 13th Pisa Meeting on Advanced Detectors,
ISSN: 0168-9002, URL: https://www.sciencedirect.com/science/article/pii/S0168900215011122
(cit. on pp. 22, 23).

[41] J. M. Friedrich and O. Denisov, *AMBER Status Report 2022*, tech. rep., CERN, 2022,
URL: https://cds.cern.ch/record/2810822 (cit. on pp. 22, 23, 103).

[42] K. Eichhorn, *private communication*, URL: karl.eichhorn@tum.de (cit. on p. 22).

[43] M. Alexeev, *private communication*, URL: maxim.alekseev@cern.ch
(cit. on pp. 23–25).

[44] B. A. et al and,
Technical Design Report for the Upgrade of the ALICE Inner Tracking System,
Journal of Physics G: Nuclear and Particle Physics **41** (2014) 087002,
URL: https://doi.org/10.1088/0954-3899/41/8/087002 (cit. on p. 24).

[45] M. Losekamm, *private communication*, URL: m.losekamm@tum.de (cit. on p. 25).

[46] V. Frolov et al., *Data Acquisition System for the COMPASS++/ AMBER Experiment*,
IEEE Transactions on Nuclear Science **68** (2021) 1891 (cit. on p. 28).

[47] K. Eichhorn,
Monte Carlo Studies for the Proton Charge-Radius Measurement at AMBER,
Master's Thesis: E18, Technical University of Munich, 2021
(cit. on pp. 29, 40, 41, 76, 84, 190).

[48] M. Tanabashi et al., *Review of Particle Physics*, Phys. Rev. D **98** (3 2018) 030001, URL: https://link.aps.org/doi/10.1103/PhysRevD.98.030001 (cit. on p. 36).

[49] A. V. Gramolin et al., *A new event generator for the elastic scattering of charged leptons on protons*, Journal of Physics G: Nuclear and Particle Physics **41** (2014) 115001, ISSN: 1361-6471, URL: http://dx.doi.org/10.1088/0954-3899/41/11/115001 (cit. on p. 39).

[50] V. Fadin and R. Gerasimov, *On the cancellation of radiative corrections to the cross section of electron-proton scattering*, Physics Letters B **795** (2019) 172, ISSN: 0370-2693, URL: https://www.sciencedirect.com/science/article/pii/S0370269319304149 (cit. on p. 39).

[51] S. Belostotski, N. Sagidova, and A. Vorobyev, *Proton radius reconstruction from simulated electron-proton elastic scattering cross sections at low transfer momenta*, 2019, URL: https://arxiv.org/abs/1903.04975 (cit. on pp. 40, 45).

[52] X. Yan et al., *Robust extraction of the proton charge radius from electron-proton scattering data*, Phys. Rev. C **98** (2 2018) 025204, URL: https://link.aps.org/doi/10.1103/PhysRevC.98.025204 (cit. on p. 40).

[53] T. Poeschl, *private communication*, URL: thomas.poeschl@ph.tum.de (cit. on p. 45).

[54] M. Pešek, *Pion-induced polarized Drell-Yan process at COMPASS*, PhD Thesis: Charles University - Faculty of Mathematics and Physics, 2020, URL: https://wwwcompass.cern.ch/compass/publications/theses/2020_phd_pesek.pdf (cit. on p. 51).

[55] Pascal Sainvitu, *COMPASS Test Zone – Bld 888*, English, 6 pp., URL: https://edms.cern.ch/document/1936923/2, March, 2018 (cit. on pp. 53, 65, 206).

[56] L. Jones, *APV25-S1: User guide version 2.2*, RAL Microelectronics Design Group, 2001, URL: https://cds.cern.ch/record/1069892 (cit. on pp. 53, 55, 62, 168, 169).

[57] *TRLO II - flexible FPGA trigger control*, http://fy.chalmers.se/~f96hajo/trloii/man7/trloii.7.pdf (cit. on pp. 53, 66, 68, 136).

[58] K. Große, ed., *GSI Scientific Report 2010 [GSI Report 2011-1]*, vol. 2011-1, GSI Report, Wissenschaftlicher Ergebnisbericht der GSI, GSI Annual Report, GSI, 2011 582 p. URL: https://repository.gsi.de/record/53521 (cit. on pp. 53, 66).

[59] B. M. Veit, *private communication*, URL: b.veit@cern.ch (cit. on pp. 54–56, 116, 118).

[60] Saint-Gobain Crystals, *BC400 BC404 BC408 BC412 BC416 Data Sheet*, English, 2 pp., URL: https://www.crystals.saint-gobain.com/sites/imdf.crystals.com/files/documents/bc400-404-408-412-416-data-sheet.pdf, Septemper, 2018 (cit. on p. 56).

[61] O. Kisilev, *private communication*, URL: O.Kiselev@gsi.de (cit. on pp. 59, 61).

[62] *SIS3316 16 CHANNEL VME DIGITIZER FAMILY*, https://www.struck.de/sis3316.html (cit. on p. 60).

[63] M. R. Mynther, *Performanzuntersuchung von Silizium-Mikrostreifen-Detektoren im COMPASS-Experiment am CERN*, Bachelor's Thesis: E18, Technical University of Munich, 2018 (cit. on pp. 63, 182, 183, 185, 189).

[64] K. Eichhorn, *Characterization of Silicon-Microstrip Detectors in the Proton Radius Test Measurement at COMPASS*, Batchelor's Thesis: E18, Technical University of Munich, 2019 (cit. on pp. 64, 65, 189).

[65] J. Bernhard, *private communication*, URL: johannes.bernhard@cern.ch (cit. on p. 65).

[66] I. Konorov, *private communication*, URL: igor.konorov@cern.ch (cit. on pp. 67, 135).

[67] R. Brun et al., *root-project/root: v6.18/02*, version v6-18-02, 2019, URL: https://doi.org/10.5281/zenodo.3895860 (cit. on pp. 69, 133, 186).

[68] COMPASS, *PRM Test Run Runlogbook in TWiki*, 2018, URL: https://twiki.cern.ch/twiki/bin/view/Compass/ProtonRadius/Data (cit. on p. 70).

[69] A. Král and T. Liska, *The CDR subsystem of the COMPASS experiment*, Czechoslov. J. Phys. **55** (2005) A383, URL: https://cds.cern.ch/record/851770 (cit. on p. 70).

[70] S. Gerassimov et al., *PHAST is the framework for data analysis of the COMPASS (NA58) and the AMBER (NA66) experiments*, http://ges.home.cern.ch/ges/phast/ (cit. on p. 71).

[71] K. A. Bicker et al., *ANTOK is the framework for data analysis*, https://gitlab.cern.ch/compass/hadron/antok (cit. on p. 71).

[72] S. Uhl, *private communication*, URL: sebastian.uhl@cern.ch (cit. on pp. 72, 206).

[73] M. Hoffmann, *A feasibility test for measuring the proton charge radius in high-energy muon-proton elastic scattering*, Master's Thesis: HISKP, Rheinische Friedrich-Wilhelms-Universität Bonn, 2019 (cit. on pp. 72, 73, 84, 189).

[74] D. Rohr et al., *Gpu-Based Online Track Reconstruction for the Alice Tpc in Run 3 With Continuous Read-Out*, EPJ Web of Conferences **214** (2019) 01050, ed. by A. Forti et al., URL: https://doi.org/10.1051%2Fepjconf%2F201921401050 (cit. on p. 90).

[75] G. Abbiendi et al., *A study of muon-electron elastic scattering in a test beam*, Journal of Instrumentation **16** (2021) P06005, URL: https://doi.org/10.1088/1748-0221/16/06/p06005 (cit. on pp. 91, 102).

[76] S. Paul, *private communication*, URL: stephan.paul@cern.ch (cit. on pp. 91, 103).

[77] P. Banerjee et al., *Theory for muon-electron scattering @ 10 ppm*, The European Physical Journal C **80** (2020), URL: https://doi.org/10.1140%2Fepjc%2Fs10052-020-8138-9 (cit. on pp. 91, 93).

[78] G. Abbiendi, *Status of the MUonE experiment*, PoS **ICHEP2020** (2021) 223 (cit. on pp. 102, 107).

[79] S. Amendolia et al., *A measurement of the kaon charge radius*, Physics Letters B **178** (1986) 435, ISSN: 0370-2693, URL: https://www.sciencedirect.com/science/article/pii/0370269386914073 (cit. on p. 103).

[80] S. Amendolia et al., *A measurement of the space-like pion electromagnetic form factor*, Nuclear Physics B **277** (1986) 168, ISSN: 0550-3213, URL: https://www.sciencedirect.com/science/article/pii/0550321386904372 (cit. on p. 103).

[81] D. Banerjee et al., *Dark Matter Search in Missing Energy Events with NA64*, Physical Review Letters **123** (2019), URL: https://doi.org/10.1103%2Fphysrevlett.123.121801 (cit. on p. 107).

[82] *Minutes of the 137th Meeting of the SPSC, Tuesday 7 April 2020*, tech. rep., CERN, 2020, URL: https://cds.cern.ch/record/2718638 (cit. on p. 107).

[83] *Minutes of the 139th Meeting of the SPSC, Tuesday 13 October 2020*, tech. rep., CERN, 2020, URL: https://cds.cern.ch/record/2741386 (cit. on p. 107).

[84] P. Abbon et al., *The COMPASS experiment at CERN*, Nuclear Instruments and Methods in Physics Research Section A: Accelerators, Spectrometers, Detectors and Associated Equipment **577** (2007) 455, URL: https://doi.org/10.1016%2Fj.nima.2007.03.026 (cit. on pp. 117, 182).

[85] E. Maev, *private communication*, URL: evgeny.maev@cern.ch (cit. on pp. 121, 122, 147, 152).

[86] B. Grube, *The Trigger Control System and the Common GEM and Silicon Readout for the COMPASS Experiment*, Diploma Thesis: Technical University of Munich, 2001, URL: https://wwwcompass.cern.ch/compass/publications/theses/2001_dpl_grube.pdf (cit. on pp. 126, 170, 177).

[87] P. Zimmerer, *Performance of cryogenic silicon microstrip detectors at the COMPASS experiment*, 2011, URL: https://wwwcompass.cern.ch/compass/publications/theses/2011_dpl_zimmerer.pdf (cit. on pp. 126, 127).

[88] M. Leeb, *Optimization of the Clustering and Tracking Algorithms of the Silicon Microstrip Detectors for the COMPASS Experiment*, 2011, URL: https://wwwcompass.cern.ch/compass/publications/theses/2011_dpl_leeb.pdf (cit. on p. 126).

[89] Pascal Sainvitu, *M2 Test Zone – Bld 888*, English, 15 pp., URL: https://edms.cern.ch/document/2647906, October, 2021 (cit. on pp. 137, 141).

[90] A. Dziuba, *private communication*, URL: adzyuba@cern.ch (cit. on pp. 147–149, 152).

[91] S. Helbing, *Elastic muon-electron scattering in the AMBER Pilot Run*, Batchelor's Thesis (in preparation): E18, Technical University of Munich, 2022 (cit. on pp. 159, 190).

[92] A.-M. E. Dinkelbach, *Precision Tracking and Electromagnetic Calorimetry Towards a Measurement of the Pion Polarisabilities at COMPASS*, 2010, URL: https://wwwcompass.cern.ch/compass/publications/theses/2010_phd_dinkelbach.pdf (cit. on pp. 166, 167, 170).

[93] R. de Masi, *Development of a cryogenic silicon detector system and study of strange particle production in deep inelastic scattering*, 2004, URL: https://wwwcompass.cern.ch/compass/publications/theses/2004_phd_de_masi.pdf (cit. on p. 166).

[94] K. A. Bicker, *Construction and Commissioning of a Cooling and Support Structure for the Silicon Detectors for the COMPASS Experiment*, 2011, URL: https://wwwcompass.cern.ch/compass/publications/theses/2011_dpl_bicker.pdf (cit. on pp. 166, 172).

[95] K. Borer et al., *Charge collection efficiency and resolution of an irradiated double-sided silicon microstrip detector operated at cryogenic temperatures*, Nuclear Instruments and Methods in Physics Research Section A: Accelerators, Spectrometers, Detectors and Associated Equipment **440** (2000) 17, ISSN: 0168-9002, URL: https://www.sciencedirect.com/science/article/pii/S0168900299008001 (cit. on p. 166).

[96] R. M. Wagner, *Commissioning of Silicon Detectors for the COMPASS Experiment at CERN*, Diploma Thesis: Technical University of Munich, 2001, URL: https://wwwcompass.cern.ch/compass/publications/theses/2001_dpl_wagner.pdf (cit. on p. 168).

[97] S. Grabmüller, *Cryogenic Silicon Detectors and Analysis of Primakoff Contributions to the Reaction $\pi^- Pb \to \pi^-\pi^-\pi^+ Pb$ at COMPASS*, Presented 27 Sep 2012, 2012, URL: https://cds.cern.ch/record/1492155 (cit. on p. 171).

[98] P. Abbon et al., *The COMPASS setup for physics with hadron beams*, Nuclear Instruments and Methods in Physics Research Section A: Accelerators, Spectrometers, Detectors and Associated Equipment **779** (2015) 69, ISSN: 0168-9002, URL: https://www.sciencedirect.com/science/article/pii/S0168900215000662 (cit. on p. 171).

[99] CEA-Irfu, *ANIBUS Control System; 2009-2021*,
URL: https://www.automation.siemens.com/sce-static/learning-training-documents/classic/advanced-programming/b03-control-engineering-en.pdf (cit. on p. 172).

[100] K. Heinemann, *Investigation of the Alignment and Clustering Algorithm for the Silicon Microstrip Detectors of COMPASS*,
Master's Thesis: E18, Technical University of Munich, 2018 (cit. on p. 189).

[101] M. Hartmeier,
Evaluation of the MuPix8 Pixel Detector Performance for Proton Radius Measurement,
Batchelor's Thesis: E18, Technical University of Munich, 2019 (cit. on p. 190).

[102] *CERN Secondary Beam FAQ*, https://espace.cern.ch/efthymio/Lists/SecondaryBeamsFAQ/AllItems.aspx (cit. on p. 209).

List of Figures

List of Tables

List of Abbreviations

ALICE	A Large Ion Collider Experiment. 22, 24, 90
AMBER	Apparatus for Meson and Baryon Experimental Research. iii, v, vi, 3, 5, 7, 12, 16, 28, 33, 46–48, 51, 70, 71, 90, 102–105, 107, 112, 127, 128, 158, 165, 169, 170, 177, 180, 182, 187, 189–191, 196, 209, 249
COMPASS	COmmon Muon Proton Apparatus for Structure and Spectroscopy. iii, v, vi, 5, 22, 44, 46, 47, 51–55, 60, 65, 69–71, 98, 107–109, 111, 117, 123, 127, 161, 165, 168–171, 177, 179–181, 185, 187, 189–191, 206
MUONE	Muon on Electron elastic scattering. 91, 102, 105, 107
PRAD	Proton Radius. 4–6
ACTAF2	Active Target For FAIR 2. 51, 52, 59, 61, 122, 161, 246
ADC	Analog-to-Digial Converter. 60, 83, 126, 128, 168, 170, 178, 179, 181
ALPIDE	ALICE Pixel Detector. 22–25, 27, 36, 48, 109, 126
ANSIS	ANalysis SYStem. 18
ANTOK	Analysis Tool Kit. 69, 71
APV25	Analog Pipeline [Voltage Mode] in 0.25 μm silicon CMOS technology. 53, 55, 61–64, 118, 126, 128, 131, 165, 166, 168–170, 173, 177
ASIC	Application-Specific Integrated Circuit. 168
B6	Bend 6. 15
BMBF	Bundesministerium für Bildung und Forschung. 190
BMS	Beam Momentum Station. 15, 16, 48, 91, 110, 112, 126, 159, 161
BOS	Beginning Of Spill. 209
BT	Beam Trigger. 110, 112
BT1A	Beam Trigger 1A. 53, 55, 56
BT1B	Beam Trigger 1B. 53, 55, 56
BT2A	Beam Trigger 2A. 55, 56
CAD	Computer Aided Design. 70

CDR	Central Data Recording. 70
CEDAR	Cherenkov Detector with Achromatic Ring focus. 16, 107, 109, 111
CERN	Conseil Européen pour la Recherche Nucléaire. 3, 5, 12, 16, 17, 70, 107, 121, 174, 187, 190, 191, 207, 220
CMS	Compact Muon Solenoid. 168
CoG	Center-of-Gravity. 132
CORAL	COMPASS Reconstruction and Analysis. 69–71
CRC32	Cyclic Redundancy Check (32-bit). 209
CREMA	Charge Radius Experiment with Muonic Atoms. 6
CTA	CERN Tape Archive. 54, 70, 207, 220
DAQ	Data Acquisition. iii, v, 15, 23, 28, 46, 47, 51, 53–55, 58, 66–68, 70, 74, 105, 108–112, 116, 118, 135, 147, 149–151, 158, 159, 161, 162, 165, 170, 183, 187, 205, 207, 208
DFG	Deutsche Forschungsgemeinschaft. 190
DST	Data Summary Tree. 71
ECAL	Electromagnetic Calorimeter. 39, 70
ECAL2	Electromagnetic Calorimeter 2. 15
EE	Extraction End. 209
EHN2	Experimental Hall North 2. 107
EOC	End of Cycle. 209
EOS	End of Spill. 209
EP-DT	Experimental Physics - Detector Technologies. 174, 187, 190
ESEPP	Elastic Scattering of Electrons and Positrons on Protons. 39
FPGA	Field Programmable Gate Array. 28, 170, 177
FriDAQ	Free-Running Trigger-less Data Acquisition System. 15, 22, 28, 109
GDML	Geometry Description Markup Language. 70, 71
GEANT4	Geometry And Tracking 4. 13, 15, 24, 70, 84, 85, 90, 105, 189
GEM	Gas Electron Multiplier. 112, 114–116, 168
GeSiCa	GEM-Silicon Control and Acquisition. 170
GF	GEM Free-Running. 15
HCAL	Hadronic Calorimeter. 70
HLL	Halbleiter Labor. 166
HLT	High-Level Trigger. 28, 189

I^2C	Inter-Integrated Circuit. 168
iFDAQ	Intelligent FPGA-based Data Acquisition System. 109
iFTDC	Intelligent FPGA-based Time-to-Digital-Converter. 55, 66, 67, 83, 135, 136, 147, 151, 156, 208–210, 249
IKAR	Ionization Chamber for Hadronic Reactions. 17, 19, 21, 109, 112, 114, 121, 122, 138, 149, 152, 158, 162, 196, 213
ITS	Inner Tracking System. 22
LHC	Large Hadron Collider. 168
LoI	Letter of Intent. iii, v, 189
MAMI	Mainzer Mikrotron. iii, v, 17, 59
MAPS	Monolithic Active Pixel Sensor. 22
mDST	mini-DST. 69, 207, 220
MF2	Muon Filter 2. 15, 65
MUSE	Muon proton Scattering Experiment. 6
MWPC	Multi-Wire Proportional Chamber. 15, 16, 111, 112
NIM	National Instrument Module. 209
NIST	National Institute for Standards and Technology. 19
NTP	Normal Temperature and Pressure. 42, 80
PHAST	Physics Analysis Software Tools. 69, 71
PID	Proportional-Integral-Derivative. 172
PLC	Programmable Logic Controller. 62, 165, 172, 174
PMMA	Polymethylmethacrylate. 36
PMT	Photomultipier Tube. 55, 56, 117
PNPI	Petersburg Nuclear Physics Institute. iii, v, 17
PRES	Proton Radius in Electron Scattering. 17, 59
PRM	Proton-Radius Measurement. 3, 12, 14, 15, 23, 28, 33, 38, 46, 47, 107, 111, 113, 117, 162, 189, 190, 196
PRTM	Proton Radius Test Measurement. 205–207, 249
ROOT	Rapid Object-Oriented Technology. 69–71
SFH	Scintillating-Fiber Hodoscope. 22–25, 27, 28, 31, 32, 36, 46–48, 108, 109, 117, 162
SGADC	Silicon and GEM ADC. 170
SINTEF	Stiftelsen for Industriell og Teknisk Forskning. 166
SiPM	Silicon Photomultiplier. 22, 24–26
SM1	Spectrometer Magnet 1. 15, 52, 114, 196
SM2	Spectrometer Magnet 2. 15, 52, 114, 196

SPD	Silicon-Pixel detector. 22–25, 27, 29, 31, 32, 36, 46–48, 108, 109, 126, 162
SPS	Super Proton Synchrotron. 3, 16, 43, 44, 55, 67, 209
SPSC	Super Proton Synchrotron Committee. iii, v, 107, 158, 162, 190
TCS	Trigger Control System. 54, 55, 68, 69, 123, 126–128, 136, 170, 208, 209
TDC	Time-to-Digital Converter. 53, 67, 136
TGEANT	Total Geometry And Tracking. 15, 70, 85
TPC	Time Projection Chamber. iii, v, 3, 5, 11–15, 17–22, 28, 30, 32–34, 37, 38, 40–43, 47–49, 51–55, 58–61, 66–69, 73–78, 80–85, 88, 90, 95–97, 99, 103–105, 107–116, 118, 120–122, 135, 138–142, 144, 147–154, 156–159, 161, 162, 165, 189, 190, 193, 194, 206, 207, 213, 220, 246
TRLO	Trigger Logic. 66–69, 74, 81–83, 95, 135, 136, 138, 147, 208, 209, 220
TUM	Technical University of Munich. 190
UTS	Unified Tracking Station. iii, v, 22, 23, 29, 32, 36–38, 46–49, 108, 109, 117, 126, 162, 190
WE	Warning Extraction. 209
WWE	Warning Warning Extraction. 209